POLYTECHNIQUE MONTRÉAL

affiliée à l'Université de Montréal

High bit rate wireless and fiber-based terahertz communication

KATHIRVEL NALLAPPAN

Département de génie électrique

Thèse présentée en vue de l'obtention du diplôme de *Philosophiæ Doctor*

Génie électrique

Décembre 2020

POLYTECHNIQUE MONTRÉAL

affiliée à l'Université de Montréal

Cette thèse intitulée:

High bit rate wireless and fiber-based terahertz communication

présentée par **Kathirvel NALLAPPAN**

en vue de l'obtention du diplôme de *Philosophiæ Doctor*

a été dûment acceptée par le jury d'examen constitué de :

Jean-François FRIGON, président

Maksim SKOROBOGATIY, membre et directeur de recherche

Chahé NERGUIZIAN, membre et codirectrice de recherche

Christian CARDINAL, membre

Xiupu ZHANG, membre externe

DEDICATION

I would like to dedicate this thesis to my beloved parents and my brother for their unconditional love and support

ACKNOWLEDGEMENTS

RÉSUMÉ

Dans le spectre électromagnétique, la bande des térahertz s'étend de 100 GHz à 10 THz (longueurs d'onde de 3 mm à 30 µm). Des décennies auparavant, le spectre des THz était connu sous le nom de « gap térahertz » en raison de l'indisponibilité de sources et détecteurs efficaces à ces fréquences. Depuis quelques années, la science a évolué pour faire migrer la technologie THz des laboratoires aux produits commerciaux. Il existe plusieurs applications des ondes THz en imagerie, spectroscopie et communications. Dans cette thèse, nous nous intéressons aux communications THz à travers deux objectifs. Le premier objectif est de développer une source THz de haute performance dédiée aux communications et basée sur les technologies optiques avec des produits commerciaux uniquement. Le second objectif est de démontrer l'utilisation de fibres optiques afin de renforcer la robustesse des communications THz sans fil.

Nous débutons cette thèse avec une revue de la littérature scientifique sur le sujet de la communications THz sans fil et filaire. D'abord, nous discutons des deux méthodes communément utilisées (électronique et optique) pour démontrer des liens de communications THz avec leurs avantages et inconvénients. Nous présentons par la suite la possibilité d'utiliser un système de spectroscopie THz pour des applications en communications avec des modifications mineures au montage. Nous présentons ensuite plusieurs applications gourmandes en bande passante qui pourraient bénéficier du spectre THz, incluant la diffusion en continu (*streaming*) de flux vidéo aux résolutions HD et 4K non compressés. Ensuite, nous discutons de la motivation d'utiliser de longues fibres THz et notamment du fait qu'elles ne sont pas destinées à remplacer les fibres optiques conventionnelles de l'infrarouge, mais plutôt à augmenter la robustesse des liens THz sans fil. En particulier, les fibres THz peuvent être utilisées pour garantir le lien de communication dans des environnements géométriques complexes ou difficile à atteindre, ainsi que pour immuniser le lien THz aux attaques de sécurité. Plusieurs designs de fibres et guides d'onde précédemment démontrées dans la littérature sont discutés avec, entre autres, leurs méthodes de fabrication respectives. Nous discutons ensuite de la possibilité d'utiliser un simple guide d'onde diélectrique et sous-longueur d'onde pour transmettre l'information à un débit de l'ordre de plusieurs Gbps sur une distance de quelques mètres.

Deuxièmement, nous détaillons l'assemblage d'un système de spectroscopie THz à fréquence fixe (CW) pour la caractérisation de guides d'ondes de différentes longueurs. En guise d'exemple, les propriétés du Teflon et les caractéristiques modales de propagation d'un tube métallique sont montrées. Le système de spectrosopie est par la suite modifié afin de construire un système de communications THz.

Troisièmement, nous discutons du développement du système de communications THz basé sur la photonique capable d'opérer jusqu'à des débits d'au plus 6 Gbps. La caractérisation détaillée des composants utilisés dans l'assemblage du système est détaillée. Ce système peut être utilisée pour étudier plusieurs composants THz passifs tels que des coupleurs, filtres, multiplexeurs, etc. Nous démontrons ensuite la possibilité du système de diffuser en continu des flux vidéo non-compressés HD (60 fps) et 4K (30 fps). La manière de connecter la caméra 4K avec l'émetteur THz et d'enregistrer/diffuser avec le récepteur est détaillée. La performance de la transmission 4K est étudiée en mesurant les images noires (perdues). Nous en concluons qu'il est aujourd'hui possible de réaliser des liens courte-distance pour la transmission de flux vidéo de haute qualité avec l'aide des liens THz sans fil.

Quatrièmement, nous présentons une étude numérique et expérimentale détaillée d'une fibre à cœur solide sous-longueur d'onde pour transmettre de l'information. Nous définissons aussi les principaux défis et compromis dans l'implémentation du lien. En particulier, le guide d'onde sous-longueur est fait d'un cœur de polypropylène avec une gaine d'air ou de matériau poreux. Nous étudions la performance d'un lien de 10 mètres à une fréquence de porteuse de 128 GHz (longueur d'onde de 2.34 mm) pour plusieurs diamètres de cœur (0.57 − 1.75 mm) et des taux de transfert jusqu'à 6 Gbps. Nous trouvons que, dépendamment du diamètre de la fibre, la qualité du signal transmis est soit limitée par les pertes de propagation modales, soit par la vitesse de groupe (GVD). Une transmission sans erreur sur plus de 10 mètres est réalisée avec un taux de transfert de 4 Gbps en utilisant la fibre de 0.57 mm de diamètre. Finalement, le budget de puissance de ce lien fibre est comparé à celui d'un lien sur l'espace libre et nous démontrons qu'un lien fibré peut être une excellente solution pour plusieurs applications de courte distance.

Finalement, nous concluons cette thèse en présentant la fabrication de composants THz passifs tels que des polariseurs, des plaques de phase pour la génération de faisceau à moment angulaire orbital et nous proposons le design d'un photomixeur à fréquence continue de haute puissance.

ABSTRACT

The Terahertz (THz) spectral range spans from 100 GHz to 10 THz (wavelength: 3 mm to 30 µm) in the electromagnetic spectrum. Decades ago, the THz spectral range is often named as 'THz gap' due to the non-availability of efficient THz sources and detectors. In the recent years, the science has evolved in bringing the THz technology from lab scale to commercial products. There are several potential applications of THz frequency band such as imaging, spectroscopy and communication. In this thesis, we focus on THz communications by addressing two objectives. The first objective is to develop a high-performance photonics-based THz communication system using all commercially available components. The second objective is to demonstrate the THz-fiber based communications, which can be used to increase the reliability of THz wireless links.

We begin this thesis with a scientific literature review on the subject of THz wireless and fiber-based communications. First, the two different methodologies (all electronics based and photonics-based THz system) that is commonly used in the demonstration of THz communications is discussed along with their advantages and challenges. We then present the flexibility of photonics-based THz system where it is possible to switch it with minor modifications for THz spectroscopic studies and THz communication applications. Several bandwidth hungry applications that demands the use of THz spectrum for next generation communications is detailed. This includes the streaming of uncompressed HD/4K and beyond high-resolution videos, where the THz spectrum can be beneficial. Next, the motivation of using long THz fibers is discussed and we convince the readers that the THz fibers are not meant to replace the fibers in the optical-infrared region but to increase the reliability of THz wireless links. Particularly, the THz fibers can be used to provide connectivity in complex geometrical environments, secure communications and signal delivery to hard-to-reach areas. Several novel fiber/waveguide designs along with their fabrication technologies from the literature are presented. We then show that a simple solid core dielectric subwavelength fiber can be used to transmit the information in the order of several Gbps to a distance of a few meters.

Second, the assembling of continuous wave (CW) THz spectroscopy system for characterizing THz fibers/waveguides of different lengths is detailed. As an example, the measured material

properties of Teflon and the modal propagation characteristics of metallic tube waveguides are shown. The CW spectroscopy system is then modified to build the THz communication system.

Third, the development of a high-performance photonics-based THz communication system, which is capable enough to receive up to the bitrate of 6 Gbps, is discussed. A detailed characterization of the components that is used in assembling the THz communication system is presented. The THz communication system can be used to study several passive THz components such as couplers, filters, multiplexers etc. We then demonstrate the capability of the system by streaming the uncompressed HD (60 fps) and 4K (30 fps) videos for the distance of ~1 m. The methodologies to interconnect the 4K camera with THz transmitter and display/recording unit with THz receiver is shown. The performance of the uncompressed video transmission is analysed by measuring the black frames (dropped frames) and concluded that it is now possible to realize a short-range high-quality video transmission using THz wireless links for commercial applications.

Fourth, we present an in-depth numerical and experimental study of a solid core subwavelength dielectric THz fibers for information transmission and define main challenges and trade-offs in the link implementation. Particularly, we use air or foam-cladded polypropylene-core subwavelength dielectric THz fibers of various diameters (0.57-1.75 mm) to study link performance as a function of the link length of up to ~10 m, and data bitrates of up to 6 Gbps at the carrier frequency of 128 GHz (2.34 mm wavelength). We find that depending on the fiber diameter, the quality of the transmitted signal is mostly limited either by the modal propagation loss or by the fiber velocity dispersion (GVD). An error-free transmission over 10 meters is achieved for the bit rate of 4 Gbps using the fiber of smaller 0.57 mm diameter. Finally, the power budget of the rod-in-air subwavelength THz fiber-based links is compared to that of free space communication links and we demonstrate that fiber links offer an excellent solution for various short-range applications.

Finally, we conclude the thesis by presenting the fabrication of some of the essential passive THz components such as wire-grid polarizer, phase plates for orbital angular momentum generation and proposed the novel design of high-power continuous wave THz photomixer.

TABLE OF CONTENTS

LIST OF TABLES

LIST OF FIGURES

-

LIST OF SYMBOLS AND ABBREVIATIONS

c   Velocity of light

λ   Wavelength of light

μ_0 Permeability of free space

ε_0 Permittivity of free space

σ   Gaussian Beam waist parameter related to FWHM of Gaussian beam

ABS   Acrylonitrile Butadiene Styrene

AlGaAs   Aluminium Gallium Arsenide

ASK   Amplitude Shift Keying

BERT   Bit Error Rate Tester

CMOS   Complementary metal-oxide Semiconductor

CW   Continuous wave

DAST   4-N, N-Dimethylamino-4'-N'-Methyl-Stilbazolium Tosylate

DSTMS   4-N, N-Dimethylamino-4'-N'-Methyl-Stilbazolium 2,4,6-

               Trimethylbenzenesulfo-nate

DFB   Distributed Feedback

DFG   Difference Frequency Generation

EDFA   Erbium Doped Fiber Amplifier

EO   Electro-optic

FEC   Forward Error Correction

FPGA   Field-Programmable Gate Array

FWHM   Full Width Half Maximum

FSO   Free Space Optics

GaAs   Gallium Arsenide

Gbps	Giga Bit per Second
GPS	Global Positioning System
GVD	Group Velocity Dispersion
HD	High Definition
HFSS	High-Frequency Structure Simulator
InGaAs	Indium Gallium Arsenide
InP	Indium Phosphide
IP	Internet protocol
IR	Infrared
IRS	Intelligent Reflecting Surface
LAN	Local Area Network
LDPE	Low Density Polyethylene
LIDAR	Light Detection and Ranging
LiNbO$_3$	Lithium Niobate
LNA	Low Noise Amplifier
LoS	Line of Sight
MgO:PPLN	Magnesium Oxide doped Periodically Poled Lithium Niobate
MIMO	Multiple Input Multiple Output
MMIC	Microwave Monolithic Integrated Circuits
MZM	Mach-Zehnder Modulator
NaOH	Sodium Hydroxide
NEP	Noise Equivalent Power
NRZ	Non-Return to Zero
NLoS	Non-line of Sight

OH1   2-(3-(4-Hydroxystyryl)-5,5-Dimethylcyclohex-2-enylidene) malononitrile

OAM   Orbital Angular Momentum

OOK   ON-OFF keying

PCIe   Peripheral Component Interconnect Express

PDM   Polarization Division Multiplexing

PP   Polypropylene

PPG   Pulse Pattern Generator

PRBS   Pseudo Random Bit Sequence

PSK   Phase Shift Keying

QAM   Quadrature Amplitude Modulation

QCL   Quantum Cascade Laser

QPSK   Quadrature Phase Shift Keying

RADAR   Radio Detection and Ranging

RF   Radio Frequency

RI   Refractive Index

RTD   Resonant Tunneling Diode

SATA   Serial AT Attachment

SBS   Stimulated Brillouin Scattering

SHM   Second Harmonic Mixing

SOA   Semiconductor Optical Amplifier

SDM   Spatial Division Multiplexing

SNR   Signal to Noise ratio

SONAR   Sound Navigation and Ranging

SSD   Solid State Drive

THz   Terahertz

THz-TDS   Terahertz-Time Domain System

UTC-PD   Uni-traveling Carrier-Photodiode

UV   Ultra-Violet

WDM   Wavelength Division Multiplexing

ZBD   Zero Bias Schottky Detectors

LIST OF APPENDICES

CHAPTER 1 INTRODUCTION

Edholm's law of bandwidth states that the required data rate in telecommunication is doubled every 18 months [1]. At present, high-speed internet is enabled by fast communication networks, based on fiber optics that operate in the optical infrared band. At the same time, data rates of standard wireless devices that operate in the radio and microwave bands are currently orders of magnitude slower than the data rates offered by a single, fiber-optic, channel. As the fiber-optic networks are stationary, and do not offer convenient access to the increasingly mobile end users, wireless communication is the preferred solution for data transfer: as it enables mobile data access. According to the Shannon theorem, the maximum channel capacity is estimated by the channel bandwidth and the signal-to-noise ratio of the received signal [2]. On one hand, the spectral efficiency can be improved using advanced modulation and multiplexing techniques [3]. However, there is a maximum limit, beyond which the spectral efficiency cannot be improved for the given SNR. On the other hand, the channel bandwidth can be increased to improve the channel capacity. Therefore, moving towards a higher frequency band is beneficial. The high-speed wireless communications enabled by infrared and visible light frequencies can support both indoor and outdoor secure communication links [4-7]. However, the effect of thermal noise, scintillation, atmospheric turbulence, dust, fog, rain, etc., are the key challenges in establishing the wireless links in these frequency bands. Moreover, the requirement of precise alignment of optical wireless transceivers and limit in the maximum transmission power level, due to eye/skin safety, restricts the maximal bitrate and link distance [8]. At the same time, the THz waves (100 GHz-10 THz) offer much larger bandwidth when compared with microwaves, promising wireless transmission rates similar to those of fiber-optic links [9]. As shown in Fig.1.1, the THz band is located between the infrared and microwave region of the electromagnetic spectrum. Many dielectric materials, such as plastics, wood, concrete etc., are transparent to THz waves and therefore enable a wireless link between blocks (rooms) for example in the case of indoor wireless communications. Although the free space transmission of THz waves is affected by rain, snow etc., the effect is much lower when compared to the infrared and visible frequency bands [10]. In this context, the THz waves can be the next frontier in wireless communications as they offer a solution to this bottleneck, and allow wireless data rates comparable to those of optical channels [11, 12].
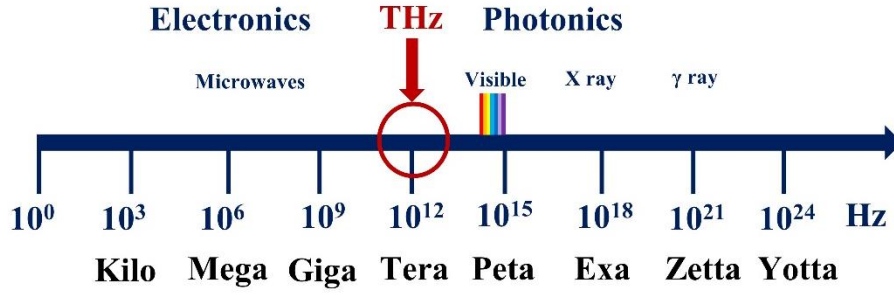
Figure 1.1: The Electromagnetic spectrum

1.1   Context and challenges

Over several years, the research on the development of high-power THz sources is being done using several methods [13]. The vacuum electronics' sources, such as backward wave oscillators [14], free electron lasers [15], synchrotrons [16] etc., have been studied for the generation of high-power THz waves . Though these devices generate high output power (>10 dBm), it is difficult to transform these devices for communication applications as they are bulky and lack several requirements, such as high-speed modulation, frequency tunability, frequency stability, etc. The prototypes for a THz wireless communication system has been proposed and demonstrated mainly using solid state electronics and photonics sources [17]. The solid-state electronics' sources, such as resonant tunneling diodes [18], frequency multiplier chains [19] etc., offer high-output power, particularly at a lower THz band (<300 GHz), which limits the maximal bitrate and link distance. On the other hand, the photonics-based THz sources (frequency difference generation using photomixing) can reach a higher THz band, enabling large bandwidth, but with relatively low optical to THz conversion efficiency [20, 21]. Even though the output THz power of the photomixing approach is low at this point, the proposed technique has several advantages. Firstly, the photonics-based THz wireless communication system can be easily integrated to the matured fiber-optic networks, which, in turn, reduces the implementation cost for the next generation high-speed wireless systems. Secondly, photonics technologies provide a high modulation index, enable easier higher order modulation (phase and amplitude coding), and wide band frequency tunability when compared with the solid-state electronics-based THz communication systems. By using proprietary system components within a photonics-based THz transmitter, and electronics-based receiver, several THz wireless communication links have been demonstrated. Therefore, the

commercial development of such a hybrid approach can be considered as the first-age, THz communication system [22].

In THz communications, until now, the main focus has been on wireless-based links; whereas the THz waveguide-based links are least explored. Wireless THz communications hold many advantages, including convenience in mobility for the end user, ease in scaling up the network, flexibility of device interconnectivity, etc. However, there are still many challenges. For example, the high directionality of the THz beams requires careful positioning of the transmitter and receiver antennas to minimize alignment errors. Similarly, for complex buildings or between moving objects, highly complex beam steering algorithms are necessary for reliable THz communication links. Moreover, free-space THz links have higher chances of eavesdropping; thereby increasing the challenges of secure communications [23]. On the other hand, the THz waveguides are compact, flexible, and provide reliable coupling to the transmitter and receiver covering complex geometrical paths in both static and dynamic environments. Moreover, the waveguide-based links are immune to external electromagnetic interference and enables secure communications. Therefore, the THz waveguide links can be used to increase the reliability of the future THz wireless networks.

In **chapter 2** of this thesis, a detailed review on both the THz wireless communication system and various novel THz waveguide designs, having low loss and low dispersion, are discussed. We then present the contribution and impact of the thesis, which is about the development of photonics-based THz communication system and THz fiber-based communication links.

1.2 General motivation and organization of the thesis

In order to meet the demand of various bandwidth hungry applications, moving towards THz frequency band is beneficial. Therefore, the development of high-performance THz communication system is the need of the hour. In achieving this goal, various research groups around the world are working on the development of system components such as modulator, transmitter, receiver, amplifier etc., in realizing an efficient communication system. The THz communication system can be developed by assembling/integrating all these efficient components together. However, the performance of these components may be different when it is assembled/integrated in the communication system when compared to their performance

individually. The performance degradation is due to several factors such as noise, stability, bandwidth etc. For example, the noise signal that arises from one of the components in the first stage may deteriorate the performance of another component in the second stage and so on. Therefore, the detailed analysis of a THz communication system that is assembled using all the high-performance components is important as it dictates the throughput of the communication link. In this view, only a very few groups in the world demonstrates the analysis of THz communication system.

As of now, most of the demonstration of high-performance THz system components are limited to the laboratory environment and their commercial availability is still in the stage of infancy. In various demonstrations of THz communication link, at least one of the components used in their system (photomixer for example) was their proprietary component. Therefore, the development and performance analysis of THz communication system that is assembled using all commercial components finds primary importance in advancing the next generation wireless communications. Therefore, the first objective of the thesis is to develop the high-performance THz communication system using all commercially available components. Based on the literature, we decided to build the THz communication system using the photonics approach. In fact, the assembled THz communication system in our laboratory is the first and, so far, only photonics-based system in Canada.

 In developing the photonics-based THz communication system, there are many approaches in the optical laser source that can be used for the generation of THz waves. This includes free running lasers [24], optical frequency combs [25], SBS [26], SOA[27], and the supercontinuum source [28]. Among all these optical sources, employing two free running lasers that are operating in the optical infrared region (with slightly different center wavelengths), for the frequency difference (THz) generation using photomixing, is a simple, cost-effective, and efficient method. Utilizing free running lasers for frequency difference generation requires careful tuning and calibration of the laser wavelengths. To simplify these processes, we purchased the CW THz spectroscopy system (TOPTICA Photonics) [29]; and, then, by using off-the-shelves photonic components, a high-performance THz communication system has been assembled. With minor modifications, the system can be switched quickly for both spectroscopic and communication experiments. In **chapter 3**, we present the CW THz spectroscopy system in detail along with the experimental set

up for characterizing THz waveguides of varying lengths. In addition to the CW THz spectroscopy system, the fabrication of plastic THz fibers using the fiber-drawing technique is also discussed in this chapter.

According to Cisco's index report, it is estimated that among various applications, the transmission of video content occupies almost 80% of the total data traffic by the year 2022 [30]. Therefore, one of the important and immediate applications of THz communication will be the transmission of high-resolution video, such as uncompressed 4K/8K, and so on. It finds applications particularly in the field of telemedicine, sports, virtual reality, etc. In **chapter 4**, we detail the development of photonics-based THz wireless communication system and the demonstration of uncompressed HD and 4K video transmission. When compared to the photonics-based THz system designs from the literature where UTC-PD is used as the THz photomixer, in this work, a PIN photodiode is used whose performance is comparably better at higher THz frequencies [31]. First, the performance of the THz communication system is analysed by measuring the BER as a function of various parameters such as transmitter bias voltage (proportional to THz power), link distance etc. Second, the transmission of uncompressed HD and 4K videos using the developed THz communication system is demonstrated. This is an important demonstration which details the method to integrate the commercially available 4K camera to the THz transmitter and recording unit to the THz receiver unit. This chapter is the transcription of the research article published in IEEE Access entitled "*Live streaming of uncompressed HD and 4K videos using Terahertz wireless links (2018)*"[24]. This work has also been presented at several conferences as shown in appendix A.

Once the THz communication system is assembled, the second objective of this thesis is to utilize the system to characterize various novel waveguide designs and THz system components for next-generation communications. As mentioned in the previous section, the THz fibers are beneficial as it increases the reliability of THz wireless communication links. It is noted that, the intention of THz fibers is to provide an additional support to the THz wireless links and not to replace the optical fibers that operate in the infrared frequency band. In **chapter 5**, we present the detailed study of the THz communication link using THz fiber. When compared to the literature, where hollow core THz fibers are generally used for the demonstration, in this work, a solid-core THz fiber (rod-in-air fiber) fabricated from one of the low-loss materials (polypropylene) is presented. The solid core fibers are generally easy to fabricate, and the propagation loss can be minimized

directly by reducing its thickness. Both theoretical and experimental studies on modal loss, dispersion, and bitrate for the solid core THz fiber are studied in detail. Moreover, this thesis proposes several use cases of THz fiber in various areas of applications. This chapter is the transcription of the research article published in the OSA photonics research journal entitled: "*Dispersion limited versus power limited terahertz communication links using solid core subwavelength dielectric fibers (2020)*"[32]. This work has also been presented at several conferences as shown in appendix A.

In **chapter 6**, the general discussion of the work presented in the thesis is detailed. Particularly, my personal contribution and challenges in the development of THz communication system is discussed. Furthermore, the preliminary experiments using THz fibers are presented. Next, the fabrication of passive components, such as polarizer and phase plates for THz OAM generation that can be used in the next generation THz communication systems is presented. As an example, a spatial division multiplexing technique using our developed THz communication system, is presented. One of the major drawbacks in the photonics-based THz communication system is the THz power. Therefore, the feasibility study on the generation of CW THz signal using difference frequency generation via non-linear crystal and photomixer, is also discussed [33].

In **chapter 7**, we conclude with the summary of the thesis and present the future outlooks of the THz wireless and fiber-based communications.

CHAPTER 2   LITERATURE REVIEW

A detailed scientific review on THz communications is presented in this chapter. The chapter is divided into two sections. The first section presents the review on solid state electronics and photonics-based THz communication systems. The maximal bitrate achieved by several techniques are also covered. In the second section, we introduce the importance of fiber-based THz communications in designing future THz networks and present various waveguide designs with their advantages and limitations. Further, the channel modelling and applications of wireless and fiber-based THz communications are briefly discussed.

2.1   THz communications

According to Edholm's law of bandwidth, the required data rate is doubled every 18 months [1]. Among total global IP data traffic, more than 82% of the traffic by 2022 will be due to all forms of video (gaming, internet video etc.) [30]. Similarly, the cellular data rates will be comparable to the wireless LAN by the year 2030 as shown in Fig.2.1 [12]. Therefore, the wireless network with
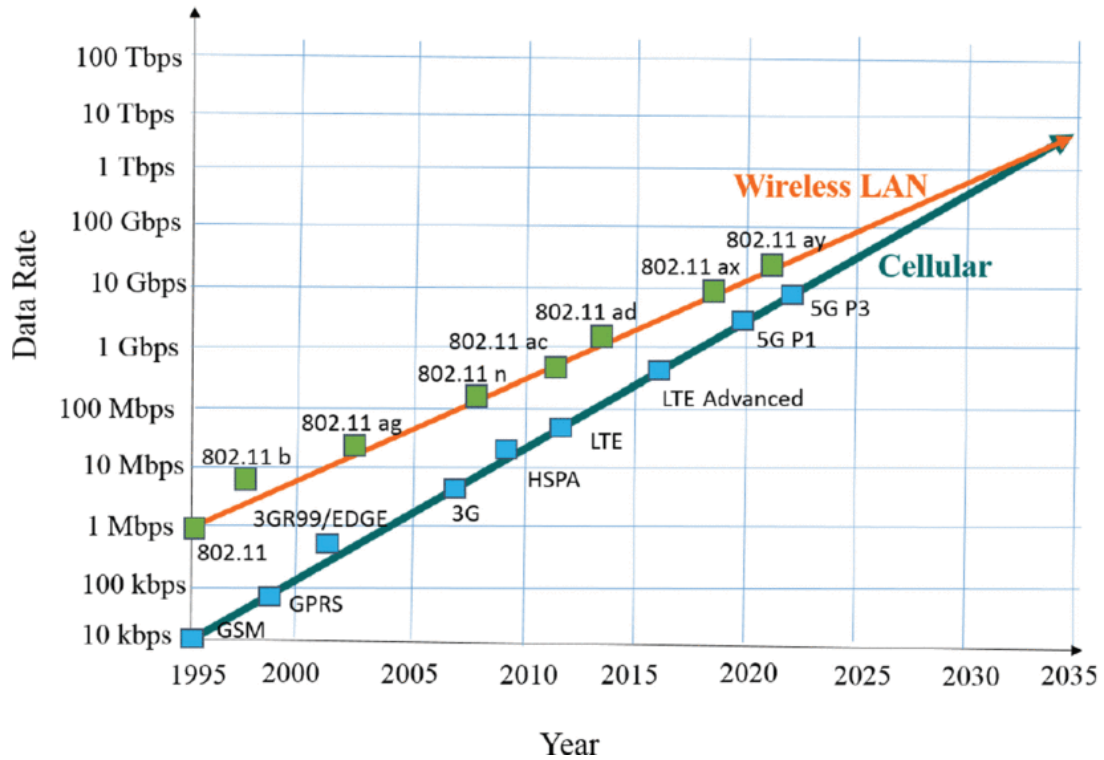
Figure 2.1: The roadmap of wireless LAN and cellular networks up to year of 2035. Reprinted from Ref. [12]

large available bandwidth is in high demand. Compared with other frequency bands, such as, UV, visible, and infrared FSO wireless systems, where the bandwidth is several times higher than the current wireless systems, the THz band offers several advantages that includes low free space attenuation, almost no effect of atmospheric turbulence (scintillation), possible of establishing NLoS communication links, and propagation through concrete wall structures etc., [34-37]. The channel capacity can be estimated using the Shannon's formula that is given in Eq.2.1.

$$C = B \cdot \log_2 \left(1 + \frac{S}{N} \right) \tag{2.1}$$

From Eq. 2.1, C is the channel capacity in bits per second, B is the bandwidth and S/N is the signal to noise ratio. Therefore, even with a simple OOK modulation, the bitrates of several 10's of Gbps can be achieved due to the broad bandwidth of the THz frequency band [38, 39]. Although the THz waves are highly absorbed by the presence of atmospheric water vapour, there are several transmission windows that can be used for short- to long-distance wireless links as shown in Fig.2.2 [20]. From Fig.2.2, we see that, the long distance (~1-10 km) communication links can be established in the frequency range of ~100-150 GHz due to low atmospheric losses, whereas the higher frequency range (~500 GHz) can be considered for the short distance links (~1-100 m) [20]. However, the free space path loss will increase with the frequency. The free space path loss can be compensated for long distance links by designing an efficient and high-gain antenna at both transmitter and receiver end. Therefore, the THz frequency band is considered as the next frontier for wireless communications [11].
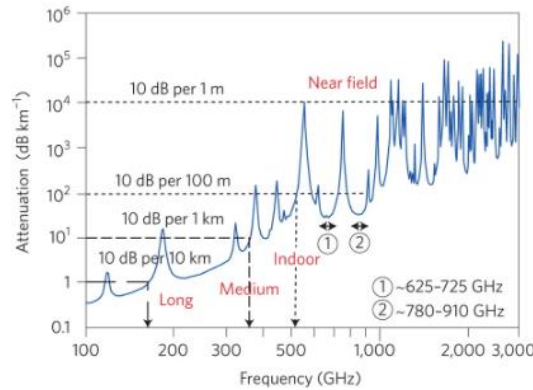
Figure 2.2: Attenuation depended link distance in the THz spectral range. Reprinted from Ref. [20]

There are several excellent review papers that detail the role of THz communications, system designs, their applications, and future research directions [9, 11, 12, 20, 40-45]. In this section, a brief review on the THz communication system based on solid state electronics will be presented. Since the work presented in this thesis is based on the photonics-based THz system, a detailed review for the photonics-based THz communication system and the transmission of ultra-high definition videos will be covered.

2.2 Solid state electronics-based THz communication system

The CW THz generation using solid state electronic sources (frequency up conversion) are one of the common methods that is used in demonstrating the wireless communications [46]. The advancement in both CMOS and MMIC based technology using Si, GaAs, and InP semiconductors offers high power, low cost and compact solutions in the development of next generation communication systems [47-49]. In most cases, the reported THz communication links using all-electronic sources are at lower THz frequency (<300 GHz) due to the maximum limit in the cut-off frequency of the circuits [12, 19]. Recently, the establishment and demonstration of THz communication links at higher frequency (>1 THz) is achieved [50, 51]. Here, we briefly discuss about the frequency multiplier chains and RTD's, which are used as THz sources for communication applications.

2.2.1 Frequency multiplier chains

The frequency multiplier chains are the commonly used circuits in generating the CW THz radiation [52, 53]. Here, the power of the fundamental frequency is transferred to the harmonic signals by utilizing the nonlinear behaviour of the circuits. By proper designs, the frequency doublers, triplers, and even quintuplers can be fabricated [54-56]. Generally, the local oscillators (fundamental frequency synthesizer) operate in the microwave or millimeter frequency band where the high-power sources are commercially available. Although a simple amplitude modulation was carried out during the earlier studies, now, a complex modulation scheme, such as QPSK is demonstrated using frequency triplers [57, 58]. When compared with frequency doublers, the frequency triplers preserves the phase information but with noise in the constellation diagram. On the other hand, the frequency mixer circuits can be used to upconvert the low frequency signals to

THz frequency range by maintaining the linear behaviour of the input at the same time [59]. The schematic of a solid-state frequency multiplier chain based THz transmitter and a coherent receiver is shown in Fig. 2.3 [60]. In this case, the output power at the transmitter is -17.5 dBm for the input power of 9.39 dBm (before SHM) and the maximal bitrate of 3 Gbps was achieved for the link distance of 50 m using QAM respectively. Similarly, in [61], Song *et.al.,* demonstrated the 50 Gbps communication link at the carrier frequency of 300 GHz using QPSK modulation. Using advanced modulation techniques (QPSK and 8PSK) and frequency multiplier chain based MMIC operating at 240 GHz, a 64 Gbps data transmission has been achieved with a link distance of 850 m [62]. By using cubic mixer (frequency Tripler) and by adjusting the power levels of the intermediate frequencies, the peak data rate of 105 Gbps was achieved over 6 channels (bandwidth of each channel is 5 GHz) in the 300 GHz frequency range [63]. Therefore, the development of the frequency synthesizer and power amplifiers using solid state electronics in the THz frequency range can be benefited for short to long range communications.
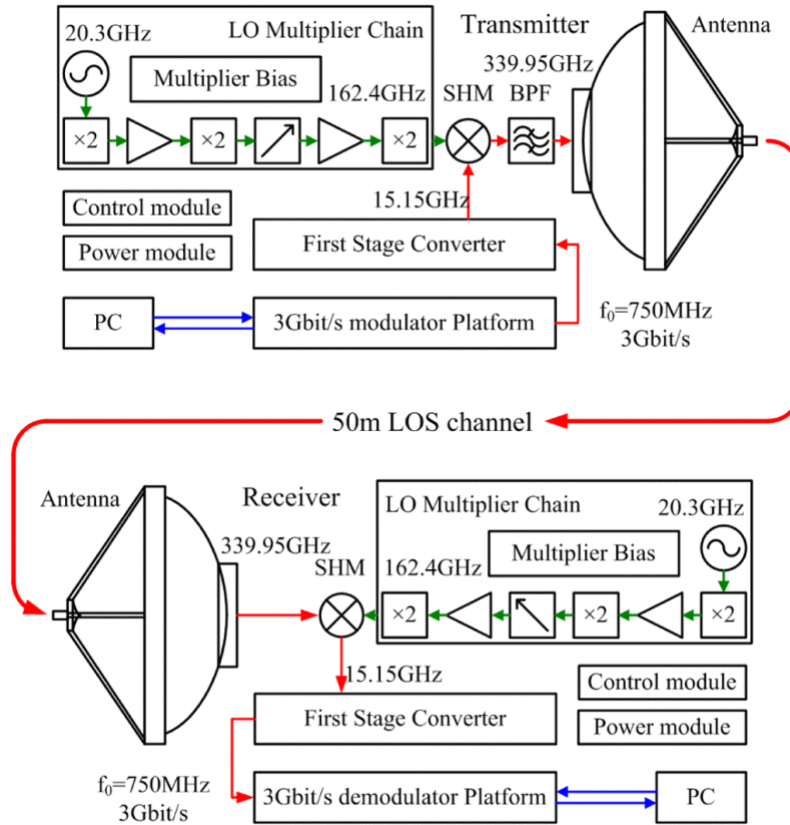
Figure 2.3: Schematic of the 0.34 THz wireless link using frequency multiplier chains. Reprinted from Ref. [60]

2.2.2 Resonant tunneling diodes

RTD's are compact diodes that are fabricated using a stack of thin semiconductor layers, where the electrons can tunnel through the resonant states at particular energy levels [64]. It can be used as high frequency (THz frequency range) oscillators and switches. There are several publications where the RTD's are used as the source to generate the signals in the THz frequency range, which can even reach up to 2 THz [65-70]. In [71], the J-band (220-325 GHz) output power up to 1 mW was demonstrated using RTD. In recent years, the RTD's are used for THz communications, where the data can be transmitted by directly modulating the bias voltage [18, 72-75]. The maximum bitrate of 30 Gbps was achieved by operating the RTD at the carrier frequency of 500 GHz [72]. Similarly, using FDM and PDM technique in the 500-800 GHz frequency band, the maximal bitrate of 28 Gbps per channel were demonstrated [18]. Here, the maximum bitrate can be further improved, however, it is limited only by the PPG and error detector used in their experiments. The RTD's can also be used as THz receivers [76, 77]. Therefore, the RTD's can be used for developing a compact THz communication system for short range links with the bitrate of several 10's of Gb's.

2.2.3 Solid state electronics-based receiver

In THz communications, the solid-state electronic circuits are used as direct or heterodyne receivers while using all-electronic based or photonics-based source as the THz transmitter [78, 79]. The quasi-optical Schottky diodes are generally used as direct detectors in which only the amplitude information is preserved [80]. In such receivers, the responsivities decreases (typically, 2000 V/W at 100 GHz and 100 V/W at 1.5 THz) and NEP's increase (typically, $1\,pW/\sqrt{Hz}$ and $100\,pW/\sqrt{Hz}$ at 1.5 THz) with increase in the THz frequency that limits the maximum bitrate at higher frequencies due to poor SNR [81, 82]. In heterodyne detection, a similar transmitter configuration is generally used at the receiver to generate the same carrier frequency. For example, as shown in fig, 2.3, the similar frequency multiplier chains are used at both transmitter and receiver ends for heterodyne detection. In [83], the carrier frequency with and without data modulation are simultaneously transmitted and the heterodyne detection using GaAs-Field effect transistor was demonstrated. A successful transmission and reception of HD video signal is also presented. We conclude that, while using Schottky diodes, a simple ASK or OOK modulated THz signals can be

detected, which limits the spectral efficiency; whereas the heterodyne detection scheme can improve the spectral efficiency by detecting complex modulation signals at a higher cost.

2.3 Photonics-based THz communication system

In solid state electronics-based THz sources, the challenges are mainly in the wideband spectral accessibility and frequency tunability. Therefore, the available bandwidth is limited for high bitrate transmission and carrier switching or multi-carrier modulation is difficult or may not be possible. On the other hand, the photonics technologies (frequency down conversion) can be an alternative solution, which is compact, low cost and provides wideband tunability, multi-carrier modulation, higher modulation depths, and easier integration with the existing fiber optic networks, etc. As the optical communication in the IR band is a matured technology, several complex modulation formats can be easily realized using off-the-shelves available components, which can be transferred to the THz carrier. Since the first demonstration of THz communication using THz-TDS by transmitting the audio signal [84], there are several approaches using photonics technologies in improving the bitrates are established [20, 85-87]. In photonics approach, the THz radiations are generated using different principles such as photo excitation in photoconductive antenna, optical rectification in nonlinear crystal, DFG in nonlinear crystal, QCL and photomixing in semiconductors [88]. Among these methods, the DFG in nonlinear crystal, QCL and photomixing are used for the generation of CW THz radiation, which is favourable for THz communications applications.

DFG is a second order nonlinear optical process, where the frequency of the generated electromagnetic radiation is the difference between the two input pump frequencies. A monochromatic and tunable THz waves can be generated by simply varying the frequency of one of the pump beams [89, 90]. When compared with the photomixers, the DFG process in nonlinear crystals are efficient, particularly at higher THz frequencies [91]. However, phase matching between the pump beams and the output THz wave is one of the major factors that minimize the thickness of the crystal, reducing the interaction length and thereby limiting the output power [92]. Therefore, in THz communications, there is no work in the literature that is demonstrated using nonlinear crystals as the source of CW THz waves.

QCL is a compact device that generates high power THz radiation with high spectral purity in both pulsed and continuous mode of operation [93]. Many thin layers of alternating semiconductors such as GaAs and AlGaAs are arranged to form periodic modules, which acts as the gain region. The electrons in the gain region are confined into the discrete energy sub bands and when the external electric field is applied, the electrons cascade from period to period emitting the photon with low energy. Therefore, the emitted photon is not determined by the bandgap of the active material but with the designed width of the semiconductor layers forming the gain medium [94]. By modifying the designs of QCL, several high-power THz sources have been demonstrated in the past years [94, 95]. There are few works that demonstrate THz wireless communications at higher frequency (>3 THz) using QCL; however, they are not widely used as they finds difficulty in operating at room temperature and also limited with modulation speed [96-98].

The photomixing in a semiconductor material is an efficient process where the frequency difference of two pump beams are generated as the output. When two CW pump beams operating in the optical IR region are focused onto the gap of the electrode in the semiconductor such as low temperature grown GaAs or InGaAs, the photocarriers are generated. The generated photocarriers oscillate at the beat frequency (THz frequency) of the two pump beams that leads the oscillation of photocurrent under DC bias of the electrodes. The oscillation of photocurrent is then radiated by the antenna into the free space as THz waves [99, 100]. By varying the center wavelengths of one of the pump lasers or both, the output THz frequency can be tuned and therefore a wideband tunability can be achieved efficiently [101]. Although, the optical to THz conversion efficiency is low, the photomixers are widely used in the THz communications due to several advantages as discussed earlier. The CW THz photomixers are generally fabricated using PIN photodiode or UTC-PD. In THz communications, the UTC-PD photomixers are widely used as THz emitters as they are more efficient in optical to THz conversion, which can generate > 10 dBm at lower THz frequencies (<200 GHz) [31, 102].

In CW THz generation using photomixing technique, a similar photomixer at the detector end (without bias voltage) is used for heterodyne detection for spectroscopic applications. However, in THz communications, the solid-state electronics-based receiver are widely used in the literature. Therefore, the hybrid technology using photonics-based THz transmitter and solid-state electronics-based THz receiver, can be considered as the 'first age THz communication system',

which can be used for several commercial applications [20]. The schematic of the basic photonics-based THz communication system is shown in Fig. 2.4. One of the free-running lasers operating in the IR C-band is modulated with a PRBS data sequence using an external LiNb based electro-optic modulator. When compared with direct modulation of the laser using injection current, the recent advances such as hybrid Silicon and LiNb electro optic modulators are capable enough for high speed modulation, which can reach >100 Gbps [103]. The modulated laser beam is then combined with the direct laser beam and focused on to the photomixer for THz generation. The generated and transmitted THz signal is then detected and demodulated using the ZBD (envelope detection). The demodulated baseband signal is then amplified using LNA and the performance is analysed using BERT and oscilloscope.
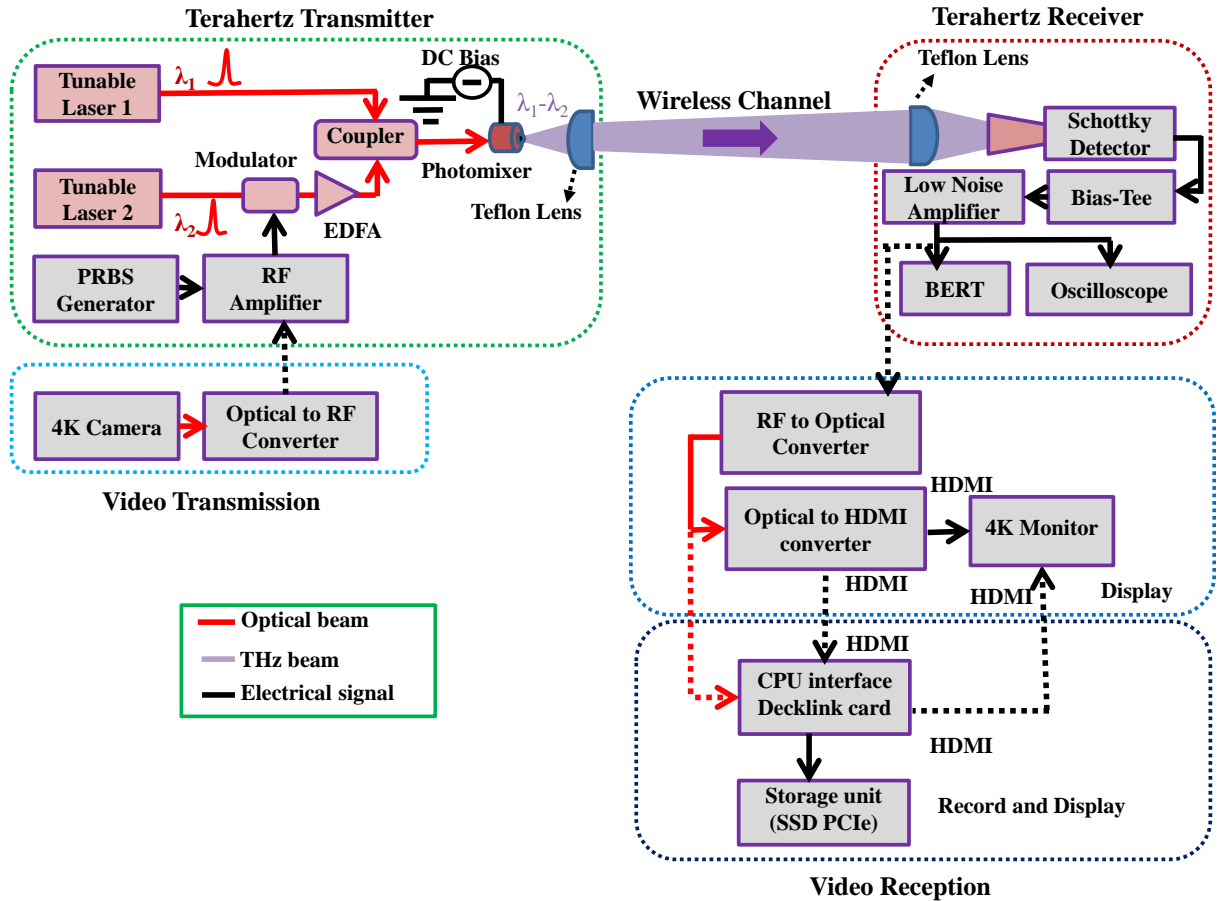
Figure 2.4: Schematic of the photonics-based THz wireless communication system with video transmission and reception modules [24]

In the following, we review the photonics-based THz communication systems that uses different laser sources such as free-running lasers, dual mode lasers and frequency comb lasers [86].

2.3.1 Free-running lasers

Photomixing using two independent free-running lasers as the optical source is the simplest system configuration used in CW THz generation. The lasers are usually operated in the IR frequency band. Since the lasers are free-running, the generated THz signal is also a free-signal with large linewidth in the order of few 10's of MHz [104]. In the case of OOK modulation, the bandwidth is larger and therefore, the broad linewidth of the THz carrier will not degrade the performance of the system [104]. There are several publications that demonstrate the transmission of high bitrate data using free-running lasers as the optical source [105, 106]. Since the lasers are free-running and both the sources are not coherent, it is expected that the performance of the system will degrade for higher order modulations such as QPSK and QAM. However, the recent work shows that, it is possible to transmit ~100 Gbps data using free-running lasers and coherent detection in the receiver at the carrier frequency of 350 GHz over the link length of 2 m [107].

2.3.2 Dual mode lasers

In the case of free-running optical laser source, the phase noise limits the maximum efficiency of a higher order modulation codes. By designing and fabricating two laser lines with different wavelengths in the same cavity, the effect of phase noise can be minimized. This is achieved because, both the laser modes experience the same fluctuations. At the same time, the lasers can be compact and consumes low power when compared with the free-running lasers [108]. There are several integration techniques used in the fabrication of dual mode lasers [109-111]. Recently, in [112], Tang *et.al.*, demonstrated the transmission of 25 Gbps data by directly modulating the laser at the carrier frequency of 96.1 GHz, 612 GHz and 1.29 THz respectively.

2.3.3 Frequency comb lasers

The optical frequency comb (OFC) source-based THz generation is the widely used technique in THz communication [86]. Here, the phase of the adjacent optical comb lines is locked and therefore, the effect of phase noise can be minimized with high spectral purity and stability.

Therefore, an efficient higher order modulation (QPSK, QAM etc.,) can be carried out. Another advantage of OFC based sources in THz communication is the possibility of multicarrier modulation. In [113], Jia *et.al* demonstrated the transmission of 120 Gbps data using QPSK modulation over 6 channels in the 350-475 GHz frequency range. A similar transmission capacity is achieved by 2 x 2 MIMO system using multicarrier modulation in the same frequency range [114]. Recently, by utilizing OFC source and polarization multiplexing, the maximum line rate of 612.5 Gbps (2 x 300 Gbps) was achieved in the 320-380 GHz frequency range [115]. The schematic of the experimental set up of OFC based THz communication link is shown in Fig. 2.5. Therefore, the OFC based THz generation is promising to achieve the full capacity of the THz frequency band.
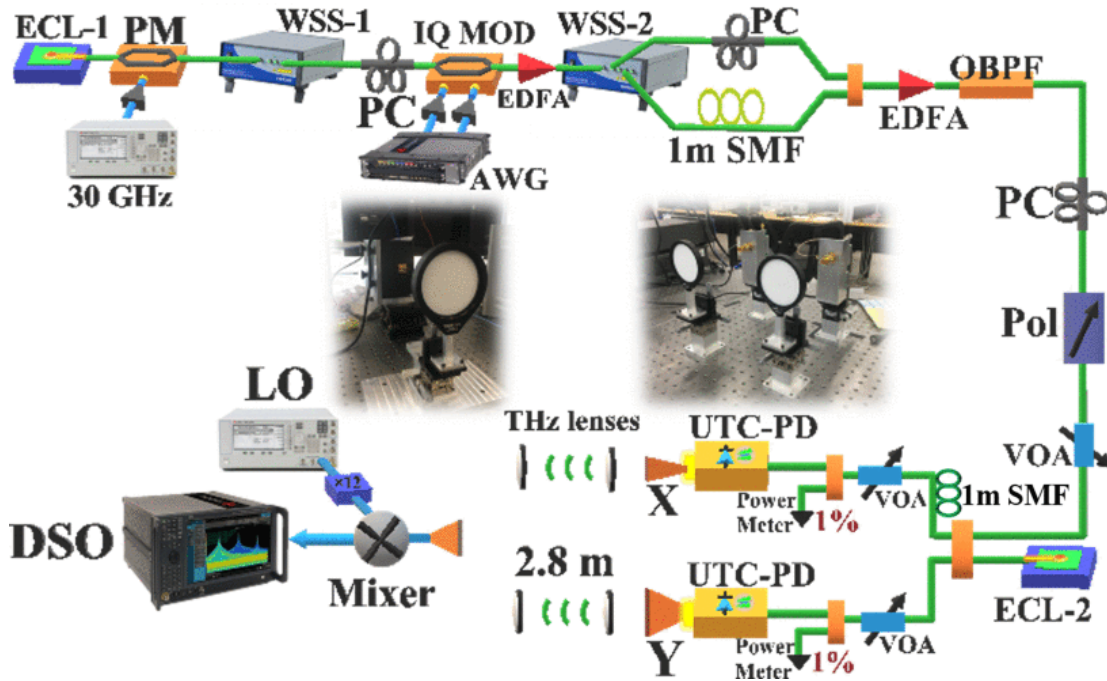
Figure 2.5: Schematic of the OFC based multicarrier THz communication system operating in the 320-380 GHz frequency range. Reprinted from Ref. [115]

2.4 THz Channel modelling

When compared with radio wave or microwave frequency band, the propagation of THz waves are highly attenuated by the presence of atmospheric water molecules, particles, snow, rain, etc., and the choice of THz carrier frequency depends on the type of applications (indoor and outdoor) [116,

117]. Therefore, a proper channel modelling must be carried out for efficient THz communications for both indoor and outdoor applications. On one hand, for the THz wireless communications, there are few studies on channel modelling that uses ray tracing algorithm [118-121]. On the other hand, the THz fiber-based communication channel require a significant research and analysis for establishing efficient short distance communication. In the following, we discuss in detail about the necessity of THz fiber-based communication and the recent developments of several designs and fabrication.

2.5 THz fiber-based communications

Up to now, we showed that most THz communications have been focused in demonstrating free-space wireless links that take advantage of several low/modest-loss atmospheric transmission windows. Although, the wireless THz communications hold many advantages including convenience in mobility for the end user, ease in scaling up the network, flexibility of device interconnectivity, etc., there are still many challenges. For example, the high directionality of the THz beams requires careful positioning of the transmitter and receiver antennas to minimize alignment errors. Similarly, for complex buildings or between moving objects, highly complex beam steering algorithms are necessary for reliable THz communications links. Moreover, free-space links have higher chances of eavesdropping thereby increasing the challenges of secure communications [23]. More often, it is said that the security of wireless THz communication is better when compared to the communication using radio waves or microwaves due to highly directional nature of the THz beam. However, the eavesdropper's technique will be different for the highly directional THz waves which can be achieved by placing an object to scatter the narrow THz beam towards the eavesdropper antenna.

In view of the limitations of wireless THz communications, short-range THz fiber links (~10 m) can provide additional flexibility and opportunities when designing future THz networks. THz waveguides have many advantages. By enclosing the THz radiation in a highly controlled propagation environment, the data stream can be more immune to environmental factors. Additionally, the waveguide can cover complex geometrical paths while offering reliable coupling to receiver and transmitter for both static and dynamic operations. Finally, in addition to the information transmission, the waveguides can also be remarkable tools as communications devices

for signal processing, beam steering, multiplexing and so on. It must be noted that, the THz fibers are not meant to replace the optical fibers that operates in the near infrared frequencies but to support the reliable communication within the THz wireless networks.

In THz wireless communication, the service towards both static (fixed transmitter and receiver) and dynamic (moving transmitter or receiver or both) link can be established. We emphasize on the fixed network links in terms of resource management (frequency reuse, effect of interference etc.,) and line of sight communication for the purpose of comparison with the THz waveguide links. The fixed networks can be established for a short term (which is event specific; telecasting live sports events for example) or long term (workspace, telecom networks etc.) depending on the application. The short-term THz networks mostly benefited from wireless based links whereas both wired and wireless link can be used in long term THz networks. In THz networks, the parameters such as transmitter power, carrier frequency, bandwidth and modulation techniques are generally predetermined and fixed. Due to high free space path loss in the THz spectrum and depending on the atmospheric loss conditions, the transmitter power plays a significant role in establishing a reliable communication. However, the transmitter power must be monitored and controlled in order to minimize the effect of interference to the neighboring wireless THz devices (ultra-dense networks) [122]. In such a scenario, using a low loss THz fiber can be an alternative solution for the link that has the freedom to choose either wireless or wired network access. Moreover, the THz fiber-based network outperforms the wireless based link in a short distance communication link, which is also efficient in terms of power consumption [32]. Although the dispersion in THz fiber limits the maximum bitrate when compared to free space link, the advanced modulation techniques can support Terabits per second data transmission. Next, due to the high reflection loss for the NLoS THz free space link, the maximal achieved bitrate can be ~10 times smaller than the line of sight communication [123]. To compensate the effect of loss in NLoS links, the researchers proposed several designs of intelligent reflecting surfaces (IRS) [124]. However, the design and implementation of IRS involves high cost and computing power. Therefore, the THz fiber can act as an intermediate platform to minimize the loss and achieve the reasonable bitrate.

In the following, we present the recent developments in THz waveguides when applied for communications and discuss about various parameters that need to be optimized for efficient waveguide/fiber design. The term waveguide and fiber are interchanged in this thesis.

2.5.1 Important parameters for THz waveguide design

In this section, we present the important parameters such as losses, excitation efficiency, dispersion, fabrication complexities etc., that needs to be considered while design the THz waveguides for communication applications. These parameters can be summarized in the following equation that relates the electric field at the output $E_{\text{out}}(\omega)$ to the input electric field at the input $E_{\text{in}}(\omega)$ for a waveguide of length L [125]:

$$E_{\text{out}}(\omega) = C_1(\omega)C_2(\omega)E_{\text{in}}(\omega) \exp(-\alpha_{\text{eff}}(\omega)L/2) \exp(-j\beta_{\text{eff}}(\omega)L) \tag{2.2}$$

where $C_1(\omega)$ and $C_2(\omega)$ are the input and output coupling coefficients; $\alpha_{\text{eff}}(\omega)$ is the effective power absorption losses; $\beta_{\text{eff}}(\omega) = \frac{\omega}{c} n_{\text{eff}}(\omega)$ is the propagation constant, where $n_{\text{eff}}(\omega)$ is the effective refractive index and c ,the speed of light.

In the THz frequency range, it is possible to measure both amplitude and phase of the THz radiation using THz-TDS and CW THz spectroscopy (frequency domain THz system, which is detailed in chapter 3). The cut-back method is one of the techniques that is used to extract the absorption losses (α_{eff}) and the propagation constant (β_{eff}) from experiments [126]. This cut-back technique is also called as destructive method since the fibers are cut during the measurements. Using this method, the transmission measurements are performed on two waveguides of lengths L_1 and L_2. Ideally, the same waveguide is used and cut to obtain a measurement for a second length. The complex transmission ratio $E_{\text{out}}^1(\omega)/E_{\text{out}}^2(\omega)$ is then computed. Here, the subscripts indicate the fiber. Because we assume that the same waveguide is used with the same experimental configuration, we can assume that the electric field inputs $(E_{\text{in}}^1(\omega) = E_{\text{in}}^2(\omega))$ are equal as well as the coupling coefficients $(C_1^1 = C_1^2, C_2^1 = C_2^2)$. Therefore, we can write:

$$\frac{E_{\text{out}}^1(\omega)}{E_{\text{out}}^2(\omega)} = \exp\left[-\frac{\alpha_{\text{eff}}}{2}(L_1 - L_2)\right] \exp[-j\beta_{\text{eff}}(L_1 - L_2)] \tag{2.3}$$

from which we can directly compute the power losses

$$\alpha_{\text{eff}}(\omega) = -\frac{2}{L_1 - L_2} \ln \left|\frac{E_{\text{out}}^1(\omega)}{E_{\text{out}}^2(\omega)}\right| \tag{2.4}$$

and the propagation constant

$$\beta_{\text{eff}}(\omega) = -\frac{1}{L_1 - L_2}\text{phase}\left[\frac{E_{\text{out}}^1(\omega)}{E_{\text{out}}^2(\omega)}\right] \tag{2.5}$$

The schematic of the experimental set up in characterizing the THz waveguide is shown in Fig.2.6.
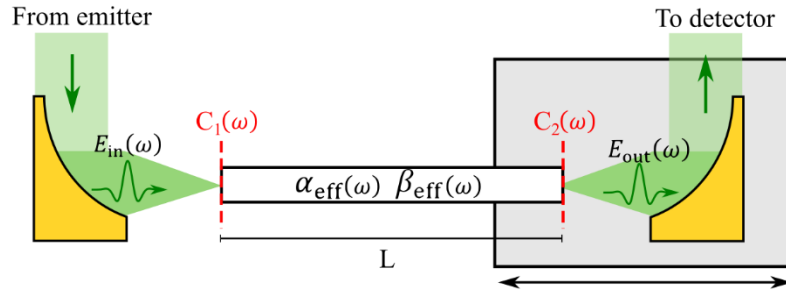
Figure 2.6: The schematic of the experimental setup in characterizing the THz waveguide

First, we discuss about losses. The parameter $\alpha_{\text{eff}}(\omega)$ describes the power losses incurred by THz radiation when propagating through the waveguide. For efficient designs, these losses must be minimized. The losses α_{eff} are mainly influenced by the choice of material and the waveguide geometry. Fig. 2.7 present the power absorption losses and refractive index of common dielectric polymers used in the fabrication of THz waveguides [127]. While the refractive indices are generally approximately constant on the THz band, their absorption losses typically increase polynomially with the frequency. Although these materials show the lowest losses in the THz range, they still can exhibit quite significant losses (~ several dB/m). In turn, this limits the maximal length of propagation inside the material before complete attenuation.

On the other hand, dry gases (such as air) show negligible absorption in the THz range. Therefore, an important strategy used in the design of THz waveguides is to maximize the power guided in air. This can be achieved using subwavelength solid-core fibers, hollow-core fibers and porous structures. Even metallic waveguides share this common idea of maximizing the fraction of power propagating in air.
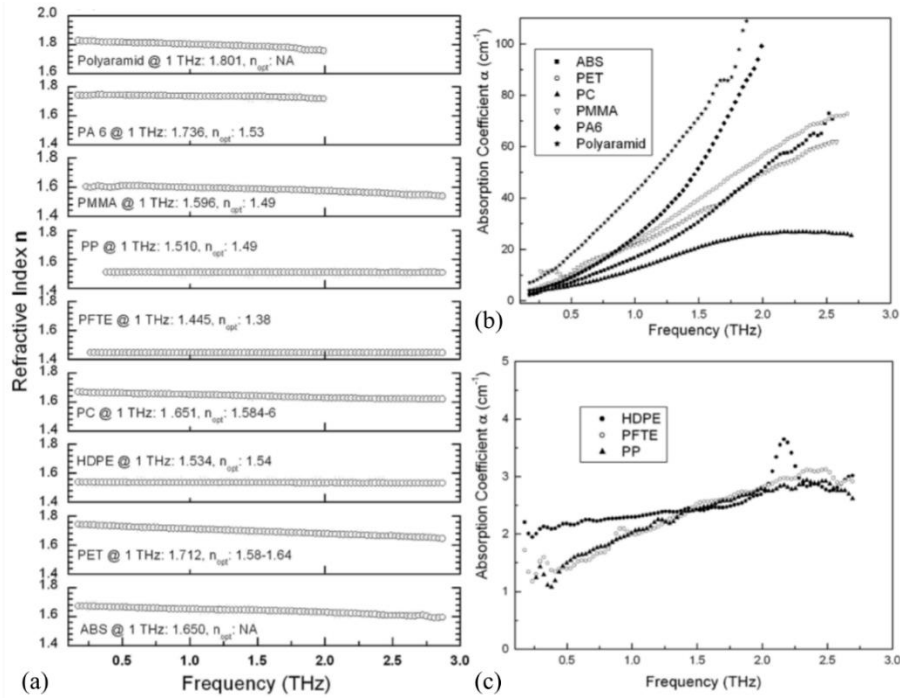
Figure 2.7: (a) Refractive index and (b), (c) power absorption coefficients of common dielectric polymers. Reprinted from Ref. [127]

Second, we discuss about excitation efficiency. The excitation efficiency (input and output) of the waveguide is an important parameter that dictates the waveguide's ability to transfer energy, and thus data. In Eq. 2.2, $C_1(\omega)$ and $C_2(\omega)$ are the frequency-dependent coupling coefficients, whose values are bounded between 0 and 1, where 0 indicates a null energy transfer, while 1 indicates a complete energy transfer. The coefficient $C_1(\omega)$ is related to the input coefficient (from air to the waveguide for example), while $C_2(\omega)$ is the output coefficient (from waveguide to air). Typically, one wants to increase both coupling coefficients to improve the transmission link distance. Under the waveguide mode theory, the coupling coefficients can be computed with an overlap integral relating the incident mode to the waveguide mode. Generally, a linearly polarized Gaussian beam is considered as the excitation source due to the commercial availability of such sources.

Third, we discuss about dispersion. The dispersion is a crucial parameter that limits the maximum bitrate in the communication channel. The cause for dispersion lies in the frequency dependence of the effective refractive index $n_{\text{eff}}(\omega)$. In simple terms, each wavelength that is contained is a pulse propagates at different velocities inside the waveguide. This causes the pulse to broaden in

time-domain, which reduces the THz bandwidth in spectral domain. In turn, this reduces the effective data rate by scrambling the pulse train when adjacent "bits" overlap with each other.

The dispersion is typically quantified using a Taylor expansion of the propagation constant $\beta_{\text{eff}} = \frac{\omega}{c} n_{\text{eff}}(\omega)$. The second-order term β_2 is the group velocity dispersion (GVD):

$$\beta_2 = \frac{d^2 \beta_{\text{eff}}}{d\omega^2} \tag{2.6}$$

When used in the THz range, the GVD is generally expressed in $\text{ps}/(\text{THz} \cdot \text{cm})$, that is ps of time broadening at a given THz frequency and for a given fiber length in cm [128]. A positive β_2 characterizes a waveguide with a normal dispersion (GVD increases with the frequency), while a negative β_2 indicates an anomalous dispersion (GVD decreases with the frequency). The broadening of the pulse caused by the fiber dispersion can be used to estimate the maximal bitrate B_{max} for a simple OOK or ASK modulated signal [129]:

$$B_{\text{max}} = \frac{1}{4\sqrt{|\beta_2|L}} \tag{2.7}$$

where the factor 4 is selected to ensure that 95% of the pulse energy remains inside the time slot of the unit bit. For example, considering a THz fiber dispersion of $\beta_2 = 1\,\text{ps}/(\text{THz} \cdot \text{cm})$, a moderate bitrate of 100 Gbit/s can be transmitted up to ~6 m. On the other hand, if $\beta_2 = 0.01\,\text{ps}/\text{THz}$, the same bitrate could be transmitted up to 600 m. Therefore, it is crucial to reduce the fiber dispersion as much as possible.

Fourth, we discuss about practical handling of THz waveguides. As we will show below, there are many advanced waveguide designs that possess low loss and low dispersion for high bitrate and long link THz communications. However, the THz waveguides must comply with several physical factors such as flexibility, compatible end connectors, easier splicing method etc., for commercial applications. The hollow core rectangular or cylindrical metallic THz waveguides are used for short distance interconnects (a few centimeters) in which a common flange type waveguide connector is used. Similarly, the polymer THz fibers with porous structures can be used for short links. For longer THz links, solid core polymer fibers are the ideal candidate as it is easy to fabricate without

any complexity. In step index solid core polymer THz fiber with air cladding, the propagating mode extends deep in the air cladding depending on the thickness of the core, which prohibits physical handling. Therefore, one can use the low index and low loss foam as cladding material surrounded by a protective tape. Adiabatic tapered end connectors can be efficient for coupling the THz source to the input/output facet of the fiber with high coupling efficiency [130]. Any defects or blocks or broken fibers that causes signal loss can be fused together by splicing. In glass fibers that is used in the visible/infrared region, the splicing technique is more advanced and robust, which leads to high efficiency. However, for the plastic fibers, the fiber splicing is more challenging. Particularly, for the graded index or porous fibers, the fiber splicing needs careful alignment as it leads to high losses even for a small mismatch. There are some promising techniques such as thermal fusion, ultrasonic splicing etc., which can be borrowed for THz fiber splicing [131, 132].

2.5.2 Types of waveguides

As we saw in the previous section, fiber parameters such as transmission losses, dispersion, excitation efficiency and ease of handling play significant roles in the design of efficient THz fiber communication links. While the fiber loss and coupling efficiency limits the communication link distance, the maximum achievable bitrate can also be limited by the fiber dispersion. Therefore, low transmission loss and low dispersion are the primary concerns when designing THz fibers. In this section, we review several types of existing THz waveguides that can be used for THz communications. We cover both metallic waveguides and dielectric waveguides.

2.5.2.1 Metallic waveguides

In metallic THz waveguides, THz radiation propagates at the boundary between a metal (support) and a dielectric (propagation medium). Generally, air is selected as the dielectric for its low losses and low dispersion values. In the following, we focus on the single-wire and two-wire waveguides as well as the parallel-plate waveguide.

First, a single-wire and two-wire waveguides are discussed. In metallic waveguides, a single wire is the simplest form of transmission line that guides electromagnetic radiation as surface waves. As the guided mode propagates in air, there is virtually no dispersion and the attenuation is mainly due to metallic ohmic losses [133]. In practice however, efficient excitation is difficult. This is

because, the fundamental mode of a single wire is radially polarized, i.e. the direction of the electric field is perpendicular to the transverse section of the bare metal wire. This polarization is incompatible with commonly used THz sources that tend to produce linearly polarized THz light. To match the symmetry of the guided mode, Jeon *et al.* and Deibel *et al.* proposed to use a radially symmetric photoconductive antenna as the THz source, achieving excitation efficiencies greater than 50% [134, 135]. Another proposed approach uses a tapered coplanar waveguide at the input end [136]. However, due to the large extension of the radiation around the wire, any disturbance such as nearby objects, micro/macro bends can lead to high radiation losses as well as difficulties in mechanical handling. Nonetheless, numerical studies have shown that transmission of over Terabits per second data stream in a distance of few hundred meters is theoretically achievable [137].
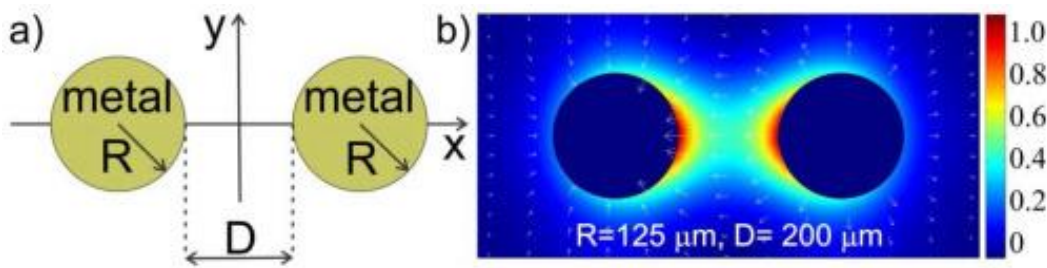
Figure 2.8: (a) Schematic of the two-wire THz waveguide (b) Longitudinal flux distribution of the TEM mode. Reprinted from Ref. [138]

To overcome the challenges posed by the single-wire waveguide, Mbonye *et al.* proposed a two-wire waveguide geometry in which a second metal wire is kept parallel to the first one [139]. The schematic and the field profile of two-wire THz waveguide is shown in Fig. 2.8. As a consequence, the propagating plasmonic mode is very well confined in the gap between the wires, which ensures a greater immunization against environmental disturbances while maintaining a low-loss and low-dispersion propagation over a broad frequency range [138]. Furthermore, the fundamental mode of the two-wire waveguide is linearly polarized (the electric field is directed from one wire to the other), which makes it compatible with most commonly used THz sources. In [126], a porous dielectric cladding (polystyrene foam) was used to further ease the handling and mechanical stability of the two-wire waveguide, at the expense of additional losses and dispersion. Moreover, long two-wire waveguide (>1 m) are generally inconvenient in practice because the gap between

the two metallic wires needs to be precisely maintained (at the subwavelength scale), which is difficult to realize for long fiber lengths.

For shorter links (<1 m), 3D printing of two-wire plasmonic waveguide is a promising fabrication method with great accuracy and reproducibility. Since the penetration depth into the metal at THz frequencies is only hundreds of nanometers, the surface of the 3D printed polymer can be coated with a μm-thick metal layer using wet chemistry for example. Furthermore, complex structures (for example curved two-wire waveguides) can be obtained in a single step process, in clear contrast with fully metallic components fabricated with CNC machining. In [140], Cao *et al.* used 3D printing to fabricate a two-wire waveguide. In their design, a long waveguide (~1 m) could be assembled by connecting multiple waveguide sections via the excavations and extrusions on both end facets of the cages that support the wires. Curved waveguides can also be fabricated and connected to the waveguide sections.

Next, the parallel plate metallic waveguides are discussed. Metallic plates placed parallel to each other are simple waveguides that have attracted a lot of attention in the THz range [141]. The parallel plate waveguide (PPWG) supports two types of modes with various dispersion. The fundamental mode of the parallel plate waveguide (PPWG) is the TEM mode. It is the lowest order TM mode (TM_0) that has no cut-off frequency and hence no dispersion. This TEM mode can be excited using a linearly polarized incident light whose electric field is normal to the parallel plates. Similarly, the TE_1 mode can be excited when the electric field is polarized parallel to the PPWG. Compared to the TEM mode, the TE_1 mode has a low-frequency cut-off at $f_c = c/(2nb)$, where b is the plate separation and n the refractive index of the medium between the plates [142]. Consequently, this cut-off frequency introduces spectral filtering at low frequencies and high dispersion for the spectral components near the cut-off. However, a careful comparison of the two types of modes show that the TE_1 mode has low ohmic losses when increasing the frequencies, in clear contrast to the TEM mode. The remaining losses of the TE_1 mode are attributed to diffraction loses, and they can be mitigated using concave structure in the plates along the propagation direction as shown in Fig.2.9 [143]. To benefit from the low-loss nature of the TE_1 mode while also maintaining low dispersion, a proposed strategy is to decrease the value of the cut-off frequency f_c by increasing the plate separation b. However, this comes with the disadvantage of multimode propagation, and thus requires careful mode matching to selectively excite the TE_1

mode. The excitation of the PPWG modes can be as simple as using focusing optics (quasi-optic coupling) and can be improved up to 80% by using adiabatic tapered coupler [144]. However, for long link THz communications, the PPWG is not an ideal candidate as they are not convenient in practical handling and manipulations. However, using flexible thin copper strips, they can be used for short link interconnects [145]. They can also be used for signal processing applications by introducing resonance/Bragg cavities [146, 147]. In order to modulate the THz pulses externally, one can insert high resistivity silicon with conducting oxide in between the parallel plates and modulate the pulse using photoexcitation [148].
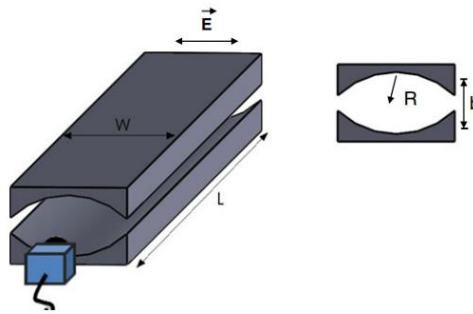
Figure 2.9: Concave parallel plate THz waveguide structure to minimize the diffraction loss.
Reprinted from Ref. [149]

2.5.2.2   Dielectric waveguides

Dielectric THz waveguide are the second class of waveguides developed in the literature. In general, low-loss dielectric materials are selected (e.g., Teflon, polyethylene, polypropylene, cyclic olefin copolymer) and their waveguide structure is engineered such that the mode is mostly propagating in the low-loss dry air region [125, 150-167], allowing to establish long THz communications links (>10 m). Typically, dielectric THz waveguides or polymer microwave fibers fall under one of three main categories: 1) hollow core waveguides (anti-resonant reflecting optical waveguides (ARROW) or photonic bandgap (PBG) waveguides) [150-156]) porous core waveguides (that use total internal reflection (TIR) or PBG guidance) [157-161]) solid core waveguides (TIR guidance) [162-165]. In what follows, we discuss each type in detail.

First, the hollow core waveguides are discussed. In the hollow core dielectric fibers, a large fraction of the modal energy propagates in the air core, which significantly reduces the material loss and dispersion. A simple hollow tube is an example of an anti-resonant reflecting optical waveguide

(ARROW) as shown in Fig.2.10. The ARROW guiding mechanism can be simply understood as follows. A fraction of the core mode leaks as radiation at the multiple core/cladding interfaces. At every interface, a portion is "reflected" back in the core. By carefully designing the cladding and core geometries, the different reflections from the interfaces can constructively interfere to increase the energy propagating in the core mode. The bandwidth of the low-loss window can be determined by the finite thickness of the thin tubular cladding. Introducing a lossy tubing material such as PMMA can help suppressing the cladding modes in favour of the core mode. Moreover, the propagation loss can be further reduced by increasing the size of the hollow core, which maximize the fraction of energy propagating in the low-loss air core. However, this comes with the excitation of higher order modes, which becomes problematic for long link THz communications due to intermodal dispersion and intermodal interference [11]. Using tube THz waveguides, several communication links have been demonstrated in the past years [168-170]. In [130], Van Thienen *et al.* demonstrated an error-free transmission of 7.6 Gbps and 1.5 Gbps over a link distance of 8 m and 15 m using a hollow core waveguide made of Teflon at 120 GHz. The modal loss of the waveguide was 2.5 dB/m. The maximum bitrate at longer link length was mainly limited by the propagation loss. Losses due to bending was also shown to be negligible at higher carrier frequencies [170].
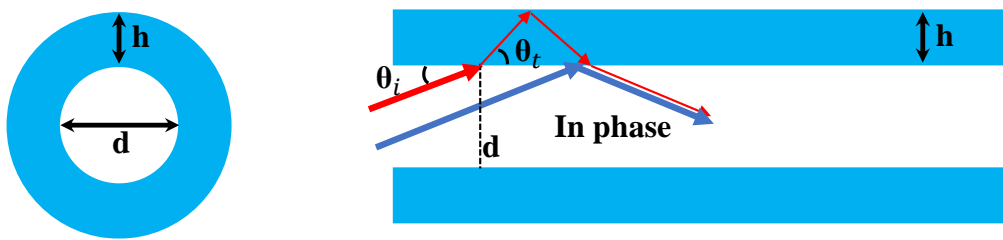
Figure 2.10: Cross-section and longitudinal view of the hollow core tube and the ARROW guiding mechanism

On the other hand, by arranging alternating layers of high and low refractive index cladding material (Bragg fibers) or by introducing judiciously designed (periodic or aperiodic) arrays of air inclusions in the cladding (photonic band gap fibers) around the hollow core, the loss and the transmission bandwidth can be improved when compared with tube-based ARROW fibers [151, 153, 156, 171-175]. By carefully designing the alternating layers, effectively single mode regime

can be achieved in long sections of such fibers, which can significantly reduce effective fiber dispersion.

Second, the porous core waveguides are discussed. In porous core fibers, both low loss and low dispersion can be achieved by using spatially variable dense arrays of subwavelength air holes both in the core and the cladding regions [157, 158]. The schematic of the porous THz waveguide is shown in Fig. 2.11. The losses of such waveguides can be reduced by using high fraction of air inclusions, as well as by selecting high refractive index contrast between air and the host dielectric. The latter allows a larger presence of the electric field in the low-loss air hole by continuity of the normal component of the displacement field across the waveguide cross-section: $E_a \propto E_m \varepsilon_m / \varepsilon_a$ [176]. This enhanced field presence allows to design low-loss and low-dispersion fibers, but also various THz components such as porous lenses [177].
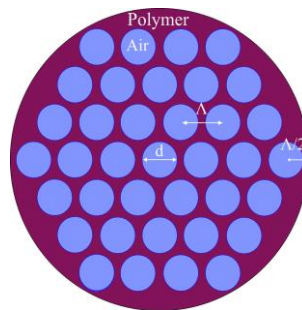
Figure 2.11: Porous core polymer fiber. Reprinted from Ref. [157]

In general, the fabrication of porous fibers involves drawing under pressure a thermo-polymer or glass-based preform with drilled or 3D printed air-inclusions. Achieving and maintaining target porosity throughout the length of the fiber requires careful calibration and monitoring of the entire drawing process, which is often challenging due to small dimensions of the structured preforms used in such drawings. Therefore, the maximum link length using porous THz fibers is determined by the efficiency of the fabrication process. Recently, an alternative method for the fabrication of THz microstructured and PBG fibers was detailed in [178], where over meter-long monocrystalline sapphire fibers were grown directly from the melt using structured dies. Apart from the circular and hexagonal porous structure [157], honey-comb [179] and rectangular [180] porous geometries were also used.

In [181], to reduce the effect of dispersion, Ma *et al.* designed a graded index porous fiber with holes of different diameters to vary the refractive index as a function of the radius. Time domain measurements of the graded index fiber showed that a THz pulse propagating inside the porous fiber was less prone to broadening compared to a porous fiber of similar porosity but with a constant index profile.

Third, the solid core waveguides are discussed. In solid core THz fibers, the transmission bandwidth is much larger than that in the hollow core fibers as the propagation mechanism is total internal reflection. However, the transmission loss in such fibers is much higher and is generally comparable to the absorption loss of the fiber material. In order to minimize the transmission loss, one usually resorts to a subwavelength dielectric simply maintained in an air cladding [163, 182]. These waveguides offer low loss and low dispersion guidance as a large fraction of the modal fields is guided in the low-loss air cladding surrounding the solid core [183, 184]. However, handling the fiber is problematic and several strategies have been used to isolate the waveguide from the environment, including suspending the solid core inside a larger dielectric cladding [185], using a foam cladding [182] or a photonic crystal fiber geometry [186]. In such fibers, scattering from inhomogeneities along the fiber length such as diameter variation, micro and macro bending, material density variation, etc. are the dominant loss mechanisms due to weak confinement in the fiber core [187]. These scattering losses can be somewhat mitigated by increasing the fiber diameter and realizing a better confinement in the fiber core at the expense of the increased losses due to material absorption. By choosing a low-loss polymer for the core material, a good compromise can be found, and THz fiber links of several meters can be realized.

2.5.3 3D printing of THz waveguides

In the past few years, the fabrication of polymer THz waveguides/components using 3D printing technology is getting more attention due to simple, high quality and cost-effective processes [188, 189]. Particularly, when the fiber design contains complex cross-section, fabricating it using a standard fiber drawing process becomes challenging. Therefore, the modern 3D printing process is considered as an alternative and efficient solution. Among many 3D printing techniques, stereolithography and fused deposition modeling (FDM) (also known as fused filament fabrication) are commonly used in the fabrication of THz waveguides and components. In stereolithography, a

liquid photopolymer is hardened upon shining with the patterned UV light to construct the 3D model in a layer by layer. A high accuracy and high precision can be achieved in stereolithography when compared with the FDM method. In [190], the dielectric properties of the photopolymers were investigated in the THz spectral region, which is promising for the fabrication of high performance THz waveguides. Using stereolithographic technique, several THz waveguides have been fabricated and characterized, which are particularly used in communication and sensing applications [153, 171, 188, 191]. In FDM technique, the filament that is extruded from the heated printer head is deposited layer by layer to print the waveguide. The most common filaments used here are ABS and PLA. Recently, low loss THz plastics such as cyclic olefin copolymer (commonly known as TOPAS) and polypropylene plastics are used to print the high-performance THz waveguides and components successfully. In most of the commercial 3D printers, the tray/bed height is limited to few tens of centimeters, which is critical to fabricate long length waveguides. Recently, we showed that the fibers of infinite length using polypropylene can be 3D printed and thanks to the contribution of Blackbelt team [192].

2.5.4 Terahertz waveguides for signal processing in communications

In addition to the potential of guiding THz radiation over large distances, waveguides can also be remarkable tools to manipulate THz beams in the communications context. In this section, we cover some recent developments in THz waveguides used as devices for communications. These devices can be placed at the output end of a THz waveguide to bridge between wired and wireless propagation for example.

First, the dispersion management is discussed. As we mentioned earlier, the dispersion is an important limitation that restricts the transmission bandwidth. Despite the fact that the THz waveguides can be designed to have low dispersion values, dispersion can still occur, especially when considering large travel distances. In those cases, dispersion compensation waveguides can be used to compress the broadened pulses and increase the data rate. These waveguides are characterized by large dispersion values of opposite signs to the dispersion being compensated.

An example of such a dispersion compensation waveguide was demonstrated by Ma *et al.* [191]. There, the authors fabricated dispersion compensation waveguides featuring several -100 ps/(THz $\cdot$ cm) at 0.14 THz. The waveguides were based on a metallic hollow-core geometry

where periodic corrugation was introduced in the inner core of the tube to ensure high coupling efficiency in the lower order mode while opening a bandgap for the higher order modes. Then, strong negative dispersion was achieved by operating near the bandgap edge.

Second, in order to increase the amount of data that is transmitted in a wireless link, it is necessary to encode information in multiple independent channels. The operation of mixing the independent channels in a communication link is known as multiplexing (mux), while demultiplexing (demux) is the opposite operation. Mux/demux can be done in various ways, by taking advantage of light properties such as polarization, spatial mode, angular momentum, but most commonly frequency. In [193], Karl *et al.* proposed to use a leaky-wave antenna based on a metal parallel-plate waveguide (PPWG). By opening a narrow slot in the PPWG, the radiation is allowed to leak out and couple to free-space modes with a frequency-dependent angle. Conversely, free-space radiation at a given frequency can couple into the PPWG at the appropriate incident angle. This rather simple geometry can then be used to achieve frequency-division multiplexing of real data flows as shown by Ma *et al.* [194].

Finally, the couplers/splitters are discussed. To enable complex THz fiber architectures, it is necessary to develop special waveguide components to route THz waves along specific paths. Examples of such couplers and splitters were demonstrated in [195]. Using 3D printing technology of polystyrene, Weidenbach *et al.* showed a Y-splitter and a multimode interference 1x3 splitter. They also demonstrated a variable waveguide coupler in which two parallel waveguides were brought close together. By varying the distance between the two waveguides, the energy could be transferred from one waveguide to another by evanescent wave coupling. In [196], this variable coupler was used in a 1 Gb/s communications system to demonstrate switching between two output waveguides. Bit error rate measurements confirmed that the distance between the two waveguides could be tuned to switch the output ports.

In , Reichel *et al.* designed a broadband T-junction variable power splitter based on the parallel-plate waveguide. The TE_1 mode was excited at the bottom of the "T" and propagates to the T-junction where a triangular septum was positioned. When the septum was in the middle of the T-junction, power was directed equally at each of the output ports, while minimizing back-reflections to the input port. By mechanically varying the lateral position of the septum, the authors were able to vary the power split on both output ports on the full single-mode range of 150-300 GHz. In

[198], the idea was pushed one step further by using electrically actuated liquid metal (Galinstan, gallium-indium-tin alloy) in the output ports. The liquid metal was introduced in rectangular glass tubes and plugged to a NaOH electrolyte solution. By applying a small ~4V voltage, the liquid metal could move in or out of the channel. Therefore, the channel could either be made of a thin metal wall (with high output transmission) or an electrolyte wall (with low output transmission). Using a similar concept, a channel add-drop filter was designed in which an actuated liquid metal was placed between two PPWGs sharing the same inner wall. When the liquid metal was in the channel, the THz radiation from the upper waveguide could couple to the bottom through the glass capillary walls at a very specific frequency. Thus, a signal propagating at the resonant frequency in the top channel could be extracted in the bottom waveguide through this add-drop functionality.
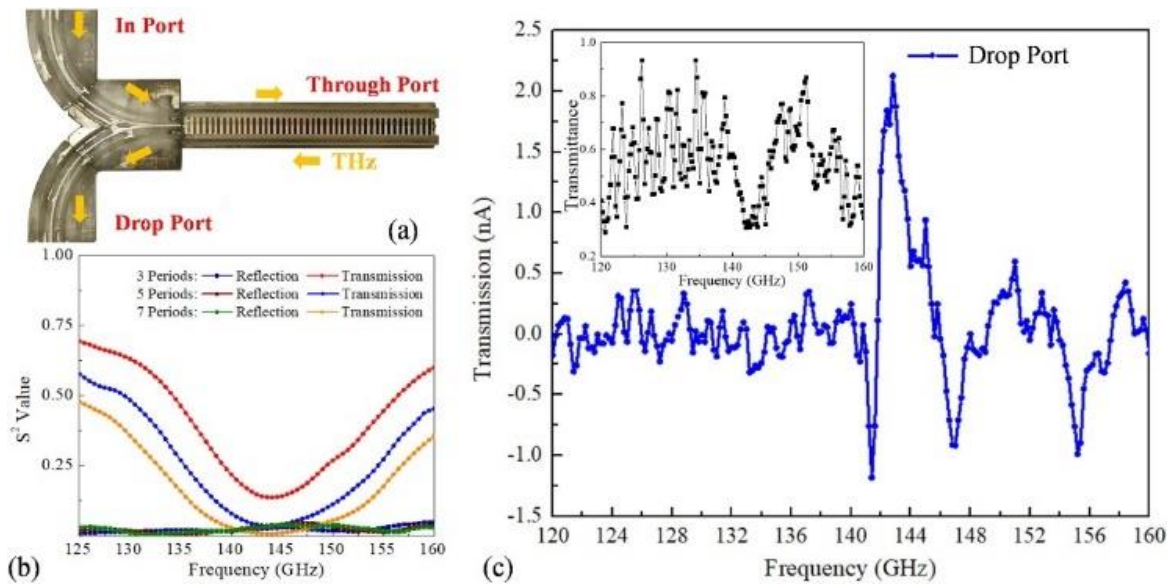
Figure 2.12: (a) Two-wire waveguide based add-drop multiplexer. (b) Numerical simulation results of transmission and reflection coefficients with the grating period of 2.3 mm and (c). Measured spectrum at the drop port. Reprinted from Ref. [140]

Another example of add-drop multiplexer was shown by Cao *et al.*[140], where Bragg gratings were used with the two-wire waveguide geometry as shown in Fig.2.12. The Bragg grating was made using the toner-assisted metal foil transfer technique (also known as hot stamping) to print metallic lines on a paper substrate. Then, the Bragg grating was inserted in the gap between the 3D printed two-wire waveguide. In this configuration, the fundamental TEM mode of the two-wire

waveguide coupled into the radiation mode, which allowed to reflect the THz wave at the Bragg wavelength.

We see that the low loss and low dispersion THz fibers/waveguides can be used to increase the reliability of the THz wireless link and at the same time a compact signal processing system can be developed. Here, the THz solid core subwavelength dielectric fibers are not explored for communication applications. Since, there are many opportunities in developing real-time signal processing elements using the subwavelength solid core fibers, we proposed to study the communication characteristics in detail. This will be the core research area in the second part of this thesis. We also presented several demonstrations of waveguide/fiber-based THz signal processing elements from the literature. This is to show that, these THz passive devices can be an additional support to the electronic signal processors and thereby reduces the cost and complexity of the transmitter/receiver front end.

2.6 Applications of THz wireless and fiber-based communications

In the next 10 years, it is expected that the maximum channel capacity of 5G networks will be reached. Therefore, the design and conceptualization of networks beyond 5G technologies (carrier frequency above 100 GHz) in the indoor and outdoor environment need to be studied. In this section, we present a few applications of THz wireless communications and propose the application of THz waveguides/fibers within the context of high-speed THz wireless communication networks.

2.6.1 Vehicular communication

The autonomous vehicles for moving passengers and cargos will play a significant role in the future transportation system. Such vehicles are integrated with several sensors such as LIDAR, RADAR, SONAR, GPS etc., that communicates with the cloud networks through the processing units within the vehicles. Increase in the number of sensors requires a large volume of data that needs to be transmitted and received in order to achieve centimeter level precision for efficient transportation. In such a scenario, the THz wireless links can handle the information transmission between the vehicle and cloud networks whereas the THz fibers can be used to communicate between the sensors and processing unit within the vehicle. Based on the requirement such as bitrate,

temperature stability, carrier frequency etc., the material and type of THz fiber can be determined and integrated inside the vehicle.

Similarly, the remote communication in airplanes and ships requires several antennas that are to be placed at different parts of the plane to receive the highly directional THz wireless signal from the ground station or geo-stationary satellite using a high-power and high gain transmitter (mostly <200 GHz). The implementation of THz fibers from the antenna and the signal processing unit that is located deep inside the vehicle can be advantageous. As the fibers allow flexibility in usage, such a design favors high speed internet service to the passengers in the moving vehicle. Although, we propose the idea of using THz links for on-road vehicular communications, the transmitter power, battery requirements, health issues must be carried out in detail.

2.6.2 Data centers

The data centers contain collection of high-performance computers and associated devices that are linked together mainly using wired networks. The wireless network using THz frequency spectrum is considered as an alternative solution for high-speed data transmission thereby reducing the cabling cost [199]. However, the use of THz fibers is unavoidable at certain conditions. For example, the THz fibers are required to route the signals between the computers or devices that lacks line-of-sight communication.

2.6.3 Workspace and home networks

The workspace or shopping malls are generally a large space where the wireless access to the user is provided currently by wireless-LAN that operates with the carrier frequency below 6 GHz. Therefore, the number of access points required for the given bandwidth is minimal. However, the THz wireless networks in indoor communication span a short distance of few meters and therefore for a high-speed data transmission, many access points are required to cover the entire area. The access points are generally placed on the ceilings and therefore, the THz fibers can be used to feed several access points from the central server. A simple solid core fiber or hollow core fibers can be implemented. A similar architecture can be used in the home networks for high-speed wireless internet access.

2.6.4 Device interconnects

With the growing bandwidth demand in the intra/inter chip communication, the input/output pins do not keep up with the requirement. Therefore, the THz interconnects holds high promises in increasing the bandwidth density and energy efficiency in the intra/inter chip communications [200, 201]. The interconnect that is fabricated using low loss material such as silicon will be an ideal choice for intra/inter chip communication. Among other fabrication techniques, the micromachining or microfabrication of silicon THz waveguides offers high precision for efficient performance of the interconnects.

2.6.5 Industrial applications

There are several industries where THz communication can be beneficial. As an example, let us consider the nuclear power plant that handles hazardous and radioactive elements. It is necessary to read the sensor outputs remotely for operation and handling of the reactors. Also, it is often essential to monitor the fuel burn-up using uncompressed high-quality videos that can be transmitted via THz wireless link [24, 202]. In such a scenario, short or long link THz fibers can be laid in the places where it is difficult to establish wireless connection. Therefore, the THz fibers can be a reliable solution for industrial applications.

2.6.6 Telecom applications

In the next generation wireless telecommunication such as beyond 5G or 6G networks, the distance between the access point or base station will be smaller (few 10's of meters). Particularly, in the outdoor environment the THz fiber links between two fixed base station can provide a reliable connection during wireless link failure due to harsh weather conditions.

2.6.7 KIOSK systems

The data KIOSK systems are generally used in the high traffic areas for instant downloading of large volume of data in a short duration. Due to the large bandwidth of THz frequency band, the THz KIOSK system can be used to transfer data such as movie poster, books, video advertisement etc. In fact, there is already a prototype that is proposed for KIOSK data downloading at 300 GHz

[203]. The THz fiber/waveguides can be used as short interconnect within the KIOSK system (intra device communication).

2.7 Contribution and impact of this thesis work

In this chapter, we have presented the literature review of different configuration of THz communication systems, their applications and the importance of THz fiber-based communication links. With an ever-increasing wireless data rate, mobile backhaul for transferring large bandwidth signals between base stations and end users is one of the primary goals using THz band. Thus, enabling photonics based wireless links (millimeter to THz frequency band) offers high efficiency and cost-effective solution to the mobile backhauling and 'last mile' connections [204, 205]. THz wireless links can be used as data showers for instant downloading of large volume of data while passing through shopping malls, airports, theaters etc. In air, road, marine and rail transportation, equipping the system with THz communications can provide a high-speed internet connection to the passengers on board. The growth in the automation in transport industries such as self-driving vehicles require high speed communications between both intra-vehicle and inter-vehicle for reduced unforeseen risks.
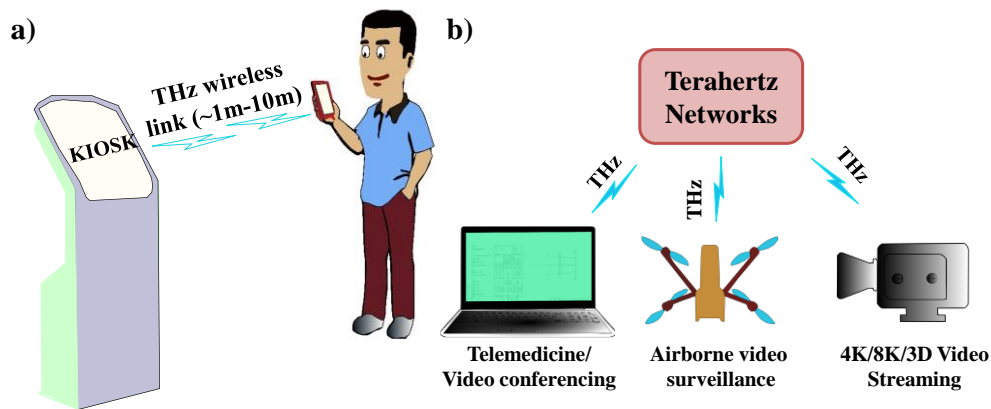
Figure 2.13: Applications of THz wireless communications in (a) Data KIOSKs for instant downloading of large volume of data while passing via shopping malls, airports etc. (b) consumer electronics including telemedicine, video conferencing, high quality video surveillance and uncompressed 4K/8K/3D video streaming

Similarly, among several bandwidth hungry applications, wireless transmission of uncompressed HD, 4K and 8K video finds importance in applications such as education, entertainment,

telemedicine, security, video conferencing to name a few. In the security screening involving drones, a large bandwidth is required to transmit the high-quality video content in a short duration. This can be extended to record and stream the footage during emergencies including natural calamities. In the broadcasting sector, capturing and telecasting the live events such as sports using high resolution 4K camera is also attracting much attention. The gaming industries are more promising in taking the user experience to next level. Thereby, the virtual realities require huge volume of video content to be transmitted with low latency for better experience. Also, we see currently that the number of users working from the remote environment has been increased significantly after the COVID-19 pandemic. Particularly, the online lectures, scientific conferences, streaming movies etc., demands high bandwidth in transmitting and receiving high quality video contents. Therefore, the wireless transmission of uncompressed high-quality videos such as 4K, 8K and beyond will be given priority in the next few years. In Fig.2.13, we show the schematic of a few application of video transmission using THz wireless communications. All of the above-mentioned examples suggest that transmission of the uncompressed 4K/8K videos can provide a significant improvement to a variety of important applications.

We believe that the hybrid, photonics-based THz transmitter and solid-state electronics-based THz receiver will form the 'first-age THz communication system' for commercial applications. In this context, we expect the technological development of THz communication system and its associated components to take the next step in moving from laboratory scale to commercial applications. In the first part of this thesis work, we have shown the development of photonics-based THz communication system using all commercially available components that can receive up to 6 Gbps over 1.75 m link distance at the carrier frequency of 138 GHz. Unlike microwave communication devices, the system development is itself a complex part for THz frequency band. Each component that is used in the development of THz communication system is detailed in this work. Moreover, we have also detailed the integration of 4K camera with the THz transmitter and THz receiver with the recording and display units. We then showed the live streaming of uncompressed HD and 4K videos and the performance was analysed by measuring the dark frames. Although, the probability of dropped frames can be estimated using the BER studies, the detailed configuration about the integration of the camera unit with the communication system and the importance of development of high-speed recording hardware is clearly shown for the commercialization opportunities. To the

best of my knowledge, this is the first study that show the development of THz communication system with the detailed information of components being used along with the performance analysis of uncompressed HD and 4K video streaming. An antenna integrated PIN photodiode is used as the THz transmitter when compared with the works published in the literature where proprietary UTC-PD THz photomixer is commonly used. Using PIN photodiode, the THz frequency can be tuned over a wide range (>1 THz), however, at the penalty of low optical-to-THz conversion efficiency. Although, the transmission bitrate and the maximal link distance is much lower when compared to the literature, the performance can be improved with minor modifications in the system such as a high-power THz transmitter, a large bandwidth digital LNA, higher order modulation schemes etc. The system can be further used to study THz integrated components for high speed communication applications. This work is highlighted by IEEE-ComSoc in its special mentioning (Tech Focus) on 'Featured technology in communication-Above 100 GHz and THz'.

In the second part of the thesis, we have shown the importance of THz fiber-based communication, which can be particularly useful for increasing the reliability of THz wireless networks. In literature, the hollow core dielectric fibers in a multimode regime were demonstrated for signal transmission. In this study, a simple solid core dielectric subwavelength fiber of different thickness in a single mode regime is used for the signal transmission. To the best of my knowledge, this is the first work that presents the detailed analysis of various parameters such as dispersion, bitrate estimation, bending loss, excitation efficiency and the link budget of a solid core subwavelength fiber in the THz regime. Further, we also carried out the real-time communication experiment to validate the theoretical results. At the same time, this is the first work that demonstrates the communication link up to 10 meters using solid core fibers in the THz regime. As most part of the modal energy in the subwavelength rod-in-air fiber propagates mainly in air, the transmission loss can be minimized, however, the practical handling and manipulation is not possible. Therefore, a rod-in-foam fiber is proposed and fabricated. From the link budget analysis, we conclude that the THz fiber-based links outperforms THz free space communication links in terms of received power for a short distance of ~10 meters. Therefore, these fibers can find applications in vehicular and indoor THz communications in the near future.

CHAPTER 3   METHODOLOGY

As mentioned in the introduction, the first objective of this thesis is to assemble a high-performance, photonics-based, THz communication system. While assembling the THz system, the calibration of lasers and control electronics is expected to delay the project duration. To simplify these processes, we purchased a frequency domain THz spectroscopy system (TOPTICA Photonics, Inc) and modified it for the communication experiments. Nevertheless, the THz spectroscopy system can be used to characterize the THz-passive components, such as waveguides, coupler, filters etc. Therefore, in this chapter, we present the assembly and characterization of a frequency-domain or CW THz spectroscopy system that is capable of measuring waveguides of varying lengths followed by the methodologies used for plastic fiber drawing and numerical studies. Due to my contribution in assembling the frequency domain spectrometer, and by carrying out the characterization experiments for novel THz waveguides, I co-authored several journal publications as shown in the Appendix A.

3.1   Frequency domain THz spectroscopy system

Since the development of THz sources, the material characterization in this spectral range seeks special attention [13, 206, 207]. The THz radiation is transparent to most of the plastics, wood, paper etc. Also, several molecules show specific resonances in this spectral range enabling molecular fingerprinting, which can be used as THz tags [208]. In THz spectroscopic studies, either the time domain or frequency domain system is used [209-211]. A single shot of THz pulse from the time-domain THz spectrometer provides the spectral information over a broad bandwidth (> 3 THz); but with moderate frequency resolution (~typically 1 GHz). On the other hand, the CW frequency domain THz spectrometer offer higher-frequency resolution (~50 MHz), but with low speed. The choice of THz spectrometer is based on specific applications. In our case, we chose the frequency domain system as it can be easily modified for THz communication experiments. Moreover, the characterization of passive components such as filters, multiplexers demands high spectral resolution, which can be achieved through the frequency domain THz spectrometer.

A complete list of active components/devices for assembling the frequency-domain THz spectrometer is purchased from TOPTICA photonics, Inc. The small optics, such as mirror, lens, optical rail, 3D stage etc., were purchased from Thorlabs, Inc. The schematic and the experimental

setup of the spectroscopic system is shown in fig.3.1. In the following, the components and assembly of the CW THz spectrometer is briefly discussed.
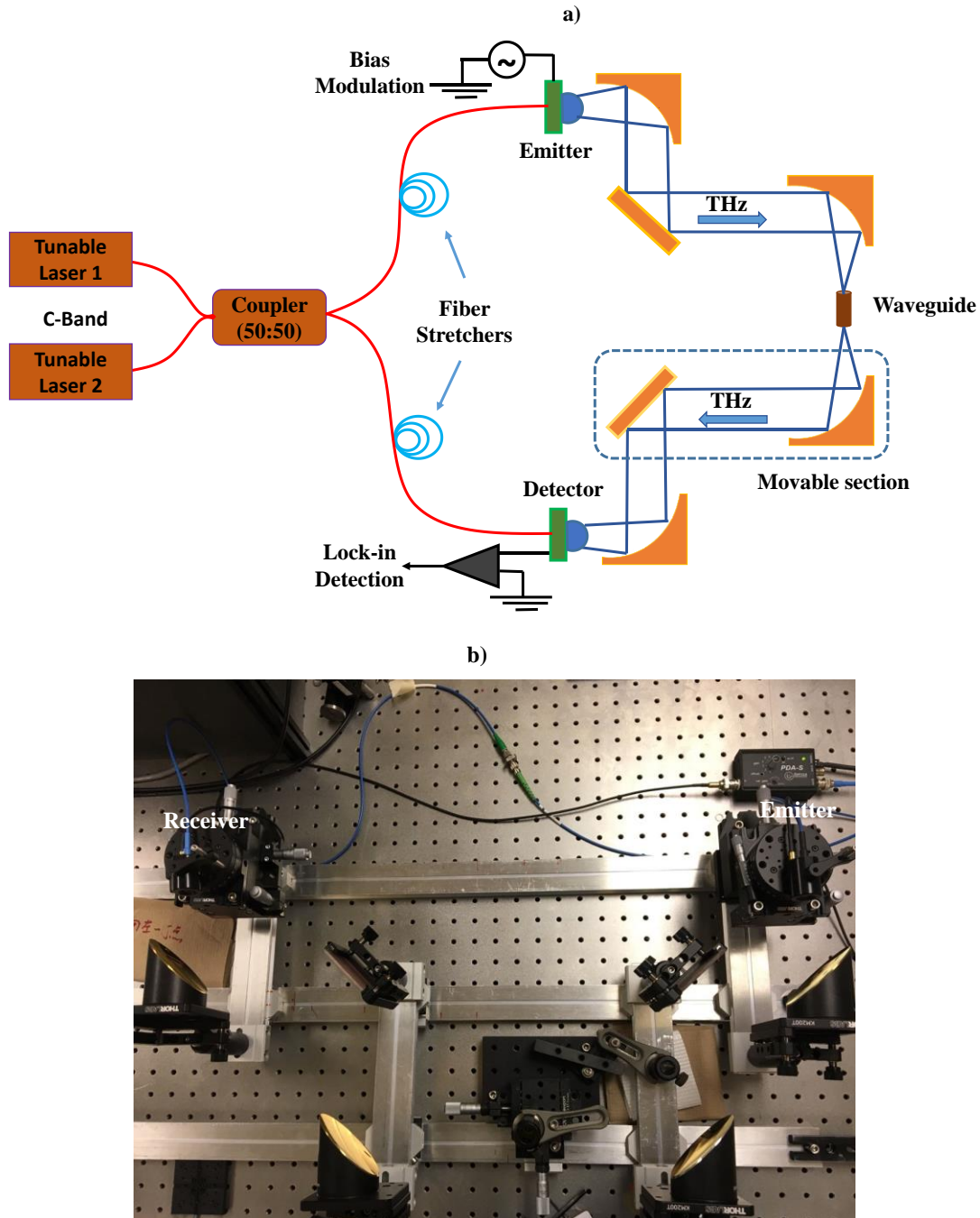
Figure 3.1: (a) Schematic and (b) the experimental set up of the CW THz spectroscopy system for waveguide measurements

3.1.1 Laser source

Two DFB lasers operating in the IR C-band, with an output power of ~30 mW each, are used as the sources for CW THz generation. The center wavelength of each laser at room temperature (25°C) is 1531.9 nm and 1536.5 nm respectively. The linewidth of each laser is 0.5 MHz on a short time scale (100 μs), and the frequency may drift to few tens of MHz depending on the stability of the ambient conditions. The lasers can be tuned by an FPGA-based control module, within the spectral range of 1529.81 nm to 1539.85 nm and thereby enabling the continuous operation of THz frequencies from 0-1200 GHz. The frequency can be tuned at the maximum speed of 100 GHz/s. The laser beams are then delivered via a polarization-maintaining, single-mode fiber. A 3 dB coupler is used to combine and split the laser beams equally into emitter and detector arms.

3.1.2 Photomixers
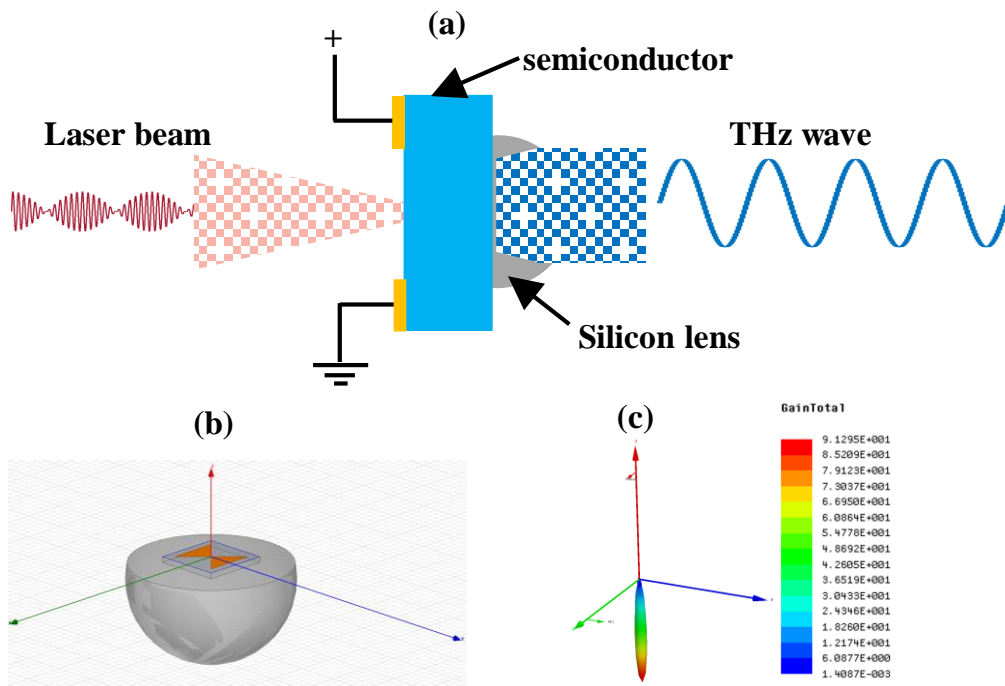
Figure 3.2: (a) Schematic of the CW frequency difference generation in the photomixer (b) and (c) HFSS modeling to calculate the antenna gain at 140 GHz. The gain is shown in linear scale (Fig. 3.2 (b) and (c) are obtained from Fraunhofer HHI, Berlin, Germany)

The photomixer is a nonlinear device, fabricated using InGaAs semiconductor (pump wavelength in the IR C-band) for the THz generation and detection. Firstly, the emitter photomixer is briefly discussed as follows. The beat frequency of the two laser beams are focused into the gap of the externally biased electrode. The excited photocarriers correspond to the beat frequency (frequency difference of two lasers), and the generated photocurrent drives the antenna for the generation of THz radiation. The schematic of the frequency difference generation principle is shown in fig.3.2 (a). To improve the coupling of THz waves from the semiconductor to the free space, a silicon lens of diameter 10±0.1 mm and thickness of 6.05±0.1 mm, is used. A finite element modeling, using HFSS, is used to calculate the gain of the photomixer antenna as shown in Fig.3.2 (b) and (c) [212]. It is estimated that the total gain is ~19 dBi at the frequency of 140 GHz. The residual beam divergence of the THz beam is approximately 12°, 15° and 15° for 200 GHz, 500 GHz and 1 THz respectively. The bias voltage to the emitter photomixer is modulated at the rate of 12 KHz for the purpose of lock-in detection.

Similarly, in the receiver section, another photomixer is used to detect the THz signal. Related to the emitter photomixer, the photocarriers are generated in the receiver photomixer by focusing the beat frequency of the two laser beams. Instead of the bias voltage that is been used in the case of emitter antenna, the electric field of the incident THz beam drives the photocarriers (interference between the THz signal and the photocarriers generated by optical beat signal) in the receiver photomixer. The generated photocurrent, which is proportional to the THz electric field (see Eq. 3.1), is measured by lock-in-detection.

$$I_{ph} \propto \cos{(\Delta\varphi)} = E_{THz} \cdot \cos{(2\pi f \Delta L/c)} \qquad (3.1)$$

Where I_{ph} is the photocurrent, E_{THz} and f is the electric field and frequency of the THz wave, $\Delta\varphi$ and ΔL are the phase difference and path length difference between the length of the receiver arm, and the length of the emitter arm including the THz path, respectively; and c is the velocity of light. The recorded photocurrent (cosine behavior) as a function of THz frequency is shown in fig.3.3. The period of the cosine function is a constant, which is determined by the path delay ΔL. The THz amplitude and phase can then be obtained from the envelope and zero crossing of the measured photocurrent. In Fig.3.3, we also observe the standing wave behavior with a period of ~4 GHz due to the presence of the silicon lens.
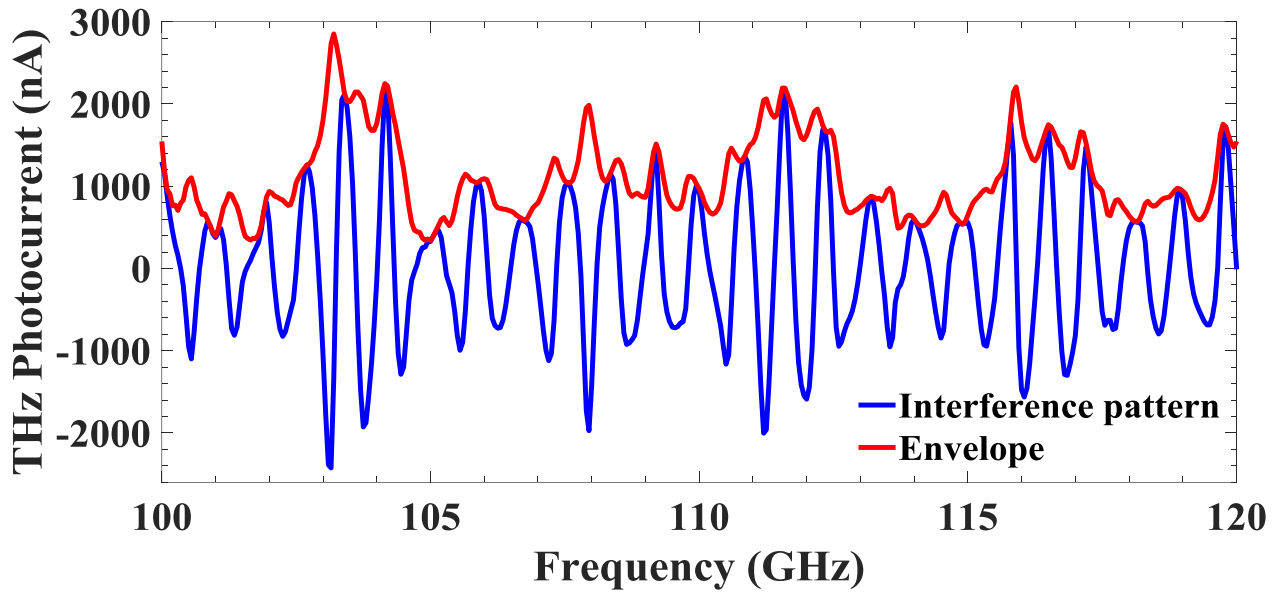
Figure 3.3: The THz photocurrent as a function of frequency. The amplitude of the photocurrent is obtained from the envelope of the signal

3.1.3 Fiber stretchers

In THz spectroscopy, both amplitude and the phase of the received THz signal must be measured to calculate the complex refractive index of the sample. The THz amplitude at a given frequency can be taken directly from the photocurrent; however, the measurement of phase requires additional steps. From Eq.3.1, we see that either the path length or the frequency of the THz wave must be varied to measure the phase of the received signal. The path length can be varied either in the optical domain or the THz path using the mechanical delay stage [213-216]. The former approach requires free space optical beam preventing the compact all-fiber system. In the latter approach, varying the THz path length affects the standing waves and thereby causing significant deviation in the recorded signal. On the other hand, by tuning the THz frequency, the phase information can be obtained but at a slower speed [217, 218]. Therefore, the optical fiber stretcher can be one of the best approaches to measure the phase information more accurately in a shorter duration and with a compact system [219]. The working mechanism of the fiber stretcher is briefly explained as follows. Two long single mode fibers wounded with piezo actuators are connected to both emitter and receiver arm. By applying the voltage to the piezo actuator, the length of the fiber can be

stretched and thereby the path length modulation is achieved. The path delay can be doubled by applying the voltage of opposite signs to the fibers relative to each other.
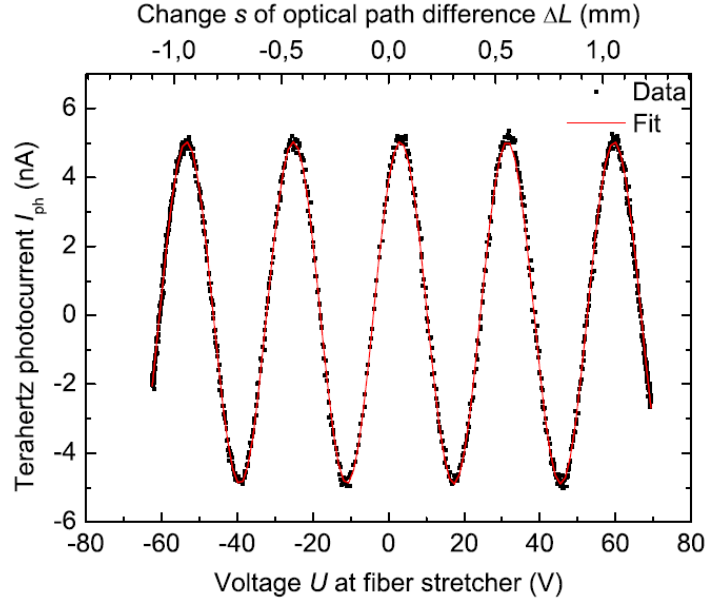
Figure 3.4: THz photocurrent versus voltage of the fiber stretcher at the frequency of 600 GHz. The amplitude and phase of the photocurrent can be obtained. Reprinted from Ref. [219]

In our THz spectroscopy system, the length of the two-piezo, actuated fiber stretcher is 62.08 m and 62.16 m with a stretch factor of 5.61 µm/V and 5.86 µm/V, respectively. For example, the applied voltage of 400 V results in the path delay of ~4.5 mm. This is already sufficient to measure the phase with a complete 2π cycle at 100 GHz (3 mm). An example plot showing the THz photocurrent versus voltage applied to the fiber stretcher is shown in fig.3.4. From this figure, the THz amplitude and phase are estimated.

3.2 Characterization of frequency domain THz spectroscopy system

The frequency domain THz spectroscopy system is characterized by measuring the refractive index of air and Teflon, identifying the absorption peak of the water vapour for frequency resolution and spot size measurement of the focused THz beam for the purpose of waveguide measurements. At the end of this section, to show the accuracy of phase measurement, the smooth transition of THz phase in a hollow metal tube for the fundamental mode at the cut-off frequency is also presented.

3.2.1 Measurement of refractive index of air and Teflon

Firstly, the THz spectroscopy system is assembled in a simple configuration by using just two parabolic mirrors for the purpose of collimating and focusing the THz beam from the emitter to detector respectively. The THz photocurrent is maximized at a given frequency by adjusting the path length using the 3D stage. The system records the actual phase (wrapped) of the THz signal as a function of frequency for two given path lengths L_1 (9 cm), L_2 (30 cm), respectively. This is shown in Fig.3.5 (a). The data can be processed by unwrapping the phase, as shown in fig.3.5 (b). The refractive index of air is then estimated using equation 3.2.
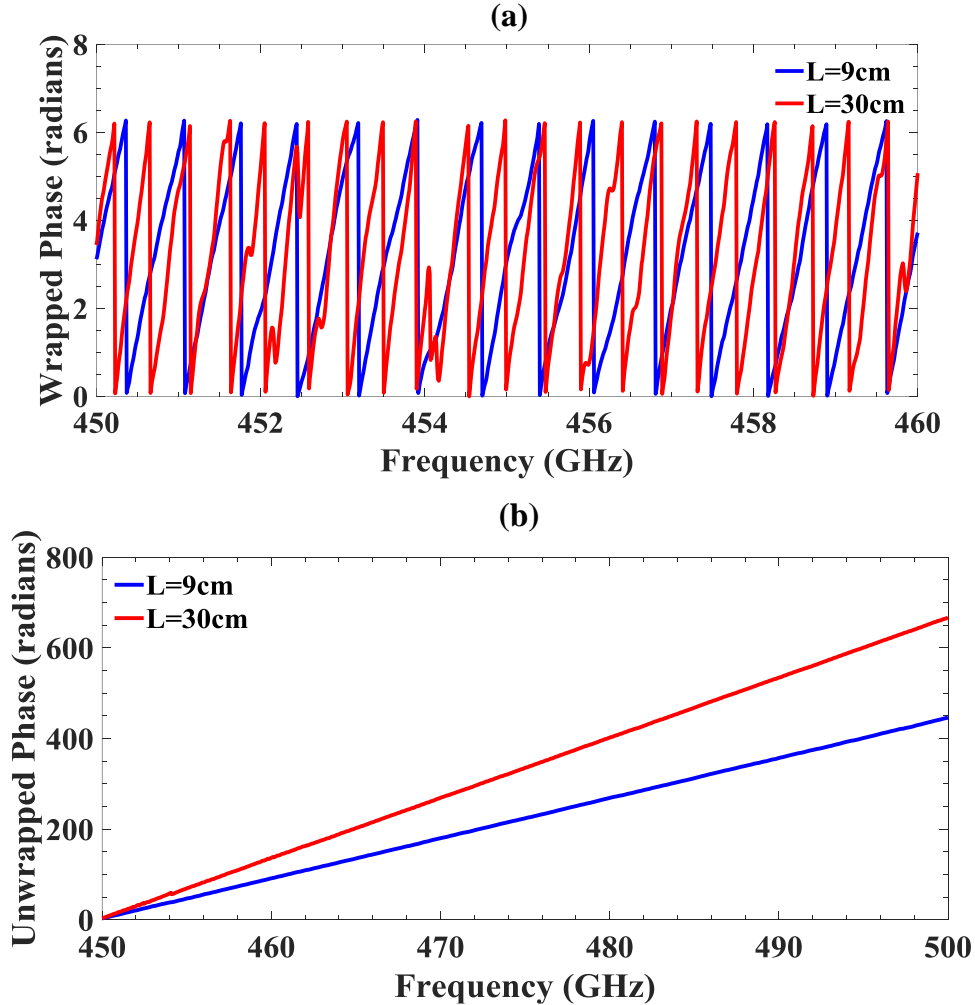
Figure 3.5: (a) The recorded phase using the fiber stretcher for two different lengths. The unwrapped phase from 450 GHz to 460 GHz is presented for the purpose of clarity and (b). The corresponding unwrapped phase for data processing

$$n_{air} = \frac{\Delta\varphi \cdot c}{2\pi \cdot \Delta f \cdot \Delta L} \tag{3.2}$$

From Fig.3.5 (b), the value of $\Delta\varphi$ at 500 GHz is 220.9447 radians. The value of Δf and ΔL is 50 GHz and 21 cm, respectively. The refractive index of air is then estimated as 1.004. The ambiguity in the accuracy of the refractive index after the second decimal point could be due to the noise present in the signal and minor error in the accurate measurement of L_1 and L_2. The influence of noise can be minimized by averaging the measured data.
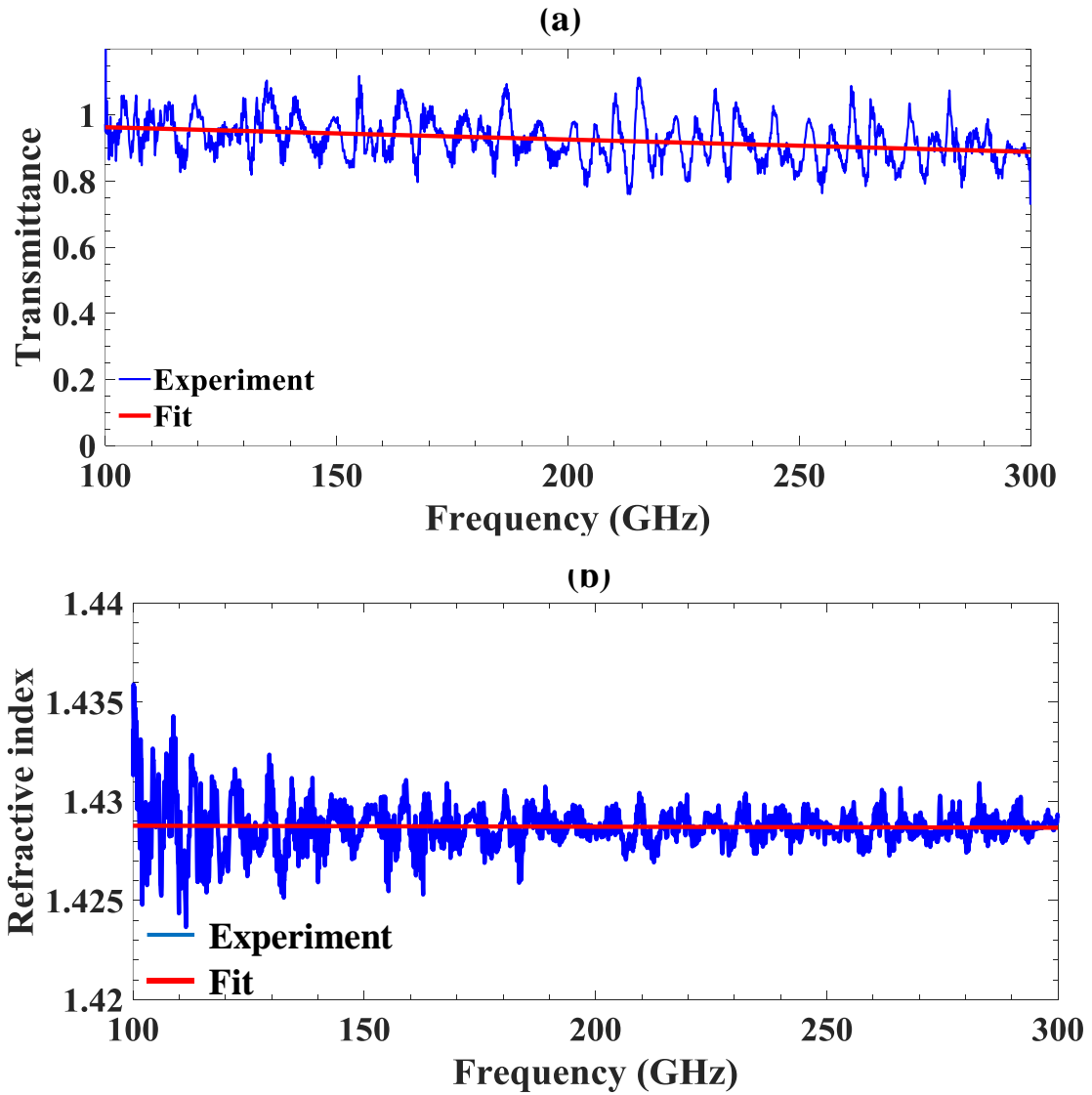
Figure 3.6: (a) Transmittance (b) Refractive index of Teflon. The measured results agree well with the literature [220]

Next, the transmittance and the refractive index of Teflon is also measured to validate the system, using the similar procedure discussed above; and that is shown in fig.3.6 (a) and (b), respectively. The amplitude and phase of the received THz photocurrent are recorded for both the reference (empty system) and the sample (Teflon) of thickness 14.3 mm. The transmittance (T) and the refractive index are then calculated using Eq. 3.3 and 3.4. This agrees well with the literature [220].

$$T = \left(\frac{I_{ref}}{I_{sample}}\right)^2 \tag{3.3}$$

$$n_{sample} = 1 + \frac{(\Delta\varphi - \varphi_0) \cdot c}{2\pi f d} \tag{3.4}$$

In the above equations, I_{ref} and I_{sample} are the THz photocurrent amplitude of reference and sample, respectively. Similarly, n_{sample} is the refractive index of sample, φ_0 is the initial phase obtained by fitting the phase difference $\Delta\varphi$, f is the frequency and d is the sample thickness.

3.2.2 Validation of frequency resolution of the CW THz spectroscopy system

Before proceeding with the experiment to characterize the waveguides, the frequency resolution of the spectrometer is validated. The CW THz spectroscopy system is configured using additional focusing and collimating optics similar to the setup shown in fig.3.1. In this configuration, the THz path length is much higher, and it leads to the large phase difference between the emitter and receiver arm. To compensate for the path delay, and to minimize the phase difference, an additional fiber-patch cord is connected to the respective arms. Ideally, we should expect a flat phase when the path difference is zero. However, we observe a small deviation from the ideal value while scanning the THz frequency over a broad spectral range, which is due to the small mismatch in the path lengths.

The frequency scan from 100 GHz to 1200 GHz was carried out with a step size of 100 MHz and an integration time of 30 ms. Since the THz output power varies significantly in the measured range (~100 μW at 100 GHz and ~1 μW at 1000 GHz), the recorded photocurrent amplitude is shown in logarithmic scale (see Fig.3.7 (a)) for better visualization. We observe several absorption dips, due

(a)

(b)
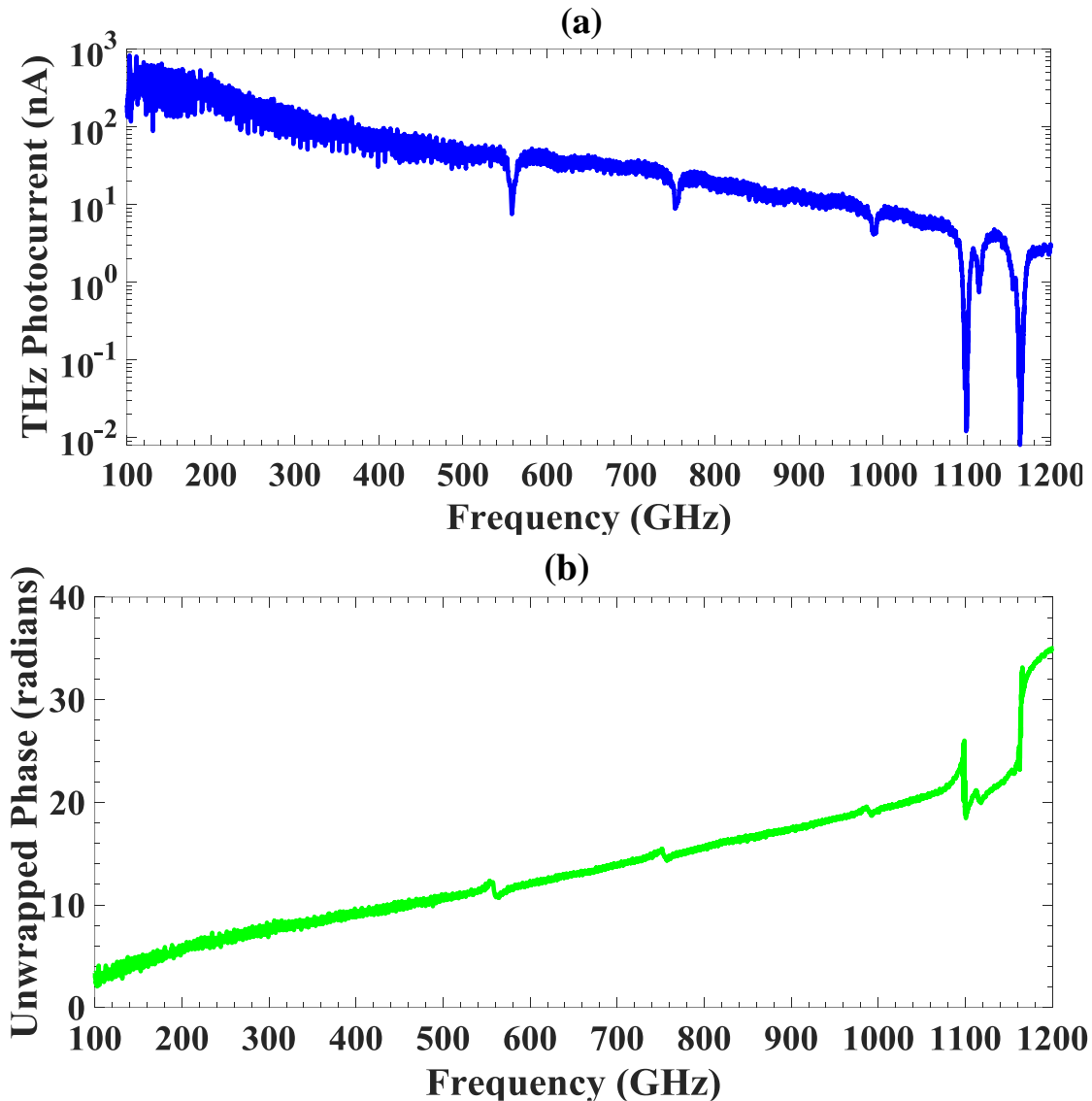
Figure 3.7: (a) The step scan of THz spectrometer from 100 GHz to 1200 GHz with a frequency resolution of 100 MHz and integration time of 30 ms. (b) The corresponding unwrapped phase information

to the presence of water vapour in the atmosphere. The water vapour absorption dips at 557 GHz, 752 GHz, 988 GHz, 1097 GHz, 1113 GHz and 1163 GHz agrees well with the literature [221, 222]. Similarly, from Fig.3.6 (b), the phase jumps at the resonance frequency clearly indicates the presence of water vapour. The validation of resonance frequency using phase spectra is significant, while measuring the waveguides having high absorption loss where a minor variation in the photocurrent amplitude can be buried in the noise. It is noted that the laser emission wavelength

might drift due to aging or thermal fluctuations. Therefore, a full spectral scan must be carried out often. That is, to make sure that there is no shift in the resonance dips of water vapour. In the case of resonance shift, the laser current must be adjusted accordingly.

3.2.3 Measurement of spot size at the focal point

In THz waveguide measurements, the excitation efficiency (also known as coupling efficiency (C_m)) is the crucial parameter that determines the amount of power coupled from the source to the waveguide (input facet), and waveguide to the detector (output facet). The coupling efficiency is estimated using Eq.3.5 [223, 224].

$$C_m = \frac{1}{4} \int dx dy \left(E_m^*(x,y) \times H_{input}(x,y) + E_{input}(x,y) \times H_m^*(x,y) \right) \tag{3.5}$$

$$\times \frac{1}{\sqrt{\frac{1}{2} Re[\int dx dy E_m^*(x,y) \times H_m(x,y)]} \times \sqrt{\frac{1}{2} Re[\int dx dy (E_{input}^*(x,y) \times H_{input}^*(x,y)}}$$

$$E_{input}(x,y) = \vec{x} \cdot \sqrt{\frac{2P}{\pi \sigma^2}} \cdot \exp\left(-\frac{x^2 + y^2}{2\sigma^2} \right)$$

$$H_{input}(x,y) = \vec{y} \cdot \frac{1}{\sqrt{\frac{\mu_0}{\varepsilon_0}}} \cdot \sqrt{\frac{2P}{\pi \sigma^2}} \cdot \exp\left(-\frac{x^2 + y^2}{2\sigma^2} \right)$$

In Eq.3.5, E_m and H_m are the electric field and magnetic field of the mth guided mode. $E_{inpu,t}$ and H_{input} are the field components of the 2D-Gaussian beam, which is normalized to carry power P. A maximum coupling efficiency is achieved when the size of the Gaussian beam is comparable to the size of the guided mode. Therefore, estimation of the frequency dependent spot size is important for processing the waveguide measurements. In the following, we show the spot size measurement in detail.

The standard, knife-edge technique is used to measure the size of the focused THz beam in the spectroscopy system [225]. A thin metallic plate on a 2D-translational stage is placed in between the two parabolic mirrors (at focal spot). The exact position of the focal spot is identified by

(a)

(b)

(c)
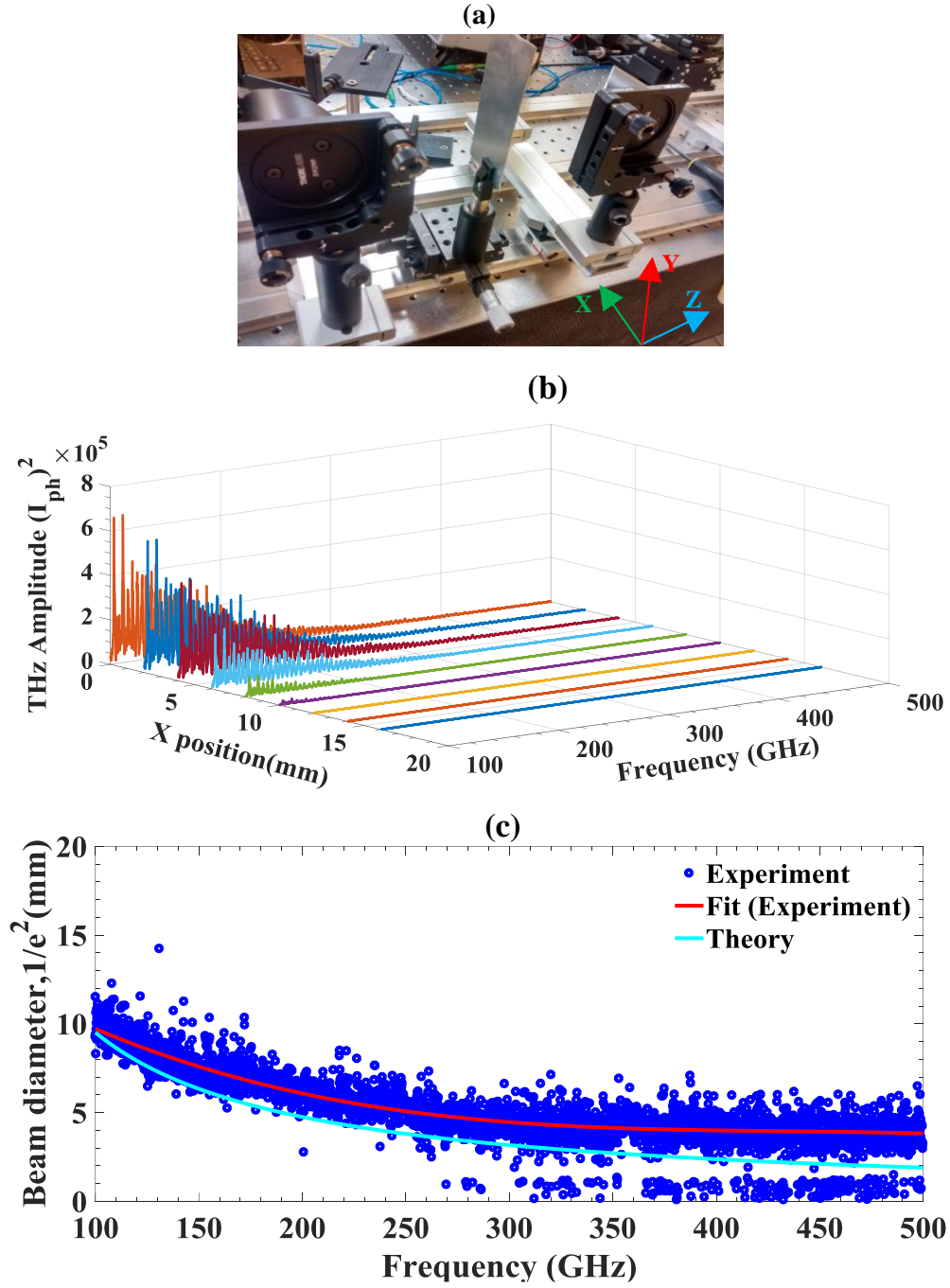
Figure 3.8: (a) Experimental set up of the knife-edge method for the spot size measurement (b) Intensity of the measured THz electric field and (c) Theoretically calculated and experimentally measured beam diameter ($1/e^2$) at the focal point

blocking a small portion of the THz beam using the metallic plate and moving the translational stage in the Z-direction. Once the position of the focal spot is identified, the THz photocurrent is

recorded as a function of frequency by moving the position of the metal plate in the X-direction until the THz beam is completely blocked. The experimental set up of the knife-edge measurement is shown in Fig.3.8 (a). Since the recorded photocurrent is proportional to the THz electric field, it must be squared (intensity) for further data processing as shown in fig.3.8 (b). Firstly, the intensity of the THz beam is normalized and fitted using Eq. 3.6.

$$\frac{I_0}{2}\left(1 - \mathrm{erf}\left(\frac{\sqrt{2}(x - x_0)}{w}\right)\right) + c \tag{3.6}$$

From equation 3.6, I_0 is the maximum intensity, x is the position of the metallic plate, x_0 is the cartesian co-ordinate at the center of the beam, w is the beam radius ($1/e^2$), and c is the background noise. Therefore, the beam radius w can be directly estimated from the fitted curve. Similarly, the beam diameter can also be obtained from the first order derivative of the fitted function. In theory, the diameter of the focused-spot size (see equation 3.7) depends on the focal length ($F=10\ cm$) of the lens, wavelength (λ), and diameter (D) of the incident beam. In our system, although the size of the parabolic mirror is 2-inch, the size of the incident THz beam is ~1.6 inch and it does not cover the entire area of the parabolic mirror. The measured beam size agrees well with the theoretical prediction as shown in Fig.3.8 (c).

$$spot\ size = \frac{4\lambda F}{\pi D} \tag{3.7}$$

3.2.4 Measurement of a metallic tube waveguide

One of the main advantages of the frequency-domain THz spectrometer is the spectral resolution. Unlike the time-domain system, the cut-off frequency, and the smooth transition of the spectral phase, can be clearly observed while measuring the THz waveguides using the frequency domain system. To demonstrate the capability of the system, a metallic tube waveguide of inner diameter 1.67 mm with varying lengths $L,$ have been measured. For a metallic tube waveguide, the cut-off frequency, f_c of the fundamental mode, can be estimated using Eq.3.8, where a is the radius of the waveguide. For the measured waveguide, the cut-off frequency is calculated as 105.2 GHz.

$$f_c = \frac{1.8412 \cdot c}{2\pi a} \tag{3.8}$$

The measured amplitude and phase spectra of the reference and metallic tube waveguide is shown in Fig.3.9. This also agrees well with the theory. It is noted that the reference measurement was carried out by keeping the size of the aperture (which also acts as the metallic waveguide holder) the same as the diameter of the waveguide.
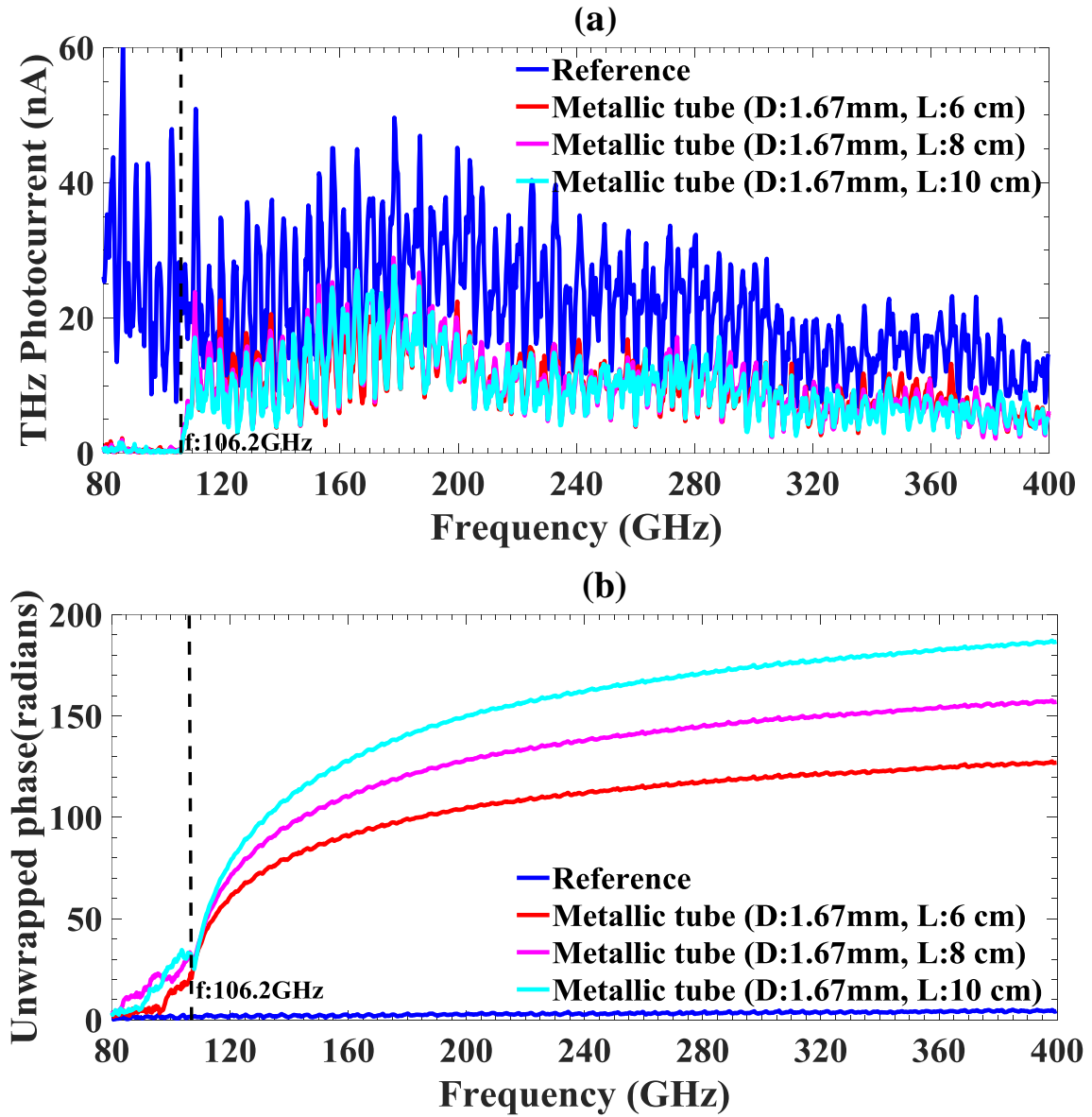
Figure 3.9: (a) THz amplitude and (b) Phase spectra of a metallic tube waveguide of different lengths

3.3   Fabrication of long THz dielectric fibers

Long, dielectric fibers are generally fabricated using the thermal fiber drawing method [226]. In this technique, the preform is heated slightly higher than the glass transition temperature in the furnace, and the fiber is then pulled off using the mechanical-tractor assembly. The thickness of the fiber can be controlled using real-time laser micrometer. A complex microstructured preform design (transverse direction) can be fabricated using techniques such as stack and draw [227], drilling [181] and extrusion moulding [228]. The fiber is then drawn under pressure (air or nitrogen) to avoid the collapsing of the microstructure. In this work, a simple solid core fiber of different thickness fabricated using polypropylene material is demonstrated for data transmission. In our experiments, the diameter of the thickest PP fiber (3D printing filament) used is 1.75 mm. In order to use the PP material from the same supplier for the purpose of comparison, a 3D printer is used to draw the fiber directly from the printing nozzle with the fiber thickness smaller than 1.75 mm. For the fabrication of THz passive components, both FDM and stereolithographic 3D printer is used.

3.4   Theoretical analysis

In this thesis, the numerical simulation has been carried out using COMSOL Multiphysics software. For the solid core THz fiber, the modal effective index, propagation loss and power fraction are computed using 2D models whereas the bend loss of the fibers are computed using 2D axis symmetric model. Similarly, transfer matrix theory, along with the mode matching technique, is used to estimate the excitation efficiency [223, 224].

To conclude, in this chapter, we have shown the development of frequency domain THz spectroscopy system for characterizing THz waveguides of various lengths. The same system is then modified as the THz communication system for wireless transmission as presented in chapter 4. Also, we have used this system for characterizing the PP material and the procedure is shown in chapter 5.

CHAPTER 4   ARTICLE 1- LIVE STREAMING OF UNCOMPRESSED HD AND 4K VIDEOS USING TERAHERTZ WIRELESS LINKS

Kathirvel Nallappan[1,2], Hichem Guerboukha[2], Chahé Nerguizian[1] and Maksim Skorobogatiy[2]

[1]Department of Electrical Engineering, Polytechnique Montréal

[2]Department of Engineering Physics, Polytechnique Montréal

Abstract: Taming the Terahertz waves (100 GHz-10 THz) is considered the next frontier in wireless communications. While components for the ultra-high bandwidth Terahertz wireless communications were in rapid development over the past several years, however, their commercial availability is still lacking. Nevertheless, as we demonstrate in this paper, due to recent advances in the microwave and infrared photonics hardware, it is now possible to assemble a high-performance hybrid THz communication system for real-life applications. As an example, in this work, we present the design and performance evaluation of the photonics-based Terahertz wireless communication system for the transmission of uncompressed 4K video feed that is built using all commercially available system components. In particular, two independent tunable lasers operating in the infrared C-band are used as a source for generating the Terahertz carrier wave using frequency difference generation in a photomixer. One of the IR laser beams carries the data, which is intensity modulated using the $LiNbO_3$ electro-optic modulator. A zero bias Schottky diode is used as the detector and demodulator of the data stream followed by the high-gain and low-noise pre-amplifier. The Terahertz carrier frequency is fixed at 138 GHz and the system is characterized by measuring the bit error rate for the pseudo random bit sequences at 5.5 Gbps. By optimizing the link geometry and decision parameters, an error-free (BER<10^{-10}) transmission at a link distance of 1m is achieved. Finally, we detail the integration of a professional 4K camera into the THz communication link and demonstrate live streaming of the uncompressed HD and 4K video followed by the analysis of link quality.

4.1 Introduction

The internet protocol data traffic is continuing its exponential increase and is expected to reach over 278 Exabytes per month by 2021 [229]. Similarly, the ever-increasing wireless

communications data rate in the commercial markets is expected to be 100 Gbps within the next 10 years [230]. To meet the bandwidth demand, a shift towards higher carrier frequencies has been considered as a solution [231, 232]. While the carrier frequency below 100 GHz is the immediate solution for high speed wireless applications, the offered data rate is still two orders of magnitude below the expected demand [233]. The availability of several atmospheric transmission windows and broad bandwidth of the channels in the Terahertz (THz) range (100 GHz-10 THz) is interested to meet the required demand. Therefore, the frequency band above 100 GHz is seen by many as the next frontier in wireless communications [11, 234]. It is worthy to mention that the start of the THz frequency spectrum is not clearly defined whether it begins from 100 GHz or 300 GHz. Some research communities define the start frequency at 100 GHz. Among the important organizations, we note that the International Telecommunication Union [235] and Asia Pacific Telecommunity [236] define the beginning of the THz region at 100 GHz. Also, the same organization (ITU) specified 30-300 GHz as millimeter waves in their later report [237]. Since in our work, we used a photonics-based source that can be tuned up to 3 THz, we preferred to refer to our system as a "THz communication system". Recently, the long distance (>2 Km) wireless links operating with a carrier frequency of 120 GHz were reported providing data rates of 10 Gbps and 20 Gbps using amplitude shift keying (ASK) and quadrature phase shift keying (QPSK), respectively [238-241].

At the same time, maturing the Terahertz (THz) wireless communication technologies from laboratories into commercial applications is facing multiple challenges. Two major technologies exist in establishing THz wireless communication links: electronics-based frequency multiplier chains and photonics-based frequency difference generation [20]. Electronics-based approaches offer high powers (thus longer link distances), but mainly at lower carrier-wave frequencies (<300 GHz), thus limiting the communication data rates [242]. On the other hand, photonics systems suffer from lower power budgets due to inefficiency in optical to THz conversion, but offer potentially higher data rates at much higher carrier frequencies [20].

From the prospective of telecommunication applications, one of the key advantages offered by infrared (IR) photonics is its ability to interface with the already existing low loss optical fibers for hybrid high speed optical to wireless radio [20, 87].Therefore, integration of the optics-based THz wireless transmitters with existing IR photonics networks can be done in a seamless fashion. Additionally, high tunability of the THz carrier frequency (between 20 GHz – 3.8 THz [243-245])

is easily achievable using photomixing, thus higher carrier frequencies and hence, higher data rates are readily achievable in optics-based THz systems. Recent advances in the uni-traveling carrier photodiodes (UTC-PD)-based THz photomixers give a new hope for commercial applications of photonics-based THz communication systems [246-249]. Such devices offer relatively high powers (~1 mW) even at the carrier frequency of 300 GHz [250]. By using a hybrid approach incorporating both UTC-PD as the emitter and solid-state devices such as Schottky diodes as receivers, several high-speed THz communication links have been demonstrated in recent years. Data rates of 48 Gbps at 300 GHz [85] and 50 Gbps at 330 GHz [86] have been achieved in real-time measurements using amplitude shift keying (ASK) modulation of the optical signals. Similarly, using higher order modulation and offline signal processing techniques, 75 Gbps at 200 GHz [251], 100 Gbps at 237.5 GHz [252], 46 Gbps at 400 GHz [253] and 60 Gbps at 400 GHz [254] have been demonstrated. Using multi-channel modulation and single emitter configuration, a higher data rate of 160 Gbps has been reported recently [255]. As a practical application, a few works have shown successful transmission of HD and 4K video in the lower THz band [77, 240, 256-259]. Similarly, using photonics based THz emitter and heterodyne receiver operating at 600 GHz, a successful transmission of HD video has been demonstrated over a short range (0.5 m) with a received THz power of 10 nW [260]. All these demonstrations have been carried out mainly using the proprietary components such as photomixer and without any analysis of the video quality.

With ever increasing wireless data rate, mobile backhaul for transferring large bandwidth signals between base stations and end users is one of the primary targets for using THz band. Employing a highly efficient wireless backhaul service by connecting multiple base stations with small cell size will ensure high data rate to the end users [261]. Thus, enabling photonics based wireless links (millimeter to THz frequency band) offers high efficiency and cost-effective solution to the mobile backhauling and 'last mile' connections [204, 205]. Similarly, the THz communication systems can be used to establish short range high-speed wireless links for applications such as chip-to-chip communications, KIOSK downloading, high-speed indoor wireless LAN to name a few [262].

Among several bandwidth hungry applications, wireless transmission of uncompressed HD, 4K and 8K video finds importance in applications such as education, entertainment, telemedicine, security, video conferencing to name a few. It is reported that the market value of 4K technology will reach $102.1 billion by 2020 [263]. Wireless streaming of high-quality videos is already used

in biomechanical analysis, unmanned aerial vehicle (UAV) unmanned ground vehicle (UGV) and telemedicine. In biomechanics, by transmitting the uncompressed video content wirelessly to a remote workstation, the motion analysis (sports person for example) can be performed in real-time [264].

In telemedicine, transmission of HD video from the remote location (ambulance for example) to the hospital, a hybrid optical-wireless technology with low latency would be the ideal solution [265]. An unprecedented level of detail to judge the patient condition can be inferred from the video using a zoom-in feature with uncompressed 4K or 8K cameras at the remote pre-medical center [266]. For such applications, a highly efficient beamforming technique is essential while using higher carrier frequency to minimize path loss and to avoid missing of communication between high speed vehicles and base station. Furthermore, the wireless streaming of uncompressed 4K video is of great importance in broadcasting, surveillance, security and ground mapping applications. For example, NHK (Japan broadcasting corporation) has already started trial experiments by telecasting 8K video using proprietary devices for Olympic games that to be held in 2020 [267]. All of the above-mentioned examples suggest that transmission of the uncompressed 4K/8K videos can provide a significant improvement to a variety of important applications in the academics and industries.

Recent developments of hardware components in the THz band promise several game-changing applications. Thus, in this article, encouraged by the recent advances in the THz and IR photonics, we show the possibility of assembling a high-performance THz communication system for real-world applications, by borrowing off-the-shelf commercial components from various communication technologies. We present the design and the performance evaluation of the photonics-based THz communication system that is built using all commercially available system components. Although several research groups have demonstrated the wireless transmission and display of uncompressed HD and 4K videos, in this work, in addition to the use of all commercial components in building the communication system, we detail the integration, record and analyzed the synchronization error of each frame over long recording duration (30 minutes) for both uncompressed HD and 4K video signals. The paper is organized as follows. Section 4.2 presents the experimental setup for the photonics-based THz communication system followed by the characterization of the communication system components in Section 4.3. Section 4.4 presents the

Bit error rate (BER) measurement results and finally Section 4.5 shows the integration and demonstration of wireless transmission of the uncompressed HD and 4K video streams.

4.2 Terahertz communication system

The schematic of the photonics-based THz wireless communication system is shown in Fig.4.1. One of the two laser beams is intensity-modulated and then amplified using the Erbium-doped fiber amplifier (EDFA). The laser beams are combined using the 3 dB coupler and then injected into the photomixer for THz generation.
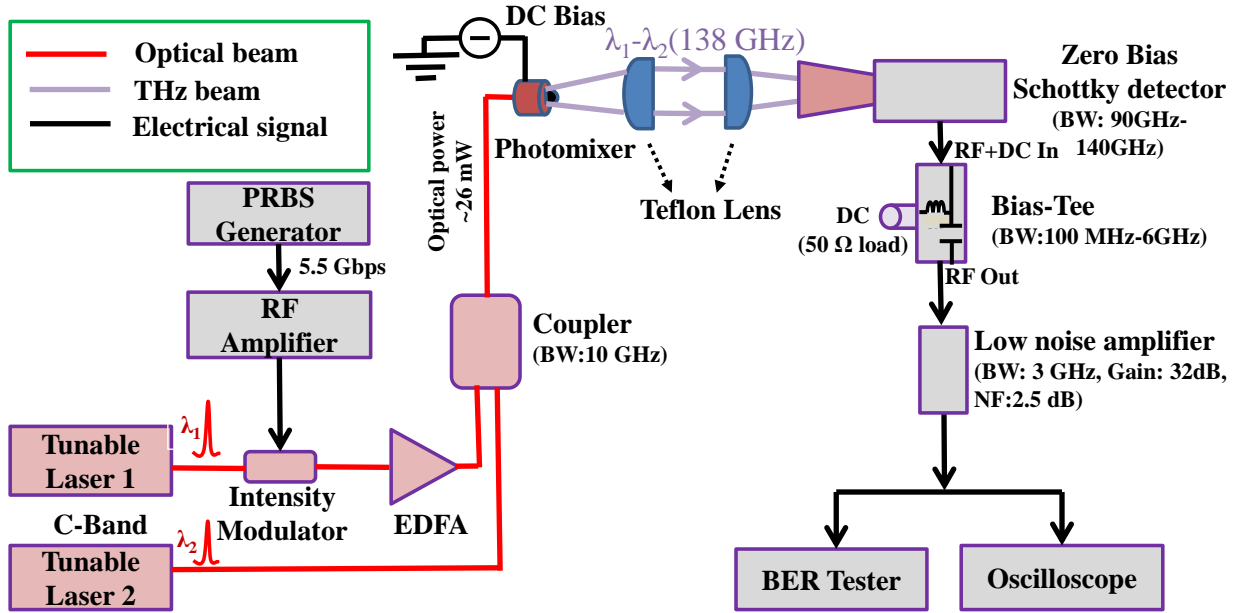
Figure 4.1: Schematic of the photonics-based THz wireless communication system. (EDFA: Erbium doped fiber amplifier, BW: Bandwidth, NF: Noise figure)

In the receiver side, a zero-bias Schottky diode (ZBD) is used to detect and directly demodulate the incoming THz signal. The DC field present in the demodulated baseband signal is filtered using Bias-Tee and amplified using a low noise amplifier (LNA) for further signal processing. The components of the THz communication system are detailed in what follows.

4.2.1 Laser source

Two tunable distributed feedback (DFB) laser diodes operating in the C-band (TOPTICA Photonics) with an output power of ~30 mW each are used to optically drive the THz emitter. The linewidth of each laser is ~0.5 MHz on a short time scale (100 μs), while the laser frequency may drift over a few tens of MHz in a few minutes depending on the stability of the ambient conditions. Both diodes are mounted in a compact laser head and the output beams are delivered via a polarization-maintaining (PM) single-mode fiber. The wavelength tuning behavior of the lasers is calibrated [29] and the output THz frequency -i.e., the frequency difference of both lasers - is tuned using an Field Programmable Gate Array (FPGA)-based control module ("Teracontrol" by TOPTICA Photonics, which controls the lasers thermally using temperature and current controller).

4.2.2 Data modulation

One of the lasers is intensity-modulated (Amplitude shift keying modulation, ASK) using an external electro-optic Mach-Zehnder modulator (MZM) (Thorlabs-LN81S-FC). The typical insertion loss and pseudo random binary sequence (PRBS) optical extinction ratio of MZM are 4 dB and 13 dB, respectively. The input signal to the MZM is split into two arms and combined at the output port. The amplified RF signal is connected to one of the arms, which changes the refractive index of the substrate resulting in either constructive or destructive interference at the output port, resulting in the modulation of optical beam. The operating bias point of the modulator is controlled by the modulator driver unit (Thorlabs-MX10A), which also acts as an RF amplifier and optical attenuator. The modulator is locked to the quadrature bias point with positive slope, which is monitored continuously using a dither tone to detect and correct any drift in the bias voltage. The frequency and amplitude of the dither tone is set to 3 KHz and 600 mV$_{pp}$, respectively. The THz communication system is characterized by transmitting the Non-Return to Zero (NRZ) PRBS data that is generated by the pulse pattern generator (PPG) unit integrated in the test equipment (Anritsu-MP2100B). The generated PRBS data with a peak-to-peak amplitude of 0.4 V$_{pp}$ is connected to the modulator driver unit while the amplified electrical data with amplitude of 5 V$_{pp}$ is fed to the optical modulator. The optical output power after the electro-optic modulator is ~200 μW and is fixed to a constant of 110 μW using the variable optical attenuator to avoid any power fluctuations during the experiments. It is further amplified using EDFA amplifier (Calmar

laser-AMP-PM-18) to ~13 mW. The pump current of the EDFA is adjusted to have an average output power similar to the unmodulated direct laser beam.

4.2.3 THz generation

A 3 dB fiber coupler is used to combine the direct and modulated laser beams and the output is fed to the photomixer (TOPTICA Photonics) for THz generation. The photomixer features a silicon lens (6.05 mm ± 0.1 mm thickness and 10.0 ± 0.1 mm diameter) to pre-collimate the output THz beam. The gain of the photomixer is contributed by both structure of the antenna (Bowtie) and silicon lens, which is ~17 dBi and ~19 dBi at the carrier frequency of 100 GHz and 140 GHz, respectively [212]. The Teracontrol module is also used as the DC voltage source to drive the photomixer electrically. The output THz power of a photomixer is shown in Fig.4.2, which is measured using calibrated Golay cell [268]. We see that the output power is not uniform, and the high power is obtained mostly below 200 GHz. Two plano-convex lenses (Thorlabs-LAT100) with a focal length of 100 mm and a diameter of 50 mm are used to collimate the THz beam in free space and focus it again into the detector.
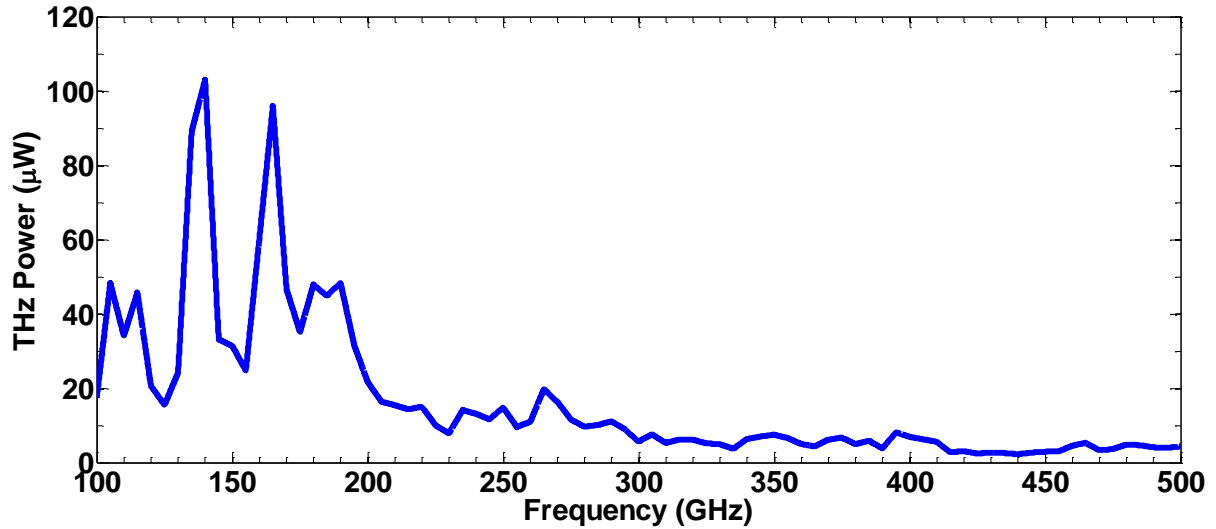
Figure 4.2: THz output power from the photomixer measured using a calibrated Golay cell with 5 GHz spectral resolution (Courtesy of TOPTICA Photonics)

4.2.4 THz detection and demodulation

A ZBD with a horn antenna is used to detect and demodulate the incoming THz signal. The choice for the THz carrier frequency is determined by the product of the output power of the THz emitter and the responsivity of the ZBD. Particularly, two ZBDs (Virginia diodes WR8.0ZBD-F and WR6.5ZBD-F) with a working range below 200 GHz were used in the analysis. The responsivity data for both detectors is shown in Fig.4.3.
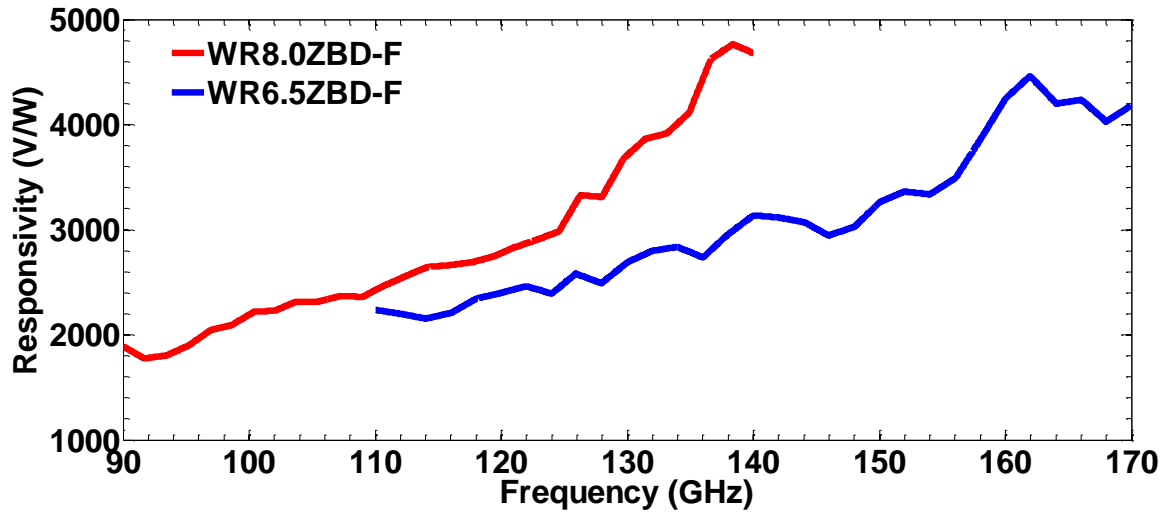
Figure 4.3: Responsivities of commercial ZBD WR8.0ZBD-F and WR6.5ZBD-F (Courtesy of Virginia Diodes)

The maximal voltages at the output of the two ZBDs are estimated by multiplying the emitted THz power as presented in Fig. 2 by the responsivity of a corresponding ZBD presented in Fig. 4.3. In Fig. 4.4, we plot such voltages as a function of the THz frequency and conclude that WR8.0ZBD-F ZBD with the conical horn antenna (Virginia diodes WR8.0CH) operating at 138 GHz results in the maximal detected signal amplitude for a back-to-back emitter/detector arrangement. This conclusion was also confirmed experimentally by performing a frequency sweep and detecting the frequency of maximal detected signal at a fixed short link length of ~30 cm. Furthermore, this frequency lies in the second atmospheric transmission window above 100 GHz [269] (grey area in Fig. 4.4), making it a natural choice as a carrier frequency for THz communications.

Finally, after ZBD, a Bias-Tee (Minicircuits-ZFBT-6GW+) is connected in sequence to block the DC voltage and let only the AC signal from 100MHz to 6 GHz passing to the next stage. Followed the Bias-Tee, a high gain (> 32 dB) and low-noise amplifier (Fairview Microwave-SLNA-030-32-30-SMA) is used to amplify the demodulated baseband signal. The noise figure and the bandwidth of the low noise amplifier (LNA) are 2.5 dB and 3 GHz, respectively. The typical output third order intercept point of the LNA is +29 dBm.
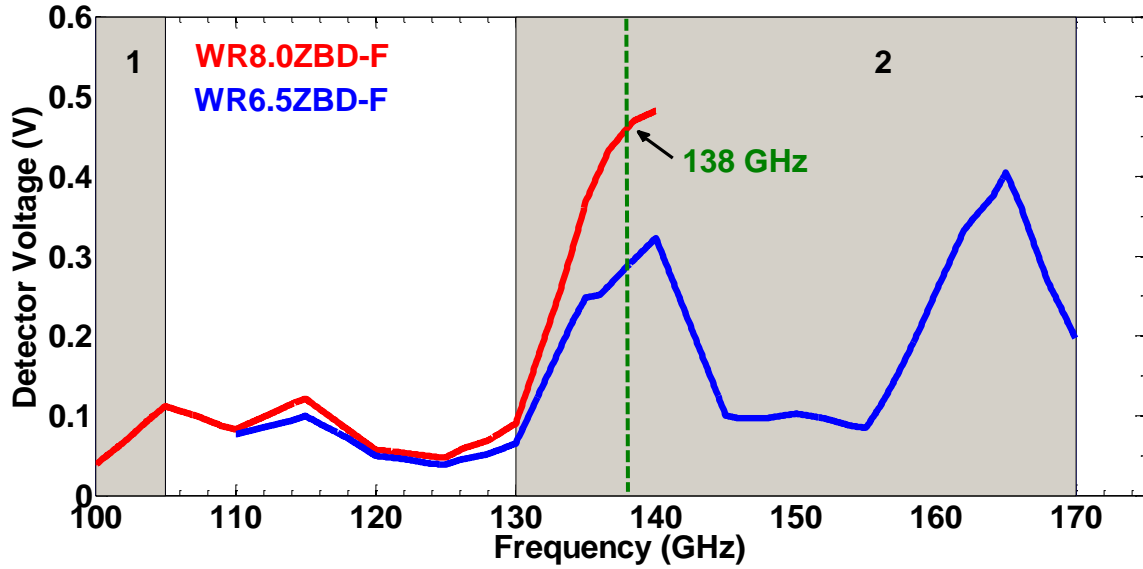
Figure 4.4: Figure Estimate of the maximal voltage at the ZBD's output when used with Toptica's THz photomixer. Grey areas correspond to the THz atmospheric transmission windows as identified in [269]

4.3 Characterization of the components used in the communication system

A single-ended, NRZ, PRBS data with a bitrate of 5.5 Gbps and a pattern length of 2^{31}-1 is used as the test signal to characterize the THz communication system. The peak-to-peak amplitude of the test signal is set to 0.4 V_{pp}. The optical spectra of the DFB lasers (before and after modulation) with a frequency separation of 138 GHz are measured using the optical spectrum analyzer (Anritsu-MS9740A) with a spectral resolution of 0.03 nm as shown in Fig. 4.5. As discussed in the previous section, one of the lasers is intensity modulated and amplified using the EDFA. First, the PRBS data is turned OFF and the optical output power from the modulator is measured. We observe a high-power loss (>10 dB) due to the optical modulator. The output from the optical modulator is

connected again to the modulator driver unit, where the adjustments of the final output power can be done using variable optical attenuator based on user requirement. It is possible to choose either constant output power or constant attenuation mode. We used constant output power mode to avoid any fluctuations in the optical power. Since the optical power from the modulator is low (~200 µW), we fixed the variable optical attenuator to provide the constant output of 110 µW to further reduce the risk of power fluctuations.
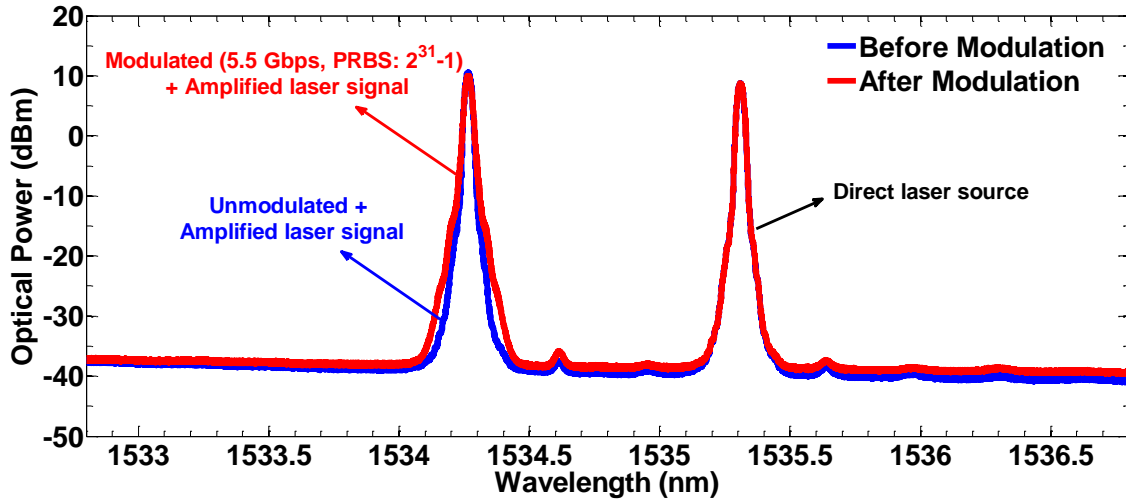
Figure 4.5: Spectra of the input optical signal injected into the THz photomixer. The SNR of >40 dB is achieved

Next, an EDFA is used and by adjusting its pump current, the amplitude of the laser beam is kept similar to that of the direct laser beam (blue curve in Fig.4.5 pointing unmodulated + amplified laser signal). When two laser beams (modulated and direct laser beam) of equal power (within the damage threshold limit of the photomixer, which is ~35 mW) is mixed in the photomixer (heterodyning) a higher THz amplitude was observed. When the PRBS data is turned ON, the laser beam is now modulated, and we observe an increase in the bandwidth of the modulated laser signal as well as the optical noise floor (~1 dB) when compared with the unmodulated laser beam as shown in Fig.4.5 (red curve pointing modulated + amplified laser signal). However, a signal-to-noise ratio (SNR) greater than 40 dB is achieved after the modulation of optical beam (at the input of photomixer), which is recorded by measuring the peak amplitude and noise floor of the laser signal using optical spectrum analyzer. The total optical input power (combined laser power) injected into the THz photomixer is ~26 mW.

At the receiver side, the Bias-Tee (operational bandwidth 100 MHz - 6 GHz) acts as a band-pass filter as well as to block the DC voltage passing to the next stage (LNA) and thereby to increase the performance. Although the LNA is AC coupled, we observe the improved performance while using the Bias-Tee. The circuit of the Bias-Tee consists of a capacitor and inductor connected in parallel with three external ports (RF+DC-input, DC and RF-output). The connection of Bias-Tee is shown in Fig.4.1. The DC port of the Bias-Tee is connected to a 50Ω load. Without Bias-Tee, the demodulated baseband signal with floating voltage values passes to the next stage (LNA) minimizing the performance. By connecting the Bias-Tee in between the ZBD and LNA, the floating voltage signals from the ZBD is adjusted to a common reference ground and thereby improves the performance with slightly higher eye amplitude.
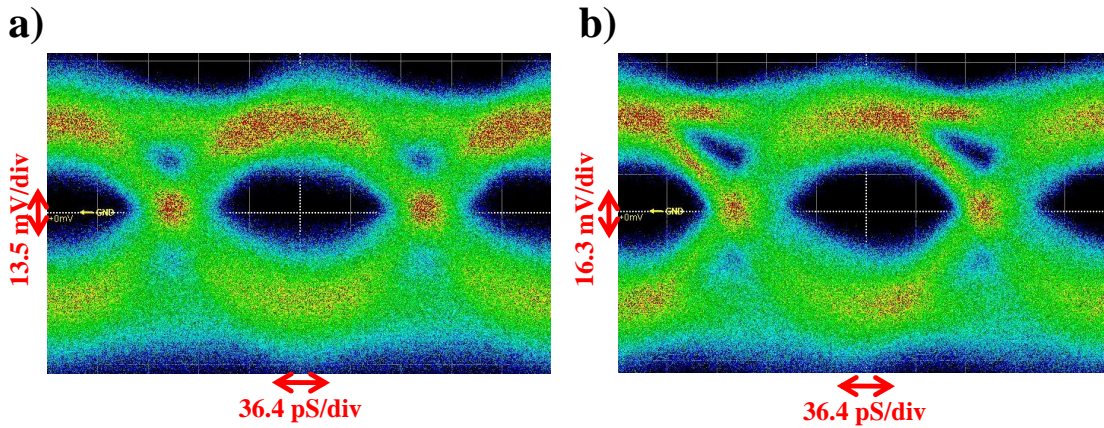
Figure 4.6: Eye patterns for the test signal (PRBS: 5.5 Gbps, 231-1), (a) without Bias-Tee and (b) with Bias-Tee

To ascertain the impact of the Bias-Tee on the signal quality, an eye pattern is recorded after the LNA using a high-speed oscilloscope (Anritsu-MP2100B) without and with Bias-Tee as shown in Fig.4.6. The link distance and the DC bias voltage of the photomixer are fixed at 1 m and -1.9 V, respectively, for this measurement. The eye pattern measured using the Bias-Tee shows higher eye (opening) amplitude (~18% increase) when compared to the eye pattern taken without Bias-Tee. While it improves the performance of the communication system by blocking the DC voltage, at the same time the Bias-Tee might cause some problems when transmitting almost constant bit patterns (like long continuous string of ones or zeros). This is related to the fact that the low

frequency components present in the long continuous pulse are filtered out by the Bias-Tee. For example, the lowest non-zero frequency component present in the PRBS test signal with a bitrate of 5.5 Gbps and a pattern length of 2^{31}-1 is 2.56 Hz ($5.5 \cdot 10^9 Hz/2^{31}$) and it is filtered out by the Bias-Tee along with its harmonics up to 100 MHz, affecting the quality in the signal reconstruction. While keeping in mind potential issues with long constant bit patterns, we nevertheless observe that using Bias-Tee generally leads to higher performance in our experiments. Because of the lower responsivity values of ZBD's (~2000 V/W) in the THz region, the corresponding output voltage from them after THz detection and baseband signal demodulation is also lower depending on the received THz power. To amplify the baseband signal, a digital amplifier with broad bandwidth (~10 GHz for data rate of ~10 Gbps), low noise-figure (<3 dB), high gain (>30 dB) and SMA connectors (since ZBD's are terminated with SMA connectors) is preferred. To the best of our knowledge, such amplifiers satisfying all the above requirements are not available in the commercial market. Therefore, we used an LNA that is designed for analogue signals in our communication system. However, it can still be used for digital signals.

To test the use of analogue LNA with digital signals, the peak-to-peak amplitude of the test signal is attenuated using a fixed attenuator to ~30 mV$_{pp}$ in order to protect the test equipment from the damage after amplification (damage threshold of electrical oscilloscope is ±2V). The evaluation of the waveform such as jitter and eye crossing are automated in the test equipment. The RMS jitter of the digital test signal after attenuation (but before LNA) was measured to be 1.28 pS and 1.48 pS for 3 Gbps and 5.5 Gbps, respectively. The attenuated digital test signal is then given as the input to the analogue LNA.
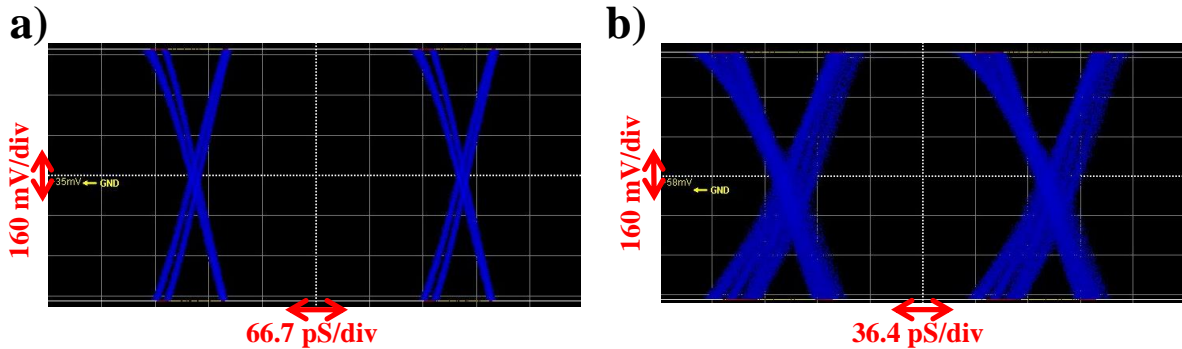
Figure 4.7: Eye patterns from the output of the analogue LNA using digital (a) 3 Gbps and (b) 5.5 Gbps signals

The measured eye pattern from the output of the LNA is shown in Fig.4.7. The RMS jitter measured after the LNA is 4.23 pS and 6.74 pS for 3 Gbps and 5.5 Gbps, respectively. Similarly, the eye crossing percentage of the digital signal after the LNA deviates from ideal 50% to ~48% and ~40% for 3 Gbps and 5.5 Gbps, respectively after amplification. This may be due to the fact that the duration of digital 0 is longer than digital 1 causing the reduction in the eye crossing percentage from the ideal value. Therefore, we conclude that while analogue LNA can be used for amplification of the digital signals, it can also significantly increase the timing jitter and deviation in the eye crossing percentage in the system while increasing the bitrate.

4.4 Evaluation of THz communication system using BER measurements
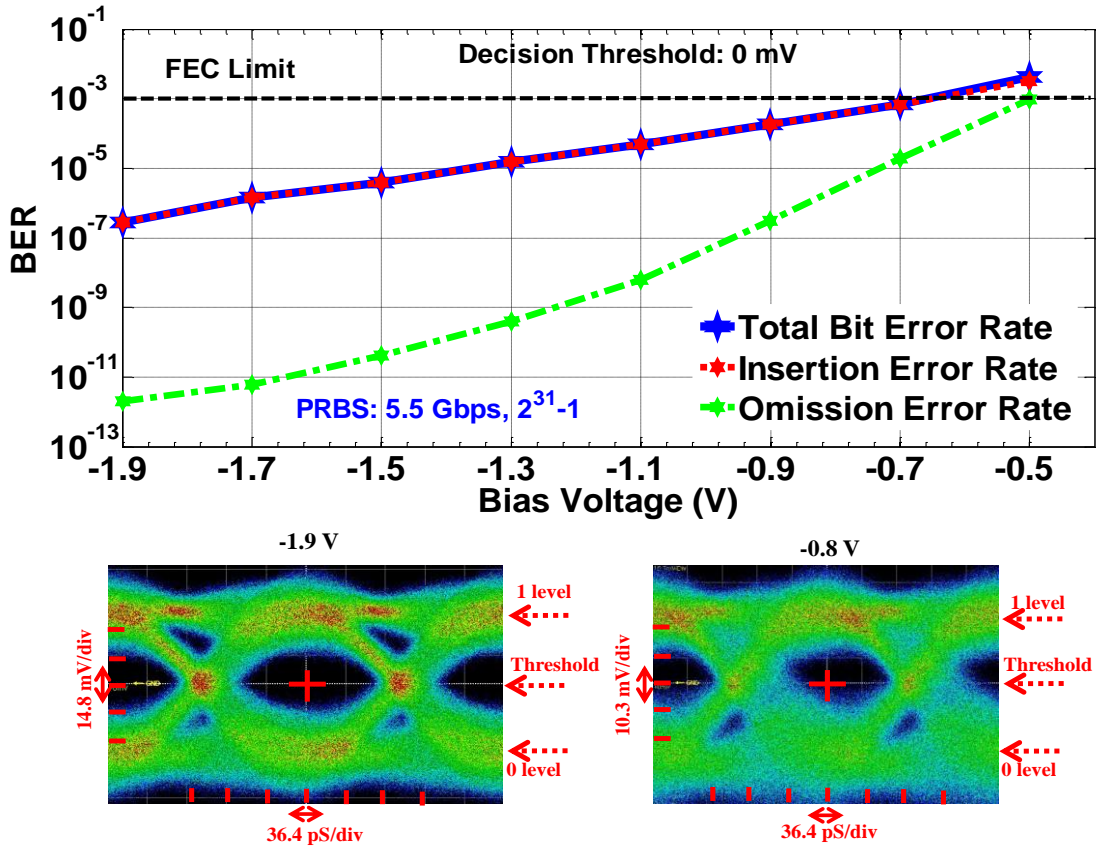
Figure 4.8: Measured BER as a function of the photomixer bias voltage for the PRBS test signal with 5.5 Gbps bitrate and 2^{31}-1 pattern length

The performance of the THz communication system was then characterized using bit error rate (BER) tester (Anritsu-MP2100B). The BER was first characterized as a function of the photomixer

bias voltage, which is a key parameter that defines the emitted THz power. To record a highly consistent BER data in short measurement duration, we choose the target BER of 10^{-12} in our experiments. For the target BER of 10^{-12}, and the bitrate of 5.5 Gbps, the duration of a single measurement is calculated as measurement duration $= 1/(\text{target BER} * \text{bitrate}) \approx 182$ sec. The THz output power from the photomixer is proportional to the illuminated optical power and applied bias voltage.

By fixing the link distance to 100 cm, illuminated optical power to 26 mW and the decision threshold to 0 mV, the BER was measured after the LNA by varying the DC bias voltage of the photomixer (Fig. 4.8). The damage threshold limit of the DC bias voltage for the THz photomixer is -2 V and therefore we limited our measurements to a maximum bias of -1.9 V. The lowest BER of ~10^{-7} was achieved for the bias voltage of -1.9 V.

By gradually decreasing the bias voltage, it was found that the BER increased exponentially fast. At the limit of the forward error correction (BER ~10^{-3}), the bias voltage was -0.7 V. From Fig. 4.8, we also observe that insertion errors (digital 0 is mistaken for the digital 1) contributes more to the total BER when compared to the omission errors (digital 1 is mistaken for the digital 0). This is due to the vertical asymmetry of the eye pattern in the received signal. The vertical asymmetry in the eye pattern arises from the optical modulation itself. The DC bias to the modulator is locked to the quadrature point (positive slope) of its transfer function. A small uncertainty in the eye amplitude could be due to the minor variation in the DC bias from its ideal position. This is especially pronounced when the data rate is greater than 2 Gbps. As seen from the eye patterns (insets in Fig. 4.8), the digital 0 is closer to the decision threshold than digital 1, which gives rise to the higher insertion error rate.

Next, we have characterized BER as a function of several communication link parameters such as link distance, as well as angular deviation of the detector antenna from the principal direction of signal propagation. Thus, in the first experiment, we have fixed the link distance of 100 cm and the photomixer DC bias voltage to -1.9 V. The BER was then measured by varying the alignment angle of the ZBD detector antenna with respect to the signal propagation direction as defined by the emitter antenna (see the inset in Fig.4.9). Experimentally this was accomplished by changing the angle of rotation using high precision rotation mount (Thorlabs-PR01), where the detector antenna

is fixed on top of it. The amount of THz power coupled into the detector antenna reduces with increased angular rotation, which results in higher bit errors. The total BER was found mainly due to the insertion errors (see Fig. 4.9) due to asymmetry of the eye pattern in the vertical direction. From these measurements, we found that in order to stay within the FEC limit, the detector has to be within ~4.8 degrees of the principal beam propagation direction.
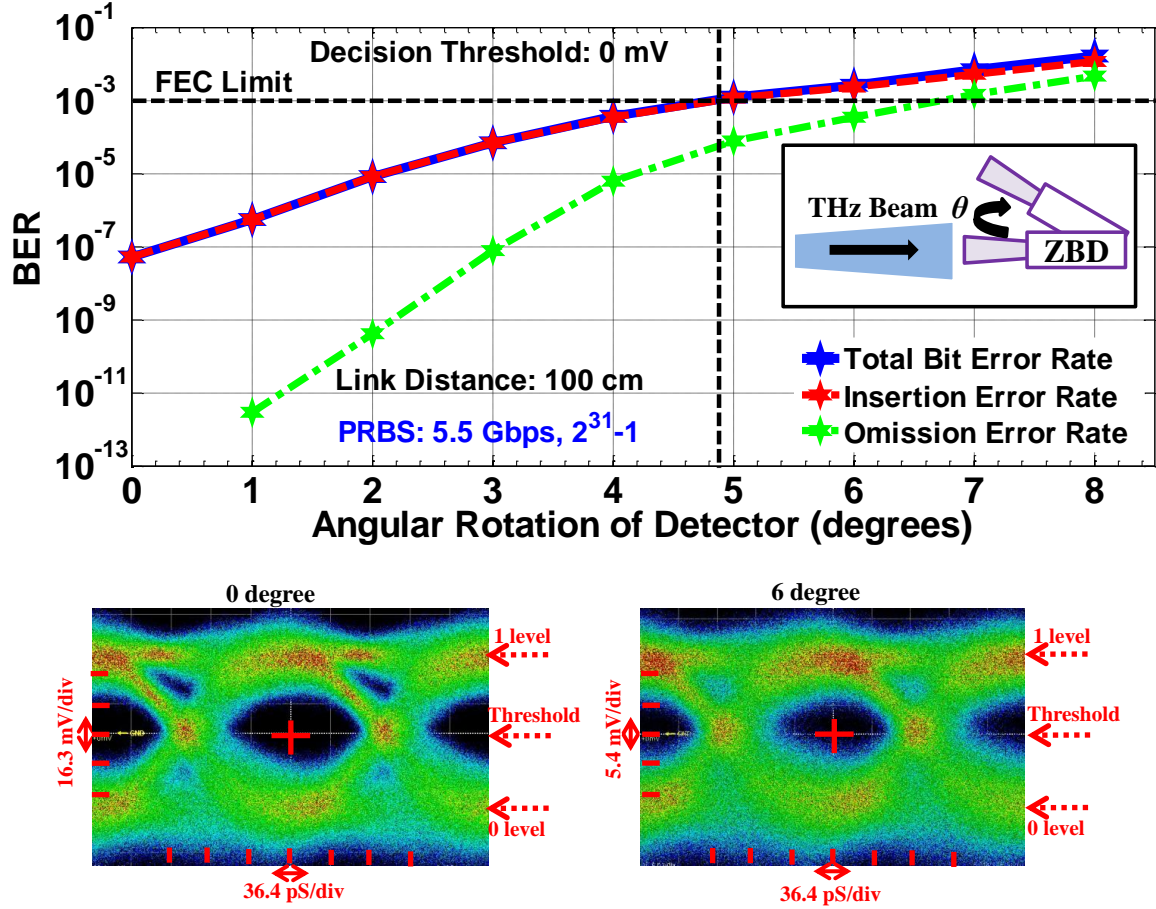
Figure 4.9: Measured BER as a function of the angle θ between the detector and the THz signal propagation direction for the PRBS test signal with 5.5 Gbps bitrate and 2^{31}-1 pattern length. Inset: schematic of the experiment

In the second experiment, the BER was measured as a function of the link distance. While evaluating the impact of the link distance, the bias voltage and the angular deviation of the detector antenna was set to -1.9 V and 0 degree, respectively. First, we fixed the decision threshold to 0 mV and measured the BER at several link distances. As our system was mounted and aligned on the optical table, the measurements were limited to 175 cm long links. The measured BER is shown in
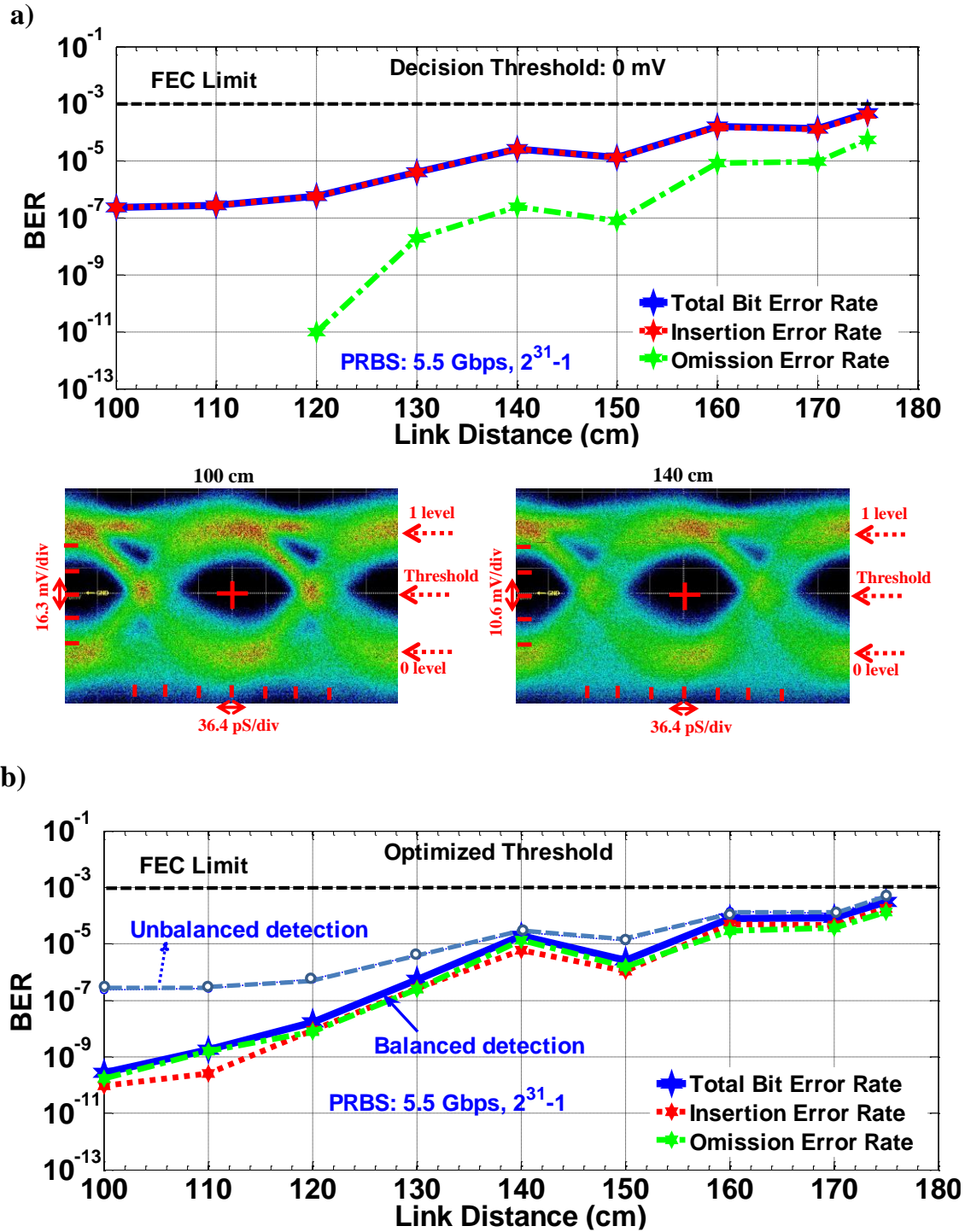
Figure 4.10: Measured BER as a function of the communication link length for the PRBS test signal (5.5 Gbps, 2^{31}-1). (a) Unbalanced system, the decision threshold is fixed at 0 mV. (b) Balanced system: for each link length, the decision threshold is optimized to balance the insertion and omission rates

Fig. 4.10 (a), we note that even at 175 cm link length, the total error is below the FEC limit. Due to vertical asymmetry in the eye diagram, the insertion error is again much higher than the omission error. This asymmetry can be addressed by adjusting the value of the decision threshold in order to equalize the insertion and omission errors, which also leads to the lower total BER.

Therefore, in the follow-up experiment we optimized the system performance by finding the optimal value for the decision threshold at each link length in order to equalize the insertion and omission errors. In Fig. 4.10 (b) we plot performance of the optimized THz communication system as a function of the link distance, where omission and insertion errors are balanced. For comparison, in the same figure we present total error of the unbalanced system (same as Fig. 4.10(a)) and note that decision threshold optimization indeed reduced the total BER, which is especially pronounced at shorter link lengths.

In passing we note that for shorter communication links, the main reason for the BER increase with the link distance is divergence of the THz beam, and a consequent reduction of the THz power at the detector site. Particularly, due to diffraction of the collimating lens, the diameter D_{THz} of the THz beam as a function of the link distance L can be approximated as $D_{THz} \sim L \cdot \lambda_c / D_l$, where λ_c is the wavelength of THz carrier wave, and D_l is the lens diameter. If two identical lenses are used to collimate the THz beam and focus that beam onto a detector, then with P_0 power emitted by the photomixer, only $P = P_0 (D_l / D_{THz})^2 \sim P_0 (D_l^2 / (L \cdot \lambda_c))^2$ will arrive to the detector. From this we conclude that two strategies can be pursued in order to increase power budget in case of short communication links. These include either using collimating lenses of larger diameter D_l, or using higher THz carrier frequencies (lower λ_c). Although increasing the carrier frequency can lead to less divergence, it can lead to higher path-loss. The path loss mainly occurs due to material absorption (in case of signal passing through the material), diffraction (due to opaque obstacles) and multipath (signal travelling from different paths to reach the receiver). Therefore, the path loss increases with increase in the frequency reducing the power budget. However, for line of sight communication as we demonstrated in this work, the effect of path loss is minimal. For longer communication links, THz absorption in atmosphere becomes important, which further decreases the power budget and increases detection errors.

Table 4.1: photonics based wireless communication system in 100-250 GHz Frequency range

Data rate (Gbps)	Frequency (GHz)	Distance (m)	Modulation	Reference
440	37.5 &100	1.5 & 0.7	QPSK	[270]
10	120	5800	ASK	[240]
1	146	0.025	ASK	[271]
11	200	0.18	ASK	[272]
75	200	0.02	QPSK	[251]
100	237.5	20	QPSK	[252]
5.5	140	1.75	ASK	**This work**

Now, we discuss several ways to increase the performance and application of the proposed system. Although the electronic based THz communication system can easily reach kilometer link distance, the short communication link distance and the data rate using a photonics approach can be improved by several folds by changing the critical components such as high performance photomixer and LNA. A waveguide integrated UTC-PD photomixing antenna (NTT Electronics) offers output power of ~-5 dBm at 140 GHz can be used. On the other hand, if the power of the THz source is higher, one can take advantage of using commercial broadband digital LNA's with gain less than 30 dB and noise figure greater than 3 dB (products from SHF communication technologies for example). Similarly, multi-carrier modulation along with switching of carrier frequency has no equivalent in electronics-based approach [20]. Although the electronics-based approach is less expensive compared to the photonics-based THz system, the cost can be scaled down commercially by fabricating dual lasers with modulator on a single chip associated with mass production of photomixers. In Table 4.1, we compare the THz wireless communication systems

based on photonics approach in the 100-250 GHz range. In [270], [251] and [251], higher data rates were easily achieved by using higher order modulation schemes (Quadrature phase shift keying-QPSK). In [271], the wireless transmission was demonstrated using a monolithically integrated dual laser to reduce the phase noise and in [272] coherent detection scheme was employed. In [240], a longer link distance of 5.8 km was achieved by proprietary UTC-PD photomixer antenna combined with the Indium phosphide high electron mobility transistor (HEMT) millimeter wave monolithic integrated circuit (MMIC). The link distance and the data rate are comparatively low in our demonstration, which is due to the low output power of the photomixer. However, the methodology for building a long link communication system is the same. By replacing the low power photomixer with a high power photomixer (~ mW), we could readily reach up to 100s of meters and the distance would mainly be limited by the divergence of the beam, which requires large collecting optics (e.g., large dish antenna). The increased link distance will be sufficient to cover the end users within the femto cell to near pico cell range. In the receiving electronics, by using a high gain amplifier (>30 dB) with broad bandwidth (~15 GHz) and low noise figure (<3 dB), the data rate up to 10 Gbps could be easily reached using the basic ASK modulation. By replacing the intensity modulator with a high bandwidth phase modulator and by employing higher order modulation schemes, the data rate could be readily improved to few 10s of Gbps. The performance of the system could be further improved by locking the free running independent lasers to a common reference or by using dual lasers fabricated on a single chip. By implementing all the above modifications, the proposed system architecture is greatly suitable for practical applications.

We would like now to comment on the advantages of the system that we have presented in this work. First, the system was assembled by using all commercial components. It means that the result is reproducible and interesting to readers who want to build their own THz communication system. Second, on top of only displaying the wirelessly received video, we also detailed the integration of the communication system to a professional 4K camera along with the required computer configuration for recording and processing the high-resolution uncompressed video content (see section 4.5). Therefore, the proposed system can be used in the nuclear power plants for example, which demand wireless transmission of high-resolution video content from many nearby inaccessible areas. Another interesting application of the developed communication system is to

characterize the THz integrated components and devices such as waveguides, metamaterials, to name a few. Even with the short communication link system, it is possible to experimentally validate several designs of low loss THz waveguides for real-time signal processing. Multiplexing schemes such as frequency division multiplexing, spatial division multiplexing can be studied to increase the channel capacity of the system. Further, with minor modifications in the proposed optical-THz system, several higher order modulation algorithms, multi-carrier modulations (by adding another laser line for example) can be investigated. Beamforming is one of the primary requirements for next generation wireless communication system due to line of sight links. Such techniques using optical phase shifters and new novel materials can be studied using the short communication link photonics-based THz communication system. As the DFB laser can be easily tunable, characterization of the wireless channel (indoor) over a wide frequency range from 50 GHz to 3 THz (using antenna integrated photomixers at both transmitter and receiver) can be performed. Also, by using widely tunable THz system it is possible to experimentally study various THz sensors and THz imaging algorithms. As said, either by using the proposed design directly or with minor modifications, it is possible to address several applications in both academics and industry.

4.5 Transmission of uncompressed HD and 4K videos using THz communications

As indicated in the introduction, one of the important practical applications of THz communications is wireless transmission of high-quality video. In what follows, we first detail integration of the professional 4K camera into the THz communication system detailed earlier, and then demonstrate successful transmission of the uncompressed HD and 4K videos at 60 frames per second (fps) and 30 fps, respectively. Additionally, we discuss two different strategies for the integration of 4K cameras at the transmitter side of a THz communication system depending whether electrical or optical outputs of the camera are used.

A 4K camera (Blackmagic studio camera) with a wide-angle lens (Olympus M. Zuiko Digital ED 12-40mm f/2.8 PRO Lens) was used in our experiments. The camera was equipped with two output ports (optical and electrical). The standard output from a 4K camera is an uncompressed video with 10-bit color depth and Chroma sub-sampling of 4:2:2. The peak-to-peak output voltage from the

SDI (Serial Digital Interface) electrical cable is 800 mV$_{pp}$. In Fig.4.11 (a) we present integration of a 4K camera with THz transmitter when using electrical output from the camera. The electrical cable from the 4K camera has a BNC connector with an impedance of 75Ω, whereas the RF amplifier present in the optical modulator driver has a SMA connector with an impedance of 50Ω. Therefore, an impedance matching pad with a bandwidth of 2 GHz (Fairview Microwave-SI 1560) is used in the design for the demonstration of 4K video transmission. To our knowledge, currently, this is the only commercially available impedance matching pad with BNC to SMA connectors that offers broadband operation.
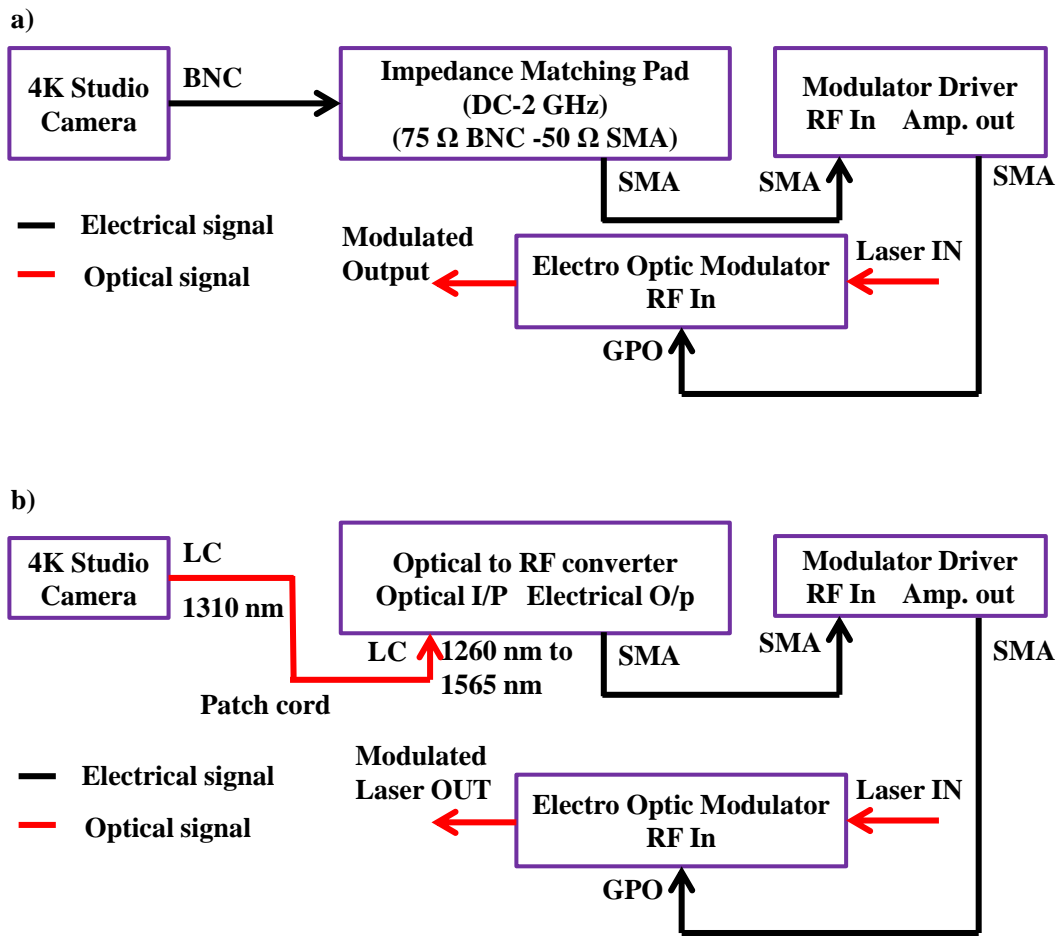
Figure 4.11: Block diagram for the integration of a 4K video camera with transmitter of the THz communication system using a) electrical and b) optical signal output from the camera

However, due to 2 GHz bandwidth limitation of the impedance matching circuit, we find that transmission of the uncompressed 4K video is limited to 30 fps (~6 Gbps). While feeding the video

signal from the camera to the optical modulator, the control settings (amplified RF voltage level and modulator bias voltage) for RF amplifier and the external modulator are kept similar to the BER measurements.

Alternatively, in Fig.4.11 (b) we present integration of a 4K camera with THz transmitter when using optical signal from the camera output. In order to use optical video signal with the THz transmitter, it has to be converted to electrical signal to feed the optical modulator. Therefore, an optical transceiver (Finisar-FTLX1471D3BCL), which is integrated with the test equipment (Anritsu-MP2100B) is used for the optical to electrical conversion. The optical signal from the 4K camera was carried via a single mode fiber. The electrical output of the optical transceiver features SMA connector with 50Ω impedance, which was then connected to the SMA input RF port of the optical modulator driver. Using both designs presented in Fig.4.11, an uncompressed 4K video up to 30 fps can be transmitted. The advantage of using electrical output from the camera (Fig.4.10 (a)) is that, the impedance matching pad is compact, less expensive and does not require the power supply for the operation. However, the RF cable is bulky to handle and suffers from high signal loss as the length increases.
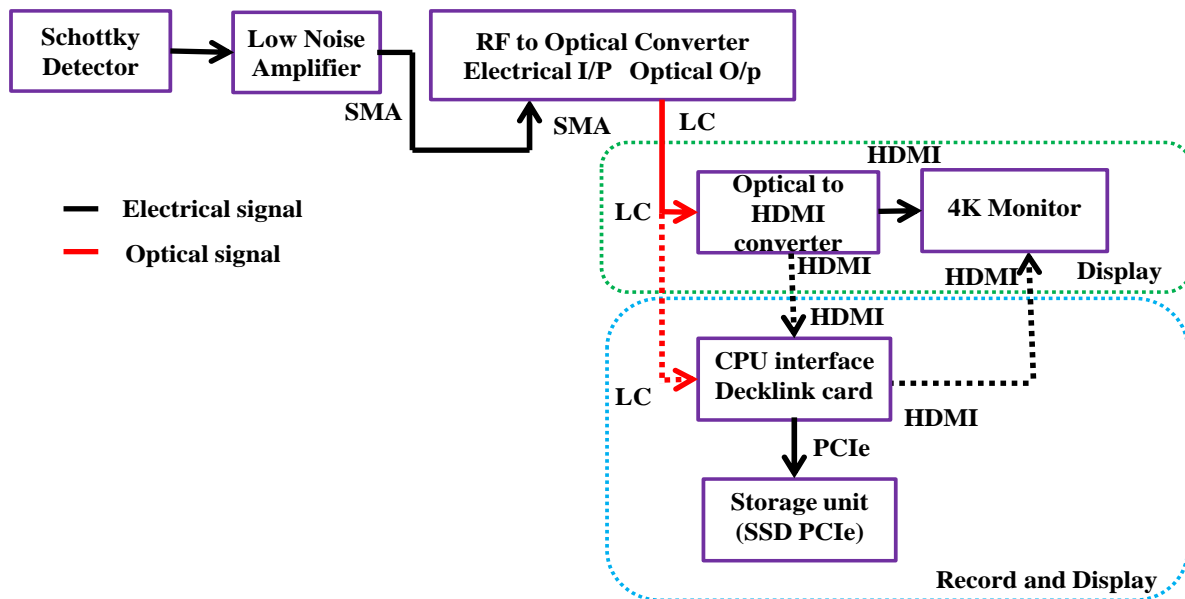
Figure 4.12: Block diagram for the receiving, visualization and recording of the transmitted uncompressed HD and 4K video

Conversely, while using optical output from the camera (Fig.4.11 (b)), we benefit from low losses of the optical fiber and it also supports large bandwidth of the baseband video signal. At the same time, the maximum data rate of the optical transmitter supported by the 4K camera is 6 Gbps, limiting the uncompressed 4K video frame rate to 30 fps. For our demonstration, we used the optical signal from the 4K camera to integrate with the THz transmitter (Fig.4.11, b) as it favors easy handling and integration using plug-in connectors.

While so far, we have discussed transmitter side of the THz communication system for video transmission, we now focus on the receiver side. At the receiver side, in order to present and analyze the transmitted video, we have explored two options including a 4K-capable display (ASUS-MG28UQ), and a 4K-capable video receiver (Blackmagic) and a storage unit. The received, demodulated and amplified electrical signal is converted into optical signal using optical transceiver of the Anritsu-MP2100B test equipment for further processing as shown in Fig.4.12. It is possible to use the impedance matching pad (similar to the transmitter integration) after the LNA without converting it to the optical signal to connect it to the computer interface card. But, the high frequency components (>2 GHz) present in the baseband signal will be filtered by the impedance matching pad (Bandwidth: DC-2 GHz), which is not favorable in signal reconstruction. Therefore, we preferred to use the optical conversion as the fiber can carry all the frequency components present in the amplified baseband signal, favoring efficient signal reconstruction and easy handling. Particularly, the electrical to optical conversion corrects the amplitude distortions that are present in the electrical signals (see the eye pattern in Fig.4.13).

The receiver configuration presented in Fig.4.12 can be modified depending on the end requirement (display or record). If displaying the 4K video is the only requirement, an optical to HDMI converter (Blackmagic-Teranex Mini Optical Fiber) is used. A high-speed computer interface card (Blackmagic-Decklink 4K Extreme 12G) is employed when both recording and displaying the 4K video simultaneously is required. The computer interface card supports SDI (electrical), HDMI and optical input/output interfaces allowing to record the received uncompressed video signal on the solid state hard drive (SSD). In order to test the capability of the SSD to record uncompressed video signals, we first analyzed the writing and reading speed of the SSD with PCIe 3.0 interface (SAMSUNG-960 PRO M.2 2 TB NVMe PCIe 3.0) and SSD with SATA interface (SAMSUNG-MZ75E500) using Blackmagic disk speed test software. Particularly,

we connected four SSD's (500 GB each) with SATA interface using RAID 0 configuration to increase the data transfer speed. The analysis showed that it is possible to write and read 2000 MB/s using SSD with PCIe3.0 interface whereas, the data transfer speed of the SSD with SATA interface is slower (Writing speed: 1197.4 MB/s and Reading: 1473.2 MB/s). Therefore, we used the SSD with PCIe3.0 interface to record the uncompressed HD and 4K video.
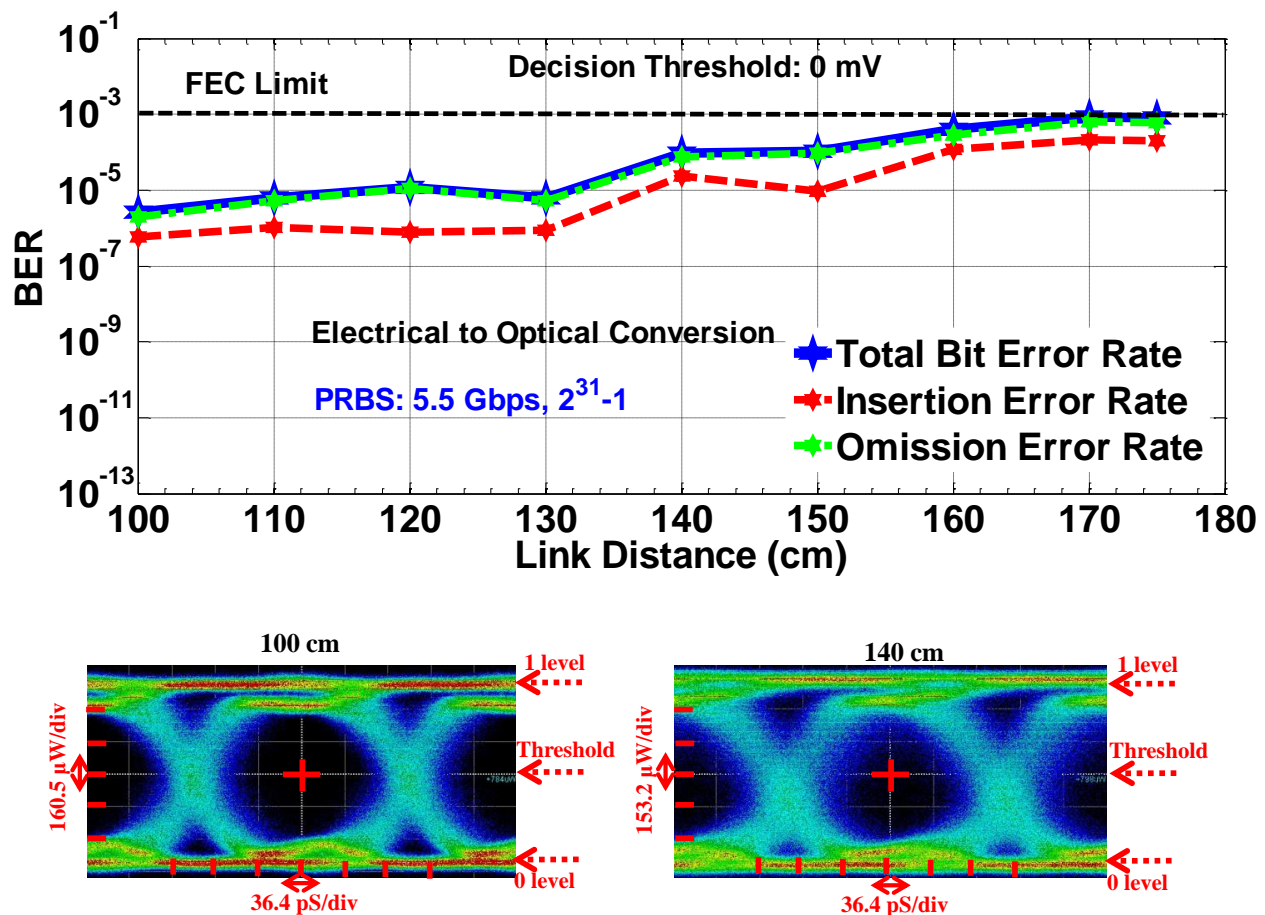
Figure 4.13: Measured BER after converting electrical output signal of LNA to optical signal and then again to electrical signal (Fixed decision Threshold: 0 mV). The eye diagram is recorded after converting electrical output signal of LNA to optical

Before performing the video transmission experiment, the BER measurement is conducted again using PRBS data in order to compare whether the total BER after electrical (output of LNA) to optical conversion is similar to the total BER measured before conversion. Since, the BER can be measured only for the electrical signals in our test equipment, the optical signal is further converted

to electrical signal using optical transceiver (only for BER measurements in this case). The BER measurement is conducted at several link distances with fixed decision threshold (0 mV) as shown in Fig.4.13. However, the eye pattern in the inset of Fig.4.13 is measured for optical signal. We observe that the total BER after optical conversion is slightly increased when compared to the BER that is measured with the electrical signal after LNA (Fig.4.10 (a)). Therefore, we conclude that the effect of converting the electrical signal to optical signal for the video transmission experiment is negligible.
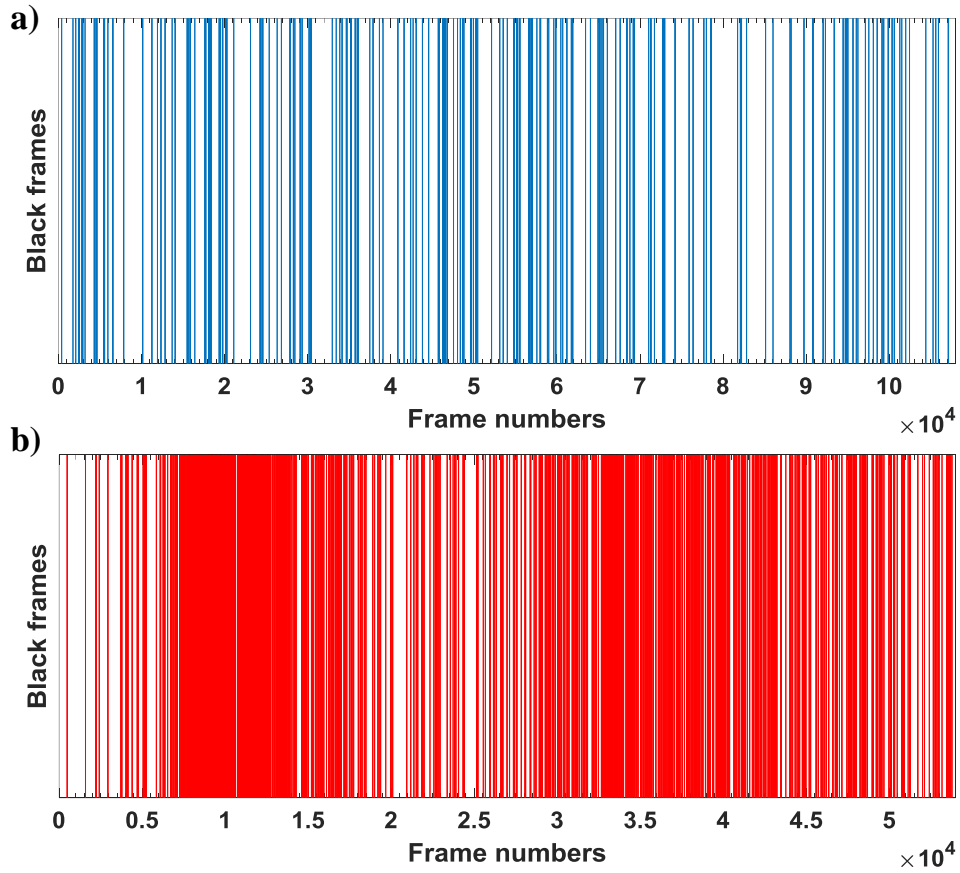
Figure 4.14: Identified black frames which is recorded for 30 minutes at a link distance of 30 cm. (a) HD video (60 fps) and (b) 4K video (30 fps)

For the demonstration of video transmission wirelessly, an uncompressed HD (1920 x 1080 at 60 fps) and 4K (3840 x 2160 at 30 fps) videos are transmitted individually through the THz communication system at the carrier frequency of 138 GHz. The corresponding data rates are

2.97 Gbps and 5.94 Gbps for HD and 4K video, respectively. For the ease of analysis, the received video is recorded as image data (Digital Picture Exchange format) where individual frame from the video is recorded as an image. The received frames are recorded at a given link distance for a duration of 30 minutes. We analyzed only the synchronization errors in this work by analyzing the black frames. Although the clarity of the video is not visually degraded except the black frames, a standard metrics may be applied to validate the quality of the received video. However, analysis of full frame requires both video signals (video signal directly from the camera and the video signal after wireless reception) need to be recorded at the same time for better comparison, which is beyond the scope of this paper. Therefore, we limited our experiments by studying the black frames (synchronization error) only. The number of black frames is identified by taking the small portion (5x5 pixels) in each frame and analyzing the average RGB value. The RGB value of the black frame is zero and therefore any frame that is having the average RGB value above this threshold is identified as a valid frame.
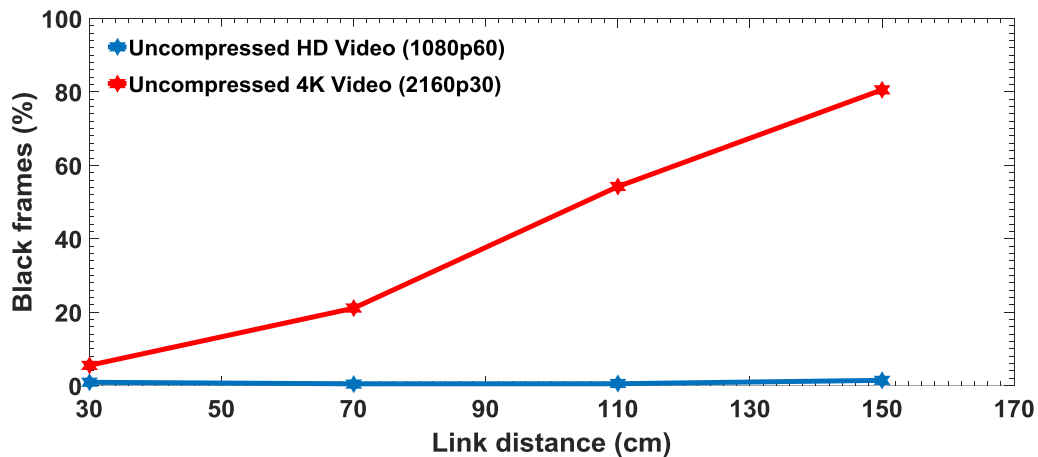
Figure 4.15: Percentage of black frames for HD and 4K video as a function of link distance

The black frame is a tool to measure the performance of the wireless streaming, which is caused due to the error in the synchronization packets. The timing synchronization of the digital video is provided by the End of Active Video (EAV) and Start of Active Video (SAV) sequences with a unique hexadecimal word pattern. The hexadecimal word pattern refers to 3FF (all bits are 1), 000 (all bits are 0), 000 (all bits are 0), and XYZ (10-bit word). The XYZ of a 10-bit word corresponds to bit numbers 8, 7 and 6 which is used to indicate whether the video scanning is progressive or

interlaced, active video or blanking interval and EAV or SAV, respectively. Therefore, any error in this synchronization packet leads to the black frame. The identified black frames for the HD (60 fps) and 4K (30 fps) video, which is recorded at the link distance of 30 cm for the duration of 30 minutes (HD-108000 frames and 4K-54000 frames) is shown in Fig.4.14. We see that the possibility of black frame is higher for 4K video transmission when compared with the HD video due to minor instability of the THz communication system during the measurement duration.

We also did the similar experiment by increasing the wireless link distance and the percentage of black frames is calculated for both HD and 4K videos as shown in Fig.4.15. We see that, the percentage of black frames is less than 0.5% for HD video and ~5% for 4K video at the link distance of 30 cm. By increasing the link distance, the percentage of black frames is almost constant for HD video but increases for 4K video. It indicates that the probability of errors in the timing synchronization packets is higher for the 4K video due to high bit error rate.

4.6 Conclusion

To conclude, we showed the design and evaluated the performance of a photonics-based THz wireless communication system that is built using all commercially available system components. Two independent tunable lasers operating in the infrared C-band are used as the source for the generation of THz carrier wave in the photomixer. A zero bias Schottky diode is used as the detector and demodulator followed by a high gain and low noise amplifier. The optimum carrier frequency (138 GHz) is chosen by analyzing the THz output power and the responsivity of commercially available ZBDs. The performance of the built system is evaluated by measuring the BER for the PRBS data at the bitrate of 5.5 Gbps. By optimizing the decision threshold, an error-free data transmission is achieved at a link distance of 1 m. As a practical demonstration, we detailed the integration of a 4K camera at the THz transmitter and the video receiver electronics at the THz receiver. We showed the successful transmission of uncompressed HD and 4K video. The link quality for the video transmission is analyzed and the percentage of black frames is measured. It is observed that the percentage of black frames is higher for the transmitted uncompressed 4K video due to the high bit errors at the increased link distance, whereas ~99% of the uncompressed HD video is received successfully. The obtained results confirm that it is now possible to realize a short-range high-quality video transmission using THz wireless communication system for

commercial applications. Finally, we also discussed about several methods for increasing the link distance and data rate along with the potential academic and industrial applications of the proposed system.

Acknowledgment

In this chapter, we have detailed the development of photonics-based THz communication system in which antenna-integrated PIN photomixer from TOPTICA Photonics was used as transmitter. We observed that, the maximum link distance is limited by the THz power. Also, while carrying out the experiments using THz fibers, the butt coupling was challenging due to the presence of silicon lens. Therefore, a waveguide integrated UTC-PD antenna (NTT Photonics) that operates in the range between 110 GHz-170 GHz with comparably higher output power was used in the later experiments. In this case, the butt coupling of THz fiber with horn antenna of the emitter was simple and holds the fiber firmly. In the next chapter, we detail the characterization of solid core subwavelength THz fiber using the developed THz communication system with UTC-PD antenna as transmitter.

CHAPTER 5   ARTICLE 2-DISPERSION LIMITED VERSUS POWER LIMITED TERAHERTZ COMMUNICATION LINKS USING SOLID CORE SUBWAVELENGTH DIELECTRIC FIBERS

Kathirvel Nallappan[1,2], Yang Cao[2], Guofu Xu[2], Hichem Guerboukha[2], Chahé Nerguizian[1] and Maksim Skorobogatiy[2]

[1]Department of Electrical Engineering, Polytechnique Montréal

[2]Department of Engineering Physics, Polytechnique Montréal

Abstract: Terahertz (THz) band (0.1 THz-10 THz) is the next frontier for the ultra-high-speed communication systems. Currently, most of communications research in this spectral range is focused on wireless systems, while waveguide/fiber-based links have been less explored. Although free space communications have several advantages such as convenience in mobility for the end user, as well as easier multi-device interconnectivity in simple environments, the fiber-based communications provide superior performance in certain short-range communication applications such as multi-device connectivity in complex geometrical environments (ex. intra-vehicle connectivity), secure communications with low probability of eavesdropping, as well as secure signal delivery to hard-to-reach or highly protected environments. In this work, we present an in-depth experimental and numerical study of the short-range THz communications links that use subwavelength dielectric fibers for information transmission and define main challenges and trade-offs in the link implementation. Particularly, we use air or foam-cladded polypropylene-core subwavelength dielectric THz fibers of various diameters (0.57-1.75 mm) to study link performance as a function of the link length of up to ~10 m, and data bitrates of up to 6 Gbps at the carrier frequency of 128 GHz (2.34 mm wavelength). We find that depending on the fiber diameter, the quality of the transmitted signal is mostly limited either by the modal propagation loss or by the fiber velocity dispersion (GVD). An error-free transmission over 10 meters is achieved for the bitrate of 4 Gbps using the fiber of smaller 0.57 mm diameter. Furthermore, since the fields of subwavelength fibers are weakly confined and extend deep into the air cladding, we study the modal field extent outside of the fiber core, as well as fiber bending loss. Finally, the power budget

of the rod-in-air subwavelength THz fiber-based links is compared to that of free space communication links and we demonstrate that fiber links offer an excellent solution for various short-range applications.

5.1 Introduction

Terahertz (THz) frequency spectrum (0.1 THz-10 THz) holds high promises for many applications that include communications [20], imaging [88] sensing [171] and spectroscopy [171]. In communications, in order to meet the bandwidth demand set by the next generation of wireless systems, a shift in the carrier frequency towards the THz band is unavoidable [231, 232]. THz communications have been already demonstrated in the context free-space wireless links that profit from the presence of several low/modest-loss atmospheric transmission windows [269]. Although there are many advantages of wireless communications including convenience in mobility for the end user, ease in scaling up the network, flexibility of device interconnectivity etc., they also possess many challenges. Particularly, due to high directionality of the THz beams, THz wireless links are known for their high sensitivity to alignment errors, thus requiring careful positioning of the transmitters and receivers [42]. Moreover, reliable communications in non-static environments (ex. between moving objects) require complex beam steering solutions. The situation is further exacerbated in geometrically complex environments (such as inside vehicles, buildings, etc.), where highly complex channel modeling is required. Moreover, free space links have higher chances of eavesdropping thereby increasing the risks for secure communications [273]. Finally, the atmospheric weather conditions such as rain, snow, fog etc. play a major role in affecting the performance and reliability of the wireless THz links. In view of these limitations of wireless THz communications, short-range THz fiber links (~10 m) can offer an alternative solution as THz fibers present a closed highly controlled propagation environment, they can span complex geometrical paths, and they can offer reliable coupling to receiver and transmitter for both static and dynamic applications. One interesting area of applications for THz fiber links is in reliable onboard connectivity and intra-vehicle communications for military and civil transportation. In Fig.5.1, we show the schematic of various communication modalities within and between the airborne vehicles, as well as place of THz fibers in such applications. For example, a high-speed THz data link with a moving vehicle can be established using a tracking ground station or another

vehicle. A high power and high gain transmitter antenna can be used for such a long distance communication [274]. Given high directionality of the THz signals, multiple antenna modules have to be installed on the vehicle surface to cover several possible directions of communication. Next, received THz signals have to be demodulated and interpreted using expensive and environmentally sensitive signal processing units, which should be preferably located deep inside the vehicle.
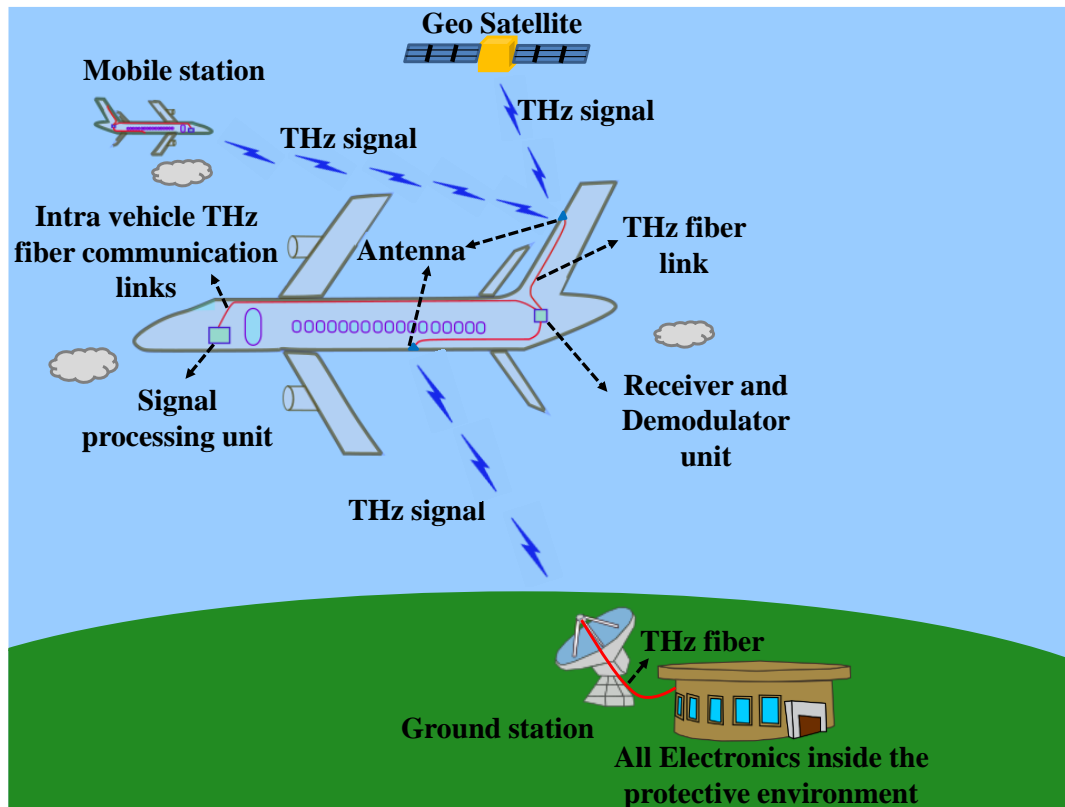
Figure 5.1: Schematic of the THz wireless and fiber communication links for reliable and versatile intra/inter vehicle communication applications

This type of scenario where THz signals are detected using multiple antennas, and then relayed over the complex geometrical paths to a central processing unit can profit greatly from the flexible THz fiber links. Another scenario is using THz fiber links for reliable delivery of high-speed data through a partially blocked or geometrically complex areas, which is of importance for hard-to-reach or highly protected environments such as enclosures for aggressive environments (ex. bio-enclosures), protected structures (ex. shelters and bunkers), as well as for intra- and inter-device THz communications where different parts of the same system can be conveniently linked using

flexible fibers. Finally, THz fiber links can be used as a backup solution for short-range wireless communications in case of sudden deterioration of the atmospheric conditions, which can be of particular important for places with harsh weather.

In designing an efficient THz fiber communication link, the fiber parameters such as transmission loss, bend loss, dispersion, coupling strength and ease of handling plays a significant role. Furthermore, the degree of complexity in the fiber fabrication process determine the cost and commercialization opportunities. While the fiber loss and coupling strength limits the communication link distance, the maximum achievable bitrate can also be limited by the fiber dispersion. Therefore, low transmission loss and low dispersion are the primary concerns for the THz fiber designs. We start by reviewing several types of existing THz fibers. The choice of waveguide material is one of the key factors in achieving THz guidance with low loss and low dispersion. In the case of metallic waveguides, the finite conductivity of metallic layers leads to ohmic losses, whereas in dielectric waveguides the loss is mainly due to material absorption. Independently of the materials used, longer THz waveguides (over 1m) are frequently designed to use modes predominantly guided in the low-loss dry air region. Most recently in [137] bare metal wires in air were proposed as open waveguides for 5G communication applications, however such waveguides suffer from high coupling losses and difficulty in mechanical handling due to wire waveguide open structure. Both, low loss, low dispersion and efficient coupling can be achieved using two-wire plasmonic THz waveguides, however longer (over 1m) two-wire waveguides are inconvenient in practice due to challenges in packaging and handling [126]. This is because in the two-wire plasmonic waveguides, the air gap between the two metallic wires should be precisely maintained along the whole fiber length, which is difficult to achieve in long fiber links. While encapsulating the two metallic wires within a porous dielectric cladding using fiber drawing offers a solution to the mechanical stability and handling problem, this also leads to addition losses and dispersion due to coupling of a plasmonic mode to the dielectric cladding [138].

Alternatively, by selecting proper dielectric materials with low absorption loss (Teflon, polyethylene, polypropylene, cyclic olefin copolymer to name a few) and engineering the waveguide structure to expel the mode into the low-loss dry air region, highly efficient THz waveguides can be demonstrated [125, 150-167]. In general, dielectric THz waveguides or polymer microwave fibers (PMF) fall under one of the three main categories: hollow core waveguides (anti-

resonant reflecting optical waveguides (ARROW) or photonic bandgap (PBG) waveguides) [150-156], porous core waveguides (that use total internal reflection (TIR) or PBG guidance) [157-161] and solid core waveguides (TIR guidance) [162-165]. In the hollow core dielectric tube fibers, the finite thickness of a thin tubular cladding determines the bandwidth of the low-loss ARROW guidance regime, while such waveguides are generally multimode and can support many core and cladding modes. By increasing the size of the hollow core, the propagation loss can be further minimized (in expense to beam quality) as guided modes propagate almost completely in the low-loss air core [150]. Although the cladding modes can be suppressed and the transmission bandwidth can be improved by introducing lossy tubing material such as PMMA, in such fibers one still excites multiple core modes, which becomes problematic for long link THz communications due to inter modal dispersion and inter mode interference [152]. Similarly, in the hollow core THz fibers, by arranging alternative layers of high and low refractive index (RI) cladding material (Bragg fibers) or by introducing judiciously designed (periodic or aperiodic) arrays of air inclusions in the cladding (Photonic Band Gap fibers), the loss and the transmission bandwidth can be improved when compared with the tube-based ARROW fibers [151, 153, 156, 171-175]. Moreover, effectively single mode regime can be achieved in long sections of such fibers, which can significantly reduce effective fiber dispersion. Additionally, low loss and low dispersion can be achieved when using spatially variable dense arrays of subwavelength air holes both in the core and cladding regions (porous fibers) [157, 158]. Apart from the circular and hexagonal porous structure [157], honey-comb [179] and rectangular [180] porous geometries were introduced for which the dispersion is comparable to the THz microwires (subwavelength rod-in-air fibers). Similarly, using dispersion flattened porous THz waveguides, an ultra-wide transmission bandwidth (>1 THz) [275], which is comparable to the free space THz wireless channel can be achieved for short distances. Finally, porous fibers with graded density of pores have been demonstrated to significantly decrease inter-mode dispersion when operated in the multimode regime [181]. Both hollow core and porous fiber, however, are challenging to fabricate as they rely on precise arrangements of air inclusions in a polymer, glass, or crystalline matrix [175]. Fabrication of most of such fibers involve drawing under pressure a thermo-polymer or glass-based preforms with drilled or 3D printed air-inclusions. Achieving and maintaining target porosity throughout the length of the fiber requires careful calibration and monitoring of the entire drawing

process, which is often challenging due to small dimensions of structured preforms used in such drawings. Recently, an alternative method for the fabrication of THz microstructured and PBG fibers was detailed in [175], where over meter-long monocrystalline sapphire fibers were grown directly from the melt using structured dies. Alternatively, such fibers could be 3D printed directly using infinity 3D printing techniques, which was recently demonstrated in [192] where authors continuously printed several meters of a wagon wheel highly porous ARROW fiber using PP.

In the solid core THz fibers, the transmission bandwidth is much larger than that in the hollow core fibers as the propagation mechanism is TIR. However, the transmission loss in such fibers is much higher and is generally comparable to the absorption loss of the fiber material. In order to minimize the transmission loss, one usually resorts to either subwavelength core dielectric fibers, which are simple rod-in-air fibers or rod-in-foam fibers [163, 182] or small solid-core photonic crystal fibers (PCF) with porous claddings [276]. The rod-in-air/foam THz fibers with subwavelength size cores offer low loss and low dispersion guidance as large fraction of the modal fields in such waveguides is guided in the low loss air or foam regions [163-165, 182]. In such fibers, scattering from inhomogeneities along the fiber length such as diameter variation, micro and macro bending, material density variation. etc. are the dominant loss mechanisms due to weak confinement in the fiber core [187]. Scattering loss in such fibers can be somewhat mitigated by increasing the fiber diameter and realizing better confinement in the fiber core in the expense of the increased losses due to materials absorption. By choosing low loss plastics for the core materials, as we show in the following, a good compromise can be found, and multi-meter THz fiber links can be realized. Therefore, despite of all these challenges, the rod-in-air/foam subwavelength fibers is a simple, but reliable platform for enabling various short-range THz communication applications. Furthermore, such fibers can be used to fabricate non-trivial signal processing components such as directional coupler, power dividers, band pass filter etc. capable of real-time THz signal processing, which potentially allows building complete transmission/signal processing subsystems using the same base technology [277-279].

As discussed earlier, although, simple rod-in-air subwavelength fibers are easy to fabricate and potentially offer low propagation loss and low dispersion, however, mechanical manipulation of such fibers and their integration into systems is problematic due to significant extent of the modal fields into air [280]. Therefore, for practical applications, such fibers have to be encapsulated in

such a way as not to significantly affect the weakly core-bound guided modes, while allowing direct mechanical handling of the fibers. One solution to this problem is a wagon-wheel structure where solid core is suspended in air using several deeply subwavelength bridges [164]. Fabrication of such fibers is, however, challenging due to complexity of the fiber cross-section. Alternatively, solid subwavelength cores can be encapsulated using low-loss, low-RI (~1) dielectric foams, resulting in what we call throughout the paper rod-in-foam fibers (see Fig. 5.2).
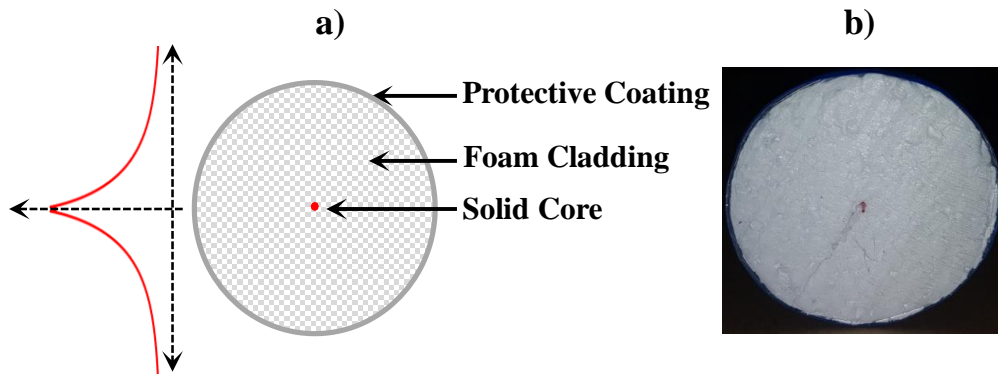
Figure 5.2: (a)Schematic of the rod-in-foam subwavelength THz fiber. Fiber outer diameter is chosen to accommodate ~90% of the power guided by the identical rod-in-foam waveguide with infinite cladding (b) Photograph of the rod-in-foam fiber

In practical terms, high porosity low-loss material foams with deeply subwavelength air cells are virtually indistinguishable from the uniform air cladding, while providing the necessary mechanical stability and ease of manipulation [281, 282]. Although, in principle, the dielectric foams can contribute to additional propagation losses, the effect is negligible for short distances (several meters) and lower THz frequencies (below 200 GHz) for many of the common foams.

Now, we briefly review some of the recent demonstration of THz communications using THz fibers [130, 283-288]. In [130] an error free transmission of 7.6 Gbps and 1.5 Gbps data over the link distance of 8 m and 15 m has been demonstrated using a hollow core waveguide made of Teflon at the carrier frequency of 120 GHz. The modal loss of the waveguide was 2.5 dB/m. The maximum bitrate at longer link length here was mainly limited by the propagation loss. Recently, an 1m expanded porous polytetrafluoroethylene terahertz fiber link have been established together with the resonant tunneling diode integrated with photonic crystal waveguide for 10 Gbps and

uncompressed 4K video transmission [289]. For completeness, we note that one promising approach for high-speed THz interconnects at short distances (millimeters to few centimeters) for on chip and inter-chip communications is based on silicon as the core material as such waveguides feature low transmission loss, high refractive index contrast and strong confinement, as well as mature fabrication technology [200]. For example, in [290] ortho-mode sub-THz interconnect channel for planar chip-to-chip communications using silicon dielectric waveguide has been investigated. By engineering the waveguide structure, silicon based photonic crystal waveguides were proposed and demonstrated for efficient data transmission [291-293]. Moreover, by functionalizing silicon with other materials such as graphene, active components such as THz waveguide-based modulators can be fabricated [294]. Additionally, advanced shaped growth techniques [175, 295] can be used to extend the use of low-loss, high refractive index monocrystalline materials such as silicon or sapphire to longer THz transmission lengths up to 1m, however, application of such waveguides in THz communications have not yet been reported. In all these works, however, no in-depth analysis was presented as to the key reasons for the limitations in the transmission length and maximal bitrate in such fiber links. While, the most obvious reason for such limitations is often claimed to be fiber losses, in our following analysis we conclude that fiber dispersion is another major factor that is often overlooked. In fact, we find that depending on the fiber design and operation frequency, one can be in the power-limited or dispersion-limited regime even in the case of short several-meter-long fiber links. From the practical point of view, in the power-limited regime, transmission is possible up to the highest communication bitrate supported by the available hardware even when approaching the maximal link length when signal strength becomes comparable to the noise level. In this regime, the eye diagram opening collapses along a single vertical direction, while no significant degradation in its overall form (skewedness) is observed. In the power-limited regime, negative effects of the modal loss dominate over those due to modal dispersion. In contrast, in the dispersion-dominated regime, even for short fiber links when signal strength is significantly larger than the noise level, one cannot achieve maximal bitrate as allowed by the hardware. In this case, eye diagram shows significant asymmetry and shape contortion due to modal group velocity dispersion and resultant pulse spreading. In the dispersion-limited regime, negative effects of the modal dispersion dominate over those due to modal loss.

In this work we aim at deeper understanding of the limitations of the fiber link quality posed by the combined effects of the modal loss and dispersion. Without the loss of generality, we concentrate on a pure system of rod-in-air dielectric THz subwavelength fiber for a short-range (~10 meters) communication links with up to 6 Gbps data speeds. In fact, the rod-in-air fiber can be used in further studies as a performance benchmark for the more practical fibers such as rod-in-foam and suspended core fibers. In the following, we fix the carrier frequency at 128 GHz, while using fibers of various diameters to realize power-limited or dispersion-limited transmission regimes. The dielectric fibers are made of low loss polypropylene material with three different diameters of 1.75 mm, 0.93 mm and 0.57 mm. Both theoretical and experimental studies are then carried out and comparative analysis of the two is presented. Experiments were conducted using a photonics-based Terahertz (THz) communication system reported in [24, 296].We then demonstrate that the limitation in the error free link distance is mainly due to the modal loss for the 1.75 mm diameter fiber, while for the 0.93 mm and 0.57 mm diameter fibers the link distance is limited due to modal dispersion. By optimizing the decision threshold, an error free ~10m-long link at 4 Gbps is achieved with the 0.57 mm-diameter fiber, while the argument is made for over 10 Gbps fiber links with over 10 m length when designing the fiber to operate near zero dispersion frequency. Furthermore, study of the bending losses of the rod-in-air fibers is presented where we conclude that even relatively tight bends of sub 10 cm-radius can be well tolerated by such fibers. Finally, the power budget of the fiber-based link is compared with that of the free space links and case is made for the strong potential of the rod-in-air fibers in short range communications. To the best of our knowledge, this is the first comprehensive study of all the major limiting factors and comparative advantages that relate to design and operation of the short-range fiber-assisted THz communications links.

5.2   Theory of rod-in-air dielectric THz fibers

Many polymers possess almost constant RI and low absorption losses at lower THz frequencies (<300 GHz). Polypropylene (PP), in particular, has one of the lowest losses over the wide THz frequency range (<2 cm^{-1} below 1 THz) [127, 297, 298]. Moreover, this material is compatible with 3D printing using cost effective Fused Deposition Modeling (FDM) technique, which opens many exciting opportunities in design and manufacturing of various 3D patterned bulk optical

components and photonic integrated circuits. Due to importance of PP material for THz application, in our studies we therefore used PP filaments of three different diameters (D=1.75 mm, 0.93 mm and 0.57 mm) as rod-in-air fibers. The filaments having smaller diameters (0.93 mm and 0.57 mm) were extruded using FDM printer. Optical characterization of the fibers were then carried out using an in-house photonics-based THz communication system detailed in [24, 296] that operates at 128 GHz carrier frequency. Complex RI of PP was measured using THz-continuous wave spectroscopy system (see Appendix 5.7.1). Mode analysis of the rod-in-air fibers was carried out using commercial finite element software COMSOL Multiphysics. As the goal of this work is to establish limiting factors in transmission of high bitrate data streams over long distances, therefore modal loss, group velocity dispersion, coupling efficiency and bending losses are the key parameters to model.

5.2.1 Effective index, Modal losses, Excitation efficiency

The normalized electric field distribution |E| of the fundamental HE_{11} mode (normalized to 1W of carrying power) for the PP fibers of different diameters at 128 GHz are shown in Fig.5.3 (a), (b) and (c). The normalized power fraction of the fundamental mode containing within the aperture of a variable diameter centered around the fiber is presented in Fig.5.3(d). Clearly, for the fibers of larger diameter, the modal field is mostly confined within the fiber, while for smaller diameters the modal fields are strongly present in the low-loss air cladding, which is also the reason for lower absorption losses of smaller diameter fibers. In Fig.5.3(e) we present the effective refractive indices of the fundamental fiber guided modes as a function of the fiber core diameter at 128 GHz operation frequency, the corresponding modal absorption losses (in straight fibers) are presented in Fig.5.3(f). At the carrier frequency of 128 GHz, the fiber operates in a single mode regime up to the fiber diameter of 1.63 mm. For a 1.75 mm fiber one expects excitation of three modes (HE_{11}, TE_{01} and TM_{01}), while in practice excitation of TE_{01} and TM_{01} does not happen as such modes are incompatible by symmetry with the mode of a WR-6 waveguide (THz emitter waveguide flange) that is centered with respect to the fiber input facet. Thus, all the waveguides used in this work are effectively single mode.
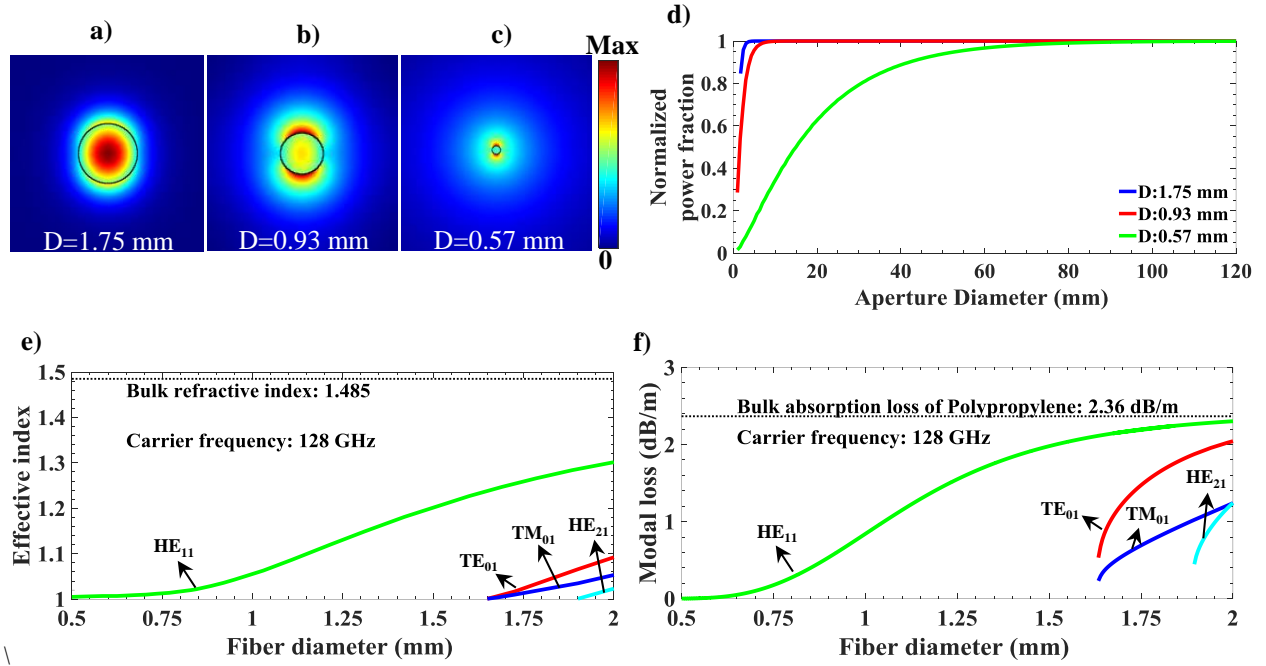
Figure 5.3: The normalized electric field profile |E| of the fundamental mode at the carrier frequency of 128 GHz (a) 1.75 mm fiber, (b) 0.93 mm fiber, and (c) 0.57 mm fiber. (d) The power fraction of the fundamental mode within the aperture of a variable diameter. (e) The effective refractive indices of the guided modes, and f) the corresponding modal absorption losses for the rod-in-air fibers of different diameters at the carrier frequency of 128 GHz. As a reference: the bulk refractive index and absorption loss of the fiber Polypropylene core is 1.485 and 2.3 dB/m, respectively, at 128 GHz

We next study excitation efficiency of the fiber fundamental modes using external THz sources. Generally, the excitation efficiency is maximized when the size of the source field distribution is comparable to that of the fiber mode. In our experiments, the subwavelength fibers are butt coupled to the conical horn antenna that is connected to the WR-6 waveguide flange of the THz emitter. The horn antenna is a mode converter with the tapered structure that converts the fundamental TE_{10} mode of a rectangular waveguide to the Gaussian-like mode at the output. Coupling efficiency can be further optimized by properly positioning of the fiber input end inside of the horn antenna. While many coupling scenarios have been considered in the literature [289, 299-301], they all essentially result in a similar coupling efficiency as achieved by a simple free space coupler that uses a single planoconvex lens. Schematic of such a coupler is shown in the inset of Fig.5.4(a). By optimizing the lens parameters (focal length, diameter) so as to match the size of the focused Gaussian beam

with that of the fiber mode (or alternatively by matching the numerical apertures of the lens with that of the fiber), one can optimize excitation efficiency of the fiber guided modes.
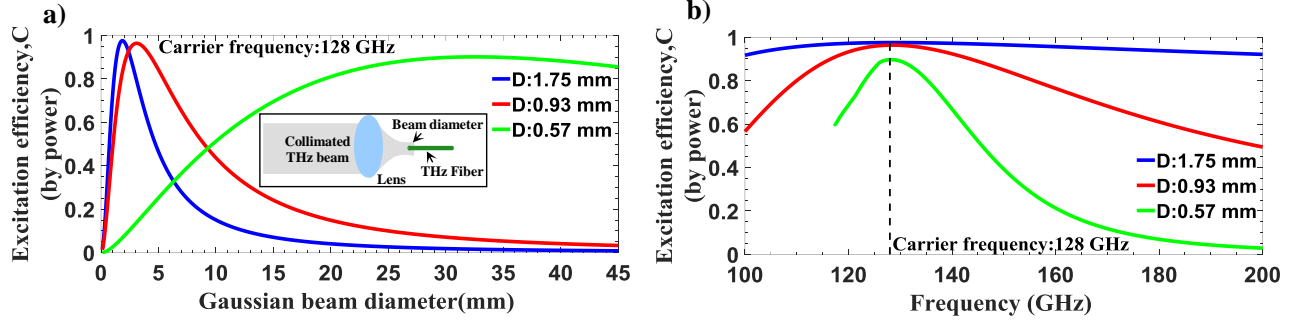
Figure 5.4: Excitation efficiency by power of the fundamental HE_{11} mode of a rod-in-air fiber of three different diameters. a) Excitation efficiency versus Gaussian beam diameter b) Excitation efficiency as a function of frequency for the optimized Gaussian beam diameter. Inset in Fig.5.4(a): schematic of a simple free space coupler

Next, we use transfer matrix theory and a mode matching technique to estimate excitation efficiency of the fiber fundamental mode with the focused linearly polarized Gaussian beam generated by such a coupler/taper at the input facet of a fiber [223, 224]. In Fig.5.4 (a), the excitation efficiency (by power) of the fundamental mode for rod-in-air fibers of three different diameters is presented as a function of the Gaussian beam diameter $(1/e^2)$. The maximum excitation efficiency and the corresponding Gaussian beam diameter for all three fibers at 128 GHz carrier frequency is summarized in Table 5.1. Similarly, by using the optimized Gaussian beam size, the fundamental mode excitation efficiency is calculated as a function of frequency, which is presented in Fig.5.4 (b). The bandwidth of the excitation efficiency is one of the critical parameters that determines the maximum channel capacity. Even if we disregard the frequency dependent sensitivity of the receiver and assume dispersion-less transmission, the maximal channel bandwidth in the fibers is still limited by the frequency dependent transmission loss and excitation efficiency. Therefore, maximizing the THz communication link bandwidth is a very challenging problem as it depends on a large number of factors from emitter/receiver hardware to the fiber design. In the particular case of our fibers, as seen from Fig. 5.4(b), over 90% excitation efficiency of the fiber fundamental mode with the bandwidth of at least 20 GHz is achieved for 1.75 mm and 0.93 mm fiber whereas for 0.57 mm fiber, the bandwidth of ~10 GHz with the excitation efficiency of 80% is achieved. Although the available transmission bandwidth (in terms of excitation efficiency) is

sufficient for the transmission of greater than 10 Gbps data (ASK modulation), the maximal bitrate is limited by the group velocity dispersion, which is discussed in section 5.2.3.

Table 5.1: The maximum excitation efficiency and its corresponding Gaussian beam size for the fibers of different diameters.

THz fiber	Maximum Excitation Efficiency, C	Gaussian beam diameter
1.75 mm fiber	0.97	1.85 mm
0.93 mm fiber	0.96	3.2 mm
0.57 mm fiber	0.90	32.7 mm

From the data presented earlier in this section we can now estimate the maximal fiber link distance given a ~35dB power budget that is typical for our optics-based THz communication system (for the moment we ignore modal dispersion and bending loss). Thus, received power at the end of the fiber link can be estimated using the following expression:

$$P_r = P_t \cdot C^2 \cdot e^{-\alpha_{wg}L} \tag{5.1}$$

where P_r is the power at the receiver end, P_t is the power at the transmitter end, C is the input/output power coupling efficiency per facet (see Fig.5.4) and α_{wg} is the modal propagation loss by power. The modal loss α_{wg} for all three fibers is obtained from the numerical simulation (see Fig.5.3 (f)) as 2.2 dB/m, 0.62 dB/m and 0.01 dB/m for 1.75 mm fiber, 0.93 mm fiber and 0.57 mm fiber, respectively). The transmitter power is -6.6 dBm (~218 µW, which is used in our experiments) and the received power after propagation along the distance L is shown in Fig.5.5.

The signal loss level for the error free transmission of data with the bitrate of 6 Gbps is found to be ~-20 dBm (10 µW), while the absolute noise level below which transmission is impossible is found to be at ~-34 dBm (0.4 µW) (see Appendix 5.7.4). From these measurements and from Fig.5.5, we can estimate maximal distances of the fiber links capable of error-free 6 Gbps data

transmission, which are 5 m for the 1.75 mm fiber and 20 m for the 0.97 mm fiber. Note that transmission with errors is possible up to ~10 m in 1.75mm fiber and 43 m in 0.97mm fiber. Finally, we note that while for 0.57 mm fiber the power budget considerations limit transmission distances to ~1 km range, in practice the dispersion and bending loss result in much shorter fiber link distances of several 10's of meters.
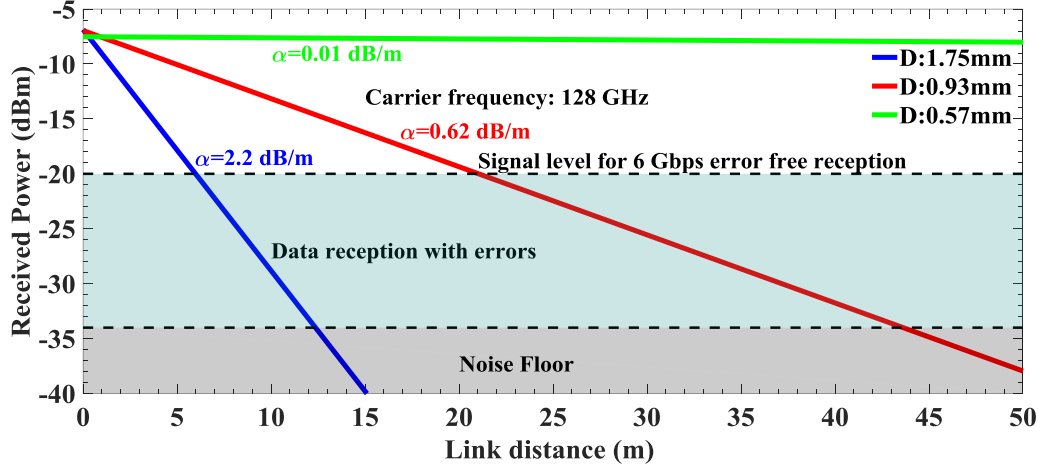
Figure 5.5: Power budget considerations for the fiber links of variable distance and 6 Gbps data transmission rates used in our experiments. Transmitter THz power is -6.6 dBm (~218 µW). The signal loss level for the error free data transmission is experimentally found at -20 dBm and the absolute noise floor is -34 dBm

5.2.2 Bending Losses

The bending losses of the guided modes of the rod-in-air THz fibers are calculated using both numerical simulation and analytical approximations. The numerical simulations were carried out using 2D axis-symmetric model in COMSOL Multiphysics. Here, the radiating wave propagates in the azimuthal direction, φ, and the electric field is expressed as

$$E(r, \varphi, z, t) = E(r, z)e^{j(\omega t - \beta r_0 \varphi)} \tag{5.2}$$

where r_0 is the fiber bending radius, while β is the leaky mode propagation constant. Computational cell is a rectangle with a circular fiber core positioned at r_0 from the axis of rotation, while the other boundaries are perfectly matched layers terminated with a perfect magnetic

conductor. Furthermore, we use reflection symmetry with respect to the horizontal plane crossing the fiber center together with the perfect electric conductor or perfect magnetic conductor boundary conditions at the plane to calculate bent fiber modes of two polarizations (electric field at the symmetry plane directed parallel (Y polarization) or perpendicular (X polarization) to the bend axis). Fiber materials are considered lossless for this simulation.
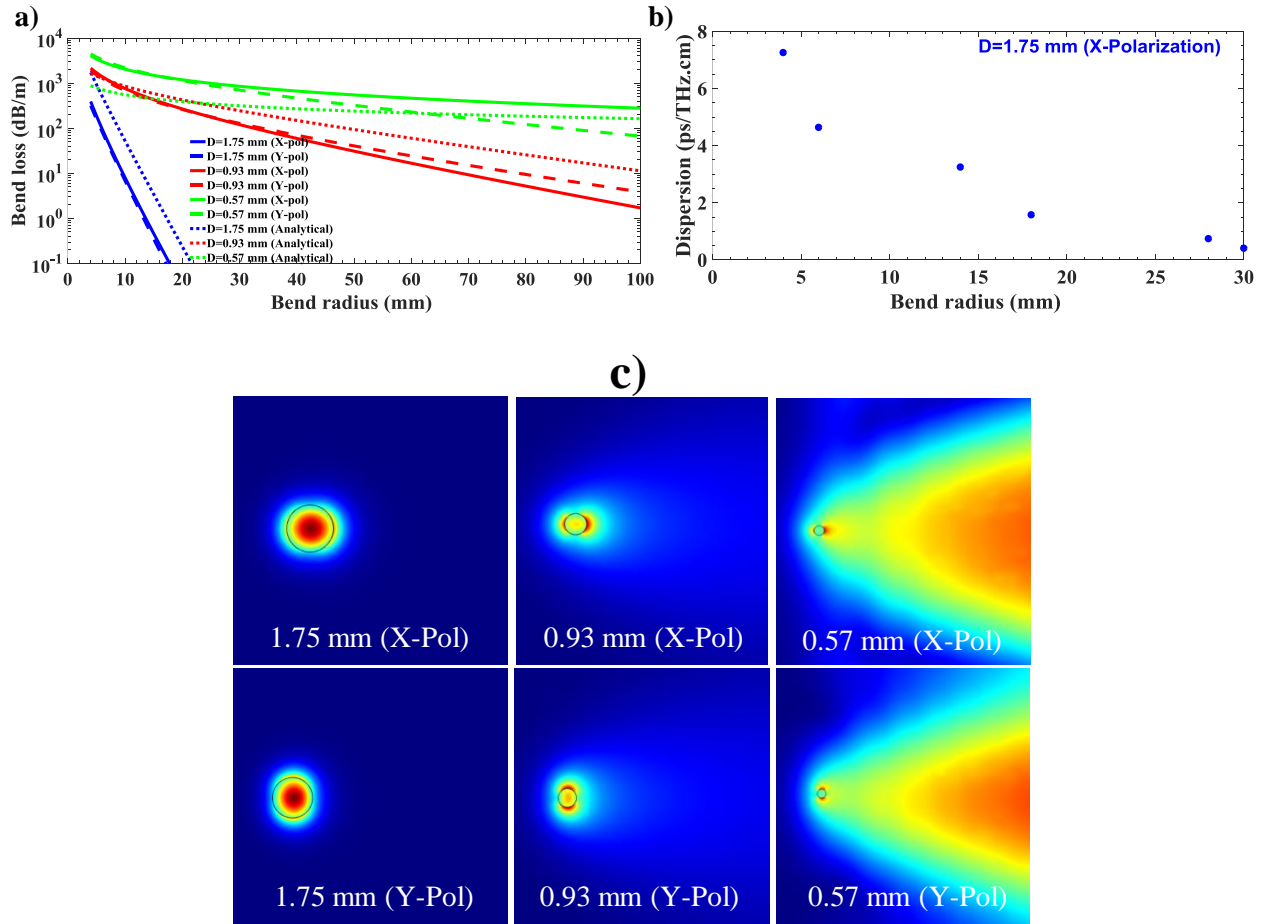
Figure 5.6: (a) Bending losses of the 1.75 mm, 0.93 mm and 0.57 mm fibers for different bend radius and polarizations. The solid curve corresponds to the X-polarized leaky mode and dashed curve corresponds to the Y-polarization leaky mode of a bend modeled using COMSOL software. The dotted lines correspond to the analytical estimations of the bending loss given by Eq.5.3. (b) The group velocity dispersion of the fundamental X-polarized leaky mode of the 1.75 mm fiber as a function of the bend radius. (c) The field distributions correspond to those of the bend leaky modes for fibers of different diameters and bend radius of 3 cm

Bending losses of the fiber fundamental mode α_{bend} in [dB/m] are computed for the bend radii R in the range of 4 mm – 30 mm. The calculated and fitted values of the bending loss are presented on the logarithmic scale in Fig.5.6 (a) as solid and dashed curves for X-and Y-polarizations, respectively. In the inset of Fig.5.6, the normalized electric field profile of the bend fundamental mode for the bend radius of 3 cm is presented. For 1.75 mm fiber, the bending loss become smaller than the modal absorption loss in a straight fiber (~2.2 dB/m) for bending radii as small as ~2 cm or larger. At the same time, for the 0.93 mm fiber bending radius should be larger than ~10 cm in order for the bending loss to be smaller than the modal absorption loss (~1 dB/m). We note that optical performance of both fibers (1.75 mm and 0.93 mm) is quite robust with respect to bending as in many practical applications bending radii superior to 2-10 cm can be easily accommodated, however, using fibers of smaller diameters becomes challenging. This is due to the fact that for smaller core diameters, the fundamental mode is only weakly confined to the fiber core leading to higher radiation losses due to bending. For example, as seen from the inset of Fig. 5.6 for the 0.57 mm diameter fiber at 3 cm bending radius, leaky mode of a bent has a much stronger contribution of the radiation continuum to its modal field distribution when compared to the leaky modes of the fibers of larger core diameters. Therefore, while straight 0.57 mm diameter fiber features very low absorption loss <0.1 dB/m, at the same time it is strongly affected by the radiation loss due to micro and macro bending.

Bending loss can also be estimated analytically using the classical expression for the bending loss of step-index fibers in the regime of weak modal confinement [302, 303]:

$$2\alpha = \frac{\sqrt{\pi}\kappa^2 \exp\left(-\frac{2\gamma^3 R}{3\beta_z^2}\right)}{2\sqrt{R}\gamma^{\frac{3}{2}}V^2 K_{m-1}(\gamma a)K_{m+1}(\gamma a)} \tag{5.3}$$

$$\kappa = \sqrt{k_{core}^2 - \beta_z^2}, \qquad \gamma = \sqrt{\beta_z^2 - k_{clad}^2}$$

$$V = ka\sqrt{n_{core}^2 - n_{clad}^2}, k = \frac{2\pi}{\lambda}$$

where, 2α is the power loss coefficient, a is the fiber radius, R is the bending radius, β_z is the modal propagation constant in a straight fiber and K is the modified Bessel functions where m is the

azimuthal mode number corresponding to the subscript LP_{mn}. As HE_{11} corresponds to the LP_{01} mode within scalar approximation we use $m = 0$ in Eq. 5.3. The propagation constants β_z of the fundamental modes at 128 GHz for all three fibers are obtained from numerical simulations using COMSOL. Estimated bending losses using analytical expression (Eq.5.3) are presented in Fig.5.6 (a) as dotted lines and show reasonable correspondence with the losses of the bend leaky modes described earlier.

5.2.3 Modal group velocity dispersion and maximal bitrate estimation

Next, we study modal group velocity dispersion and maximum error-free bit rate for the three fibers assuming a 10 m-long fiber link. The link length of 10-m is chosen to be long enough to be of practical importance, while making sure that all the fibers have no more than 25-dB loss (by power) over the link distance. In general, the maximum bitrate in the communication link is limited by the pulse dispersion and propagation loss. The dispersion parameter, $\beta_2 \left(\dfrac{\partial^2 \beta}{\partial \omega^2} \right)$ and $\beta_3 \left(\dfrac{\partial^3 \beta}{\partial \omega^3} \right)$ are the

second and third order derivate of the propagation constant $\left(\beta = \dfrac{2\pi n_{eff}}{\lambda} \right)$ with respect to the angular

frequency ω, which is used to characterize the degree of pulse broadening in fibers. Particularly, considering only the second order modal dispersion, the maximum bitrate 'B' (for ASK modulation) supported by the fiber of length 'L' can be estimated using Eq. 5.4, which is derived by requiring that ~95% of the power of the broadened pulse form still remains within the time slot allocated to logical "1" [129]. In Fig.5.7 (a), the β_2 of all the three fibers is presented along with their single mode cut-off frequency f_{sm}. We see that dispersion (β_2) of the 0.93 mm fiber (~40 ps/THz.cm) is much higher than those of the 1.75 mm and 0.57 mm fibers at 128 GHz carrier frequency, thus significantly limiting maximal bitrates for the 0.93 mm fiber. Moreover, dispersion of the 1.75 mm fiber is near zero at 128 GHz, thus promising very high bitrates at this carrier frequency. The estimated bitrates for different fibers and different carrier frequencies are presented in Fig.5.7 (b). At 128 GHz and a 10 m-long fiber link, the maximum error-free bitrates of 4.7 Gbps and 1.2 Gbps are predicted for fibers of 0.57 mm and 0.93 mm diameter.

$$B = \frac{1}{4\sqrt{|\beta_2|L}}$$ (5.4)
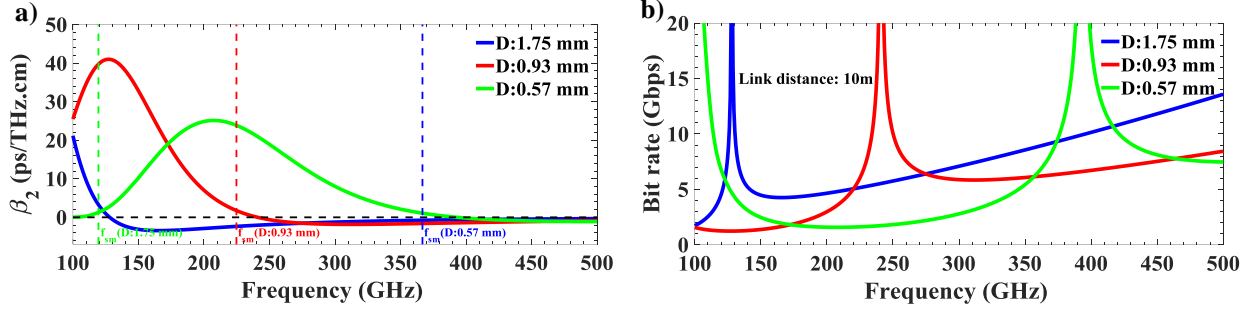
Figure 5.7: (a) The second order dispersion β_2 of the fundamental mode for 1.75 mm, 0.93 mm and 0.57 mm fibers. The dashed vertical line corresponds to the single mode cut-off frequency of respective fibers. (b) The maximum bitrate supported by the fibers in a 10 m link with zero modal loss

Table 5.2: The ZDF for 1.75 mm, 0.93 mm and 0.57 mm fibers and their maximal supported bitrates estimated using third order dispersion

THz fiber	Zero dispersion frequency (ZDF)	Bitrate at ZDF for a 10 m link
1.75 mm fiber	128 GHz	9 Gbps
0.93 mm fiber	241 GHz	13.8 Gbps
0.57 mm fiber	393.5 GHz	19.2 Gbps

It is important to mention that as 1.75 mm diameter fiber has a Zero-Dispersion Frequency (ZDF, at which $\beta_2 = 0$) in the immediate vicinity of 128GHz carrier frequency used in our experiments. The maximum error-free bitrate B_{ZDF} supported by such a fiber at ZDF is, thus, limited by the third order dispersion β_3, and can be estimated using expression (Eq.5.5) [129]. Applying Eq. 5.5 to all the three fibers operating at their respective ZDFs and assuming a link distance of 10 m, we estimate for B_{ZDF} in the 10-20- Gbps range (see Table 5.2). We thus conclude that, by

optimizing the fiber diameter to achieve low dispersion at a given carrier frequency, 10m fiber links can be realized with rod-in-air fibers capable of over ~10 Gbps error-free bitrates per channel, which is sufficient for many practical THz fiber-based communication applications.

$$B_{ZDF} = \frac{0.324}{\sqrt[3]{|\beta_3|L}}$$ (5.5)

Finally, we note that dispersion of a bent fiber can be different from that of a straight fiber, especially at smaller bending radii. In Fig. 5.6 (b), for example, we show dispersion of the fundamental X-polarized leaky mode of a bent 1.75 mm fiber. At large bending radii dispersion approaches zero (that of a straight fiber), while at bending radii smaller than several cm it grows rapidly and can become as large as ~10 ps/THz·cm. Additionally, ZDW can shift to a somewhat different value in bent fibers, which should be considered when designing fiber links.

5.3   Experimental characterization of the rod-in-air subwavelength fibers

5.3.1 THz communication system, fiber holding method and principal measurement challenges

The experimental characterization of the fibers was carried out using an in-house photonics-based THz communication system reported earlier in [24, 296].The schematic and the experimental set up of the THz communication system are shown in Fig.5.8 (a) and (b), respectively. Particularly, two-independently tunable distributed feedback lasers (TOPTICA photonics) operating in the infrared C-Band with slightly different center frequencies are used to optically drive the photomixer. The laser beams are combined using a 3dB coupler and intensity modulated (ASK) using an external electro-optic Mach-Zehnder modulator. A baseband signal source of pseudo random bit sequence (PRBS) with varying bitrate from 1 Gbps to 6 Gbps and pattern length of 2^{31}-1 is used. The modulated laser beams are amplified using an erbium doped fiber amplifier (EDFA) and injected into the waveguide coupled uni-traveling-carrier-photodiode (UTC-PD) photomixer (NTT Electronics) for THz generation. In the receiver section, a zero bias Schottky diode (WR8.0 ZBD-F) is used to detect and demodulate the baseband signal. The baseband signal is then

amplified using a high gain low noise amplifier (LNA) and the bit error rate (BER) is measured using the test equipment (Anritsu -MP2100B).
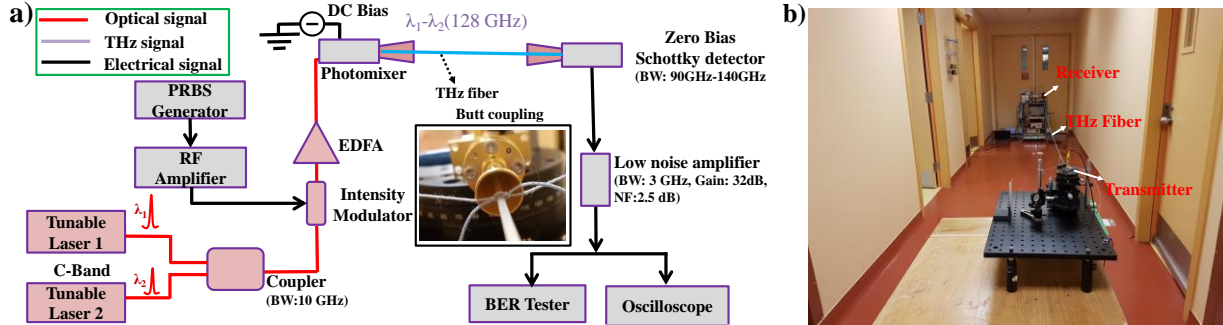
Figure 5.8: (a) Schematic of the photonics-based THz communication system. Inset: Butt coupling of the THz fiber with the horn antenna using fisherman's knot assembly (b) The photograph of the 6 m-long 1.75 mm diameter rod-in-air fiber THz communication link

The largest rod-in-air fiber used in our experiments is the 1.75 mm fiber, which is a commercial 3D printing PP filament (Verbatim) with the diameter of 1.75±0.05 mm. The 0.93mm fiber was fabricated by reducing the diameter of the 1.75 mm PP filament using a 3D printer (Raise3D Pro2). The temperature of the extruder was set to 220˚C and 1 mm nozzle was used for the extrusion. A motorized spinning tool is used to precisely control the diameter of the filament that is extruded from the nozzle by adjusting the drawing speed. Thus, fabricated fiber had 0.93±0.03 mm diameter along the 8-m length. Similarly, a 10 m long 0.57±0.03 mm fiber is fabricated by using the same 1 mm nozzle at increased drawing speed. While characterizing fiber links, a stable and consistent fiber coupling must be used. This is of particular importance for subwavelength fibers that can have significant modal presence in the air cladding. In our experiment, we used butt coupling with the fiber ends judiciously positioned inside the horn antenna. To counter the weight of the free-hanging fiber, the fiber is held tightly using an arrangement of two fisherman's knots made of thin threads and positioned at both emitter and detector ends (see inset of Fig.5.8 (a)). Additionally, rod-in-air fibers do not preserve the in-coupled light polarization state as the light propagates along the fiber. The birefringence is caused by local imperfections in the rod shape (ellipticity, for example), as well as material property fluctuations, which alters the polarization state of the propagating field. Stochastic polarization rotation becomes an issue for fiber links longer than several meters and must be considered while aligning the fiber at the detector side. The optimal

alignment is achieved by rotating the fiber end at the detector side until a maximum signal amplitude is recorded.

5.3.2 Measuring fiber propagation loss using cut back technique

The modal propagation loss of the PP fiber is studied experimentally using the THz communication system and a cutback method, which is then compared to the theoretical values (see Fig. 5.3(f)). Without the loss of generality, here we detail only the measurement for the 1.75mm fiber, while smaller diameter fibers can be characterized in a similar manner. Firstly, the detector electronics is calibrated for direct power estimation from the eye pattern as discussed in the Appendix 5.7.3. Secondly, a 1 m long 1.75 mm fiber is butt coupled at both emitter and detector antenna by direct insertion into the horn antenna linked to the WR-6 hollow rectangular waveguide flange. By fixing the DC bias voltage of the emitter to -2 V, the infrared optical power is increased using EDFA and the eye pattern for 1 Gbps is recorded using the test equipment. When the emitter photocurrent reaches to 4 mA, the eye pattern starts clipping indicating that maximum threshold of the oscilloscope is reached.
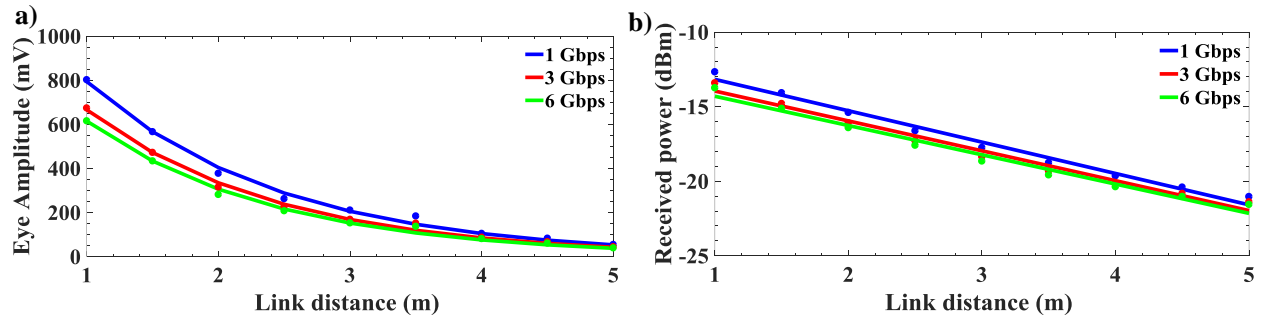
Figure 5.9: Measuring propagation losses of a 1.75mm fiber using cutback technique (a) Measured eye amplitude for 1 Gbps, 3 Gbps and 6 Gbps signals as a function of the fiber length (b) Power loss estimation using detector pre-calibration and recorded eye amplitude

Therefore, in the following modal loss measurement, the emitter photocurrent is fixed to 4 mA, which corresponds to the THz power of -11.5 dBm (~70 µW). Next, the 1.75 mm fiber of length 5m is butt coupled at both emitter and detector antenna. The eye amplitude for three bitrates (1 Gbps, 3 Gbps and 6 Gbps) were recorded. Then the fiber is cut back from the detector side with a step of 0.5 m and the eye amplitude is recorded until the fiber reaches 1 m as shown in Fig.5.9 (a). At each cutback length, the fiber is carefully inserted into the detector horn antenna, while position

of the fiber tip is minimally adjusted to achieve the largest opening in the eye diagram. The recorded eye amplitude is then fitted using the form $a \cdot \exp(-bx)$. In Fig.5.9 (b), the estimated THz power is presented in logarithmic scale. It is observed that the modal loss of 1 Gbps, 3 Gbps and 6 Gbps is 2.10±0.37dB/m, 2.00±0.39 dB/m and 1.96±0.40 dB/m, respectively which agrees well with the theoreticallyestimated absorption loss.

5.3.3 Modal field extent in the air

As mentioned earlier, subwavelength fibers can have significant modal presence in the air cladding. In practice, one has to choose the size of fiber cladding (foam, for example) in such a way as to incapsulate most of the modal field. Experimentally, to measure the extent of modal field into air, we place the fiber in the center of a circular metallic aperture of the variable diameter (1 mm – 25mm). The eye amplitude for 1 Gbps bitrate is then recorded as a function of the aperture diameter, from which the fraction of the received THz power is estimated (see Fig. 5.10 (a)) by normalizing with respect to the corresponding value measured for the fully open aperture.
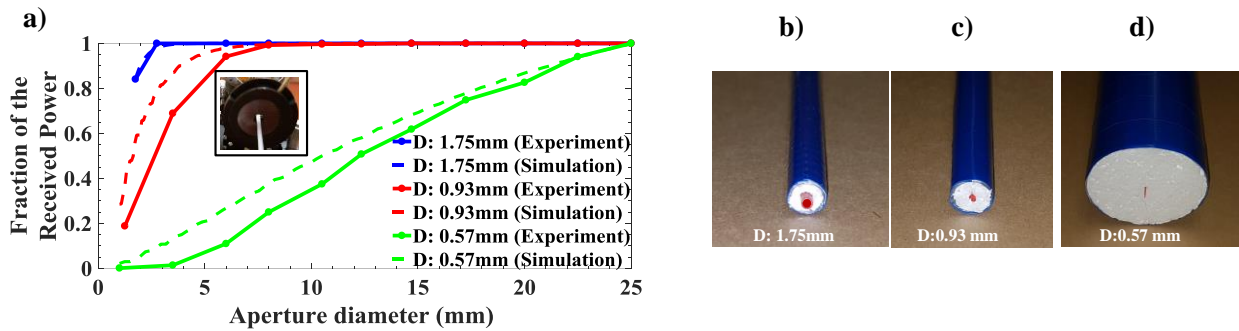
Figure 5.10: (a) Fraction of the modal power inside the aperture of a variable diameter. Inset: Circular aperture centered around the rod-in-air fiber. Photograph of the THz subwavelength fibers with polystyrene foam cladding (b) 1.75 mm fiber with 5mm diameter foam cladding (100% of power) (c) 0.93 mm fiber with 6 mm diameter foam cladding (90% of power) (d) 0.57 mm fiber with 45 mm diameter foam cladding (90% of power)

From this measurement we conclude that 90% of guided power for the 1.75 mm and 0.93 mm fibers is contained within the circles of ~ 2 mm and ~6 mm, respectively and thus define characteristic sizes of the claddings to be used with practical fiber designs. At the same time, the corresponding size for the 0.57 mm fiber is theoretically estimated to be ~45 mm and could not be

measured directly due to small size of the used aperture. At the same time, the measured results agree well with the numerical simulations (see Fig.5.3(d)).

As mentioned earlier, one of the major challenges posed by the rod-in-air subwavelength fibers is the difficulty in their handling to significant presence of the modal field in the air cladding. To counter this problem, and to enable easy handling and manipulation of such fibers in practical installations, one can insert the subwavelength THz fiber core for example in a circular/square shaped low loss foam that features refractive index close to that of air. In our experiments we realized some of such fibers using polystyrene foams with refractive index of 1.0104 and losses <1 dB/m[126]. In Fig.5.10 (b) (c) (d), we present photographs of several THz subwavelength fibers with fiber diameters of 1.75 mm, 0.93 mm and 0.57 mm surrounded by the polystyrene foam cladding of size 5 mm, 6 mm, and 45 mm, respectively, which are chosen from Fig. 5.10 (a) to guarantee that 90% of the modal power is confined within the cladding.

5.4   Bit error rate measurements

The bit error rate (BER) measurements were carried out to study the fiber link performance under the laboratory environment. In the measurements, the emitter photocurrent is set to 7.5 mA, which corresponds to the THz power of -6.6 dBm (~218 µW). A non-return to zero (NRZ) pseudo random bit sequence (PRBS) with the bitrates between 1 Gbps and 6 Gbps and a pattern length of 2^{31}-1 were used as a baseband signal. For the target BER of 10^{-12} (error-free detection), the duration of a single measurement was 1/(target BER · bitrate)~1000s. Furthermore, the decision threshold is optimized so that insertion error (digital 0 is mistaken as digital 1) and omission errors error (digital 1 is mistaken as digital 0) are approximately the same.

5.4.1 BER measurement for the 1.75 mm and 0.93 mm fibers at 8 m link length

Firstly, we identify the maximal fiber length of the 1.75 mm fiber for BER measurements in our system. For that we consider the eye pattern and observe that beyond 8 meters of fiber length, the eye amplitude becomes comparable to the 0 and 1 noise levels, thus resulting in impractical BER values. Therefore, the maximum link length is fixed at 8 m. Similar to the modal loss measurement, an 8-meter long 1.75 mm fiber is butt coupled to the emitter and detector units using fisherman's knots to hold the fiber in place. First, the BER measurement is carried out for the 1.75 mm fiber by

varying the bitrate from 1 Gbps to 6 Gbps. At each bitrate, the decision threshold is optimized so that both insertion and omission errors are the same.

The total BER of the 8 m link is presented in Fig.5.11 (blue solid line). Similarly, for the purpose of comparison, the BER measurements of the 8 m-long 0.93 mm fiber link is carried out. In our measurements, we did not observe any error (for optimized decision threshold) for the bitrates below 2.4 Gbps, within the measurement duration. At the same time, we were not able to measure BER for the bitrates beyond 2.8 Gbps due to high group velocity dispersion of the guided mode. The BER recorded for the bitrates between 2.4 Gbps and 2.8 Gbps is presented in Fig.5.11 (red solid line). The inset in Fig.5.11 shows the recorded eye patterns for both the 1.75 mm and 0.93 mm fibers.
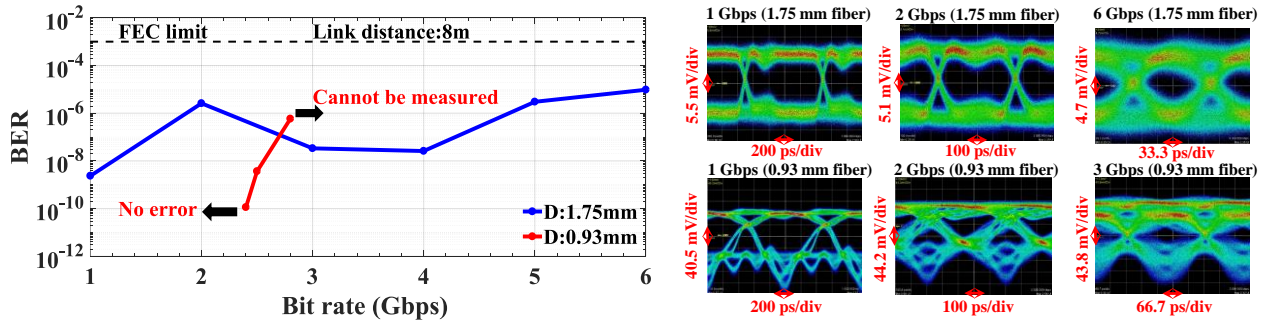
Figure 5.11: Measured BER versus bitrate for the 1.75 mm and 0.93 mm fibers, and the link length of 8 m. Inset: eye patterns for the two fibers at various bitrates

From the eye patterns we can judge the effects of modal loss and modal dispersion on the fiber link performance. Thus, in the case of 1.75 mm fiber, the eye amplitude is much smaller than that for the 0.93 mm fiber indicating that 1.75 mm fiber link performance is limited by the modal absorption loss. The error-free operation for the 1.75 mm fiber is observed for the link lengths shorter than 5 meters (Input THz power is ~218 µW) and bitrates of up to 6 Gbps (currently limited by the THz communication system and the input THz power is ~218 µW (-6.6 dBm)). At the same time, even at the link distance of 8 m, the measured BER of 10^{-5} is well below the forward error correction (FEC) limit (10^{-3}). As the eye patterns for the 1.75 mm fiber stay relatively symmetric even for longer fiber links (8 m) and at high bitrates (6 Gbps), we believe that such a fiber can support at least 9 Gbps up to 10 m (as predicted theoretically), by compensating modal absorption losses with higher input powers (above ~550 µW (-2.6 dBm)). In contrast, for the case of 0.93 mm

8 m-long fiber, although its absorption loss is much lower than that of the 1.75 mm fiber, however, due to much higher group velocity dispersion in such fibers (~40 ps/THz·cm) the maximal bitrate is limited to only 3 Gbps. This is also confirmed by the shapes of the eye patterns for the 0.93 mm fiber that show significant shape degradation at higher bitrates, while also featuring almost 10 times higher powers of the received signals that in the case of the 1.75mm fiber.

5.4.2 BER measurement for the 0.57 mm fiber at 10 m link length

We now consider the 0.53 mm fiber that is theoretically predicted to have a very small absorption loss and a relatively small value of dispersion (~4ps/THz·cm). As predicted theoretically, an error free transmission of up to 4.7 Gbps can be achieved using 0.57 mm 10 m-long straight fiber link. Experimentally, we use the same arrangement as discussed earlier, and then conduct BER measurements for data bitrates between 1 Gbps and 6 Gbps and a fiber length of 10 m. Error-free transmission with an optimised decision threshold is observed up to 4 Gbps (measured in steps of 1 Gbps) as shown in Fig.5.12, which is in good agreement with theoretical predictions. The inset in Fig.5.12 presents the eye patterns for 1, 2 and 6 Gbps bitrates. Although propagation loss of the 0.57 mm straight fiber is much lower than those of the 1.75 mm and 0.93 mm fibers, due to considerable modal diameter of the 0.53 mm fiber (~45 mm), a significant portion of the modal power is cut by the horn antenna of 10.8 mm-diameter aperture.
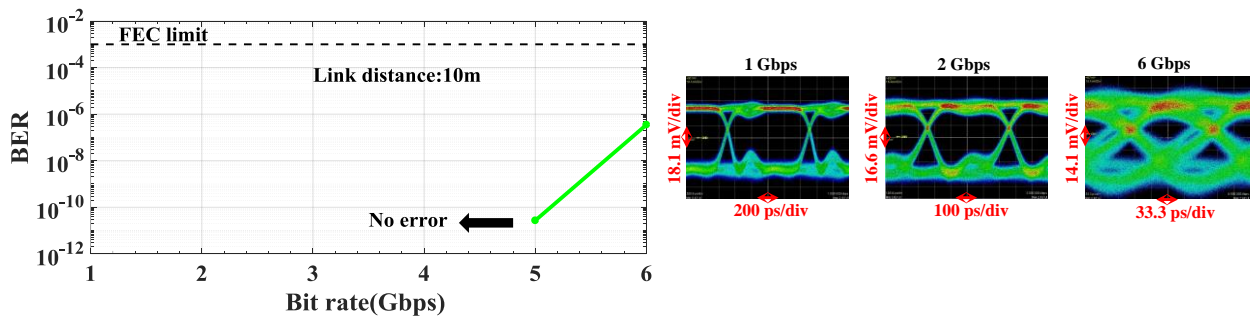
Figure 5.12: Measured BER versus bitrate for the 0.57 mm fiber and the link length of 10 meters.
Inset: eye patterns for 1,2 and 6 Gbps

5.4.3 BER measurement for the 1.75 mm fiber and a 90° bent

Effect of bending on performance of the 8 m-long 1.75 mm fiber is studied using a 90° bend of 6.5 cm bending radius. The BER measurement (see Fig. 5.13) was carried out in the configuration

similar to that of a straight fiber detailed earlier, while the fiber bend was realized by suspending the fiber using several knots and holders. For thus chosen bending radius, we observe only a small increase in the measured BER of a bend fiber compared to that of a straight fiber, which is consistent with theoretical observation that bending loss of the 1.75 mm fiber at 6.5 cm bending radius is much smaller than the modal absorption loss, while dispersion of the mode of a bend at this bending radius is also small (<1 ps/THz·cm). We note that performing a reliable measurement of the bending loss using subwavelength rod-in-air fibers is difficult as such fibers cannot be conveniently handled due to significant extent of the modal fields in air. Therefore, we defer a more detailed experimental study of the bending loss to future works which will be conducted using rod-in-foam fibers placed into predesigned bending molds.
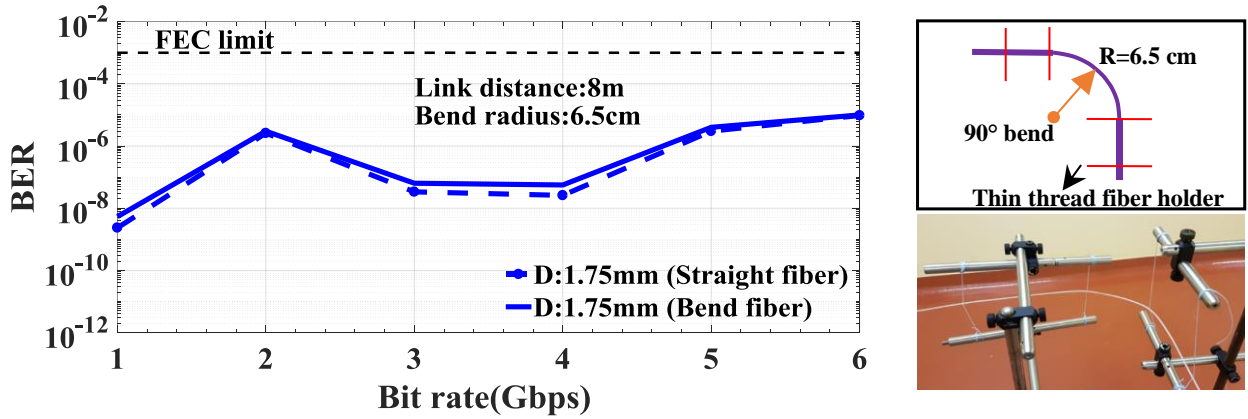
Figure 5.13: Measured BER for the 90° bent of 1.75 mm fiber with the bend radius of 6.5 cm versus bitrate. The schematic and experimental set up of the bent fiber is shown in the inset

5.5 Power budget comparison of the rod-in-air THz fiber links with the free space communication links

In this section we highlight the advantages of the fiber-based communication links by comparing them with the free space communications assuming a simple ASK modulation scheme. In free space optics, the power received at a distance L from the source is given by Eq.5.6:

$$P_r \approx P_t \cdot \frac{D_{RX}^2}{\left(D_{TX} + (L\theta)\right)^2} e^{-\alpha L} \tag{5.6}$$

$$\theta \approx 2 \cdot \frac{\lambda}{\pi w_0}$$

where, P_r is the received power, P_t is the transmitter power, D_{TX} and D_{RX} are the aperture size of the source and detector antenna (lens diameter or horn antenna aperture, for example). The angle θ is a full divergence angle of the beam, w_0 is the beam waist size at the transmitter end and α is the air attenuation coefficient. The equation is valid in the far field region i.e. at distances $L > 2 \cdot D_{TX}^2/\lambda$. A typical power attenuation coefficient α in air at the carrier frequency of 128 GHz is ~6.5 dB/km [304]. The received THz power using fiber link can be estimated using Eq. 5.1. As a value for D_{TX} (assuming that $D_{TX} = D_{RX}$) the aperture sizes of a standard horn antenna (10.8 mm), and a lens (2" optics: 50.8 mm) where considered. In free space communication, the received power is mainly limited by the divergence of the propagating beam.
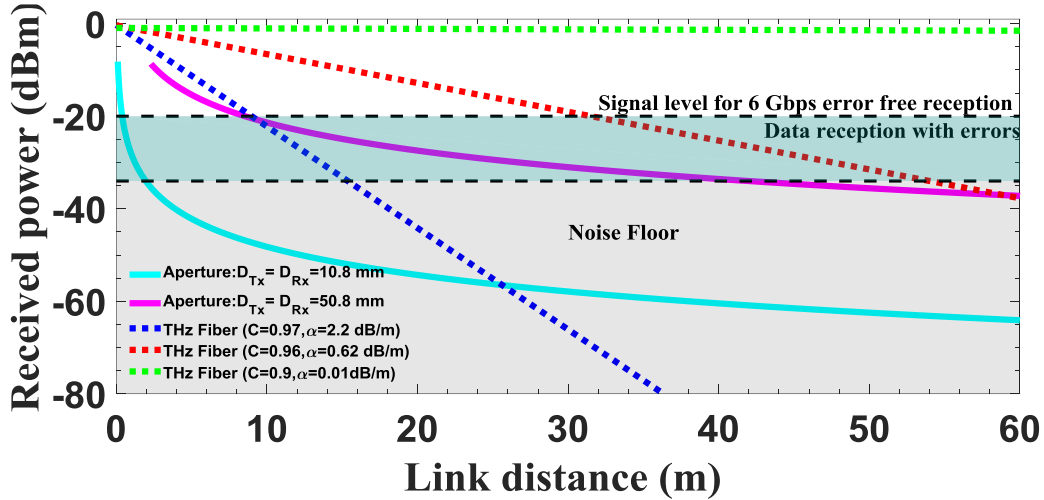
Figure 5.14: Comparison between free space and rod-in-air fiber (straight)-based THz communication links at 128 GHz carrier frequency. The emitter power is set at 0 dBm

By using large area lens or parabolic reflector antenna, it is possible to collect most of the transmitted energy. However, using large collecting optics is not favorable in many space limited applications. For the emitter power of 0 dBm (1 mW), the received power after distance L for both

fiber and free space links are shown in Fig.5.14. From this figure we see that at shorter distances fiber-based links are superior to free space beams in terms of received power due to fast divergence of the THz beams, while at longer distances, free space links are generally superior to fiber links due to smaller atmospheric losses compared to absorption losses of the fiber materials. From the figure we see that when using a relatively small horn antenna (aperture size of 10.8 mm) at both emitter and detector sides, performance of the 1.75 mm fiber-based communication link is superior to that of a free-space link in terms of the received power for the link lengths of up to 24 m. However, at this link distance, the received THz power is well below the noise floor (-34 dBm) for both free space and 1.75 mm fiber-based links. Moreover, even when using relatively bulky 2" optics (lens) for collimating and collecting the THz beam in free space, the performance of 1.75 mm fiber is still superior to a free space link of up to 8 m in length. By reducing the fiber diameter, the modal loss can be further reduced thereby increasing the link distance. Alternatively, the noise floor and the minimal power required for the error-free transmission can be further improved as they depend on many factors including the type of modulation, responsivity of the detector, bandwidth and gain of LNA etc. Although the link distance can be improved by using subwavelength fibers of smaller diameters or by better system design, the maximal achievable bitrate in the fiber links is still much lower compared to the free space THz communication links as fibers feature much higher group velocity dispersion than free space. The maximal bitrate in the free space THz links can be estimated by considering the dispersion of dry air (2.5×10^{-4} ps/THz·cm) [304].

In Table 5.3 we use both theoretical and experimental data (pertaining to our system) to summarise some estimates for the power budget and maximal bitrates of the fiber-based and free-space THz communication links using ASK modulation mechanism. Here we use experimentally found -20 dBm as a minimal signal level to achieve the error-free transmission at 6 Gbps bitrates; moreover, since the ZDF for the 1.75 mm fiber is 128 GHz, therefore, third order dispersion β_3 is used to estimate the maximal bitrate, while for the 0.93 mm and 0.57 fibers we use β_2 instead. It is clear from the Table 5.3 that, while the fiber-based communication links offer higher transmitted powers at shorter distances, nevertheless, they also consistently underperform in terms of the maximal achievable data rates compared to the free space links due to higher dispersion. To increase data transmission rates in fiber links, the modal dispersion (as well as modal loss) can be reduced by

reducing the fiber diameter to deep subwavelength sizes, however it comes with a higher sensitivity to bending and larger mode diameters. Alternatively, dispersion compensation techniques can be used to compensate for the fiber-link dispersion as we have recently demonstrated using strong hollow-core waveguide Bragg grating [191], however such devices tend to have limited operation bandwidth and further studies are necessary to establish feasibility of this approach. Alternatively, using higher order modulation schemes such as orthogonal frequency division multiplexing (OFDM), the effect of dispersion can be minimized due to smaller bandwidth required at each carrier frequency [305]. This could potentially increase the bitrate several folds in longer THz fiber links.

Table 5.3: The maximal bitrate (ASK Modulation) at different link distances and the required emitter power to result in the -20 dBm signal power (error-free transmission) at the receiver end for both free space and fiber communication links. The carrier frequency is 128 GHz

Link distance, L		8 m	15 m	30 m
Maximal bitrate in Gbps for different link distances, carrier frequency is 128 GHz	Free space	560	410	290
	1.75 mm fiber	10.5	8.4	6.7
	0.93 mm fiber	1.3	1	0.7
	0.57 mm fiber	5.2	3.8	2.7
Required transmitter power in dBm so that the received signal power is above the minimal -20 dBm level required for the 6 Gbps error-free transmission	Free space ($D_{TX} = D_{RX} = 10.8$ mm, α=6.5 dB/km)	26.3	31.8	37.9
	Free space ($D_{TX} = D_{RX} = 50.8$ mm, α=6.5 dB/km)	-0.57	4.9	11.0
	1.75 mm fiber, α=2.2 dB/m, C=0.97	-2.1	13.2	46.1
	0.93 mm fiber, α=0.62 dB/m, C=0.96	-14.6	-10.3	-0.9
	0.57 mm fiber, α=0.01 dB/m, C=0.90	-19.0	-18.9	-18.8

5.6   Conclusion

 In this work we presented a comprehensive theoretical and experimental study of simple, yet practical dielectric rod-in-air/foam THz fibers in view of their potential applications in short-range THz communication applications. The THz fibers under study were made of polypropylene and featured three different core diameters of 1.75 mm, 0.93 mm and 0.57 mm. Furthermore, THz communication link performance was characterized with fibers of length 8 m and 10 m as a function of the variable data bitrate 1 Gbps – 6 Gbps at the carrier frequency of 128 GHz. Our main conclusion was that depending on the fiber diameter the communication links were operating either in the power-limited or dispersion-limited regime. Thus, the 1.75 mm fiber featured ~2.2dB/m loss and zero dispersion at the carrier frequency, and it could carry the highest bitrate of 6 Gbps up to the maximal distance of 8 m only limited by the fiber absorption loss, while error-free transmission with such fiber was observed up to 5 m link length. Modal field extent of the core-guided mode into air cladding was only several mm deep due to relatively strong confinement of the modal field in the fiber core. As a result, the 1.75 mm fiber was also well tolerant to bending with virtually no degradation in the link performance when inserting a 90° tight bend of 6.5 cm radius. Further encapsulation of the fiber with polystyrene foam of sub-1cm diameter makes such a fiber an excellent candidate for practical short-range THz communication links due to its ease of handling and installation, as well as good optical properties and tolerance to perturbations such as bending. Similarly, the 0.57 mm straight fiber featured very low absorption loss ~0.01dB/m, and a relatively small dispersion of ~3 ps/THz·cm. The resultant performance was similar to that of a 1.75 mm fiber, however, maximal link length was rather limited by dispersion than by the modal loss. As a result, error-free transmission was realized for a 10m link with up to 4 Gbps data rates, while signal strength was considerably higher than the noise level. One of the major disadvantages of this fiber is high sensitivity to bending and several cm-deep penetration of the modal fields into the air cladding, thus making even the foam-cladded fibers inflexible and somewhat difficult to handle. Finally, the 0.93 mm fiber, while featuring relatively small absorption loss of <1 dB/m, also featured relatively high dispersion of ~40 ps/THz·cm, thus significantly limiting the maximal supported bitrate even for a good signal strength. Aa a result, a maximal bitrate of only 2.4 Gbps was demonstrated for an 8 m fiber link. Finally, we compared the THz fiber communication links with free space links that use relatively small focusing optics (up to 5 cm diameter) and concluded

that in this case fiber links are generally more efficient in terms of the power budget for short-range communications up to several 10's of meters. Fiber links are also more reliable and easier to install, maintain and reconfigure than free space links, especially in complex communication environments (on-board communications, for example). At the same time, free space communications outperform fiber-based links in terms of maximal bitrate as air features significantly lower dispersion than fiber.

5.7   Appendices

5.7.1 Complex refractive index measurement of the PP filament

The refractive index of the PP fiber is measured using the continuous wave (CW) THz spectroscopy system [191, 219]. The schematic of the experimental set up is shown in Fig.5.15, which is briefly explained as follows. The setup has two Distributed Feedback (DFB) lasers with slightly different center wavelengths and uniform power (~30 mW each) operating in the telecom region. A 50:50 coupler combines and splits the two wavelengths equally into the emitter and detector arm, respectively. Two single mode polarization maintaining fibers wounded with piezo actuators, which stretches in the opposite directions were connected to both the arms for the measurement of phase. The symmetric arrangement of the fiber stretchers provides the additional path delay as well as uniform disturbance due to any variation in the external environment. The path lengths between the emitter and detector arms were balanced to have a flat phase. The generated THz waves, which is the frequency difference of the two lasers, were modulated using the bias voltage for lock-in detection. The THz beams were collimated and focused into the detector using the parabolic mirrors. The generated photocurrent in the detector were recorded along with the phase information as a function of frequency. The sample is kept in the collimated THz path for the RI measurement.

The PP sample for RI measurement is prepared as follows. A circular slab of PP material is fabricated by melting the PP fiber in a crucible at a temperature of 240°C for 35 minutes followed by 20 minutes of cooling. The density of the PP fiber and the fabricated slab after melting is 898.02 kg/m^3 and 869.92 kg/m^3, respectively, with the difference of only <4%. Therefore, it is concluded that the melting process doesn't affect the density of the material and no significant amount of air inclusions were introduced.
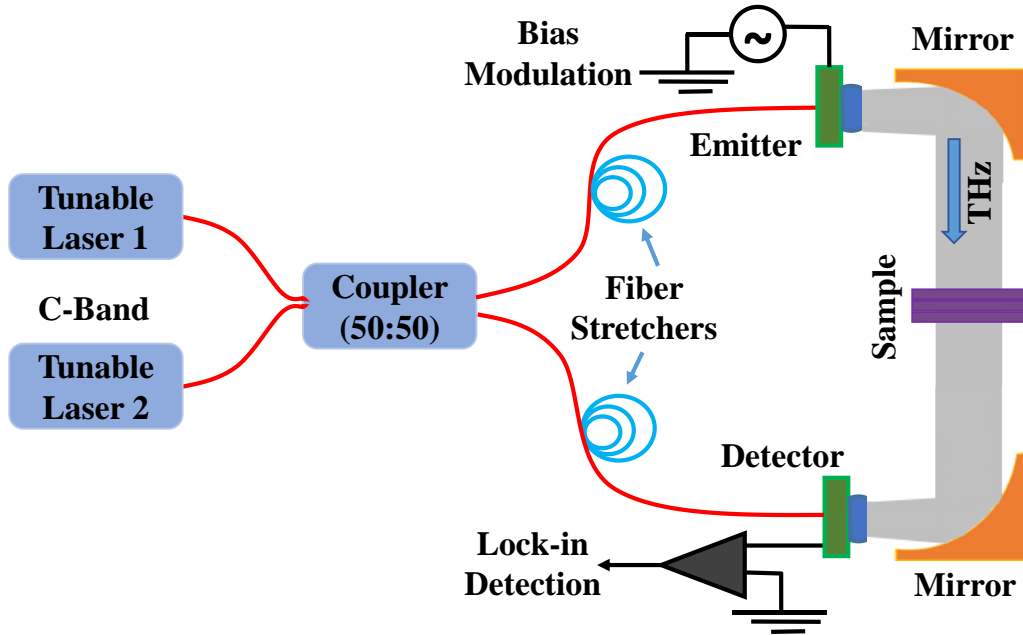
Figure 5.15: Schematic of the CW THz spectroscopy system for RI measurements

Three slabs with slightly different thicknesses *d* were fabricated and then polished on both sides to get a smooth surface. A cutback measurement technique was used to measure the real part of the RI using the CW THz system. Both the amplitude and phase are recorded after removing each slab. The unwrapped phase for different sample (PP) thickness is shown in Fig.5.16(a). Using the phase information, the real part of the RI of PP is extracted using Eq.5.7, where, $n(\omega)$is the frequency dependent real part of RI, $\Phi(\omega, d)$ is the measured phase difference due to the presence of a sample and c is the speed of light. The RI of PP is measured as 1.485 in the measured frequency range, which is shown in Fig.5.16 (b).

$$n(\omega) = 1 - \frac{\Phi(\omega, d) \cdot c}{\omega \cdot d} \tag{5.7}$$

Although the real part of the RI of PP is measured using the CW THz spectroscopy system, extracting the imaginary part accurately requires thick sample (~in meters) due to very low PP material loss. Therefore, we used the modified THz communication system for the loss measurement. The instrumental setups for both the CW THz spectroscopy system and the THz

communication are similar (TOPTICA Photonics) except for the additional data modulation unit and detector in the communication system.
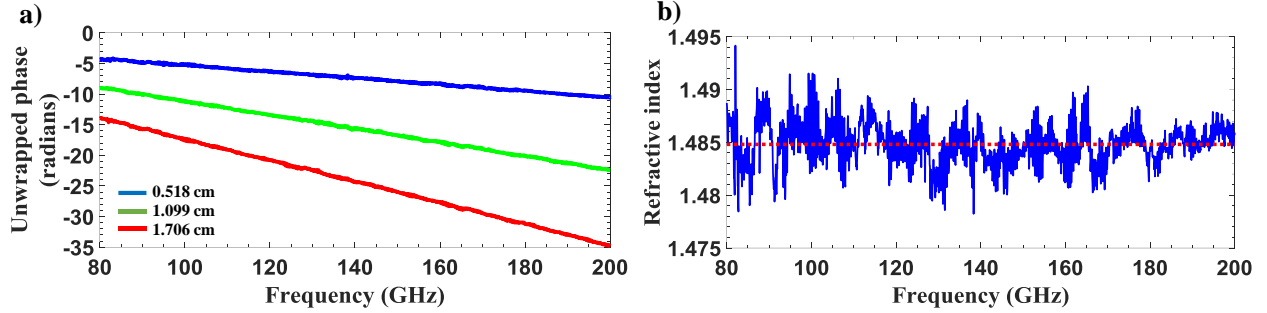
Figure 5.16: (a) Unwrapped phase for different PP slab thicknesses (b) The refractive index of the PP fiber as a function of frequency

In spectroscopy a heterodyning detection scheme is used whereas in communication system, direct detection scheme using Schottky detector is employed. To measure the PP loss, the data modulation unit is disabled, however the bias to the emitter antenna is modulated at lower frequency (12 kHz) for lock-in detection. In the detector section, a trans-impedance amplifier is placed after the LNA where the voltage is amplified and converted to photocurrent, which is proportional to the received THz power. In order to measure the loss of the PP fiber, we used the 1.75 mm fiber and the similar fiber holding arrangement is used as for the BER measurement, as well as a metallic aperture at the detector side that was closed around the fiber. By keeping the input coupling undisturbed, the fiber is cut from the detector side during the cutback measurement. The photocurrent of two fiber lengths (5 m and 1 m) were recorded from 100 GHz to 150 GHz as shown in Fig.5.17 (a). The fiber loss is then estimated using Eq.5.8 (see Fig.17 (b))

$$Loss\left(\frac{dB}{m}\right) = \frac{1}{(L_5 - L_1)} \cdot 10 \log_{10}\left(\frac{I_5}{I_1}\right) \tag{5.8}$$

where, L_5 and L_1 are the fiber lengths and I_5 and I_1 are the corresponding THz photocurrents, respectively. We note that from Eq.5.8, one can now extract the bulk absorption loss of the PP material by dividing (Eq.5.8) by a certain frequency dependent normalization function ξ*(f)*. Such function can be computed numerically by assuming a certain frequency independent bulk

absorption α_b, then finding numerically the corresponding absorption loss of a 1.75 mm rod-in-air fiber $\alpha_f(f)$ made of such a material, and then defining $\xi(f) = \alpha_f(f)/\alpha_b$. Such a function is universal as long as bulk loss used in simulations α_b is small. Thus, extracted bulk absorption loss (black curve in Fig. 5.17 (b)) can then be fitted using second order polynomial (Eq 5.9) where f is the frequency in THz.

$$Loss\left(\frac{dB}{m}\right) = 236 \cdot 31f[THz]^2 - 37.75f[THz] + 3.32$$

(5.9)

Finally, bulk absorption loss of Polypropylene at 128 GHz is estimated to be 2.36 dB/m.
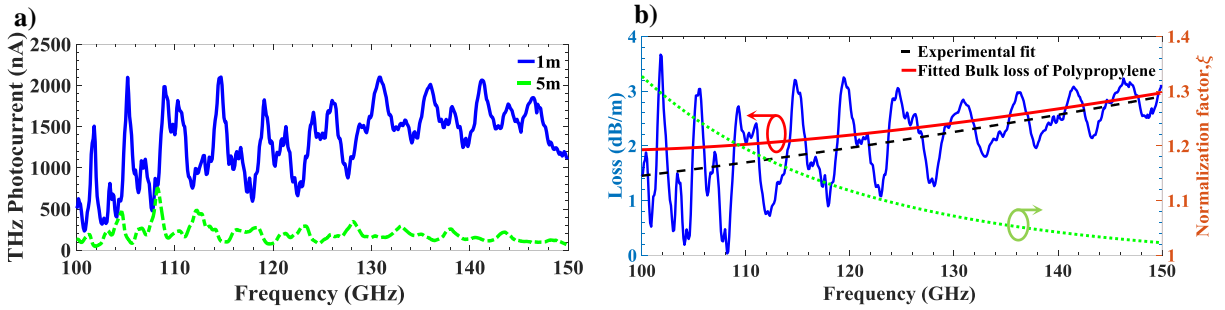
Figure 5.17: (a) THz photocurrent for different fiber lengths (b) Absorption loss of the 1.75 mm PP fiber (blue) as well as inferred bulk absorption loss (black) and a corresponding square fit (red)

The dispersion of THz fibers can be measured using both continuous wave and time-domain THz spectroscopy systems as detailed in In [152, 191, 306]. In [306] it was demonstrated that for subwavelength fibers in particular, experimentally measured dispersion agrees well with the theoretical estimations and therefore, in our work, only the theoretically calculated dispersion values were used to estimate the maximal bitrate for all the three fibers.

5.7.2 Selection of the THz carrier frequency

The choice of carrier frequency is determined by the output THz power and responsivity of the detector antenna. In Fig.5.18 (a), the THz power versus frequency measured using a calibrated power meter (PM3-Erickson power meter, Virginia diodes) is presented. Similarly, the

corresponding developed DC voltage (without data modulation) is recorded (see Fig.5.18(b)) using the oscilloscope (Anritsu-MP2100B). Both these measurements were carried out independently by keeping the DC bias voltage (-2 V) and photocurrent (7.5 mA) of the emitter antenna constant. A higher DC voltage is recorded for the frequency of 130 GHz. However, we observe a better eye pattern at 128 GHz, which is also verified by doing the frequency sweep from 125 GHz to 135 GHz.
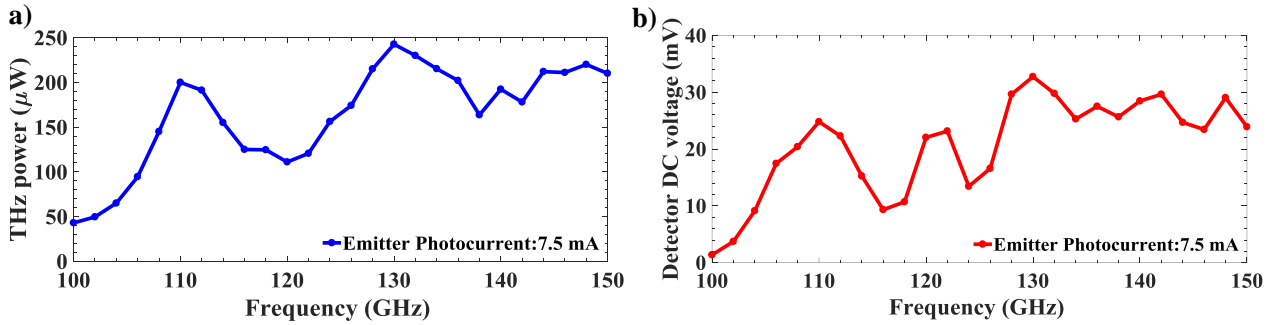
Figure 5.18: (a) THz output power from the photomixer versus frequency and (b) Developed DC voltage in the detector corresponding to the input THz power shown in (a)

5.7.3 Calibration of detector electronics for direct THz power estimation

The calibrated calorimetric THz power meter is standard when measuring the absolute power over the broad frequency range. In communications, such THz power meters are integrated with hollow rectangular metallic waveguides for direct coupling with an electronic source. However, for fiber-based links, the absolute power measurement is challenging due to fluctuations caused by coupling consistency issues between the fiber and a waveguide flange. In fact, we find that using horn antenna coupled to a Schottky diode as a detector allows efficient and more consistent optimization of the coupling conditions at the fiber/detector side. Therefore, we first calibrate the detector antenna for direct power measurement using the received digital signal in the communication system. To calibrate the zero bias Schottky diode (ZBD) detector for direct power measurement we proceed as follows. The data modulation unit in the communication system is disabled for the purpose of power measurement. First, the THz output power is measured using calorimetric THz power meter by fixing the output frequency at 128 GHz and the DC bias voltage to -2V. The infrared optical input power to the emitter antenna is varied, which is controlled in

terms of the photocurrent. The measured THz power as a function of the photocurrent is shown in Fig.5.19 (a).
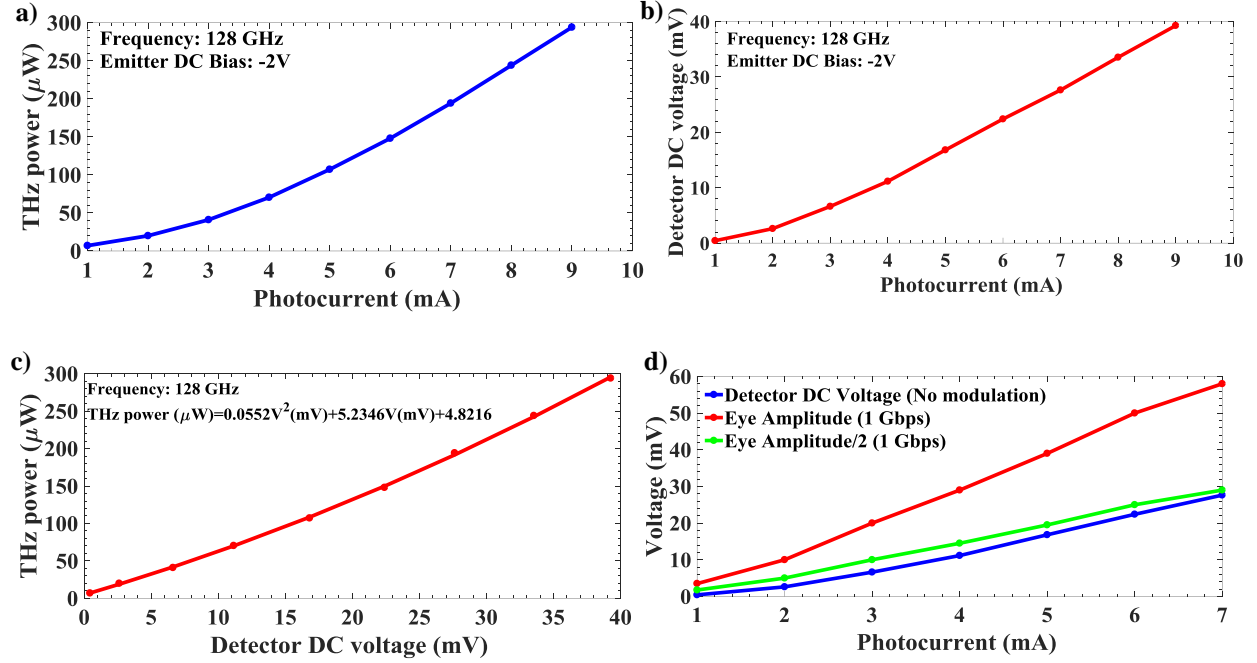
Figure 5.19: (a) Measured THz power and (b) Developed DC voltage in the ZBD at the frequency of 128 GHz by varying the input infrared optical power (c) Developed DC voltage in the ZBD versus THz power at the frequency of 128 GHz (d) Relation between the developed DC voltage from the ZBD for the coupled THz signal, eye amplitude and digital one level of the 1 Gbps eye pattern at the carrier frequency of 128 GHz

Second, the THz emitter is butt coupled to the ZBD by removing the horn antenna attached to it. Similar to the above measurement, the emitter photocurrent is varied, which is proportional to the THz output power and the developed DC voltage (without the low noise amplifier) in the ZBD is measured by the oscilloscope with a load resistance of 50Ω. The developed DC voltage as a function of emitter photocurrent is shown in Fig.5.19(b). Then, the photocurrent in Fig.5.19(a) and (b) is replaced with the THz power as shown in Fig.5.19 (c). The measurement in Fig.19 (c) is fitted using the second order polynomial:

$$P[\mu W] = 0.0552 \cdot V[mV]^2 + 5.2346 \cdot V[mV] + 4.8216 \qquad (5.9)$$

where, P is the THz power in microwatts and V is the developed DC voltage in millivolts. Since, the LNA is connected after ZBD during the real-time communication measurements, the additional amplification factor needs to be considered. The LNA is A.C coupled and therefore we cannot measure the amplification of the DC voltage. Therefore, the data modulation unit is now enabled and the 6 Gbps eye pattern is recorded using the high-speed oscilloscope before and after LNA for the THz power of -16.98 dBm (~20 µW). The eye amplitude of the 1 Gbps eye pattern without and with LNA is 9.35 mV and 430.66 mV, respectively. The voltage gain in dB is given below.

$$Gain(dB) = 20 \cdot \log_{10}\left(\frac{430.66}{9.35}\right) = 33.26dB \tag{5.10}$$

Similarly, the gain factor of the LNA is calculated as below.

$$Gain\ factor = 10^{\frac{Gain(dB)}{20}} = 10^{\frac{33.26}{20}} = 46.02 \tag{5.11}$$

The DC voltage developed in the ZBD by varying the emitter photocurrent (see Fig.5.19 (b)) is recorded when there is no data modulation, which is shown in Fig.5.19 (d) as blue solid line. It means that the measured DC voltage is same as logical 1 of the modulated signals (for binary modulation). In our experiments, the digital logical 1 is represented as +1 and logical 0 is represented as -1. Therefore, measuring the eye amplitude and dividing it by 2 is equivalent to the DC voltage measured when there is no modulation as shown in fig.5.19 (d) (red line and green line). The developed DC voltage in the ZBD is referred here as mean DC voltage recorded when the data modulation unit is disabled. We see a small deviation between the mean DC voltage and eye amplitude/2, which could be due to the amplifier noise and minor discrepancy in estimating the eye amplitude. To summarize the calibration process, the measured eye amplitude is divided by 92.0512 (2*46.0256) and used in the equation 9 to estimate the received THz power.

5.7.4 Noise floor and error-free detection using THz communication system

The following experiment has been carried out to measure the effect of signal level on the BER in our communication system and in order to characterize the noise floor and minimal signal power necessary for error-free detection (BER<10^{-12}). In the THz receiver unit, we have used the LNA with the bandwidth of 3 GHz. Therefore, the bitrate in the communication system is limited to the

maximum of 6 Gbps (ASK modulation). In this measurement the emitter antenna is butt coupled to the ZBD. The output from the LNA is connected to the test equipment (oscilloscope and BER tester). The DC bias voltage to the emitter antenna is set to -2 V. The emitter photocurrent is varied by increasing the infrared optical power to vary the THz signal power in the system. The eye pattern and BER with optimized decision threshold for the bitrate of 6 Gbps is then recorded. Since the emitter and detector are butt coupled, the received THz power is considered the same as the transmitted THz power, which is extracted from Fig.5.19(a).
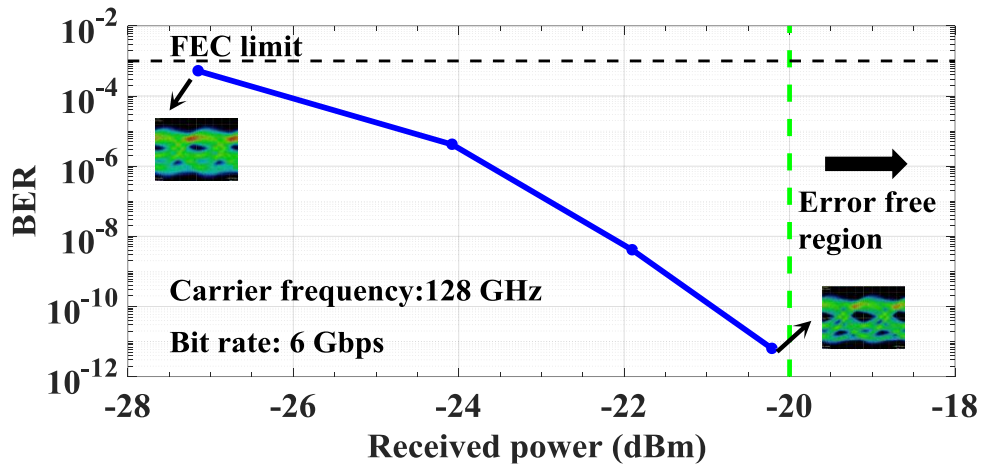
Figure 5.20: BER measurement in our communication system as a function of the received signal power for the bitrate of 6 Gbps

From Fig.5.20, for the received THz power of ~-20 dBm (10 µW) and higher, we did not observe any errors within the measurement duration for the optimized decision threshold. Therefore, the signal level of -20 dBm for 6 Gbps is defined as a minimal signal power required for the error-free transmission in our THz communication system.

The noise floor of our THz communication system is measured by decreasing the emitter power, while the mean and standard deviation of one level and zero level of the 6 Gbps data is recorded from the eye pattern. The noise floor is considered as the THz power at which the distance between the mean one and zero levels equals to the average of standard deviations of the one and zero levels. In Fig.5.21, we show the eye pattern of the 6 Gbps data recorded for various emitter powers. The noise floor for 6 Gbps data in our system is ~-34 dBm.
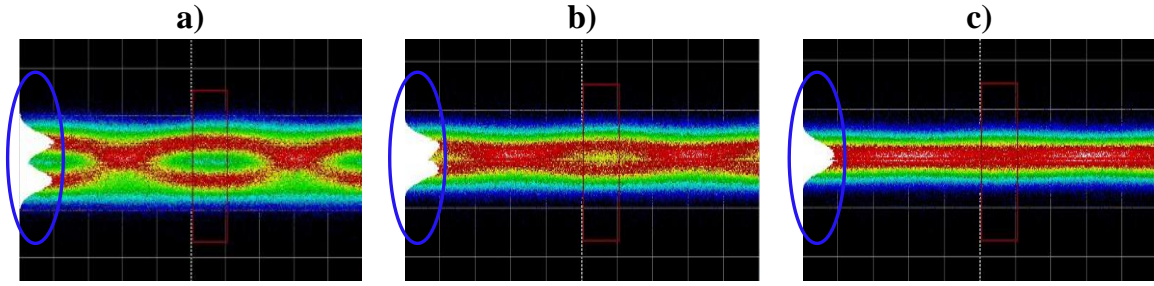
Figure 5.21: Eye pattern of 6 Gbps data for the emitter power of (a) 0.8 µW (-30.96 dBm), (b) 0.6 µW (-32.21dBm) and (c) 0.4µW (-33.97 dBm).

5.5.5 Modal properties of rod-in-foam fibers

The refractive index of highly porous foams (polystyrene foam, for example) is close to that of air. Therefore, the modal propagation properties of fibers with foam cladding (such as mode size, dispersion etc.) are similar to those of fibers with air cladding. In Fig. 5.22 we show normalized electric field profiles of the fundamental modes of the rod-in-foam fibers of different core diameter, which look very similar to those of air-clad fibers shown in Fig. 5.3. The main effect of the foam claddings is in the additional transmission losses due to foam material absorption and scattering on the foam microstructure. Therefore, by replacing the air cladding of rod-in-air fibers with a foam, one should mostly observe changes in the modal propagation loss. Thus, considering, for example, the experimentally measured refractive index and loss of a polystyrene foam in the THz region as 1.0104 and 1 dB/m (see reference [126]), the total loss of the fundamental mode of the straight rod-in-foam fiber is then computed as 2.4 dB/m, 1.45 dB/m and 1.01 dB/m for the fiber diameters of 1.75 mm, 0.93 mm, and 0.57 mm, respectively. These losses should be compared to those of the air-clad fibers, which are 2.2 dB/m, 0.6 dB/m and 0.01 dB/m for the same fiber diameters. As propagation of the fundamental mode in the 1.75 mm fiber is mostly inside of the polypropylene core, the effect of the foam cladding is minimal, thus resulting in only 0.2 dB/m increase in the modal loss compared to the air-clad fiber. In contrast, for the smaller diameter fibers, a significant part of the mode propagates outside of the fiber core and in the foam cladding, which can potentially lead to significant increase in the modal losses and reduction of the maximal error free link distance if the foam losses are important.
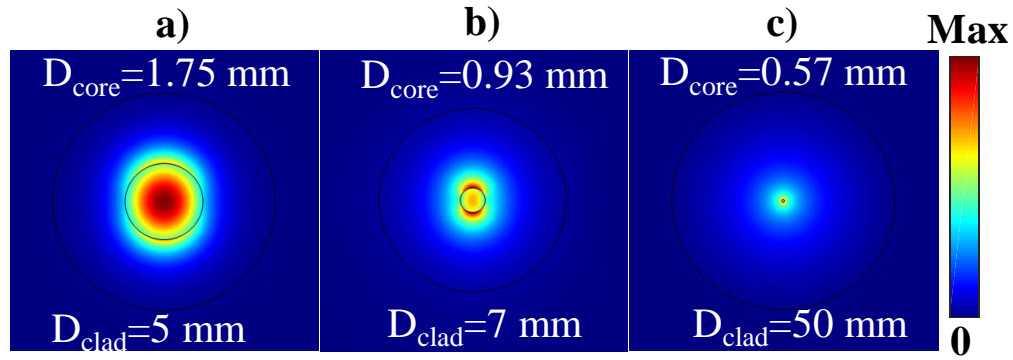
Figure 5.22: The normalized electric field profiles |E| of the fundamental modes at the carrier frequency of 128 GHz for rod-in-foam fibers of various diameters; (a) 1.75 mm-diameter core and 5 mm-diameter foam cladding, b) 0.93 mm-diameter core and 7 mm-diameter foam cladding, (c) 0.57 mm-diameter core and 50 mm-diameter foam cladding

Funding

Acknowledgment

Disclosures

The authors declare no conflicts of interest.

In the next chapter, we present the experimental challenges and general discussions for the advancement of next generation communication systems.

CHAPTER 6   GENERAL DISCUSSIONS

The aim of this thesis is to assemble a photonics-based THz communication system and to demonstrate the performance of THz communication link using solid core subwavelength dielectric fibers. We showed that, the assembled THz communication system can receive up to the bitrate of 6 Gbps, which is mainly limited by the bandwidth of LNA and the link distance is limited due to the low THz power. On the other hand, within the capability of the THz communication system, it is possible to study on improving the spectral efficiency by various multiplexing techniques such as PDM, OAM, etc. Therefore, to demonstrate the multiplexing techniques, the development and optimization of passive THz components are necessary. Next, in THz fiber communications, the design and fabrication of optimal holder is important to minimize the coupling loss between the THz source and the fiber and from the fiber to the detector. In this chapter, we first present the general discussions on the development of THz communication system and THz fiber-based communication. Next, we present the challenges in the design and fabrication of THz passive components that are developed using our research facilities. Particularly, the fabrication of wire-grid polarizer and vortex phase plate are presented. We also present the challenges in fabricating the subwavelength THz fibers and the solution for practical handling and manipulation. Finally, one of the challenges in the developed photonics-based THz communication system, the low optical to THz conversion efficiency is addressed. We present the feasibility studies on the generation of high-power CW THz waves using nonlinear crystal and proposed the novel design of the THz photomixer.

6.1   Personal contribution in the development of THz communication system

The first task assigned to me when I started my graduate program is to develop a high-performance THz communication system. After a careful literature review, we are convinced that the THz communication system using photonics approach is advantageous when compared with solid state all electronics-based system. First, I assisted my supervisor Prof. Maksim Skorobogatiy in writing the research grant (Canada Foundation for Innovation) and secured the funding to carryout the project. Next, the methods for the development of THz communication system was carried out. There were few publications that presents the outline of the THz communication system, however, a detailed description of the components/devices such as model number and name of the

manufacturer were not mentioned. For example, in the schematic diagram of the experimental set up presented in [238], it is shown that, an external electro-optic modulator is used for the data modulation. I learnt later that it also needs an additional driver to maintain the smooth modulation by avoiding the effect of drift in the RI of the modulator. Similarly, in all those demonstrations, UTC-PD was used as the THz transmitter, but it was not commercially available during that time. Therefore, before purchasing any component, a detailed analysis with their data sheet has been carried out. During this period, I have improved my skills in the areas such as funding management, effective communication with industries, collaboration with engineers from various fields, debugging the system and fixing the errors etc.

6.2 THz wireless communication system

The articles presented in chapter 4 and 5 of this thesis are descriptive and contains most of the information that has been carried out in that research work. In this section, the general discussion about the development of photonics-based THz communication system such as data modulation, link distance, etc., will be presented. Initially, the aim of the project is to develop the THz communication system that operates at the carrier frequency of 300 GHz and higher. However, due to the low output power of the THz photomixer (<50 µW at 300 GHz) and the low responsivities of the commercial ZBD's (<2000 V/W at 300 GHz), we decided to choose the carrier frequency below 150 GHz.

6.2.1 Optical modulation and maximal bit rate supported by the developed THz communication system

As the optical modulation of the IR signal is directly transferred to the THz signal, the detailed characterization of the modulation process is essential. The characteristics of DFB lasers and THz photomixers are detailed in chapter 3 and therefore, we limit ourselves to data modulation in this section. Since the maximum bit rate supported by the PPG in our test equipment is 12.5 Gbps, the electro-optic modulator that is capable enough to modulate the optical signal up to 12.5 Gbps is sufficient. Therefore, in our experiment a 10 GHz bandwidth EO modulator is used. However, a large bandwidth (>40 GHz) EO modulators are commercially available which can be used to increase the maximal bit rate. The EO modulator (intensity modulator) is simply an MZM

fabricated using a non-linear material such as LiNbO₃. Here, the optical signal at the input port is divided into two arms; and after propagating with the equal distance, it is combined at the output port. The PRBS signal (RF) is applied to one of the arms which changes the RI of the non-linear material. Therefore, the change in the phase of the optical signal leads to either constructive or destructive interference at the output port. The transfer function of the EO modulator is shown in Fig.6.1. The external bias voltage is applied to choose one of the quadrature operating points (positive or negative slope). In our experiments, the positive slope is used. During a long-term measurement, there will be a drift in the transfer function and therefore the applied bias voltage must be continuously monitored and adjusted accordingly using the real-time feedback loop.
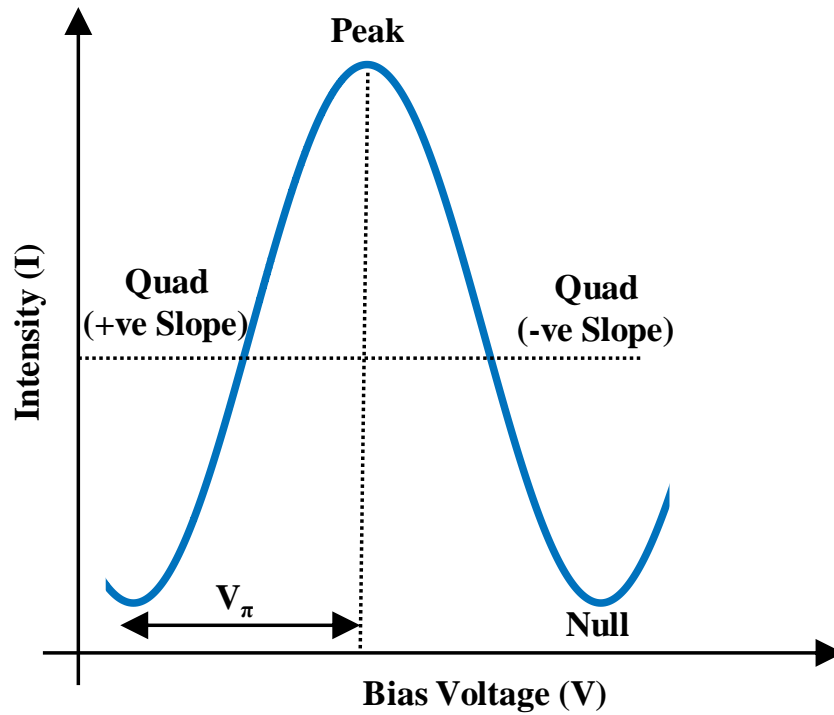
Figure 6.1: Transfer function of EO Mach Zehnder Modulator

Next, the PRBS data with a pattern length of 2^{31}-1 and bit rate up to 12 Gbps is modulated to the optical signal. In this experiment, the modulation is carried out for the combined optical signal (λ_1 and λ_2) that is used for THz generation. It is noted that, the optical modulation can be carried out for just one of the laser signals, however, the performance is better while modulating both the laser signals. The eye pattern is measured for the bit rate of 5 Gbps and 12 Gbps as shown in Fig.6.2.
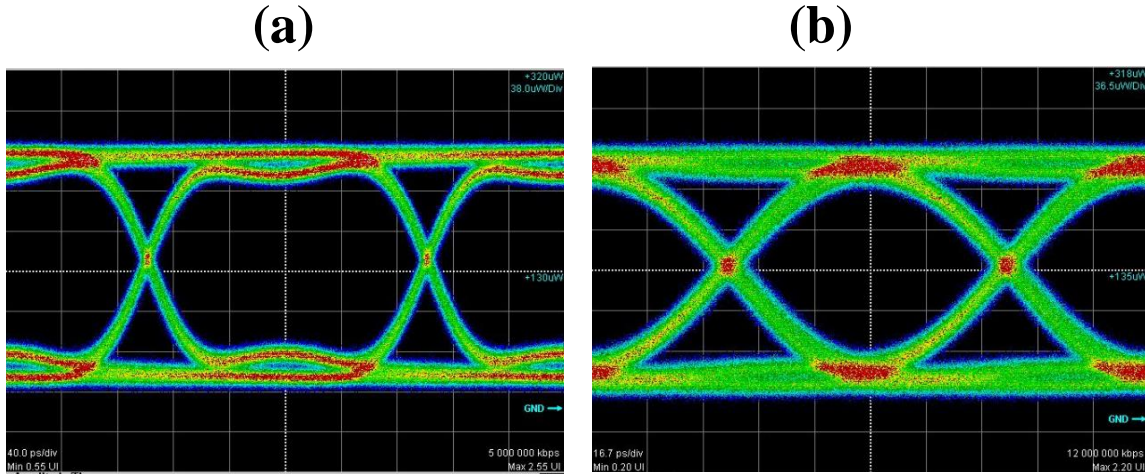
Figure 6.2: Measured eye pattern for the modulated optical signal (a) 5 Gbps and (b) 12 Gbps

From Fig.6.2, we see that the eye opening of the modulated optical signal is larger even for the bit rate of 12 Gbps. Since the electrical bandwidth and output power of the THz transmitter is sufficient for the transmission of 12 Gbps for a short link distance, the maximal bit rate is then limited by the receiver electronics. Particularly, due to the commercial non-availability of large bandwidth and high-gain digital LNA, the maximal bit rate is limited to less than 12 Gbps in our system. Therefore, in all our experiments, we used a 3 GHz bandwidth LNA (>30 dB gain) which supports the bit rate up to 6 Gbps. Recent advancements in the development of high performance LNA made its availability in the commercial market. We purchased a 25 GHz bandwidth LNA with a gain of ~30 dB (Model: SHF S126 A) that is capable enough to amplify the low power received baseband signal greater than 30 Gbps. In order to study the maximal bit rate supported by the developed THz communication system, the following experiment has been carried out. In this experiment, a high power (>300 µW at 128 GHz) UTC-PD is used as the THz transmitter instead of PIN photomixer that is detailed in chapter 4. The THz transmitter and receiver are butt coupled as shown in Fig.6.3 (a). The large bandwidth LNA (Model: SHF S126 A) with integrated bias-tee is connected next to the THz receiver. The eye pattern for the received and demodulated baseband signal for 6 Gbps, 10 Gbps and 12.5 Gbps are recorded using the oscilloscope and is shown in Fig.6.3 (b), (c) and (d) respectively. We see that, a clear eye opening is achieved for the maximum bitrate that is supported from our PPG which is 12.5 Gbps. The bitrate can be further increased to several folds, if we use the higher order modulation and coherent reception techniques.
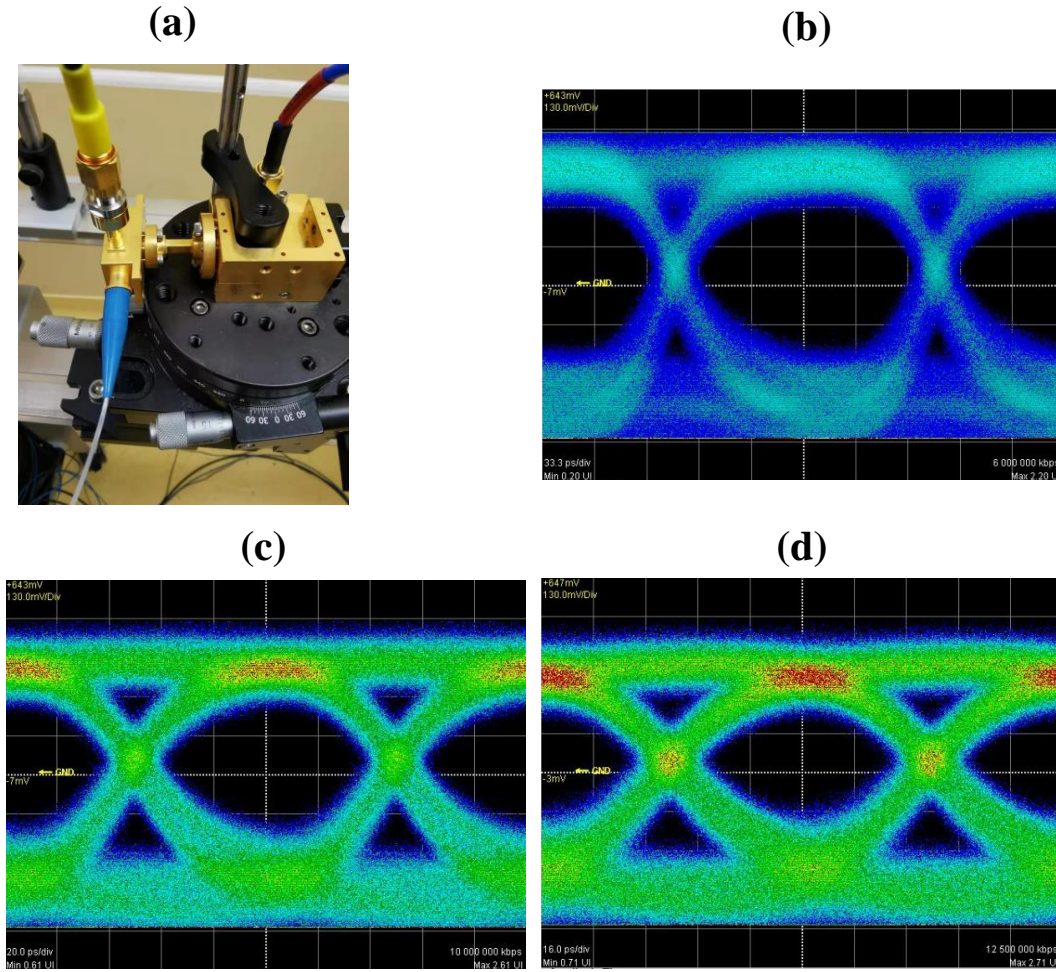
Figure 6.3: (a) Butt coupling of THz transmitter and receiver modules. The demodulated baseband signal is amplified using large bandwidth digital LNA and the eye pattern is recorded for (b) 6 Gbps, (c) 10 Gbps and (d) 12.5 Gbps respectively

6.2.2 Communication link distance

In our THz communication system, the maximal link distance is limited to ~2 m due to the divergence of the propagating THz beam in the free space. The link distance can be improved either by using a high-power THz transmitter and/or the high gain transmitter and receiver antenna. When compared with other types of antenna such as dipole antenna, Yagi antenna, microstrip antenna, the high gain can be achieved using the parabolic reflector antenna. In the parabolic reflector antenna, the maximum gain is affected by three parameters. 1. Area of the reflector, 2. Wavelength

of operation and 3. Efficiency of the antenna. The gain of the parabolic reflector antenna with respect to the isotropic antenna can be estimated using Eq.6.1.

$$Gain = 10 \cdot \log_{10} k \left(\frac{\pi D}{\lambda}\right)^2 \qquad (6.1)$$

Where, k is the efficiency of the antenna, λ is the wavelength of operation and D is the diameter of the parabolic reflector antenna. The efficiency of the parabolic reflector antenna generally varies from 50% to 70% which is affected by several factors such as surface roughness, ohmic losses, etc. The schematic of the THz communication system with parabolic reflector antenna is shown in Fig.6.4 (a). Similarly, the gain of the parabolic reflector antenna is estimated using Eq.6.1 and is presented in Fig.6.4 (b). In this calculation, the antenna efficiency k is assumed as 50% and the diameter of the antenna used is 50.8 mm (Standard 2" optics).

(a)

(b)
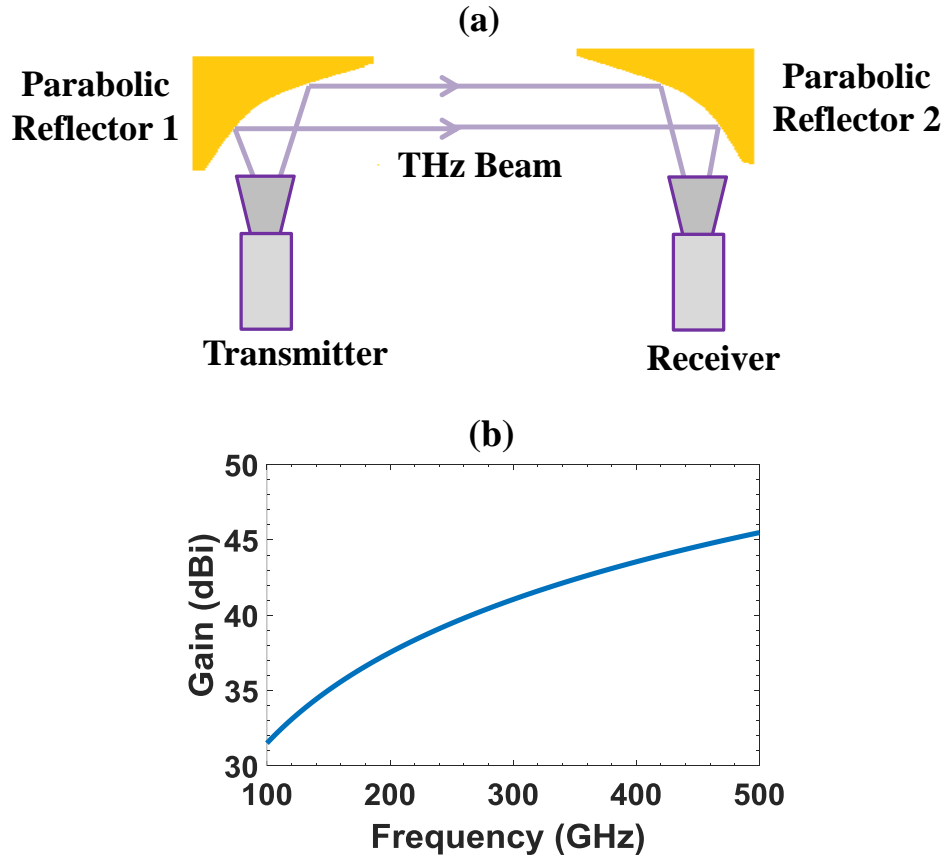
Figure 6.4: (a) Schematic of the THz communication system with parabolic reflector antenna. (b) The estimated gain of the parabolic reflector antenna.

It is noted that, for a very long distance THz communication (ground to satellite communication for example), the communication modules (transmitter and receiver on ground station) with high gain antennas must be placed in a dry location on earth where the precipitable water vapor content is lower [305]. In this way, a high-speed THz communication between airplanes and ground station is also possible.

6.2.3 Performance of recording hardware

In chapter 4, the development of photonics-based THz communication system is presented along with the demonstration of live streaming of uncompressed HD and 4K videos. Although the BER measurement is sufficient to present the performance of the communication system, the video transmission is demonstrated due to two main reasons. Firstly, as we believe that the video transmission will be one of the immediate applications of THz communication, the demonstration will attract the industries towards developing the commercial products. Secondly, the demonstration will show the requirement of other supporting hardware for real-world applications such as interconnects, splitters, recording modules etc. In this section, the choice of recording unit is briefly discussed. In video communications, the bit rates for the uncompressed videos are much higher than the compressed videos. Particularly, for 4K and beyond, the bit rates are higher than 5 Gbps for the frame rate of 30 fps. Therefore, the recording hardware must be fast enough to store the received video data.

In the following experiment, we compared the performance of SSD with PCIe 3.0 and SATA interface. In our workstation, the maximum memory capacity of 4 TB is used. It includes 2TB single SSD drive with PCIe 3.0 interface and 4*500 GB SSD with SATA interface connected as RAID 0 (4 drives act as a single drive with parallel connections to increase the speed). The performance of these two configurations are analysed using the disk speed test software from Blackmagicdesign as shown in Fig.6.5. The result shows that the SSD with PCIe3.0 is faster with read and write speed of 2000 MB/s (see Fig.6.5 (a)). For the 4K video, it can read and write as fast as 89 frames per second. Similarly, the SSD with SATA configuration is slower with the write and read speed of 1197.4 MB/s and 1473.2 MB/s respectively (see Fig.6.5 (b)). In this case, it is possible to record only 53 fps of 4K video. Therefore, the memory interface using PCIe3.0 or higher is recommended for recording the live uncompressed video feed.
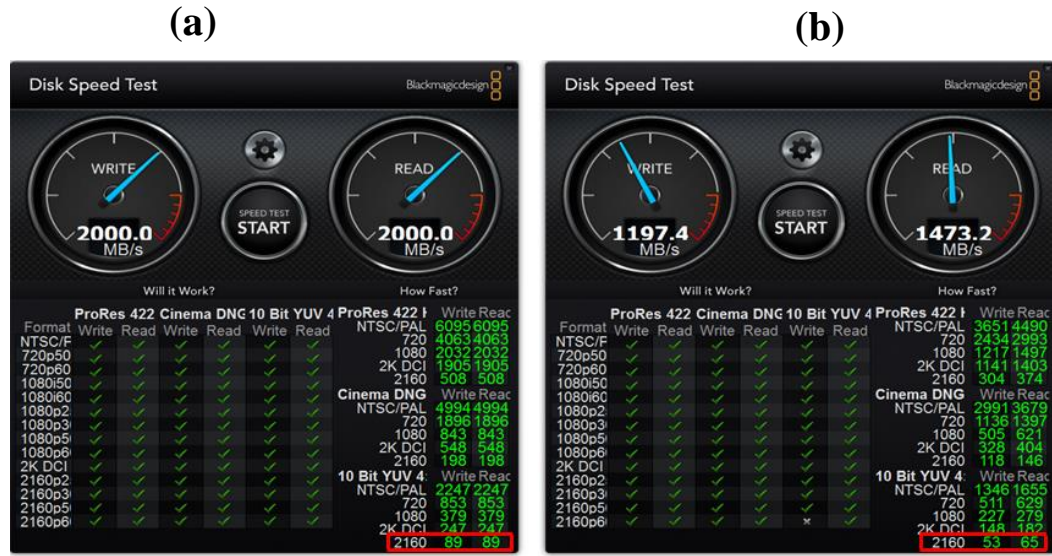
Figure 6.5 The performance of SSD memory analysed using the disk speed test software (a) SSD with PCIe 3.0 interface (b) SSD with SATA interface using RAID 0 configuration

6.3 Fiber-based THz communication

As presented in chapter 5, the THz subwavelength solid core fibers are promising in increasing the reliability of next generation communication links in both static and dynamic environments. The initial studies on the feasibility of subwavelength THz fibers, and the design and fabrication of practical THz fibers, are discussed briefly here. First, the attempt on designing efficient fiber holders are discussed, followed by the design of subwavelength and suspended core fibers.

6.3.1 Holders/connectors for subwavelength fibers

In the fiber-based THz communication link, the major challenge next to the efficient fiber design is the free space coupling loss. Particularly, for subwavelength fibers, the THz power-coupling from the emitter to the fiber is critical, which leads to higher coupling loss. Since the propagating modal field is loosely confined to the subwavelength fibers, it leads to higher bending loss as well. Therefore, the fiber needs to be tightly held at both ends to avoid bending. The schematic of the fiber-based communication link with free-space fiber coupling is shown in Fig.6.6 (a). For holding the fibers, we investigate two types of holders: namely, aperture holder and tapered horn as shown in Fig.6.6 (b) and (c), respectively. The aperture holder is 3D printed using standard ABS plastic

with the aperture diameter similar to the thickness of the fiber. In this method, inserting the fiber into the aperture might cause deformation in the shape of the fiber, which requires careful attention. The focal spot size (radius of beam waist) of the THz beam is ~2λ, where λ is the wavelength of the carrier frequency. However, due to high absorption loss of the holder material and large spot size of the THz beam, the coupling is inefficient.

Next, we investigated the tapered horn structure for holding the THz fiber, which is fabricated by 3D printing and metalized using the conductive paint. The horn is used to reduce the modal size from the collimated THz beam to the size of the fiber. This is similar to the butt coupling of the fiber to the emitter/detector horn antenna. Although the tapered structure is efficient, the poor conductivity of the paint leads to high loss. Therefore, for this thesis, we preferred to butt couple the fiber directly to the emitter and detector horn antenna for the data transmission. We find that to avoid bending for the long length fiber link, holding the fiber by a fisherman's knot, using thin thread, is simple and effective. However, for practical applications, a stable holder design or optimal connector is preferred, which must be investigated in future studies.
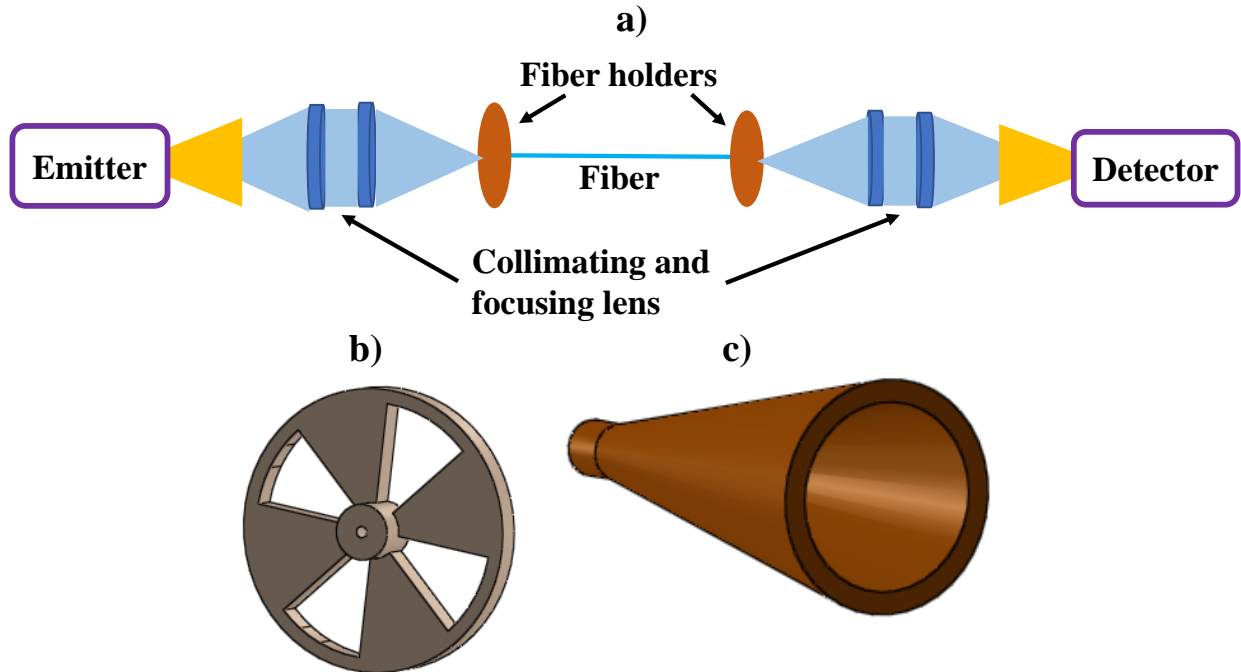
Figure 6.6: (a). Schematic of the THz fiber-based communication link using free space collimating and focusing optics (b) Aperture holder and (c) tapered horn for holding the fiber

6.3.2 Teflon tape subwavelength fiber

Before beginning the detailed investigation of rod-in-air THz subwavelength fiber, that is made up of PP, the feasibility of the subwavelength fibers in communication was carried out using Teflon as the core material. A one-meter long Teflon tape is rolled over until the thickness reaches ~1 mm, as shown in Fig.6.7 (a). The photonics-base THz communication system and butt coupling of fibers that is discussed earlier is applied for the characterization. The eye patterns for 1 Gbps, 5 Gbps and 12 Gbps are recorded, and are shown in Fig.6.7 (b), (c), and (d), respectively. Although the recorded eye amplitude is much lower (<20 mV) due to scattering of THz waves by the non-uniform structure of the fiber, a better performance is expected for uniform dielectric fiber. This is proved by the demonstration of rod-in-air subwavelength THz fibers in chapter 5.
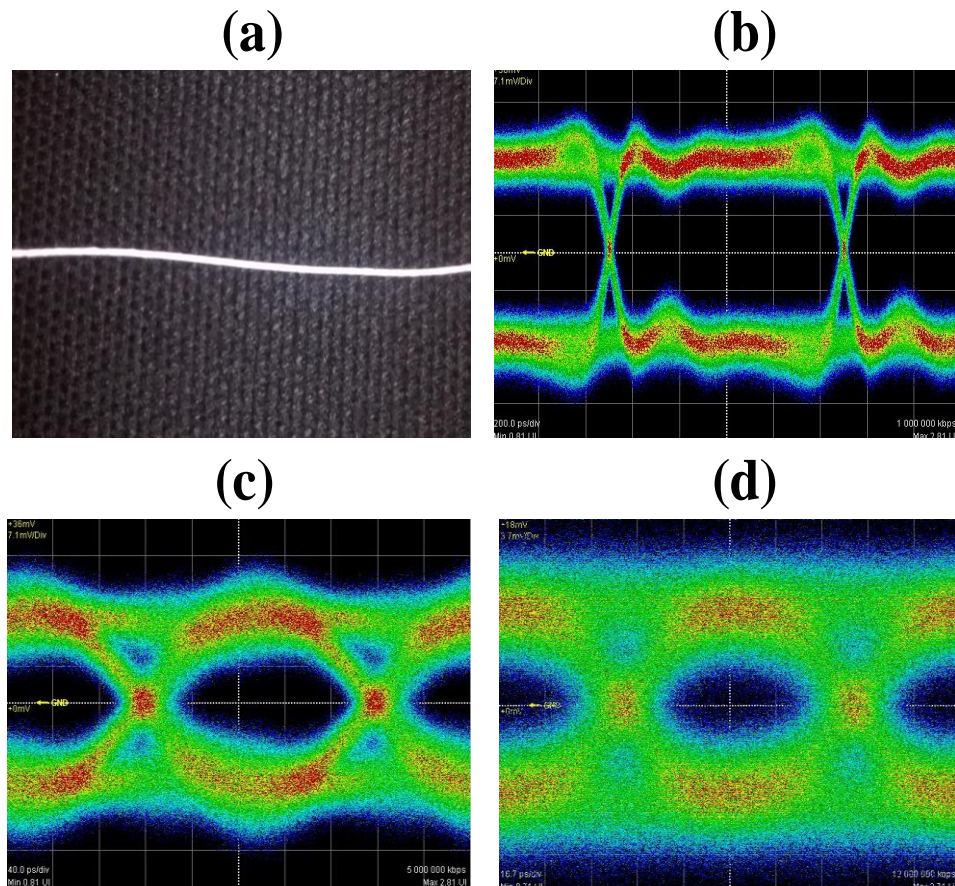
Figure 6.7: (a) THz subwavelength fiber fabricated using Teflon tape. The recorded eye pattern for 1 m fiber (b) 1 Gbps, (c), 5 Gbps and (d) 12 Gbps

6.3.3 Bit rate and BER measurements

The bit rate and BER of a free space communication system depends on the type of modulation, bandwidth, dispersion and SNR respectively. Particularly, even if the desired SNR is achieved, the dispersion parameter plays a major role in the maximal bit rate supported by the fiber when compared with the free-space communication link. Therefore, in chapter 5, the maximal bit rate is estimated by the second order dispersion of the fiber for a simple ASK modulation. Although, the BER can be theoretically estimated using the SNR, it is measured experimentally in this thesis work. Particularly, I fixed the target BER as 10^{-12} which is sufficient to measure the performance of the communication link and estimated the measurement duration by 1/(target BER * bit rate).

6.4 Practical THz subwavelength fibers

Low-loss waveguides are highly desired to provide efficient data transmission for commercial applications. In general, co-axial cables with different bandwidths, depending on the applications, are widely used in the radio frequency range. However, for the frequency range above 100 GHz, the dimension tolerance of the co-axial cable must be tighter, which limits the length of the cable mostly below 1 m. Therefore, the low loss plastic fibers can be used as waveguides for the frequencies above 100 GHz. In this section, the practical microstructured THz fibers are discussed.

6.4.1 Microstructured suspended core fiber

In chapter 5, we showed that a solid core subwavelength THz fiber fabricated using PP material can support efficient inter-device/back-up communication links over the length of greater than 10 meters. Due to the subwavelength dimension of the fiber, the modal field propagates mostly in the air, which limits practical handling and manipulation. To physically handle such fibers, we proposed to encapsulate it with a low-loss foam material, which is an additional step in the fiber fabrication process. To provide a practical solution, we designed and fabricated a wagon wheel fiber (suspended core fiber) at the carrier frequency of 128 GHz. Although the similar design with a length of few centimeters was demonstrated earlier by our group using fiber drawing tower[164], the aim of this work is to optimize the design for the carrier frequency of 128 GHz and to fabricate the fiber with length greater than 2 m using 3D printing [192]. The advantages of fabricating the proposed design using 3D printing is that it is not required to fabricate a preform, not necessary to

apply air pressure and can be printed without much complexity. In this design, the outer and inner diameter of the fiber is 8 mm and 7.6 mm, respectively. Similarly, the core diameter and the thickness of the bridge that is connecting the central fiber core to the outer jacket is 1.6 mm and 0.4 mm, respectively.
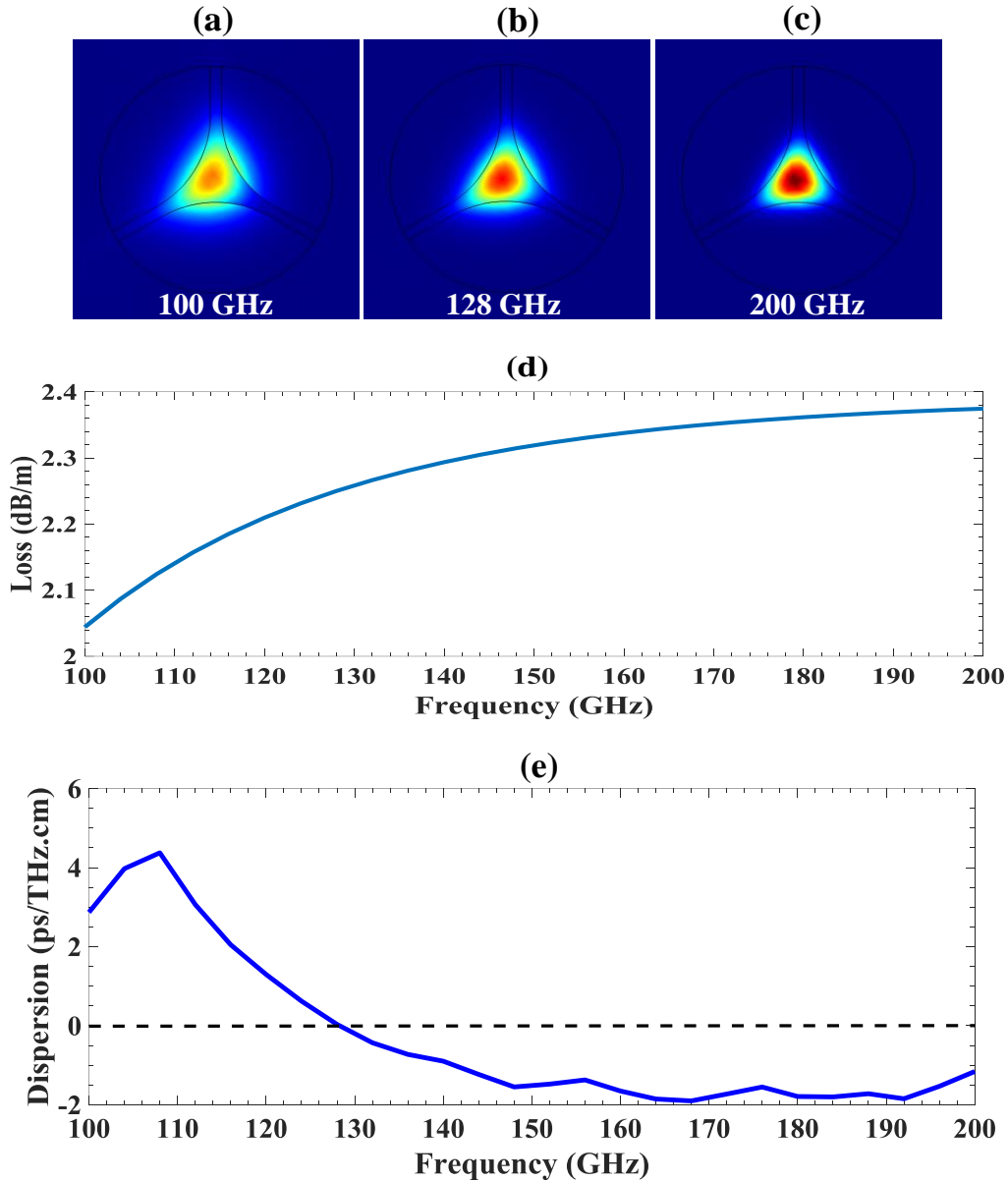
Figure 6.8: The normalized electric field profile of the fundamental mode of the suspended core fiber at the carrier frequency of (a) 100 GHz, (b) 128 GHz and (c) 200 GHz. The loss and dispersion of the fundamental mode is shown in (d) and (e), respectively

The electric field profile of the fundamental mode of the suspended core fiber is shown in Fig.6.8 (a), (b), and (c), respectively. The transmission loss of the fundamental mode is numerically estimated and is shown in Fig.6.8. (d). We see that, the modal loss at lower frequency is less than the material absorption loss (2.36 dB/m at 128 GHz), as some part of the mode propagates in the low-loss air cladding. When the frequency increases, the propagating mode is tightly confined in the central core and thereby the loss value approaches towards the material absorption loss. In Fig.6.8 (d), the dispersion of the fundamental mode is presented in which a near zero dispersion is achieved for the carrier frequency of 128 GHz.
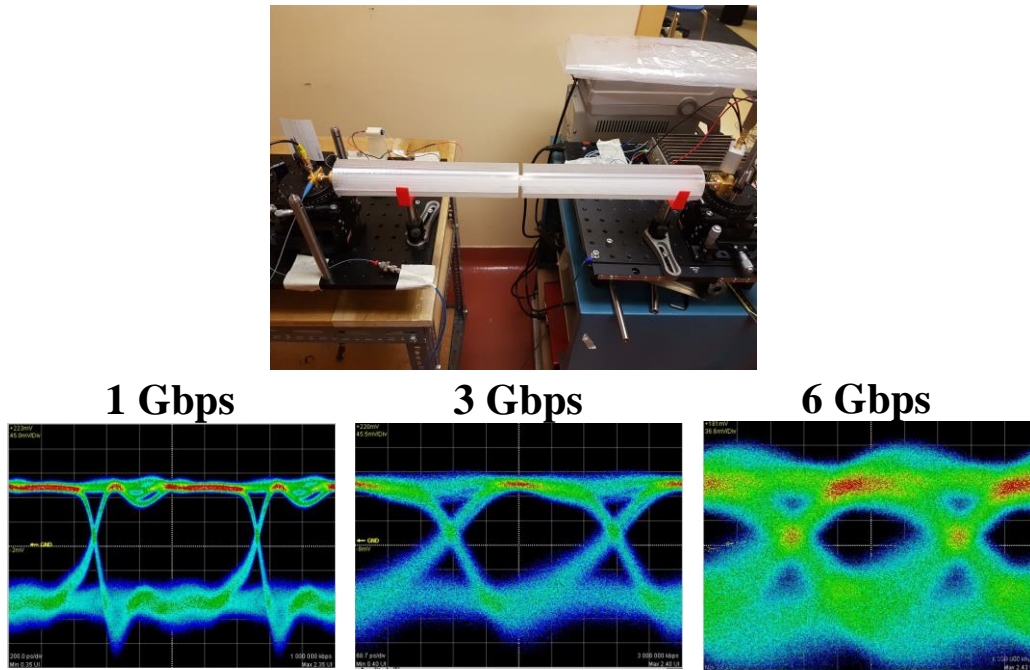
1 Gbps   **3 Gbps**   **6 Gbps**

Figure 6.9:   Experimental characterization set up for suspended core fiber (50 cm long) and the corresponding eye patterns for 1 Gbps, 3 Gbps and 6 Gbps

The designed suspended core fiber is fabricated using 3D printing and the preliminary experimental characterization has been carried out. We have 3D printed several sections (each section with the length of 25 cm) of suspended core fiber with a large extra layer which acts as the support during fabrication. In Fig.6.9, the experimental set up for two fiber sections (50 cm long) and the eye patterns for 1 Gbps, 3 Gbps and 6 Gbps were shown. Since the fabrication length is limited to the height of the 3D printer (in vertical direction), we also carried out the fabrication of the proposed fiber design using Blackbelt 3D printer in which it is possible to fabricate the fiber without any

limitation in the length. The detailed theoretical and experimental characterization for both the 3D printed fibers are in the progress and will be completed in the near future.

6.4.2 Bending measurements of graded index THz fibers
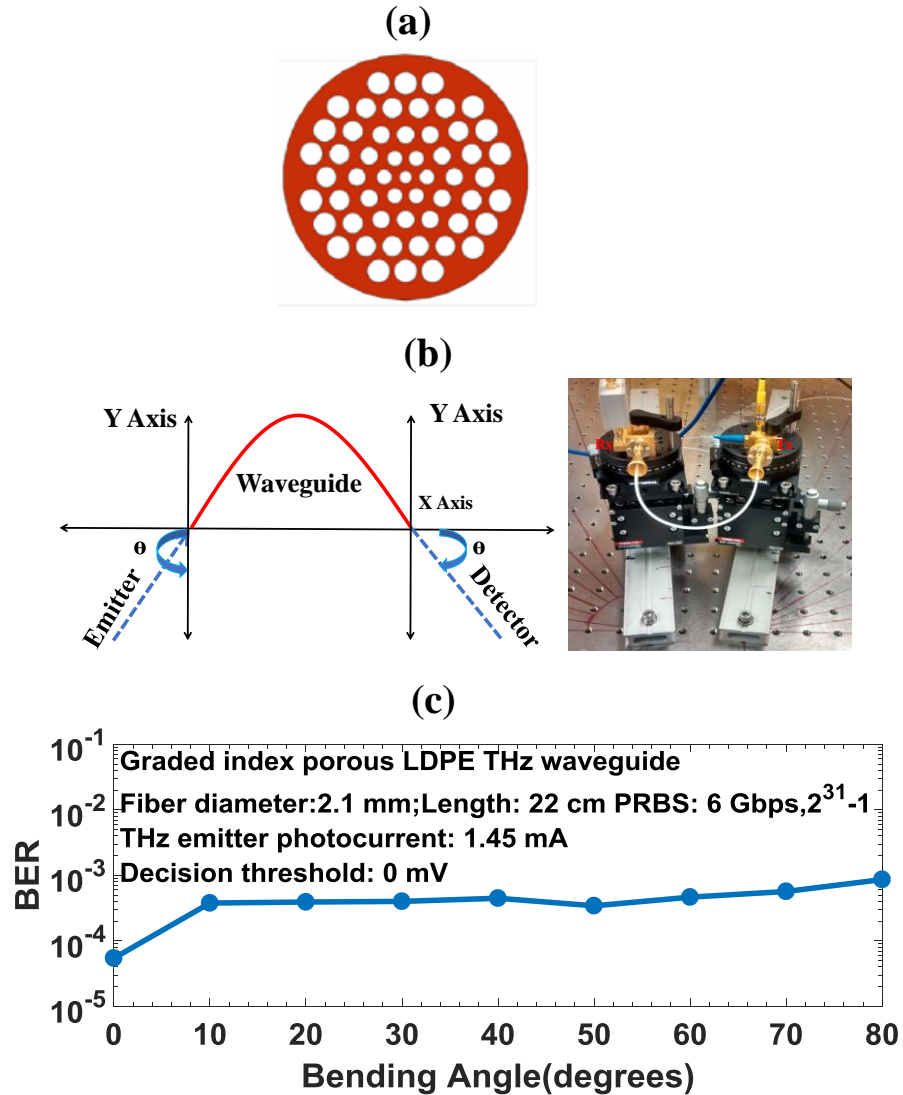
Figure 6.10: (a) Schematic of the graded index porous core THz fiber (b) The schematic and the photograph of the experimental set up (c) The measured BER as a function of bending angles

One of the important parameters that must be considered while designing the THz fibers for practical applications is the tolerance to the fiber bend. It is shown in chapter 5 that, if the

propagating mode is tightly confined to the solid core of a THz fiber, a lower bend loss can be observed for the bend radius >3 cm. A graded index, porous-core THz fiber is proposed and fabricated using LDPE for low-loss, and low dispersion, THz guidance, which can be used as a short distance (few cm's) interconnect [181]. The schematic of the fiber is shown in Fig.6.10 (a). The following communication experiment is carried out to verify the performance of a bent porous core fiber at the carrier frequency of 140 GHz. A 22 cm-long, graded-index porous core fiber with the outer diameter of 2.1 mm is used for the study. The schematic and the photograph of the experimental setup is shown in Fig. 6.10.(b), in which the bending angles of the emitter and detector antenna are pre-calibrated. The bending angle of zero degree refers to the straight fiber. It is noted that while using a higher THz power in a short fiber link, it is not possible to observe any errors in the received data. In order to measure the BER, and to avoid the saturation of the receiver antenna, the THz power is minimized (photocurrent: 1.45 mA at 140 GHz), which results in the BER slightly below the FEC limit. The angles of both the emitter and detector antenna is varied simultaneously, and the BER is recorded for the bitrate of 6 Gbps and decision threshold of 0 mV, as shown in Fig.6.10. (c). We see that, even for the bending angle of 80 degrees, the deviation in the BER measured for the straight fiber (zero degree) is minimal. Therefore, we conclude that, the graded index porous core fiber is highly tolerant to bending at the carrier frequency of 140 GHz.

6.5 Passive components for THz communication

In order to increase the bit rate and the efficiency of the THz communications, the support of passive components such as polarizers, interconnects, couplers, phase plates etc., are necessary. In this section, we particularly discuss about wire-grid polarizer and OAM phase plate.

6.5.1 Wire-grid THz polarizer

A THz polarizer is a passive component that allows the transmission of a specific polarization of the incoming unpolarized beam, while filtering other polarization directions [307]. In communications, the THz polarizer can be used to increase the channel capacity by multiplexing different polarizations at the same carrier frequency. In the simplest case, the channel capacity can be doubled by using vertical (TE) and horizontal (TM) polarization for the given carrier frequency. Among several polarizer designs [308-312], the free-standing, wire-grid polarizer is simple in

fabrication and it transmits the linearly polarized light, whose electric field's direction is perpendicular to the wire-grids. The presence of electric fields in the incoming beam that is parallel to the wires are reflected. The working principle is briefly explained as follows: when the electric field of the incoming light is aligned parallel to the wires, it induces the movement of electrons along the length of the wires.

(a)

(b)
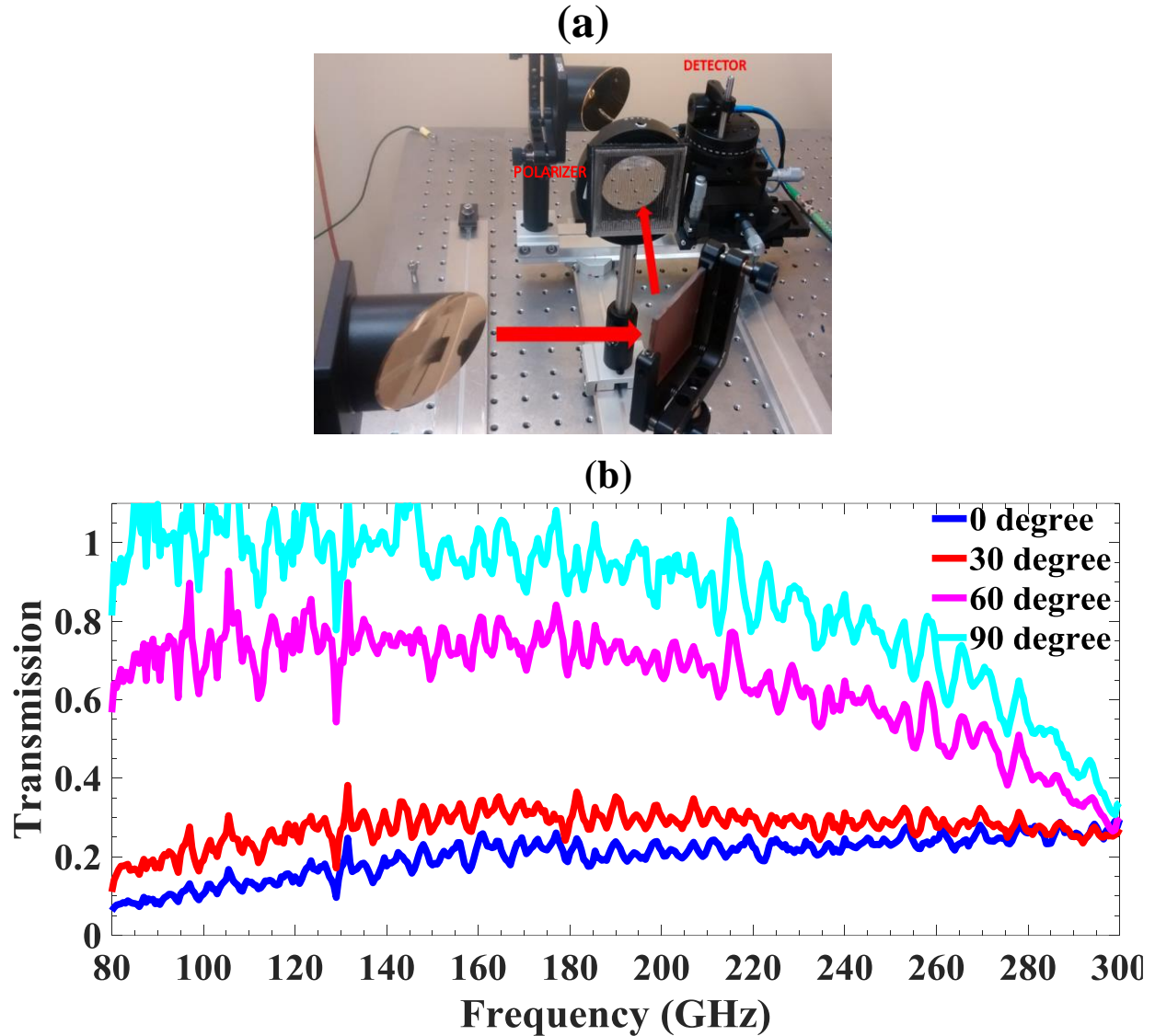
Figure 6.11 (a) Experimental setup for the characterization of wire-grid polarizer (b) Transmission spectra of a single polarizer at different angles of rotation. Zero degree refers to the wires of the polarizer that is aligned parallel to the electric field of the incident THz beam

This is similar to the behaviour of a metal surface, and, therefore, reflects the light. On the other hand, the movement of electrons in the wires are restricted to the width of the wires for the electric field lines that are aligned perpendicular to it and leads to the transmission of the light. The fabrication of wire-grid polarizers is even simpler for the lower-THz band (<300 GHz), due to large wavelengths (>1 mm). That means that the inter-wire separation can be easily maintained, which should be less than the wavelength. Thus, a commonly used 3D printing technique, such as fused deposition modelling (FDM) with a lateral resolution of 100 µm followed by the metallization process, can be utilized for the mass production of THz wire-grid polarizers.

In our experiments. the THz wire-grid polarizer was 3D printed using commonly used ABS polymer. The outer dimension of the polarizer, thickness of the wire, and the spacing between the wires are 5 cm, 400 µm, and 400 µm, respectively. The metallic coating process was carried out using E-beam evaporation, where a 100 nm thick Nickel was deposited on both the sides of the polarizer. The polarizer is then characterized using the frequency domain THz spectroscopy system.

The experimental setup for the characterization of the wire-grid polarizer is shown in Fig.6.11 (a). The polarization of the emitter THz antenna is fixed in the vertical direction (TE polarization). Firstly, a single wire-grid THz polarizer, with the wires standing in the vertical direction, is placed along the path of collimated THz beam (0 degree). The frequency of the THz beam is tuned from 80 GHz to 300 GHz; and the THz photocurrent, which is proportional to electric field, is recorded as shown in Fig.6.11 (b). The frequency resolution and integration time for this measurement is 100 MHz and 30 ms, respectively. As expected, the transmission is low when the wires are aligned along the direction of the electric field. Next, the direction of the polarizer is rotated at several angles and the transmission spectrum is recorded. When the wires are aligned perpendicular to the electric field direction of the incoming beam (90 degrees), the maximum transmission can be observed, particularly for the frequencies below 200 GHz.

Next, the leakage of arbitrary polarization states through the fabricated THz polarizer is further improved by adding similar polarizer in the THz path. The recorded transmission spectra are shown in Fig.6.12. In Fig.6.12 (a), the wires of the first and second polarizer are aligned parallel (0 degree) to the direction of the electric field of the incident THz beam. Then, the orientation of the second polarizer is rotated at several angles until the wires are aligned perpendicular to the direction of the
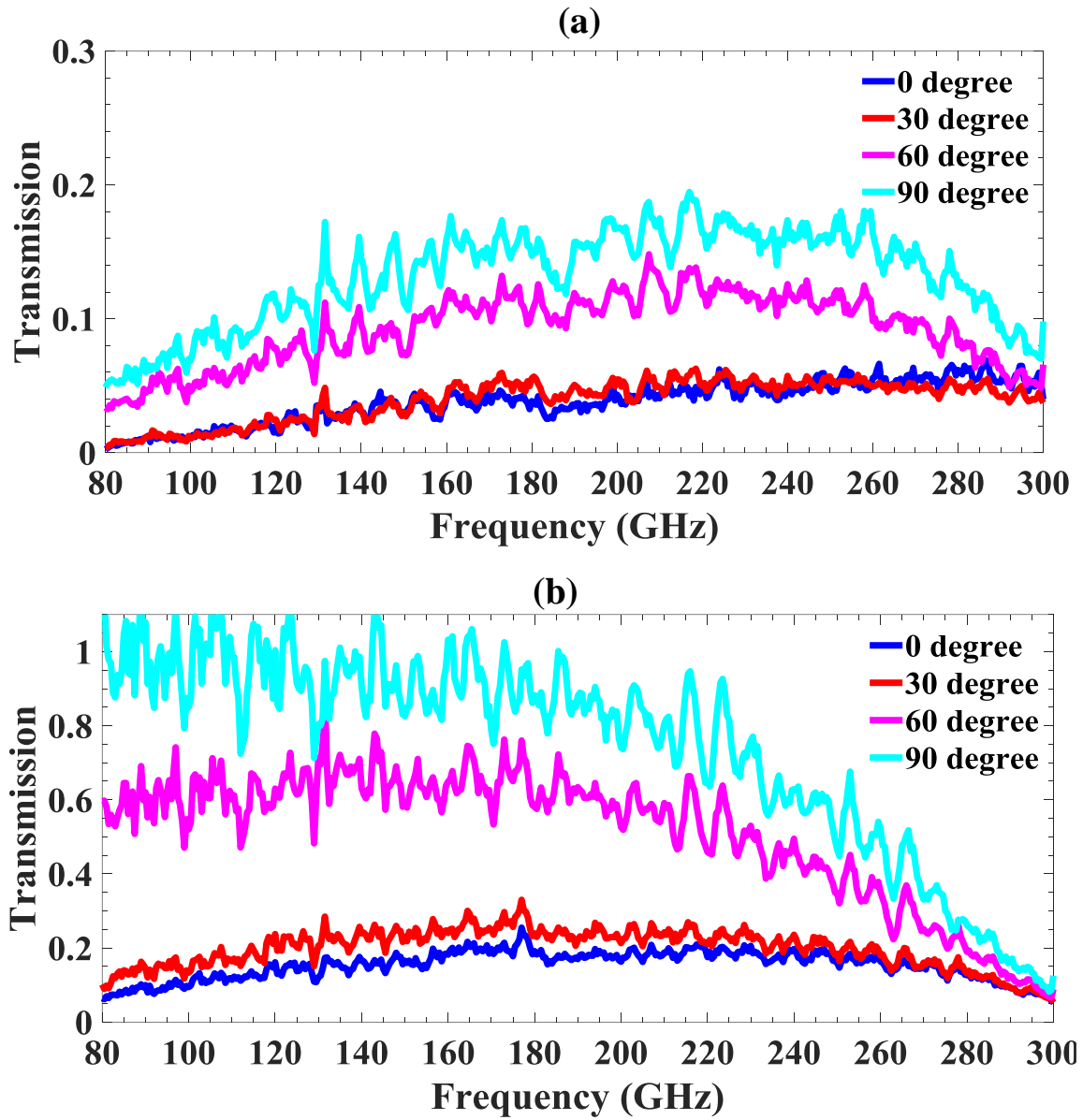
Figure 6.12: Transmission spectrum of two polarizers placed in series (a) The first polarizer is fixed, and the wires are aligned parallel to the direction of the electric field of the incident beam. The second polarizer is rotated from 0-degree (wires parallel to the direction of the electric field of the incoming beam) to 90-degree (wires perpendicular to the direction of electric field of the incoming beam) (b) The first polarizer is fixed, and the wires are aligned perpendicular to the direction of the electric field of the incident beam. The second polarizer is rotated from 0-degree (wires parallel to the direction of the electric field of the incoming beam) to 90-degree (wires perpendicular to the direction of electric field of the incoming beam)

incoming THz beam (90 degree). We observed that, the transmission of unwanted polarization is less than 20% around the frequency of 200 GHz. Similarly, the maximum transmission in this configuration is achieved by placing both the polarizers in the horizontal direction (i.e. the wires of the polarizers are aligned perpendicular to the direction of the electric field of the incident THz beam).

The design and performance of the 3D printed, and metallized, wire-grid polarizer can be further improved at higher THz frequencies by minimizing the wire diameter and distance between the wires. Recently, a broadband THz polarizer that is 3D printed using conductive PLA polymer is demonstrated [313]. By using the conductive polymer, the additional metallization process as shown in our fabrication steps can be avoided. Therefore, the fabrication of 3D printed polarizers using various conductive polymers and their performance can be further studied in detail.

6.5.2 THz communications using vortex beam

In communications, space division multiplexing (SDM) is one of the emerging techniques that is used to increase the information capacity and the spectral efficiency of the communication channel. One of the SDM techniques is the channel multiplexing using vortex beams (also known as orbital angular momentum (OAM) beams), which increases the transmission capacity by a factor equal to the number of transmitted spatial modes [314-316]. An electromagnetic wave carrying OAM has a helical transverse phase in the form of $exp(im\phi)$, where m is the charge of the OAM beam and ϕ is the azimuthal angle. The value of m is either positive or negative, which represents the number of 2π changes in the azimuthal direction [317]. The pictorial representation of the helical phase fronts for $m = 0, 1, 2\ and\ 3$ is shown in Fig.6.13. In optics, the vortex beams are generated using several tools such as spiral phase plate, q-plate, spatial light modulator etc. Similarly, several techniques have been used to generate the vortex beams in the radio frequencies. The vortex beams at 90 GHz were generated using a spiral-phase plate [318, 319]. Conventional phase array antennas were used to generate the vortex beam by configuring each antenna element with an appropriate phase delay [320]. This technique can also be used in the generation of vortex beam and beam steering simultaneously [321]. Another interesting technique for the generation of THz-vortex beams is by using liquid crystals, where the phase is manipulated using spatially varying orientation of the liquid crystals [322, 323]. The radially symmetric airy beams are also demonstrated recently

to carry the OAM charge in the terahertz region [324].The generation of THz vortex using 3D printed structures is promising, as this technique is cost effective and enables mass production [319, 324].
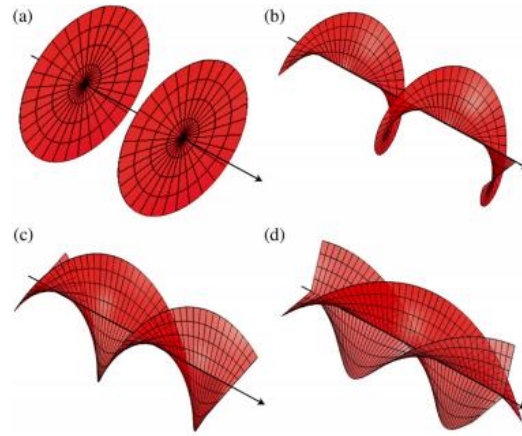
Figure 6.13: Helical phase fronts for (a) m=0, (b) m=1, (c) m=2 and (d) m=3. Reprinted from the Ref. [317]

We see that the spiral phase plates are the commonly used method for vortex beam generation at THz frequencies, due to its simple design and fabrication abilities. In the simple case, the thickness of the spiral phase plate is varied azimuthally from 0 to 2π for the generation of a vortex beam with charge $m = 1$ at a given carrier frequency. However, there are some challenges. Although the material loss of most common dielectric materials (Teflon, polyethylene etc.,) that is used in the fabrication of a phase plate is smaller at lower THz frequencies (<300 GHz), the efficiency at higher frequencies is not appreciable. Similarly, the alignment of several spiral phase plates together for the generation of higher vortex charges ($m = \pm2, \pm3, \pm4, \pm5$ and so on,) is difficult due to uneven shape of the spiral structure. In such cases, the porous planar structure is preferred. Instead of changing the plate thickness for the variation in the refractive index, the fill factor of the porous structure can be varied along the azimuthal direction of the planar structures. In this approach, both low-loss and reconfigurable vortex phase plates can be fabricated. The proposed porous planar phase plate design (for 140 GHz) is printed using 3D stereo-lithography technique (Asiga) with PlasCLEAR as the photopolymer resin material as shown in Fig.6.14.

(a) **(b)**
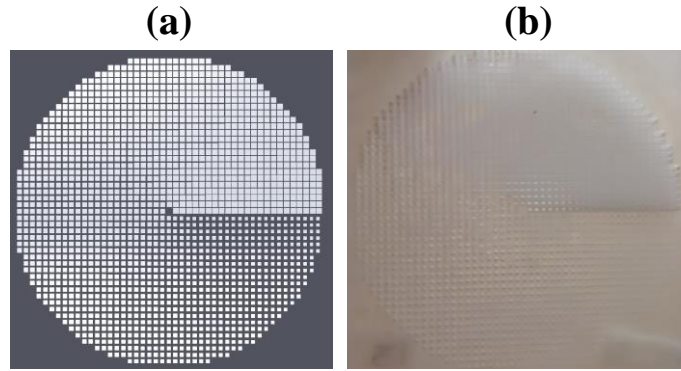
Figure 6.14: Porous planar THz phase plate (a) proposed design and (b) 3D printed structure

The 3D-printed, porous planar phase plate is treated with isopropanol, followed by the high-pressure air blow to remove the presence of unwanted photo resins inside the porous structure. Finally, the phase plate is UV treated before experimental characterization. Firstly, the quality of the porous structure in the phase plate is characterized using optical microscope as shown in Fig.6.15.
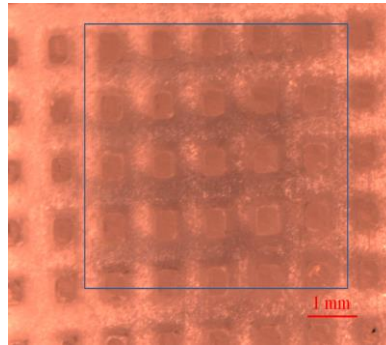
Figure 6.15: Optical microscope image of the 3D printed porous planar phase plate. The marked area shows that the photo resin is not completely removed after treating with isopropanol and high-pressure air jet

It is observed that the photo resins are not completely removed, particularly at smaller pore sizes. At the same time, the trade-off between the maximum pore size and thickness of the phase plate depends on the carrier frequency and must be considered. The maximum pore size cannot be increased beyond the size of the wavelength (3 mm at 100 GHz carrier frequency); and, therefore, the presence of unwanted photo resins in the phase plate remains as a challenge, which needs to be investigated further. We then carried out the THz imaging experiment to measure the amplitude

and phase image of the 3D-printed porous planar phase plate. The THz time domain system described in [88] was used for the experiment. From the experiments, the recorded amplitude and phase image at 100 GHz and 140 GHz are shown in Fig.6.16. We observed a better donut-shaped amplitude at 100 GHz when compared with 140 GHz, which is attributed to both the presence of unwanted photo resin and frequency dependent material loss. We then decided to fabricate the porous planar phase plate using laser drilling, which is also a low-cost method and enables mass production. The porous planar phase plate is then fabricated using laser drilling with PMMA as the host material and the detailed characterization has been carried out and is presented in [177].
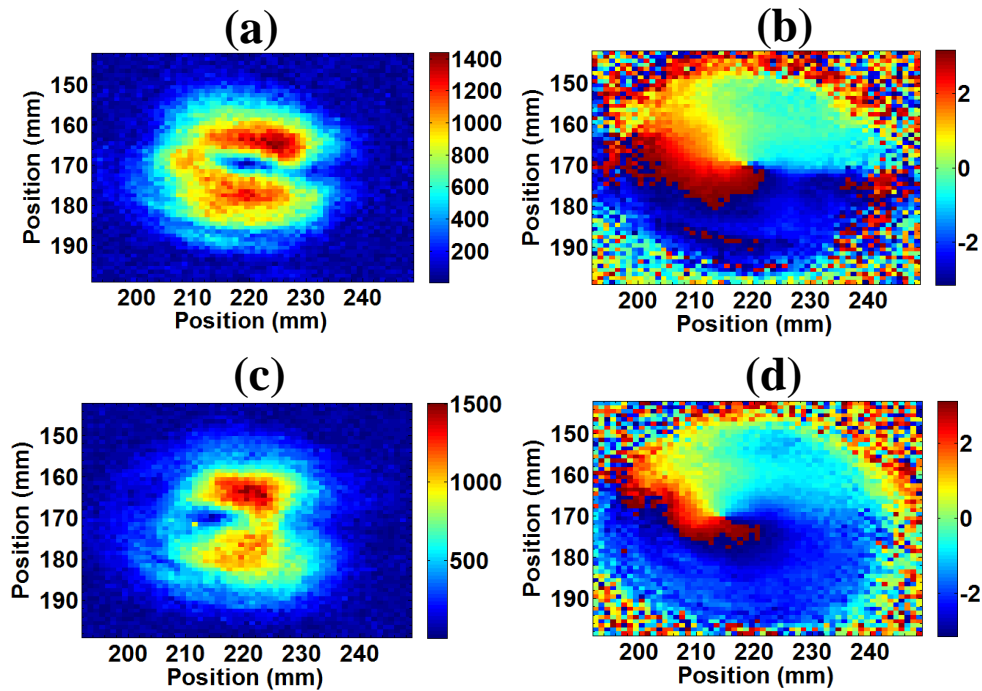
Figure 6.16: The measured amplitude and phase image of the 3D printed porous planar phase plate (a) The amplitude and (b) phase image at 100 GHz (c) The amplitude and d) phase image at 140 GHz

One of the objectives of design and fabrication of a porous planar phase plate is to demonstrate the channel multiplexing using vortex beams. In the literature, there are few works that present the vortex beam communications in millimeters and THz frequency bands [325-329]. In [330], Ahmed *et.al* studied the effects of other channel conditions beyond line-of-sight links, such as multipath and object obstructions. It was shown that the multipath propagation due to reflections distorts the vortex beams resulting in the intra and inter-channel crosstalk, thereby degrading the link

performance [331]. Recently, the transmission of vortex beams using THz fibers is also demonstrated [332, 333]. Therefore, a detailed research on the channel modelling and multiplexing, demultiplexing principles in THz communications using vortex beams are expected.
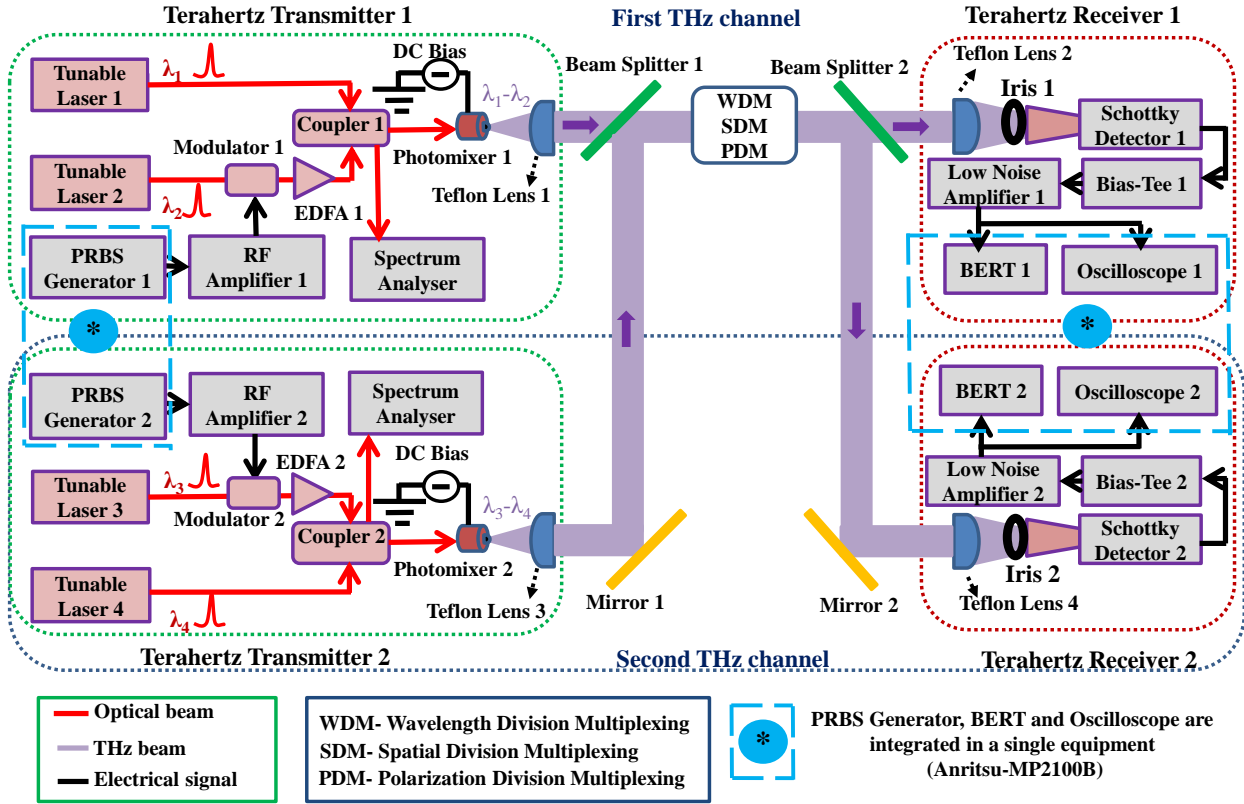
Figure 6.17: The schematic of the two-channel photonics-based THz communication system to carry out multiplexing, demultiplexing, channel crosstalk measurements. The test equipment Anritsu-MP2100B can support up to four channels of PPG and BERT

In order to achieve high-speed data transmission for practical applications, the researchers are currently working towards developing novel components, such as couplers, wavelength add/drop filters, band pass filters, and tapers for device fabrication in the THz frequency range [140, 334-337]. Similarly, several multiplexing schemes such as PDM, WDM, SDM, and efficient algorithms are being investigated to further increase the data rate [18, 193, 338, 339]. To study the challenges that arises due to channel crosstalk, a minimum of two THz channels is necessary. Therefore, establishment of a multifunctional test bed to carry out various such communication modalities is the need of the hour. In Fig.6.17, the proposed schematic of the photonics-based, two channel THz

communication system, that is combined with the our already existing THz system (first THz channel) in our laboratory, is shown [340]. The test equipment (Anritsu-MP2100B) can support up to 4 channels of PPG and BERT. As of now, we are limited with one THz channel and therefore, by adding more THz channels to the existing THz system, several advanced studies can be carried out.

6.6 High power CW THz generation

In THz communications, the main parameter that determines the maximal link distance is the output power. Similarly, in several THz imaging applications, a single THz frequency is already sufficient to obtain a high-resolution image of an object under study. In such cases, the choice of the THz frequency can be dynamic depending upon the requirement at the application end. Therefore, the demand for a widely tunable, CW high-power THz source in the commercial market will increase in the next few years. As we discussed in chapter 2, the electronics-based sources offer higher CW THz power with a limitation of wide tuning range. At the same time, the photonics-based THz system can offer wide tuning range (> 3 THz), but relatively lower output power due to poor optical-to-THz conversion efficiency. In the photonics-based approach, there are several methods that are used to generate both pulsed and CW THz radiation [88, 99, 100]. In the following, the feasibility study on the generation of CW THz radiation using non-linear crystals and novel photomixer design are discussed. The study of DFG using crystals comes under the subject 'nonlinear optics', however, this is important in designing a high-power THz transmitter (front-end) for long distance communication applications.

6.6.1 THz generation using nonlinear crystals

The nonlinear optical crystals, such as $LiNbO_3$, DAST, DSTMS, OH1 etc., are used in the generation of THz radiation using difference frequency generation [341-343]. The magnesium oxide doped periodically poled $LiNbO_3$ crystal (MgO: PPLN) is one of the attracting candidates, due to its high non-linearity (25 pm/V), high pulse energy, and narrow linewidth of the generated radiation [344]. Generally, two-color pulsed optical pump sources are used to generate the THz waves using DFG principle. In the following, the feasibility of generating THz waves using high-power CW optical pumps operating in the IR C-band is studied. The motivation of this study is to

generate high power THz waves at frequencies greater than 500 GHz for a long link, THz wireless communications, however, we study the efficiency at 140 GHz due to comparably low loss of MgO:PPLN.

The proposed experimental setup is similar to the configuration presented in chapter 4, and the schematic is shown in Fig.6.18. Two continuously tunable DFB lasers operating in the IR C-band is the optical source. These laser beams are amplified further using high power EDFA (up to 30 Watts, IPG Photonics) and focused on the nonlinear crystal with the spot size of ~100 µm. The estimation of the generated THz power from MgO:PPLN is studied theoretically as follows.
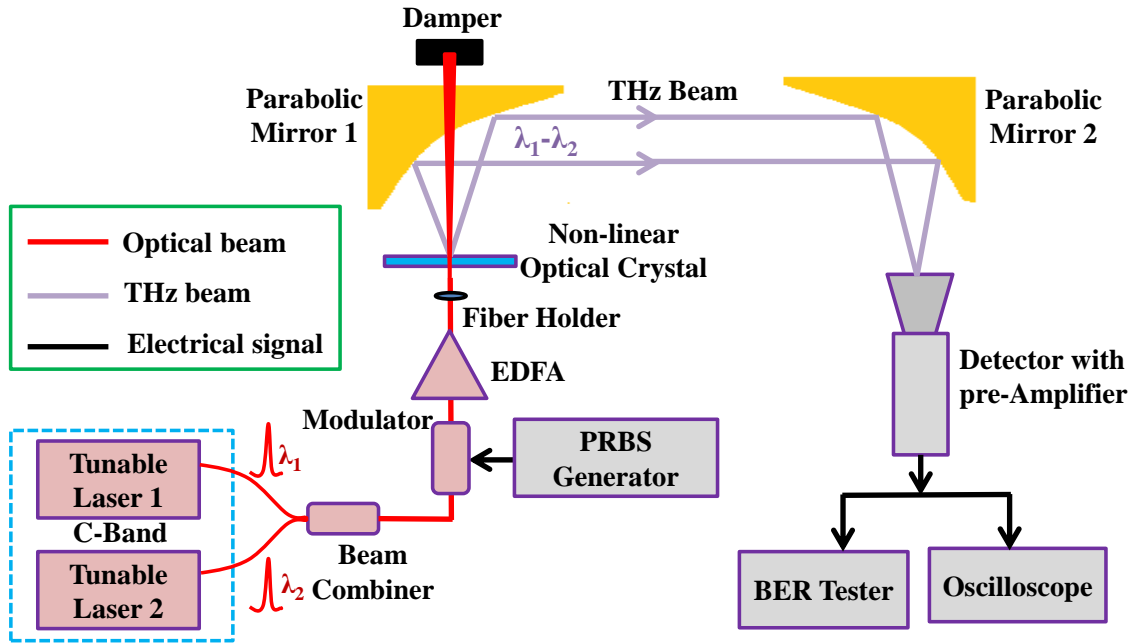
Figure 6.18: Schematic of the proposed THz communication setup with nonlinear crystals as the THz generator

In our studies, a quasi-phase matching theory is used, which explains that when both energy and momentum is conserved by all the three waves involved in the process in a nonlinear medium, an efficient DFG can be achieved [345, 346]. Let us consider, K_1 and K_2 are the wavenumbers of the IR pump beams; K_3 is the wavenumber of the generated difference frequency (THz frequency in our studies). The wavenumber of the generated difference frequency is equal to the difference in the wavenumbers of the pump beams (i.e. $K_3 = K_1 - K_2$) for a non-dispersive nonlinear media. The concept is illustrated in Fig.6.19.
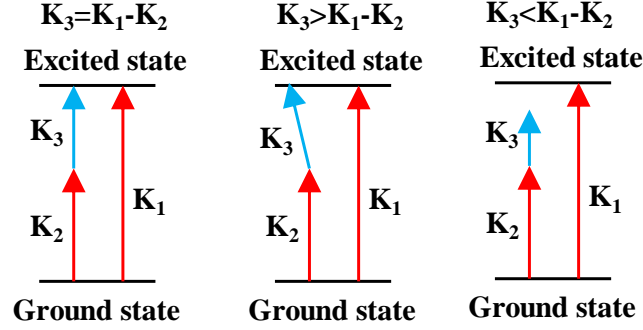
Figure 6.19: Wavevectors of the pump beams and the generated wave

However, for the dispersive media, the RI of pump beams and the generated difference frequency will be different $(K = 2\pi n(\lambda)/\lambda)$ and leads to a non-zero wavevector, ΔK (i.e. $K_3 + K_2 - K_1 = \Delta K \neq 0$), preventing the efficient DFG. One of the methods to compensate for the mismatch in the wavevector is by writing a Bragg grating (periodic poling) into the nonlinear media (crystal). The coherent length and the period of the Bragg grating is calculated by Eq.6.2.

$$Coherent\ length = \frac{\pi}{\Delta K} \tag{6.2}$$

$$Period\ of\ Bragg\ grating = 2 \cdot coherent\ length$$

The poling period for the MgO:PPLN is ~764.2µm for 140 GHz generation when pumped by the IR beams of wavelength in the C-band. Similarly, the maximum interaction length of the non-linear crystal is determined by the absorption loss for the generated difference frequency (140 GHz). For LiNbO$_3$ crystal, the absorption loss, α is 2 cm^{-1} (at 200 GHz) [347] and therefore the interaction length, L is limited to ~70 mm, which is estimated by Eq.6.3. It is noted that the RI of MgO:LiNbO$_3$ is similar to LiNbO$_3$ for the simplicity.

$$L = \frac{20 \cdot \ln{(2)}}{\alpha} \tag{6.3}$$

The DFG using quasi phase matching theory is calculated using Eq.6.4 [346].

$$\frac{P_3}{P_1} = \frac{8\pi^2 d_{eff}^2 L^2 P_2}{\varepsilon_0 c n_1 n_2 n_3 \lambda_3^2 A} \cdot \exp{\left(-(\alpha_1 + \alpha_2 + \alpha_3) \cdot \left(\frac{L}{2}\right)\right)} \tag{6.4}$$

$$\cdot \frac{\sin^2\left(\frac{\Delta K - \left(\frac{2\pi m}{\Lambda}\right) \cdot L}{2}\right) + \sinh^2\left[(\alpha_1 + \alpha_2 + \alpha_3)\left(\frac{L}{4}\right)\right]}{\left(\frac{\Delta K - \left(\frac{2\pi m}{\Lambda}\right) \cdot L}{2}\right)^2 + \left[(\alpha_1 + \alpha_2 + \alpha_3)\left(\frac{L}{4}\right)\right]^2}$$

where,

P_1 & P_2=Power of IR pump beams, P_3=Power of the generated wave (THz), $d_{eff} = \left(\frac{2}{m\pi}\right) \cdot d_{33}$ (Nonlinear optical coefficients), L=Length of the crystal, ε_0=Permittivity of free space, c=velocity of light, n_1 & n_2=RI for the IR pump beams, n_3=RI of the generated difference frequency (THz), λ_3=Wavelength of the generated wave (THz), $A=\pi r^2$=Area of the pump beams, α_1 & α_2= Absorbance of IR pump beams, α_3=Absorbance of generated wave (THz), ΔK=Difference in wave vector $(K_3+K_2-K_1)$, m=Order of the grating, Λ=Period of the grating.

For the first order grating, and by using the following values, the power of the generated difference frequency (at 140 GHz) is estimated and is shown in Fig.6.20.

Values: d_{33}=25 pm/V and d_{eff}=(2/π)d_{33}, r=100 µm and A=πr^2, P_1=P_2=15 Watts, n_1=2.1448, n_2=2.1447, n_3=5.1, α_1=1 m^{-1}, α_2=1 m^{-1}, α_3=200 m^{-1}.
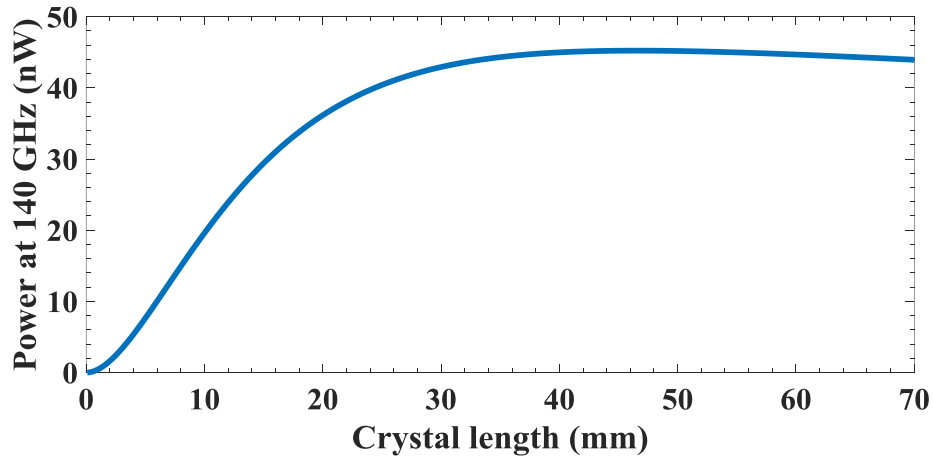
Figure 6.20: Simulation for the generation of 140 GHz in a MgO:PPLN for the CW input power of 30 Watts

From the theoretical analysis for the DFG at 140 GHz, we observe that a maximum power of only 45 nW can be generated. Also, the thermal effect due to high pump power is not considered in this simulation. Therefore, the MgO:PPLN is not ideal for the generation of high power THz waves using CW pump lasers. On the other hand, a non-linear media with high nonlinearity and low absorption loss can be considered for the study. The recent studies show that, the pulsed THz waves can be generated using flowing metallic liquids [348]. The similar method can be investigated for the generation of CW THz radiation.

6.6.2 THz generation using CW photomixers

For telecommunication applications, the CW THz photomixer is generally fabricated using two types: PIN photodiode and uni-travelling carrier photodiode (UTC-PD) [31]. In PIN photodiode, both electrons and holes contribute to the photocurrent, which, in turn, determines the maximal cut-off frequency. In UTC-PD, only the fast-moving electrons contribute to the photocurrent and hence both high power and broad frequency range can be achieved. Recently plasmonic 2D nano antennas-based THz photomixers operating at the pump wavelength of 1.5 µm is also demonstrated [349, 350]. The plasmonic photomixers can generate higher output powers if the duty cycle of the pump laser beams is modulated. However, it is a challenge to use this approach for THz communications as the radiation must be continuous and optical modulation must be carried out to encoded data only. In the following, the photomixer design considerations using arrayed antenna structures for the CW optical pump power of 30 Watts is proposed and discussed.

For the pump wavelength of 1.5 µm (optical telecom band), the suitable bandgap material is Indium Gallium Arsenide (InGaAs). However, the InGaAs semiconductor is highly conductive and possess low resistance. This leads to higher dark current. Also, the trapping of generated photo carriers is poor while using unintentionally-doped intrinsic InGaAs [351]. The carrier lifetime of the emitter antenna must be much lower when it is used for the CW THz emission. Therefore, additional care must be taken to reduce the carrier lifetime. In the array antenna design, alternating layers should be blocked to avoid the destructive interference as well as the propagation of THz radiation in the opposite direction [352].

Alternatively, injection of Erbium Arsenide semi-metal in the intrinsic InGaAs improves the carrier trapping efficiency [353]. Similarly, fabrication of the photomixer with alternating layers of

InGaAs and InAlAs was proposed for high power THz generation [352, 354]. Therefore, either ErAs:InGaAs on InP substrate or alternating layers of InGaAs and InAlAs on InP substrate can be used for fabricating the antenna array.

Generally, Si_3N_4 is used as both the passivation layer and antireflection coating. However, while using Si_3N_4 on top of InGaAs, the resistance of the photomixer decreases at least for a factor of 2 [355]. Though, the Si_3N_4 layer improves the resistivity for GaAs, it does not function the same way for InGaAs.

Applying the bias voltage to the emitter depends on the gap size between the electrodes. For large gap size, higher bias voltage must be applied. The higher bias voltage leads to thermal breakdown due to increased joule heating. Therefore, an optimum gap size of 7 µm to 10 µm is recommended for InGaAs photomixers [352]. For the gap size of 9 µm and the electric field of 15 KV/cm, the bias voltage can be 14V.

Next, the spot size is estimated for high pump power. In InGaAs photomixers, the spot size where the output THz power is saturated (not the damage threshold) is 100 µm for 80 mW input power[355]. The power density is ~10 MW/m^2. Therefore, by linear scaling, for the pump power of 30 W, the spot size must be ~2 mm.
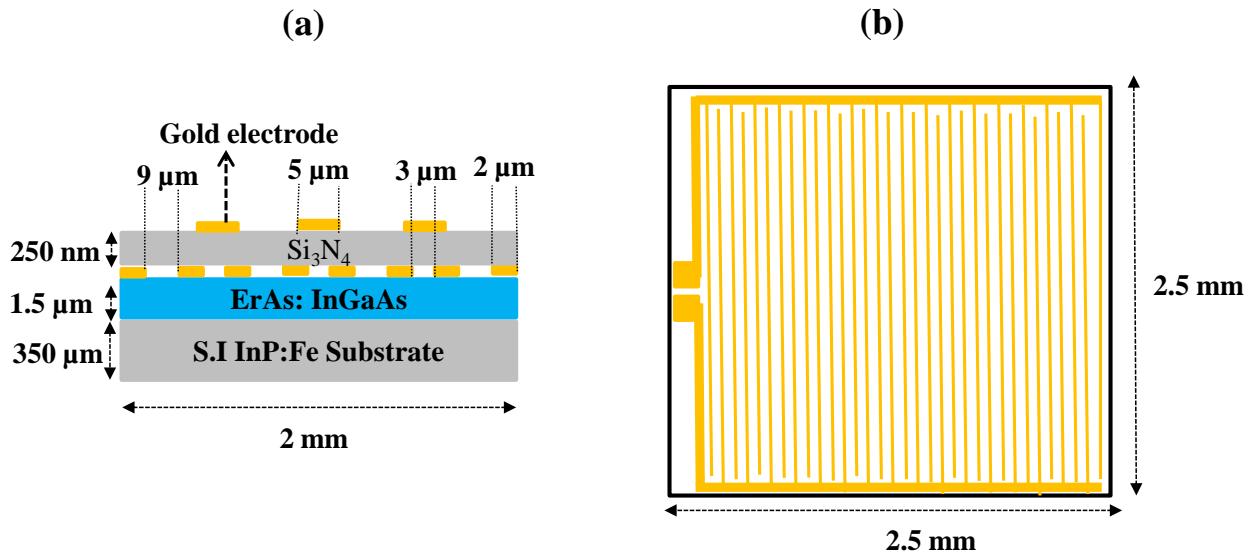
Figure 6.21: Schematic of the large area arrayed THz photomixer design (a) Side view (b) Top view. In top view, the additional metallization layer is not shown

In Fig.6.21, the schematic of a simple design of an arrayed photomixer with just two layers of the semiconductor is proposed. The semi-insulating InP:Fe and ErAs: $In_{0.53}Ga_{0.47}As$ is the substrate layer and active layer, respectively. The concentration of ErAs must be optimized to improve the resistivity and at the same time without affecting the mobility of the carriers. However, the effect of capacitance must be studied as mentioned in the literature before fabrication of the proposed design [356].

To conclude, in this chapter, we have shown the design and the challenges in the fabrication of passive THz components, such as the wire-grid polarizer, OAM phase plates, that is used for the THz communication applications. The experimental design and the challenges in demonstrating the channel multiplexing is presented. The fabricated passive components can be used in the proposed set up (see Fig.6.17) for channel multiplexing and the detailed characterization will be carried out in the future studies. Next, the optimization of suspended core dielectric subwavelength THz fiber is discussed. Here, we proposed two 3D printing approaches and the preliminary experimental characterization results were presented. Finally, the feasibility studies on the generation of CW high-power THz waves using nonlinear crystals has been carried out a novel photomixer design is proposed for the same.

CHAPTER 7   CONCLUSION AND PERSPECTIVES

In this thesis work, we have presented the development of photonics-based THz communication systems using all commercially available components and demonstrated the live streaming of uncompressed HD and 4K videos. Then we presented the motivation of using fiber-based THz communications and showed that the THz fibers can be used to increase the reliability of THz wireless communication links. Finally, the experimental procedure and challenges in the fabrication of novel THz components/devices for THz communication applications are discussed. In this chapter, the summary of this thesis and concluding remarks are presented.

Firstly, a detailed literature review covers the advantages of photonics-based THz communication system and the motivation for using THz fibers to increase the reliability of THz wireless links. Following that, we presented the assembling of CW THz spectroscopy system, which is the basis for building the high-performance THz communication system. Moreover, the spectroscopy system is used to characterize the THz fibers. The amplitude and phase measurements from the frequency range of 100 GHz to 1.2 THz was presented. The higher frequency resolution of the CW THz spectroscopy system is demonstrated from the presence of strong and clear water vapor absorption dips. Then, as an example, the characterization of the material properties was carried out by measuring the refractive index and transmission of Teflon, which will be useful while measuring the THz waveguides. Next, the CW THz spectroscopy system is modified to characterize the waveguides of varying lengths. In this configuration, the path length of free space THz waves is larger; and, therefore, it is compensated by adding a patch cord of appropriate length in the receiver section. Then the spot size of the THz beam at the focal point was measured and compared it with theoretical calculation, which agrees well. Finally, the spectroscopic measurement of a metallic tube waveguide was carried out to show the cut-off frequency of the fundamental mode and the smooth transition of the phase with increase in the frequency. We then concluded that the high-resolution CW THz spectroscopy system is an ideal choice for characterizing the waveguides and other THz passive components.

Secondly, in chapter 4, the development of photonics-based communication system, using all commercial components, were detailed. This was realized by modifying the CW THz spectroscopy system with additional communications devices such as modulator, Schottky detector, LNA, and

test equipment. The characterization of the transmitter, detector, choice of carrier frequency, and NRZ modulation parameters are presented. Next, the performance of the system is characterized by measuring the BER as a function of THz power, link distance, and angular deviation of the receiver antenna. We showed that an error-free transmission up to the bitrate of 5.5 Gbps was achieved for the link distance of 1 m. Since uncompressed high-resolution video transmission will be one of the immediate applications of THz communications, the same is demonstrated using our system. The different configurations for the integration of 4K camera with the transmitter and the recording/display unit with the receiver was proposed and detailed. The link quality for the uncompressed video transmission is then analyzed by measuring the black frames as a function of link distance. It is concluded that the number of black frames was higher for uncompressed 4K videos due to high bit errors for higher bitrates. However, the developed THz communication system with minor modifications can be used to characterize various THz passive components, modulation algorithms, channel modelling, etc.

Thirdly, in chapter 5, the necessity of THz fibers for increasing the reliability of THz wireless links were presented in detail. As an example, the application of THz fibers in vehicular communications was described. Several designs of THz fibers, with their advantages and challenges, were detailed. For the demonstration of fiber-based THz communication, a simple, yet reliable, solid core dielectric fiber of different thickness was chosen for the study. For the rod-in-air fibers, several parameters such as modal index, excitation efficiency, dispersion, maximal bitrate, field extension, etc., were studied in detail. Since the modal field extends deep into the air cladding, a rod-in-foam fiber was proposed instead, for practical handling and manipulations. The THz communication link using the proposed rod-in-air fiber of length up to 10 meters at the carrier frequency of 128 GHz was carried out and the error free bitrate up to 4 Gbps was achieved. It was also shown that depending on the thickness of the fiber, the dispersion differs and limits the maximal bitrate that can be transmitted. Finally, the performance of rod-in-air dielectric fibers were compared with the free-space THz communication link and concluded that the fiber-based links are better for short-range communication links in terms of received power whereas the free space THz communication outperforms the fiber links in terms of maximum achieved bitrate.

Finally, we detailed the challenges in the design and fabrication of passive THz components such as wire-grid-polarizer, phase plates for OAM generation and subwavelength Teflon fiber for

communication applications. The schematic of the experimental set up for various multiplexing modalities were shown. Then various THz fiber holding methods were discussed and the practical design of suspended core THz fiber, optimized for the carrier frequency of 128 GHz was briefly discussed. As we showed in the earlier chapters, the THz power determines the maximal link distance. We then study here, the feasibility of the generation of high-power CW THz waves for communication applications using MgO:PPLN nonlinear crystal. It is concluded that, we need to look for a high nonlinear material with low absorption in the THz spectral range. Finally, a novel photomixer design for high-power THz generation is proposed, which requires further theoretical analysis before proceeding towards fabrication.

7.1   Future works

In this last section, we propose some of the future works that can be carried out using the developed THz communication system.

In this thesis work, the performance of the photonics-based THz communication system up to the bitrates of 6 Gbps was demonstrated using the single channel NRZ signal generator (supports up to 12.5 Gbps) and 3 GHz bandwidth LNA at the receiver. The capability of the system can be improved to the maximum available bitrate (up to 12.5 Gbps in a single channel) by using a high-gain and broadband digital LNA as discussed in chapter 6. A second channel can be added to the all-in-one test equipment (ANRITSU-MP2100B) to reach the bitrates up to 25 Gbps, which will be good enough for the next couple of years to work with the carrier frequencies below 200 GHz. Further, several higher order multiplexing schemes such as SDM, FDM, etc., can be studied by modifying the assembled THz communication system. In particular, the THz channel modelling for different SDM techniques that uses MIMO, OAM etc., can be investigated. Next, the generation of high-power CW THz waves using photonics technologies remains challenging and limits the maximum link distance at higher THz frequencies (>300 GHz). In the case of nonlinear crystals, we need to look for the material with high nonlinearity and low absorption loss in the THz spectral range. An efficient phase matching technique in such cases can improve the optical to THz conversion efficiency, particularly at higher THz frequencies. Similarly, a novel photomixer design using semiconductors with plasmonic electrodes can be studied for high-power CW THz generation.

On the other hand, the fiber-based THz communications and the fabrication of associated components/devices are getting attention. As we have demonstrated, a simple rod-in-air dielectric fibers can be used for the communication link up to 10 meters, with a bitrate of ~4 Gbps. Similarly, a practical suspended core fiber or other novel designs, on the other hand, can be proposed for even longer link distances and higher bitrates. Similar to the THz wireless communications, the SDM techniques using THz fibers/waveguides can be investigated. One of the challenges in the efficient THz fiber communication link is the design and fabrication of an efficient fiber connector/holder. Therefore, an optimal and a standard connector that is compatible with source/detector and various test equipment can be designed. Moreover, the fiber/waveguide-based, real-time signal processing elements such as bandpass filters, multiplexers/de-multiplexers, Bragg gratings, etc., can be designed and realized using advanced fabrication techniques such as 3D printing and characterized using the THz communication system. Therefore, a compact all fiber/waveguide devices can be a game changer in the next generation THz communications.

REFERENCES

[1] S. Cherry, "Edholm's law of bandwidth," *IEEE Spectrum,* vol. 41, no. 7, pp. 58-60, 2004.

[2] C. E. J. B. s. t. j. Shannon, "A mathematical theory of communication," vol. 27, no. 3, pp. 379-423, 1948.

[3] J. M. Kahn and K.-P. J. I. J. o. s. t. i. q. e. Ho, "Spectral efficiency limits and modulation/detection techniques for DWDM systems," vol. 10, no. 2, pp. 259-272, 2004.

[4] A. Malik and P. Singh, "Free space optics: current applications and future challenges," *International Journal of Optics,* vol. 2015, 2015.

[5] A. K. Majumdar, *Advanced free space optics (FSO): A systems approach*. Springer, 2014.

[6] P. H. Pathak, X. Feng, P. Hu, and P. Mohapatra, "Visible light communication, networking, and sensing: A survey, potential and challenges," *IEEE communications surveys & tutorials,* vol. 17, no. 4, pp. 2047-2077, 2015.

[7] S. U. Rehman, S. Ullah, P. H. J. Chong, S. Yongchareon, and D. Komosny, "Visible light communication: a system perspective—overview and challenges," *Sensors,* vol. 19, no. 5, p. 1153, 2019.

[8] S. Chaudhary and A. Amphawan, "The role and challenges of free-space optical systems," *Journal of Optical Communications,* vol. 35, no. 4, pp. 327-334, 2014.

[9] H. Elayan, O. Amin, R. M. Shubair, and M.-S. Alouini, "Terahertz communication: The opportunities of wireless technology beyond 5G," in *2018 International Conference on Advanced Communication Technologies and Networking (CommNet)*, 2018: IEEE, pp. 1-5.

[10] J. F. Federici, J. Ma, and L. Moeller, "Review of weather impact on outdoor terahertz wireless communication links," *Nano Communication Networks,* vol. 10, pp. 13-26, 2016.

[11] I. F. Akyildiz, J. M. Jornet, and C. Han, "Terahertz band: Next frontier for wireless communications," *Physical Communication,* vol. 12, pp. 16-32, 2014.

[12] H. Elayan, O. Amin, B. Shihada, R. M. Shubair, and M.-S. Alouini, "Terahertz band: The last piece of RF spectrum puzzle for communication systems," *IEEE Open Journal of the Communications Society,* vol. 1, pp. 1-32, 2019.

[13] R. A. Lewis, "A review of terahertz sources," *Journal of Physics D: Applied Physics,* vol. 47, no. 37, p. 374001, 2014.

[14] Q.-L. Liu, Z.-C. Wang, P.-K. Liu, C.-H. Du, H.-Q. Li, and A.-Y. Xu, "A THz backward-wave oscillator based on a double-grating rectangular waveguide," *IEEE Transactions on electron devices,* vol. 60, no. 4, pp. 1463-1468, 2013.

[15] W. Liu, Y. Lu, L. Wang, and Q. Jia, "A compact terahertz free-electron laser with two gratings driven by two electron-beams," *Physics of Plasmas,* vol. 24, no. 2, p. 023109, 2017.

[16] C. Evain *et al.*, "Stable coherent terahertz synchrotron radiation from controlled relativistic electron bunches," *Nature Physics,* vol. 15, no. 7, pp. 635-639, 2019.

[17] K. Tekbıyık, A. R. Ekti, G. K. Kurt, and A. Görçin, "Terahertz band communication systems: Challenges, novelties and standardization efforts," *Physical Communication,* vol. 35, p. 100700, 2019.

[18] N. Oshima, K. Hashimoto, S. Suzuki, and M. Asada, "Terahertz wireless data transmission with frequency and polarization division multiplexing using resonant-tunneling-diode

oscillators," *IEEE Transactions on Terahertz science and Technology,* vol. 7, no. 5, pp. 593-598, 2017.

[19]   A. Ali, J. Yun, M. Kucharski, H. J. Ng, D. Kissinger, and P. Colantonio, "220-360-GHz Broadband Frequency Multiplier Chains (x8) in 130-nm BiCMOS Technology," *IEEE Transactions on Microwave Theory and Techniques,* 2020.

[20]   T. Nagatsuma, G. Ducournau, and C. C. Renaud, "Advances in terahertz communications accelerated by photonics," *Nature Photonics,* vol. 10, no. 6, pp. 371-379, 2016.

[21]   T. Kawanishi, "THz and photonic seamless communications," *Journal of Lightwave Technology,* vol. 37, no. 7, pp. 1671-1679, 2019.

[22]   K. Sengupta, T. Nagatsuma, and D. M. Mittleman, "Terahertz integrated electronic and hybrid electronic–photonic systems," *Nature Electronics,* vol. 1, no. 12, pp. 622-635, 2018.

[23]   J. Ma *et al.*, "Security and eavesdropping in terahertz wireless links," *Nature,* vol. 563, no. 7729, pp. 89-93, 2018.

[24]   K. Nallappan, H. Guerboukha, C. Nerguizian, and M. Skorobogatiy, "Live Streaming of Uncompressed HD and 4K Videos Using Terahertz Wireless Links," *IEEE Access,* vol. 6, pp. 58030-58042, 2018.

[25]   H. Shams, M. J. Fice, K. Balakier, C. C. Renaud, A. J. Seeds, and F. van Dijk, "Multichannel 200GHz 40Gb/s wireless communication system using photonic signal generation," in *Microwave Photonics (MWP) and the 2014 9th Asia-Pacific Microwave Photonics Conference (APMP) 2014 International Topical Meeting on*, 2014: IEEE, pp. 366-369.

[26]   L. Yi *et al.*, "300-GHz-band wireless communication using a low phase noise photonic source," in *2019 49th European Microwave Conference (EuMC)*, 2019: IEEE, pp. 816-819.

[27]   M. Tang, H. Minamide, Y. Wang, T. Notake, S. Ohno, and H. Ito, "Tunable terahertz-wave generation from DAST crystal pumped by a monolithic dual-wavelength fiber laser," *Optics express,* vol. 19, no. 2, pp. 779-786, 2011.

[28]   Y. V. Grachev *et al.*, "Wireless data transmission method using pulsed thz sliced spectral supercontinuum," *IEEE Photonics Technology Letters,* vol. 30, no. 1, pp. 103-106, 2017.

[29]   D. Stanze, A. Deninger, A. Roggenbuck, S. Schindler, M. Schlak, and B. Sartorius, "Compact cw Terahertz Spectrometer Pumped at 1.5 μm Wavelength," *Journal of Infrared, Millimeter, and Terahertz Waves,* vol. 32, no. 2, pp. 225-232, 2011/02/01 2011, doi: 10.1007/s10762-010-9751-8.

[30]   G. Forecast, "Cisco visual networking index: Global mobile data traffic forecast update 2017–2022," *Update,* vol. 2017, p. 2022, 2019.

[31]   S. Nellen *et al.*, "Experimental Comparison of UTC-and PIN-Photodiodes for Continuous-Wave Terahertz Generation," *Journal of Infrared, Millimeter, and Terahertz Waves,* pp. 1-12, 2019.

[32]   K. NALLAPPAN, Y. CAO, G. XU, H. GUERBOUKHA, C. NERGUIZIAN, and M. SKOROBOGATIY, "Dispersion limited versus power limited terahertz communication links using solid core subwavelength dielectric fibers."

[33]   K. Nallapan, R. Morandotti, and M. Skorobogatiy, "Feasibility Study for the Generation of High Power Continuous Wave Terahertz Radiation using Frequency Difference Generation," *arXiv preprint arXiv:1711.07830,* 2017.

[34] J. Ma, L. Moeller, and J. F. Federici, "Experimental comparison of terahertz and infrared signaling in controlled atmospheric turbulence," *Journal of Infrared, Millimeter, and Terahertz Waves,* vol. 36, no. 2, pp. 130-143, 2015.

[35] J. Ma, F. Vorrius, L. Lamb, L. Moeller, and J. F. Federici, "Experimental comparison of terahertz and infrared signaling in laboratory-controlled rain," *Journal of Infrared, Millimeter, and Terahertz Waves,* vol. 36, no. 9, pp. 856-865, 2015.

[36] M. R. Biswal, S. Arya, and Y. H. Chung, "Effect of turbulence and noise on ultraviolet and mid-infrared spectrum in optical wireless communications," *Photonic Network Communications,* pp. 1-6, 2020.

[37] M. A. A. Ali and A. Ali, "Atmospheric turbulence effect on free space optical communications," *International Journal of Emerging Technologies in Computational and Applied Sciences,* vol. 5, no. 4, pp. 345-351, 2013.

[38] S.-R. Moon *et al.*, "Demonstration of photonics-aided terahertz wireless transmission system with using silicon photonics circuit," *Optics Express,* vol. 28, no. 16, pp. 23397-23408, 2020.

[39] K.-C. Huang and Z. J. I. M. M. Wang, "Terahertz terabit wireless communication," vol. 12, no. 4, pp. 108-116, 2011.

[40] H.-J. Song and T. Nagatsuma, "Present and future of terahertz communications," *IEEE transactions on terahertz science and technology,* vol. 1, no. 1, pp. 256-263, 2011.

[41] T. Kleine-Ostmann, T. J. J. o. I. Nagatsuma, Millimeter,, and T. Waves, "A review on terahertz communications research," vol. 32, no. 2, pp. 143-171, 2011.

[42] Z. Chen *et al.*, "A survey on terahertz communications," *China Communications,* vol. 16, no. 2, pp. 1-35, 2019.

[43] M. H. Alsharif, A. H. Kelechi, M. A. Albreem, S. A. Chaudhry, M. S. Zia, and S. Kim, "Sixth Generation (6G) Wireless Networks: Vision, Research Activities, Challenges and Potential Solutions," *Symmetry,* vol. 12, no. 4, p. 676, 2020.

[44] I. F. Akyildiz, A. Kak, and S. Nie, "6G and beyond: The future of wireless communications systems," *IEEE Access,* vol. 8, pp. 133995-134030, 2020.

[45] J. Federici and L. Moeller, "Review of terahertz and subterahertz wireless communications," *Journal of Applied Physics,* vol. 107, no. 11, p. 6, 2010.

[46] J. Hesler, R. Prasankumar, and J. Tignon, "Advances in terahertz solid-state physics and devices," ed: AIP Publishing LLC, 2019.

[47] K. Kenneth *et al.*, "Opening terahertz for everyday applications," *IEEE Communications Magazine,* vol. 57, no. 8, pp. 70-76, 2019.

[48]   J. Hacker *et al.*, "THz MMICs based on InP HBT technology," in *2010 IEEE MTT-S International Microwave Symposium*, 2010: IEEE, pp. 1126-1129.

[49] M. Urteaga, Z. Griffith, M. Seo, J. Hacker, and M. J. Rodwell, "InP HBT technologies for THz integrated circuits," *Proceedings of the IEEE,* vol. 105, no. 6, pp. 1051-1067, 2017.

[50] P. Sen, D. A. Pados, S. N. Batalama, E. Einarsson, J. P. Bird, and J. M. Jornet, "The TeraNova platform: An integrated testbed for ultra-broadband wireless communications at true Terahertz frequencies," *Computer Networks,* vol. 179, p. 107370, 2020.

[51] X. Mei *et al.*, "First demonstration of amplification at 1 THz using 25-nm InP high electron mobility transistor process," *IEEE Electron Device Letters,* vol. 36, no. 4, pp. 327-329, 2015.

[52] A. Maestrini *et al.*, "Schottky diode-based terahertz frequency multipliers and mixers," *Comptes Rendus Physique,* vol. 11, no. 7-8, pp. 480-495, 2010.

[53] A. Maestrini, J. Ward, G. Chattopadhyay, E. Schlecht, and I. Mehdi, "Terahertz sources based on frequency multiplication and their applications," *Frequenz,* vol. 62, no. 5-6, pp. 118-122, 2008.

[54] R. Han and E. Afshari, "A high-power broadband passive terahertz frequency doubler in CMOS," *IEEE transactions on microwave theory and techniques,* vol. 61, no. 3, pp. 1150-1160, 2013.

[55] Z. Ahmad, I. Kim, and K. Kenneth, "0.39–0.45 THz symmetric MOS-varactor frequency tripler in 65-nm CMOS," in *2015 IEEE Radio Frequency Integrated Circuits Symposium (RFIC)*, 2015: IEEE, pp. 275-278.

[56] Q. Xiao, Y. Duan, J. L. Hesler, T. W. Crowe, and R. M. Weikle, "A 5 mW and 5% efficiency 210 GHz InP-based heterostructure barrier varactor quintupler," *IEEE microwave and wireless components letters,* vol. 14, no. 4, pp. 159-161, 2004.

[57] S. Kang, S. V. Thyagarajan, and A. M. Niknejad, "A 240 GHz fully integrated wideband QPSK transmitter in 65 nm CMOS," *IEEE Journal of Solid-State Circuits,* vol. 50, no. 10, pp. 2256-2267, 2015.

[58] Y. Wang, B. Yu, Y. Ye, C.-N. Chen, Q. J. Gu, and H. Wang, "A G-Band on-off-Keying Low-Power Transmitter and Receiver for Interconnect Systems in 65-nm CMOS," *IEEE Transactions on Terahertz Science and Technology,* vol. 10, no. 2, pp. 118-132, 2019.

[59] C. Jastrow *et al.*, "Wireless digital data transmission at 300 GHz," *Electronics Letters,* vol. 46, no. 9, pp. 661-663, 2010.

[60] C. Wang *et al.*, "0.34-THz wireless link based on high-order modulation for future wireless local area network applications," *IEEE Transactions on Terahertz Science and Technology,* vol. 4, no. 1, pp. 75-85, 2014.

[61] H.-J. Song, J.-Y. Kim, K. Ajito, N. Kukutsu, and M. Yaita, "50-Gb/s direct conversion QPSK modulator and demodulator MMICs for terahertz communications at 300 GHz," *IEEE Transactions on Microwave Theory and Techniques,* vol. 62, no. 3, pp. 600-609, 2014.

[62] I. Kallfass *et al.*, "64 Gbit/s transmission over 850 m fixed wireless link at 240 GHz carrier frequency," *Journal of Infrared, millimeter, and terahertz waves,* vol. 36, no. 2, pp. 221-233, 2015.

[63] K. Katayama *et al.*, "20.1 A 300GHz 40nm CMOS transmitter with 32-QAM 17.5 Gb/s/ch capability over 6 channels," in *2016 IEEE International Solid-State Circuits Conference (ISSCC)*, 2016: IEEE, pp. 342-343.

[64] J. P. Sun, G. I. Haddad, P. Mazumder, and J. N. Schulman, "Resonant tunneling diodes: Models and properties," *Proceedings of the IEEE,* vol. 86, no. 4, pp. 641-660, 1998.

[65] E. Brown, J. Söderström, C. Parker, L. Mahoney, K. Molvar, and T. McGill, "Oscillations up to 712 GHz in InAs/AlSb resonant-tunneling diodes," *Applied Physics Letters,* vol. 58, no. 20, pp. 2291-2293, 1991.

[66] E. Brown, T. Sollner, C. Parker, W. Goodhue, and C. Chen, "Oscillations up to 420 GHz in GaAs/AlAs resonant tunneling diodes," *Applied Physics Letters,* vol. 55, no. 17, pp. 1777-1779, 1989.

[67] M. Asada, S. Suzuki, and N. Kishimoto, "Resonant tunneling diodes for sub-terahertz and terahertz oscillators," *Japanese Journal of Applied Physics,* vol. 47, no. 6R, p. 4375, 2008.

[68]   S. Suzuki, M. Asada, A. Teranishi, H. Sugiyama, and H. Yokoyama, "Fundamental oscillation of resonant tunneling diodes above 1 THz at room temperature," *Applied Physics Letters,* vol. 97, no. 24, p. 242102, 2010.

[69]   M. Asada and S. Suzuki, "Room-temperature oscillation of resonant tunneling diodes close to 2 THz and their functions for various applications," *Journal of Infrared, Millimeter, and Terahertz Waves,* vol. 37, no. 12, pp. 1185-1198, 2016.

[70]   T. Maekawa, H. Kanaya, S. Suzuki, and M. Asada, "Oscillation up to 1.92 THz in resonant tunneling diode by reduced conduction loss," *Applied Physics Express,* vol. 9, no. 2, p. 024101, 2016.

[71]   A. Al-Khalidi *et al.*, "Resonant Tunneling Diode Terahertz Sources With up to 1 mW Output Power in the J-Band," *IEEE Transactions on Terahertz Science and Technology,* vol. 10, no. 2, pp. 150-157, 2019.

[72]   N. Oshima, K. Hashimoto, D. Horikawa, S. Suzuki, and M. Asada, "Wireless data transmission of 30 Gbps at a 500-GHz range using resonant-tunneling-diode terahertz oscillator," in *2016 IEEE MTT-S International Microwave Symposium (IMS)*, 2016: IEEE, pp. 1-4.

[73]   X. Yu, R. Yamada, J.-Y. Kim, M. Fujita, and T. Nagatsuma, "Integrated circuits using photonic-crystal slab waveguides and resonant tunneling diodes for terahertz communication," in *2018 Progress in Electromagnetics Research Symposium (PIERS-Toyama)*, 2018: IEEE, pp. 599-605.

[74]   S. Diebold, K. Tsuruda, J.-Y. Kim, T. Mukai, M. Fujita, and T. Nagatsuma, "A terahertz monolithic integrated resonant tunneling diode oscillator and mixer circuit," in *Terahertz Physics, Devices, and Systems X: Advanced Applications in Industry and Defense*, 2016, vol. 9856: International Society for Optics and Photonics, p. 98560U.

[75]   J. Webber, N. Nishigami, J.-Y. Kim, M. Fujita, and T. Nagatsuma, "Terahertz Wireless CDMA Communication Using Resonant Tunneling Diodes," in *2019 IEEE Globecom Workshops (GC Wkshps)*, 2019: IEEE, pp. 1-6.

[76]   N. Nishigami, Y. Nishida, S. Diebold, J. Kim, M. Fujita, and T. Nagatsuma, "Resonant tunneling diode receiver for coherent terahertz wireless communication," in *2018 Asia-Pacific Microwave Conference (APMC)*, 2018: IEEE, pp. 726-728.

[77]   S. Diebold *et al.*, "High-speed error-free wireless data transmission using a terahertz resonant tunnelling diode transmitter and receiver," *Electronics Letters,* vol. 52, no. 24, pp. 1999-2001, 2016.

[78]   H.-W. Hubers, "Terahertz heterodyne receivers," *IEEE journal of selected topics in quantum electronics,* vol. 14, no. 2, pp. 378-391, 2008.

[79]   R. Han, Y. Zhang, D. Coquillat, H. Videlier, W. Knap, and E. Brown, "A 280-GHz Schottky diode detector in 130-nm digital CMOS," *IEEE Journal of Solid-State Circuits,* vol. 46, no. 11, pp. 2602-2612, 2011.

[80]   M. Ali, R. C. Guzman, A. Rivera-Lavado, O. Cojocari, L. E. Garcia-Mufioz, and G. Carpintero, "Quasi-optical schottky barrier diode detector for mmWave/sub-THz wireless communication," in *2018 25th International Conference on Telecommunications (ICT)*, 2018: IEEE, pp. 279-282.

[81]   J. L. Hesler, L. Liu, H. Xu, Y. Duan, and R. M. Weikle, "The development of quasi-optical THz detectors," in *2008 33rd International Conference on Infrared, Millimeter and Terahertz Waves*, 2008: IEEE, pp. 1-2.

[82] J. L. Hesler and T. W. Crowe, "Responsivity and noise measurements of zero-bias Schottky diode detectors," *Proc. ISSTT,* pp. 89-92, 2007.

[83] S. Blin, P. Nouvel, A. Pénarier, and J. Hesler, "Terahertz heterodyne communication using GaAs field-effect transistor receiver," *IEEE Electron Device Letters,* vol. 38, no. 1, pp. 20-23, 2016.

[84] T. Kleine-Ostmann, K. Pierz, G. Hein, P. Dawson, and M. Koch, "Audio signal transmission over THz communication channel using semiconductor modulator," *Electronics Letters,* vol. 40, no. 2, pp. 124-126, 2004.

[85] T. Nagatsuma *et al.*, "Terahertz wireless communications based on photonics technologies," *Optics Express,* vol. 21, no. 20, pp. 23736-23747, 2013.

[86] T. Nagatsuma and G. Carpintero, "Recent progress and future prospect of photonics-enabled terahertz communications research," *IEICE Transactions on Electronics,* vol. 98, no. 12, pp. 1060-1070, 2015.

[87] H. Shams and A. Seeds, "Photonics, Fiber and THz Wireless Communication," *Optics and Photonics News,* vol. 28, no. 3, pp. 24-31, 2017.

[88] H. Guerboukha, K. Nallappan, and M. Skorobogatiy, "Toward real-time terahertz imaging," *Advances in Optics and Photonics,* vol. 10, no. 4, pp. 843-938, 2018.

[89] W. Shi and Y. J. Ding, "Continuously tunable and coherent terahertz radiation by means of phase-matched difference-frequency generation in zinc germanium phosphide," *Applied physics letters,* vol. 83, no. 5, pp. 848-850, 2003.

[90] P. Liu *et al.*, "Widely tunable and monochromatic terahertz difference frequency generation with organic crystal 2-(3-(4-hydroxystyryl)-5, 5-dime-thylcyclohex-2-enylidene) malononitrile," *Applied Physics Letters,* vol. 108, no. 1, p. 011104, 2016.

[91] D. Mittleman, *Sensing with terahertz radiation*. Springer, 2013.

[92] Y. J. Ding, "Progress in terahertz sources based on difference-frequency generation," *JOSA B,* vol. 31, no. 11, pp. 2696-2711, 2014.

[93] R. Köhler *et al.*, "Terahertz semiconductor-heterostructure laser," *Nature,* vol. 417, no. 6885, pp. 156-159, 2002.

[94] B. S. Williams, "Terahertz quantum cascade lasers," in *Asia Optical Fiber Communication and Optoelectronic Exposition and Conference*, 2008: Optical Society of America, p. SuG3.

[95] B. Röben, X. Lü, M. Hempel, K. Biermann, L. Schrottke, and H. T. Grahn, "Terahertz quantum-cascade lasers as high-power and wideband, gapless sources for spectroscopy," *Optics Express,* vol. 25, no. 14, pp. 16282-16290, 2017.

[96] P. Grant, S. Laframboise, R. Dudek, M. Graf, A. Bezinger, and H. Liu, "Terahertz free space communications demonstration with quantum cascade laser and quantum well photodetector," *Electronics letters,* vol. 45, no. 18, pp. 952-954, 2009.

[97] Z. Chen *et al.*, "Wireless communication demonstration at 4.1 THz using quantum cascade laser and quantum well photodetector," *Electronics letters,* vol. 47, no. 17, pp. 1002-1004, 2011.

[98] S. Kindness *et al.*, "External amplitude and frequency modulation of a terahertz quantum cascade laser using metamaterial/graphene devices," *Scientific reports,* vol. 7, no. 1, pp. 1-10, 2017.

[99]   S. Preu, G. Döhler, S. Malzer, L. Wang, and A. Gossard, "Tunable, continuous-wave terahertz photomixer sources and applications," *Journal of Applied Physics,* vol. 109, no. 6, p. 4, 2011.

[100]   R. Safian, G. Ghazi, and N. Mohammadian, "Review of photomixing continuous-wave terahertz systems and current application trends in terahertz domain," *Optical Engineering,* vol. 58, no. 11, p. 110901, 2019.

[101]   S.-H. Yang and M. Jarrahi, "Navigating Terahertz Spectrum via Photomixing," *Optics and Photonics News,* vol. 31, no. 7, pp. 36-43, 2020.

[102]   T. Liu, Y. Huang, Q. Wei, K. Liu, X. Duan, and X. Ren, "Optimized uni-traveling carrier photodiode and mushroom-mesa structure for high-power and sub-terahertz bandwidth under zero-and low-bias operation," *Journal of Physics Communications,* vol. 3, no. 9, p. 095004, 2019.

[103]   M. He *et al.*, "High-performance hybrid silicon and lithium niobate Mach–Zehnder modulators for 100 Gbit s− 1 and beyond," *Nature Photonics,* vol. 13, no. 5, pp. 359-364, 2019.

[104]   H.-J. Song *et al.*, "Terahertz wireless communication link at 300 GHz," in *2010 IEEE International Topical Meeting on Microwave Photonics*, 2010: Ieee, pp. 42-45.

[105]   Z. Lu *et al.*, "26.8 m 350 GHz wireless transmission of beyond 100 Gbit/s supported by THz photonics," in *Asia Communications and Photonics Conference*, 2019: Optical Society of America, p. M4D. 6.

[106]   T. Nagatsuma *et al.*, "Millimeter-wave and terahertz-wave applications enabled by photonics," *IEEE Journal of Quantum Electronics,* vol. 52, no. 1, pp. 1-12, 2015.

[107]   K. Liu *et al.*, "100 Gbit/s THz photonic wireless transmission in the 350-GHz band with extended reach," *IEEE Photonics Technology Letters,* vol. 30, no. 11, pp. 1064-1067, 2018.

[108]   G. Carpintero *et al.*, "Microwave photonic integrated circuits for millimeter-wave wireless communications," *Journal of Lightwave Technology,* vol. 32, no. 20, pp. 3495-3501, 2014.

[109]   N. Kim *et al.*, "Distributed feedback laser diode integrated with distributed Bragg reflector for continuous-wave terahertz generation," *Optics express,* vol. 20, no. 16, pp. 17496-17502, 2012.

[110]   M. Zanola, M. J. Strain, G. Giuliani, and M. Sorel, "Monolithically integrated DFB lasers for tunable and narrow linewidth millimeter-wave generation," *IEEE Journal of Selected Topics in Quantum Electronics,* vol. 19, no. 4, pp. 1500406-1500406, 2012.

[111]   Q. Deng, J. Xu, L. Guo, S. Liang, L. Hou, and H. Zhu, "A dual-grating InGaAsP/InP DFB laser integrated with an SOA for THz generation," *IEEE Photonics Technology Letters,* vol. 28, no. 21, pp. 2307-2310, 2016.

[112]   Q. Tang *et al.*, "25 Gb/s Directly Modulated Widely Tunable 1.3 μm Dual Wavelength DFB Laser for THz Communication," *IEEE Photonics Technology Letters,* vol. 32, no. 7, pp. 410-413, 2020.

[113]   S. Jia *et al.*, "120 Gb/s multi-channel THz wireless transmission and THz receiver performance analysis," *IEEE Photonics Technology Letters,* vol. 29, no. 3, pp. 310-313, 2017.

[114]   X. Li *et al.*, "120 Gb/s wireless terahertz-wave signal delivery by 375 GHz-500 GHz multi-carrier in a 2× 2 MIMO system," *Journal of Lightwave Technology,* vol. 37, no. 2, pp. 606-611, 2019.

[115] S. Jia *et al.*, "2× 300 Gbit/s Line Rate PS-64QAM-OFDM THz Photonic-Wireless Transmission," *Journal of Lightwave Technology,* 2020.

[116] J. M. Jornet and I. F. Akyildiz, "Channel modeling and capacity analysis for electromagnetic wireless nanonetworks in the terahertz band," *IEEE Transactions on Wireless Communications,* vol. 10, no. 10, pp. 3211-3221, 2011.

[117] I. E. Gordon *et al.*, "The HITRAN2016 molecular spectroscopic database," *Journal of Quantitative Spectroscopy and Radiative Transfer,* vol. 203, pp. 3-69, 2017.

[118] C. Han, A. O. Bicen, and I. F. Akyildiz, "Multi-ray channel modeling and wideband characterization for wireless communications in the terahertz band," *IEEE Transactions on Wireless Communications,* vol. 14, no. 5, pp. 2402-2412, 2014.

[119] K. Guan *et al.*, "Channel characterization for intra-wagon communication at 60 and 300 GHz bands," *IEEE Transactions on Vehicular Technology,* vol. 68, no. 6, pp. 5193-5207, 2019.

[120] S. Priebe, M. Kannicht, M. Jacob, and T. Kürner, "Ultra broadband indoor channel measurements and calibrated ray tracing propagation modeling at THz frequencies," *Journal of Communications and Networks,* vol. 15, no. 6, pp. 547-558, 2013.

[121] F. Sheikh, N. Zarifeh, and T. Kaiser, "Terahertz band: Channel modelling for short-range wireless communications in the spectral windows," *IET Microwaves, Antennas & Propagation,* vol. 10, no. 13, pp. 1435-1444, 2016.

[122] R. Singh and D. Sicker, "An analytical model for efficient indoor THz access point deployment," *arXiv preprint arXiv:2001.11167,* 2020.

[123] A. Moldovan, M. A. Ruder, I. F. Akyildiz, and W. H. Gerstacker, "LOS and NLOS channel modeling for terahertz wireless communication with scattered rays," in *2014 IEEE Globecom Workshops (GC Wkshps)*, 2014: IEEE, pp. 388-392.

[124] X. Ma *et al.*, "Intelligent reflecting surface enhanced indoor terahertz communication systems," *Nano Communication Networks,* vol. 24, p. 100284, 2020.

[125] S. Atakaramians, S. Afshar, T. M. Monro, and D. Abbott, "Terahertz dielectric waveguides," *Advances in Optics and Photonics,* vol. 5, no. 2, pp. 169-215, 2013.

[126] A. Markov, H. Guerboukha, and M. Skorobogatiy, "Hybrid metal wire–dielectric terahertz waveguides: challenges and opportunities," *JOSA B,* vol. 31, no. 11, pp. 2587-2600, 2014.

[127] Y.-S. Jin, G.-J. Kim, and S.-G. Jeon, "Terahertz dielectric properties of polymers," *Journal of the Korean Physical Society,* vol. 49, no. 2, pp. 513-517, 2006.

[128] B. Ung, A. Mazhorova, A. Dupuis, M. Rozé, and M. Skorobogatiy, "Polymer microstructured optical fibers for terahertz wave guiding," *Optics Express,* vol. 19, no. 26, pp. B848-B861, 2011.

[129] G. P. Agrawal, *Lightwave technology: telecommunication systems*. John Wiley & Sons, 2005.

[130] N. Van Thienen, Y. Zhang, M. De Wit, and P. Reynaert, "An 18Gbps polymer microwave fiber (PMF) communication link in 40nm CMOS," in *ESSCIRC Conference 2016: 42nd European Solid-State Circuits Conference*, 2016: IEEE, pp. 483-486.

[131] G. Apollinari, D. Scepanovic, and S. White, "Plastic optical fiber splicing by thermal fusion," *Nuclear Instruments and Methods in Physics Research Section A: Accelerators, Spectrometers, Detectors and Associated Equipment,* vol. 311, no. 3, pp. 520-528, 1992.

[132] Y. Mizuno, S. Ohara, N. Hayashi, and K. Nakamura, "Ultrasonic splicing of polymer optical fibres," *Electronics Letters,* vol. 50, no. 19, pp. 1384-1386, 2014.

[133] K. Wang and D. M. Mittleman, "Metal wires for terahertz wave guiding," *Nature,* vol. 432, no. 7015, pp. 376-379, 2004.

[134] J. A. Deibel, K. Wang, M. D. Escarra, and D. M. Mittleman, "Enhanced coupling of terahertz radiation to cylindrical wire waveguides," *Optics express,* vol. 14, no. 1, pp. 279-290, 2006.

[135] T.-I. Jeon, J. Zhang, and D. Grischkowsky, "THz Sommerfeld wave propagation on a single metal wire," *Applied Physics Letters,* vol. 86, no. 16, p. 161904, 2005.

[136] T. Akalin, A. Treizebré, and B. Bocquet, "Single-wire transmission lines at terahertz frequencies," *IEEE Transactions on Microwave Theory and Techniques,* vol. 54, no. 6, pp. 2762-2767, 2006.

[137] S. Galli, J. Liu, and G. Zhang, "Bare Metal Wires as Open Waveguides, with Applications to 5G," in *2018 IEEE International Conference on Communications (ICC)*, 2018: IEEE, pp. 1-6.

[138] A. Markov and M. Skorobogatiy, "Two-wire terahertz fibers with porous dielectric support," *Optics Express,* vol. 21, no. 10, pp. 12728-12743, 2013.

[139] M. Mbonye, R. Mendis, and D. M. Mittleman, "A terahertz two-wire waveguide with low bending loss," *Applied Physics Letters,* vol. 95, no. 23, p. 233506, 2009.

[140] Y. Cao, K. Nallappan, H. Guerboukha, G. Xu, and M. Skorobogatiy, "Additive manufacturing of highly reconfigurable plasmonic circuits for terahertz communications," 2020.

[141] R. Mendis and D. Grischkowsky, "Undistorted guided-wave propagation of subpicosecond terahertz pulses," *Optics letters,* vol. 26, no. 11, pp. 846-848, 2001.

[142] R. Mendis and D. M. Mittleman, "Comparison of the lowest-order transverse-electric (TE 1) and transverse-magnetic (TEM) modes of the parallel-plate waveguide for terahertz pulse applications," *Optics express,* vol. 17, no. 17, pp. 14839-14850, 2009.

[143] M. Mbonye, R. Mendis, and D. M. Mittleman, "Inhibiting the TE 1-mode diffraction losses in terahertz parallel-plate waveguides using concave plates," *Optics express,* vol. 20, no. 25, pp. 27800-27809, 2012.

[144] M. Gerhard, M. Theuer, and R. Beigang, "Coupling into tapered metal parallel plate waveguides using a focused terahertz beam," *Applied Physics Letters,* vol. 101, no. 4, p. 041109, 2012.

[145] R. Mendis and D. Grischkowsky, "THz interconnect with low-loss and low-group velocity dispersion," *IEEE Microwave and Wireless Components Letters,* vol. 11, no. 11, pp. 444-446, 2001.

[146] Y. Zhao and D. R. Grischkowsky, "2-D terahertz metallic photonic crystals in parallel-plate waveguides," *IEEE transactions on Microwave Theory and Techniques,* vol. 55, no. 4, pp. 656-663, 2007.

[147] E. S. Lee, J.-K. So, G.-S. Park, D. Kim, C.-S. Kee, and T.-I. Jeon, "Terahertz band gaps induced by metal grooves inside parallel-plate waveguides," *Optics express,* vol. 20, no. 6, pp. 6116-6123, 2012.

[148] L. Gingras, W. Cui, A. W. Schiff-Kearn, J.-M. Ménard, and D. G. Cooke, "Active phase control of terahertz pulses using a dynamic waveguide," *Optics express,* vol. 26, no. 11, pp. 13876-13882, 2018.

[149] M. Mbonye, R. Mendis, and D. M. Mittleman, "Measuring TE 1 mode losses in terahertz parallel-plate waveguides," *Journal of Infrared, Millimeter, and Terahertz Waves,* vol. 34, no. 7-8, pp. 416-422, 2013.

[150] C.-H. Lai *et al.*, "Modal characteristics of antiresonant reflecting pipe waveguides for terahertz waveguiding," *Optics Express,* vol. 18, no. 1, pp. 309-322, 2010.

[151] A. Dupuis, K. Stoeffler, B. Ung, C. Dubois, and M. J. J. B. Skorobogatiy, "Transmission measurements of hollow-core THz Bragg fibers," *JOSA B,* vol. 28, no. 4, pp. 896-907, 2011.

[152] H. Bao, K. Nielsen, O. Bang, and P. U. J. S. r. Jepsen, "Dielectric tube waveguides with absorptive cladding for broadband, low-dispersion and low loss THz guiding," *Scientific reports,* vol. 5, p. 7620, 2015.

[153] T. Ma, H. Guerboukha, M. Girard, A. D. Squires, R. A. Lewis, and M. J. A. O. M. Skorobogatiy, "3D Printed Hollow-Core Terahertz Optical Waveguides with Hyperuniform Disordered Dielectric Reflectors," *Advanced Optical Materials,* vol. 4, no. 12, pp. 2085-2094, 2016.

[154] A. Cruz, C. Cordeiro, and M. J. F. Franco, "3D printed hollow-core terahertz fibers," *Fibers,* vol. 6, no. 3, p. 43, 2018.

[155] S. Yang, X. Sheng, G. Zhao, Y. Wang, Y. J. J. o. I. Yu, Millimeter,, and T. Waves, "Novel Pentagram THz Hollow Core Anti-resonant Fiber Using a 3D Printer," pp. 1-11, 2019.

[156] R.-J. Yu, B. Zhang, Y.-Q. Zhang, C.-Q. Wu, Z.-G. Tian, and X.-Z. J. I. P. T. L. Bai, "Proposal for ultralow loss hollow-core plastic Bragg fiber with cobweb-structured cladding for terahertz waveguiding," vol. 19, no. 12, pp. 910-912, 2007.

[157] A. Hassani, A. Dupuis, and M. Skorobogatiy, "Low loss porous terahertz fibers containing multiple subwavelength holes," *Applied Physics Letters,* vol. 92, no. 7, p. 071101, 2008.

[158] A. Hassani, A. Dupuis, and M. Skorobogatiy, "Porous polymer fibers for low-loss Terahertz guiding," *Optics express,* vol. 16, no. 9, pp. 6340-6351, 2008.

[159] S. Atakaramians, S. Afshar, B. M. Fischer, D. Abbott, and T. M. J. O. E. Monro, "Porous fibers: a novel approach to low loss THz waveguides," *Optics Express,* vol. 16, no. 12, pp. 8845-8854, 2008.

[160] A. Dupuis, J.-F. Allard, D. Morris, K. Stoeffler, C. Dubois, and M. Skorobogatiy, "Fabrication and THz loss measurements of porous subwavelength fibers using a directional coupler method," *Optics express,* vol. 17, no. 10, pp. 8012-8028, 2009.

[161] M. I. Hasan, S. A. Razzak, G. Hasanuzzaman, and M. S. J. I. P. T. L. Habib, "Ultra-low material loss and dispersion flattened fiber for THz transmission," *IEEE Photonics Technology Letters,* vol. 26, no. 23, pp. 2372-2375, 2014.

[162] K. Nielsen, H. K. Rasmussen, A. J. Adam, P. C. Planken, O. Bang, and P. U. J. O. E. Jepsen, "Bendable, low-loss Topas fibers for the terahertz frequency range," *Optics Express,* vol. 17, no. 10, pp. 8592-8601, 2009.

[163] L.-J. Chen, H.-W. Chen, T.-F. Kao, J.-Y. Lu, and C.-K. Sun, "Low-loss subwavelength plastic fiber for terahertz waveguiding," *Optics Letters,* vol. 31, no. 3, pp. 308-310, 2006.

[164] M. Roze, B. Ung, A. Mazhorova, M. Walther, and M. Skorobogatiy, "Suspended core subwavelength fibers: towards practical designs for low-loss terahertz guidance," *Optics express,* vol. 19, no. 10, pp. 9127-9138, 2011.

[165] H. Li *et al.*, "Terahertz polarization-maintaining subwavelength dielectric waveguides," *Journal of Optics,* vol. 20, no. 12, p. 125602, 2018.

[166] G. Humbert, "Optical Fibers in Terahertz Domain," *Handbook of Optical Fibers,* pp. 1-49, 2019.

[167] A. Barh, B. P. Pal, G. P. Agrawal, R. K. Varshney, and B. A. Rahman, "Specialty fibers for terahertz generation and transmission: a review," *IEEE Journal of Selected Topics in Quantum Electronics,* vol. 22, no. 2, pp. 365-379, 2015.

[168] W. Volkaerts, N. Van Thienen, and P. Reynaert, "10.2 An FSK plastic waveguide communication link in 40nm CMOS," presented at the 2015 IEEE International Solid-State Circuits Conference - (ISSCC) Digest of Technical Papers, 2015.

[169] N. Van Thienen, Y. Zhang, M. De Wit, and P. Reynaert, "An 18Gbps polymer microwave fiber (PMF) communication link in 40nm CMOS," presented at the ESSCIRC Conference 2016: 42nd European Solid-State Circuits Conference, 2016.

[170] N. Van Thienen, W. Volkaerts, and P. Reynaert, "A Multi-Gigabit CPFSK Polymer Microwave Fiber Communication Link in 40 nm CMOS," (in English), *Ieee J Solid-St Circ,* vol. 51, no. 8, pp. 1952-1958, Aug 2016, doi: 10.1109/Jssc.2016.2580605.

[171] J. Li, K. Nallappan, H. Guerboukha, and M. Skorobogatiy, "3D printed hollow core terahertz Bragg waveguides with defect layers for surface sensing applications," *Optics Express,* vol. 25, no. 4, pp. 4126-4144, 2017.

[172] B. Ung, A. Mazhorova, A. Dupuis, M. Rozé, and M. J. O. E. Skorobogatiy, "Polymer microstructured optical fibers for terahertz wave guiding," vol. 19, no. 26, pp. B848-B861, 2011.

[173] A. J. I. O. Argyros, "Microstructures in polymer fibres for optical fibres, THz waveguides, and fibre-based metamaterials," vol. 2013, 2013.

[174] J.-Y. Lu *et al.*, "Terahertz air-core microstructure fiber," vol. 92, no. 6, p. 064105, 2008.

[175] G. M. Katyba *et al.*, "Sapphire photonic crystal waveguides for terahertz sensing in aggressive environments," *Advanced Optical Materials,* vol. 6, no. 22, p. 1800573, 2018.

[176] S. Atakaramians, V. S. Afshar, B. M. Fischer, D. Abbott, and T. M. Monro, "Porous fibers: a novel approach to low loss THz waveguides," *Opt Express,* vol. 16, no. 12, pp. 8845-54, Jun 9 2008, doi: 10.1364/oe.16.008845.

[177] H. Guerboukha, K. Nallappan, Y. Cao, M. Seghilani, J. Azaña, and M. Skorobogatiy, "Planar Porous Components for Low-Loss Terahertz Optics," *Advanced Optical Materials,* vol. 7, no. 15, p. 1900236, 2019.

[178] G. M. Katyba *et al.*, "Sapphire Photonic Crystal Waveguides for Terahertz Sensing in Aggressive Environments," (in English), *Advanced Optical Materials,* vol. 6, no. 22, Nov 19 2018, doi: ARTN 1800573

10.1002/adom.201800573.

[179] K. Nielsen, H. K. Rasmussen, P. U. Jepsen, and O. J. O. L. Bang, "Porous-core honeycomb bandgap THz fiber," vol. 36, no. 5, pp. 666-668, 2011.

[180] S. Atakaramians *et al.*, "THz porous fibers: design, fabrication and experimental characterization," vol. 17, no. 16, pp. 14053-14062, 2009.

[181] T. Ma, A. Markov, L. Wang, and M. Skorobogatiy, "Graded index porous optical fibers– dispersion management in terahertz range," *Optics express,* vol. 23, no. 6, pp. 7856-7869, 2015.

[182] M. De Wit, Y. Zhang, and P. Reynaert, "Analysis and Design of a Foam-Cladded PMF Link With Phase Tuning in 28-nm CMOS," (in English), *Ieee J Solid-St Circ,* vol. 54, no. 7, pp. 1960-1969, Jul 2019, doi: 10.1109/Jssc.2019.2907163.

[183] L. J. Chen, H. W. Chen, T. F. Kao, J. Y. Lu, and C. K. Sun, "Low-loss subwavelength plastic fiber for terahertz waveguiding," *Opt Lett,* vol. 31, no. 3, pp. 308-10, Feb 1 2006, doi: 10.1364/ol.31.000308.

[184] H. S. Li *et al.*, "Terahertz polarization-maintaining subwavelength dielectric waveguides," (in English), *J Optics-Uk,* vol. 20, no. 12, Nov 2018, doi: ARTN 125602

10.1088/2040-8986/aaea58.

[185] M. Roze, B. Ung, A. Mazhorova, M. Walther, and M. Skorobogatiy, "Suspended core subwavelength fibers: towards practical designs for low-loss terahertz guidance," *Opt Express,* vol. 19, no. 10, pp. 9127-38, May 9 2011, doi: 10.1364/OE.19.009127.

[186] H. Han, H. Park, M. Cho, and J. Kim, "Terahertz pulse propagation in a plastic photonic crystal fiber," *Applied Physics Letters,* vol. 80, no. 15, pp. 2634-2636, 2002, doi: 10.1063/1.1468897.

[187] H.-W. Chen *et al.*, "Investigation on spectral loss characteristics of subwavelength terahertz fibers," vol. 32, no. 9, pp. 1017-1019, 2007.

[188] M. D'Auria *et al.*, "3-D printed metal-pipe rectangular waveguides," *IEEE Transactions on Components, Packaging and Manufacturing Technology,* vol. 5, no. 9, pp. 1339-1349, 2015.

[189] B. Zhang, W. Chen, Y. Wu, K. Ding, and R. Li, "Review of 3D printed millimeter-wave and terahertz passive devices," *International Journal of Antennas and Propagation,* vol. 2017, 2017.

[190] N. Duangrit, B. Hong, A. D. Burnett, P. Akkaraekthalin, I. D. Robertson, and N. Somjit, "Terahertz dielectric property characterization of photopolymers for additive manufacturing," *IEEE Access,* vol. 7, pp. 12339-12347, 2019.

[191] T. Ma, K. Nallapan, H. Guerboukha, and M. Skorobogatiy, "Analog signal processing in the terahertz communication links using waveguide Bragg gratings: example of dispersion compensation," *Optics express,* vol. 25, no. 10, pp. 11009-11026, 2017.

[192] G. Xu, K. Nallappan, Y. Cao, and M. Skorobogatiy, "3D Printed Suspended Core Polypropylene Fiber For Terahertz Communication System," in *Photonics North*, Canada, 2020: Submitted.

[193] N. J. Karl, R. W. McKinney, Y. Monnai, R. Mendis, and D. M. Mittleman, "Frequency-division multiplexing in the terahertz range using a leaky-wave antenna," *Nature Photonics,* vol. 9, no. 11, pp. 717-720, 2015.

[194] J. Ma, N. J. Karl, S. Bretin, G. Ducournau, and D. M. Mittleman, "Frequency-division multiplexer and demultiplexer for terahertz wireless links," *Nat Commun,* vol. 8, no. 1, p. 729, Sep 28 2017, doi: 10.1038/s41467-017-00877-x.

[195] M. Weidenbach *et al.*, "3D printed dielectric rectangular waveguides, splitters and couplers for 120 GHz," *Opt Express,* vol. 24, no. 25, pp. 28968-28976, Dec 12 2016, doi: 10.1364/OE.24.028968.

[196] J. Ma, M. Weidenbach, R. Guo, M. Koch, and D. M. Mittleman, "Communications with THz Waves: Switching Data Between Two Waveguides," (in English), *J Infrared Millim Te,* vol. 38, no. 11, pp. 1316-1320, Nov 2017, doi: 10.1007/s10762-017-0428-4.

[197] K. S. Reichel, R. Mendis, and D. M. Mittleman, "A Broadband Terahertz Waveguide T-Junction Variable Power Splitter," *Sci Rep,* vol. 6, p. 28925, Jun 29 2016, doi: 10.1038/srep28925.

[198] K. S. Reichel *et al.*, "Electrically reconfigurable terahertz signal processing devices using liquid metal components," *Nat Commun,* vol. 9, no. 1, p. 4202, Oct 10 2018, doi: 10.1038/s41467-018-06463-z.

[199] S. Mollahasani and E. Onur, "Evaluation of terahertz channel in data centers," in *NOMS 2016-2016 IEEE/IFIP Network Operations and Management Symposium*, 2016: IEEE, pp. 727-730.

[200] Q. J. J. I. C. M. Gu, "THz interconnect: The last centimeter communication," vol. 53, no. 4, pp. 206-215, 2015.

[201] M. Alonso-del Pino, C. Jung-Kubiak, T. Reck, C. Lee, and G. Chattopadhyay, "Micromachining for Advanced Terahertz: Interconnects and Packaging Techniques at Terahertz Frequencies," *IEEE Microwave Magazine,* vol. 21, no. 1, pp. 18-34, 2019.

[202] M. Ali *et al.*, "Quasi-optic transmitter and receiver modules enabling next-generation ultra-broadband wireless links at carrier-wave frequencies ranging from 60 to 180 GHz," *Journal of Infrared, Millimeter, and Terahertz Waves,* vol. 40, no. 6, pp. 688-695, 2019.

[203] H.-J. Song, H. Hamada, and M. Yaita, "Prototype of KIOSK data downloading system at 300 GHz: Design, technical feasibility, and results," *IEEE Communications Magazine,* vol. 56, no. 6, pp. 130-136, 2018.

[204] D. Bojic *et al.*, "Advanced wireless and optical technologies for small-cell mobile backhaul with dynamic software-defined management," *IEEE Communications Magazine,* vol. 51, no. 9, pp. 86-93, 2013, doi: 10.1109/MCOM.2013.6588655.

[205] P. T. Dat, A. Kanno, K. Inagaki, and T. Kawanishi, "High-Capacity Wireless Backhaul Network Using Seamless Convergence of Radio-over-Fiber and 90-GHz Millimeter-Wave," *Journal of Lightwave Technology,* vol. 32, no. 20, pp. 3910-3923, 2014, doi: 10.1109/JLT.2014.2315800.

[206] P. Shumyatsky and R. R. Alfano, "Terahertz sources," *Journal of biomedical optics,* vol. 16, no. 3, p. 033001, 2011.

[207] M. Naftaly and R. E. Miles, "Terahertz time-domain spectroscopy for material characterization," *Proceedings of the IEEE,* vol. 95, no. 8, pp. 1658-1665, 2007.

[208] S. Ray *et al.*, "Design and engineering of organic molecules for customizable Terahertz tags," in *Terahertz, RF, Millimeter, and Submillimeter-Wave Technology and Applications VII*, 2014, vol. 8985: International Society for Optics and Photonics, p. 89850P.

[209] T. D. Dorney, R. G. Baraniuk, and D. M. Mittleman, "Material parameter estimation with terahertz time-domain spectroscopy," *JOSA A,* vol. 18, no. 7, pp. 1562-1571, 2001.

[210] N. Karpowicz, H. Zhong, J. Xu, K.-I. Lin, J.-S. Hwang, and X. Zhang, "Comparison between pulsed terahertz time-domain imaging and continuous wave terahertz imaging," *Semiconductor Science and Technology,* vol. 20, no. 7, p. S293, 2005.

[211] A. J. Deninger *et al.*, "Precisely tunable continuous-wave terahertz source with interferometric frequency control," *Review of Scientific Instruments,* vol. 79, no. 4, p. 044702, 2008.

[212] S. Nellen, B. Globisch, R. B. Kohlhaas, L. Liebermeister, and M. Schell, "Recent progress of continuous-wave terahertz systems for spectroscopy, non-destructive testing, and telecommunication," in *Terahertz, RF, Millimeter, and Submillimeter-Wave Technology and Applications XI*, 2018, vol. 10531: International Society for Optics and Photonics, p. 105310C.

[213] S. Verghese, K. McIntosh, S. Calawa, W. Dinatale, E. Duerr, and K. Molvar, "Generation and detection of coherent terahertz waves using two photomixers," *Applied Physics Letters,* vol. 73, no. 26, pp. 3824-3826, 1998.

[214] A. Nahata, J. T. Yardley, and T. F. Heinz, "Free-space electro-optic detection of continuous-wave terahertz radiation," *Applied physics letters,* vol. 75, no. 17, pp. 2524-2526, 1999.

[215] K. J. Siebert *et al.*, "Continuous-wave all-optoelectronic terahertz imaging," *Applied Physics Letters,* vol. 80, no. 16, pp. 3003-3005, 2002.

[216] R. Mendis, C. Sydlo, J. Sigmund, M. Feiginov, P. Meissner, and H. L. Hartnagel, "Coherent generation and detection of continuous terahertz waves using two photomixers driven by laser diodes," *International journal of infrared and millimeter waves,* vol. 26, no. 2, pp. 201-207, 2005.

[217] A. M. Sinyukov *et al.*, "Rapid-phase modulation of terahertz radiation for high-speed terahertz imaging and spectroscopy," *Optics letters,* vol. 33, no. 14, pp. 1593-1595, 2008.

[218] T. Gobel, D. Schoenherr, C. Sydlo, M. Feiginov, P. Meissner, and H. Hartnagel, "Single-sampling-point coherent detection in continuous-wave photomixing terahertz systems," *Electronics Letters,* vol. 45, no. 1, pp. 65-66, 2008.

[219] A. Roggenbuck *et al.*, "Using a fiber stretcher as a fast phase modulator in a continuous wave terahertz spectrometer," *JOSA B,* vol. 29, no. 4, pp. 614-620, 2012.

[220] C. Winnewisser, F. Lewen, and H. Helm, "Transmission characteristics of dichroic filters measured by THz time-domain spectroscopy," *Applied Physics A,* vol. 66, no. 6, pp. 593-598, 1998.

[221] H. Pickett, R. Poynter, E. Cohen, M. Delitsky, J. Pearson, and H. Müller, "Submillimeter, millimeter, and microwave spectral line catalog," *Journal of Quantitative Spectroscopy and Radiative Transfer,* vol. 60, no. 5, pp. 883-890, 1998.

[222] A. Roggenbuck *et al.*, "Coherent broadband continuous-wave terahertz spectroscopy on solid-state samples," *New Journal of Physics,* vol. 12, no. 4, p. 043017, 2010.

[223] M. Skorobogatiy and J. Yang, *Fundamentals of photonic crystal guiding*. Cambridge University Press, 2009.

[224] M. Skorobogatiy, *Nanostructured and Subwavelength Waveguides: fundamentals and applications*. John Wiley & Sons, 2012.

[225] W. Koechner, *Solid-state laser engineering*. Springer, 2013.

[226] T. Li, *Optical fiber communications: fiber fabrication*. Elsevier, 2012.

[227] J.-Y. Lu *et al.*, "Terahertz air-core microstructure fiber," *Applied Physics Letters,* vol. 92, no. 6, p. 064105, 2008.

[228] J. Wang, X. Yang, and L. Wang, "Fabrication and experimental observation of monolithic multi-air-core fiber array for image transmission," *Optics express,* vol. 16, no. 11, pp. 7703-7708, 2008.

[229] V. Cisco, "The zettabyte era: trends and analysis. Updated (07/06/2017)," ed, 2017.

[230] T. Kürner and S. Priebe, "Towards THz communications-status in research, standardization and regulation," *Journal of Infrared, Millimeter, and Terahertz Waves,* vol. 35, no. 1, pp. 53-62, 2014.

[231] Y. Niu, Y. Li, D. Jin, L. Su, and A. V. Vasilakos, "A survey of millimeter wave communications (mmWave) for 5G: opportunities and challenges," *Wireless Networks,* vol. 21, no. 8, pp. 2657-2676, 2015.

[232] J. Zhang, P. Tang, L. Tian, Z. Hu, T. Wang, and H. Wang, "6–100 GHz research progress and challenges from a channel perspective for fifth generation (5G) and future wireless communication," *Science China Information Sciences,* vol. 60, no. 8, p. 080301, 2017.

[233] I. F. Akyildiz, J. M. Jornet, and C. Han, "TeraNets: ultra-broadband communication networks in the terahertz band," *IEEE Wireless Communications,* vol. 21, no. 4, pp. 130-135, 2014, doi: 10.1109/MWC.2014.6882305.

[234] M. A. Akkaş, "Terahertz wireless data communication," *Wireless Networks,* pp. 1-11.

[235] I. T. Union. "Technology Trends of Active Services in the Frequency Range 275-3000 GHz." https://www.itu.int/dms_pub/itu-r/opb/rep/R-REP-SM.2352-2015-PDF-E.pdf

[236] A.-P. Telecommunity, "APT Report on Technology Trends of Telecommunications Above 100 GHz," 2011. Accessed: June., 21, 2018. [Online]. Available: https://www.apt.int/sites/default/files/Upload-files/ASTAP/Rept-4-Technology%20Trends%20above%20100GHz.pdf

[237] I. T. Union, "Technical and Operational Characteristics of Land-mobile Service Applications in the Frequency Range 275-450 GHz," M.2417-0 (11/2017), 2017. Accessed: Online: June.,21,2018. [Online]. Available: https://www.itu.int/dms_pub/itu-r/opb/rep/R-REP-M.2417-2017-PDF-E.pdf

[238] A. Hirata *et al.*, "120-GHz-band wireless link technologies for outdoor 10-Gbit/s data transmission," *IEEE Transactions on Microwave Theory and Techniques,* vol. 60, no. 3, pp. 881-895, 2012.

[239] H. Takahashi, A. Hirata, J. Takeuchi, N. Kukutsu, T. Kosugi, and K. Murata, "120-GHz-band 20-Gbit/s transmitter and receiver MMICs using quadrature phase shift keying," in *Microwave Integrated Circuits Conference (EuMIC), 2012 7th European*, 2012: IEEE, pp. 313-316.

[240] A. Hirata *et al.*, "5.8-km 10-Gbps data transmission over a 120-GHz-band wireless link," in *Wireless Information Technology and Systems (ICWITS), 2010 IEEE International Conference on*, 2010: IEEE, pp. 1-4.

[241] H. Takahashi, T. Kosugi, A. Hirata, K. Murata, and N. Kukutsu, "10-Gbit/s quadrature phase-shift-keying modulator and demodulator for 120-GHz-band wireless links," *IEEE Transactions on Microwave Theory and Techniques,* vol. 58, no. 12, pp. 4072-4078, 2010.

[242] I. Mehdi, J. V. Siles, C. Lee, and E. Schlecht, "THz diode technology: status, prospects, and applications," *Proceedings of the IEEE,* vol. 105, no. 6, pp. 990-1007, 2017.

[243] A. J. Deninger, A. Roggenbuck, S. Schindler, and S. Preu, "2.75 THz tuning with a triple-DFB laser system at 1550 nm and InGaAs photomixers," *Journal of Infrared, Millimeter, and Terahertz Waves,* vol. 36, no. 3, pp. 269-277, 2015.

[244] H. Ito and T. Ishibashi, "Photonic Terahertz-Wave Generation Using Slot-Antenna-Integrated Uni-Traveling-Carrier Photodiodes," *IEEE Journal of Selected Topics in Quantum Electronics,* vol. 23, no. 4, pp. 1-7, 2017.

[245] I. Morohashi *et al.*, "Terahertz source with broad frequency tunability up to 3.8 THz using MZ-FCG for frequency reference in phase-locking of THz source devices," in *Microwave Photonics (MWP), 2016 IEEE International Topical Meeting on*, 2016: IEEE, pp. 126-128.

[246] T. Ishibashi, Y. Muramoto, T. Yoshimatsu, and H. Ito, "Unitraveling-carrier photodiodes for terahertz applications," *IEEE Journal of Selected Topics in Quantum Electronics,* vol. 20, no. 6, pp. 79-88, 2014.

[247] T. Nagatsuma and H. Ito, "High-power RF uni-traveling-carrier photodiodes (UTC-PDs) and their applications," in *advances in photodiodes*: InTech, 2011.

[248] T. Umezawa *et al.*, "Bias-free operational UTC-PD above 110 GHz and its application to high baud rate fixed-fiber communication and W-band photonic wireless communication," *Journal of Lightwave Technology,* vol. 34, no. 13, pp. 3138-3147, 2016.

[249] E. Peytavit *et al.*, "Milliwatt-level output power in the sub-terahertz range generated by photomixing in a GaAs photoconductor," *Applied Physics Letters,* vol. 99, no. 22, p. 223508, 2011.

[250] H.-J. Song, K. Ajito, Y. Muramoto, A. Wakatsuki, T. Nagatsuma, and N. Kukutsu, "Uni-travelling-carrier photodiode module generating 300 GHz power greater than 1 mW," *IEEE Microwave and Wireless Components Letters,* vol. 22, no. 7, pp. 363-365, 2012.

[251] H. Shams, M. J. Fice, K. Balakier, C. C. Renaud, F. van Dijk, and A. J. Seeds, "Photonic generation for multichannel THz wireless communication," *Optics Express,* vol. 22, no. 19, pp. 23465-23472, 2014.

[252] S. Koenig *et al.*, "Wireless sub-THz communication system with high data rate," *Nature Photonics,* vol. 7, no. 12, pp. 977-981, 2013.

[253] G. Ducournau *et al.*, "Ultrawide-bandwidth single-channel 0.4-THz wireless link combining broadband quasi-optic photomixer and coherent detection," *IEEE Transactions on Terahertz Science and Technology,* vol. 4, no. 3, pp. 328-337, 2014.

[254] X. Yu *et al.*, "60 Gbit/s 400 GHz wireless transmission," in *Photonics in Switching (PS), 2015 International Conference on*, 2015: IEEE, pp. 4-6.

[255] X. Yu *et al.*, "160 Gbit/s photonics wireless transmission in the 300-500 GHz band," *Apl Photonics,* vol. 1, no. 8, p. 081301, 2016.

[256] T. Nagatsuma, K. Oogimoto, Y. Inubushi, and J. Hirokawa, "Practical considerations of terahertz communications for short distance applications," *Nano Communication Networks,* vol. 10, pp. 1-12, 2016.

[257] J. Ma, N. J. Karl, S. Bretin, G. Ducournau, and D. M. Mittleman, "Frequency-division multiplexer and demultiplexer for terahertz wireless links," *Nature communications,* vol. 8, no. 1, p. 729, 2017/09/28 2017, doi: 10.1038/s41467-017-00877-x.

[258] S. Blin *et al.*, "Wireless communication at 310 GHz using GaAs high-electron-mobility transistors for detection," *Journal of Communications and Networks,* vol. 15, no. 6, pp. 559-568, 2013.

[259] Q. Wu *et al.*, "A 21 km 5 Gbps real time wireless communication system at 0.14 THz," in *Infrared, Millimeter, and Terahertz Waves (IRMMW-THz), 2017 42nd International Conference on*, 2017: IEEE, pp. 1-2.

[260] G. Ducournau *et al.*, "High-definition television transmission at 600 GHz combining THz photonics hotspot and high-sensitivity heterodyne receiver," *Electronics Letters,* vol. 50, no. 5, pp. 413-415, 2014.

[261] T. Narytnyk, "Possibilities of Using THz-Band Radio Communication Channels for Super High-Rate Backhaul," *Telecommunications and Radio Engineering,* vol. 73, no. 15, 2014.

[262] V. Petrov, A. Pyattaev, D. Moltchanov, and Y. Koucheryavy, "Terahertz band communications: Applications, research challenges, and standardization activities," in *Ultra Modern Telecommunications and Control Systems and Workshops (ICUMT), 2016 8th International Congress on*, 2016: IEEE, pp. 183-190.

[263] http://www.marketsandmarkets.com/PressReleases/4k-technology.asp. (accessed 09th January 2021).

[264] D. Mirzoev, "Wireless Transmission of Video for Biomechanical Analysis," *arXiv preprint arXiv:1404.2343,* 2014.

[265] M. Batistatos, G. V. Tsoulos, and G. E. Athanasiadou, "Mobile telemedicine for moving vehicle scenarios: Wireless technology options and challenges," *Journal of Network and Computer Applications,* vol. 35, no. 3, pp. 1140-1150, 2012.

[266] T. Toma, S. Suzuki, H. Tokura, Y. Inaba, T. Ogi, and a. Y. Koike, "Evaluation of 4K Ultra Definition Video for Telemedicine - Possibility of teledermatology Applications," *Japanese Journal of Telemedicine and Telecare,* vol. 9, no. 2, pp. 66-73, 2013.

[267] Y. Miki *et al.*, "Readying for UHDTV Broadcasting in Japan," *SMPTE Motion Imaging Journal,* vol. 126, no. 2, pp. 46-52, 2017, doi: 10.5594/JMI.2016.2643938.

[268] B. Globisch *et al.*, "Absolute terahertz power measurement of a time-domain spectroscopy system," *Optics letters,* vol. 40, no. 15, pp. 3544-3547, 2015.

[269] P. H. Siegel, "Terahertz technology," *IEEE Transactions on microwave theory and techniques,* vol. 50, no. 3, pp. 910-928, 2002.

[270] X. Li, J. Yu, J. Zhang, Z. Dong, F. Li, and N. Chi, "A 400G optical wireless integration delivery system," *Optics Express,* vol. 21, no. 16, pp. 18812-18819, 2013.

[271] M. Fice *et al.*, "146-GHz millimeter-wave radio-over-fiber photonic wireless transmission system," *Optics express,* vol. 20, no. 2, pp. 1769-1774, 2012.

[272] G. Ducournau *et al.*, "Coherent THz communication at 200 GHz using a frequency comb, UTC-PD and electronic detection," *Electronics Letters,* vol. 50, no. 5, pp. 386-388, 2014.

[273] J. Ma *et al.*, "Security and eavesdropping in terahertz wireless links," *Nature,* vol. 563, no. 7729, p. 89, 2018.

[274] Q. Wu *et al.*, "A 21 km 5 Gbps real time wireless communication system at 0.14 THz," in *2017 42nd International Conference on Infrared, Millimeter, and Terahertz Waves (IRMMW-THz)*, 2017: IEEE, pp. 1-2.

[275] M. S. Islam *et al.*, "Extremely low material loss and dispersion flattened TOPAS based circular porous fiber for long distance terahertz wave transmission," vol. 34, pp. 6-11, 2017.

[276] H. Han, H. Park, M. Cho, and J. J. A. P. L. Kim, "Terahertz pulse propagation in a plastic photonic crystal fiber," vol. 80, no. 15, pp. 2634-2636, 2002.

[277] H.-W. Chen *et al.*, "Subwavelength dielectric-fiber-based THz coupler," *Journal of Lightwave Technology,* vol. 27, no. 11, pp. 1489-1495, 2009.

[278] H. Li *et al.*, "Terahertz polarization-maintaining subwavelength filters," *Optics express,* vol. 26, no. 20, pp. 25617-25629, 2018.

[279] J. Ma, M. Weidenbach, R. Guo, M. Koch, and D. Mittleman, "Communications with THz waves: switching data between two waveguides," *Journal of Infrared, Millimeter, and Terahertz Waves,* vol. 38, no. 11, pp. 1316-1320, 2017.

[280] M. Taherkhani, R. Sadeghzadeh, J. Taiber, J. Ornik, M. J. J. o. I. Koch, Millimeter,, and T. Waves, "The Effect of Humidity and Temperature on Dielectric Fibre–Bound THz Transmission," vol. 40, no. 11, pp. 1092-1102, 2019.

[281] H. Guerboukha, G. Yan, O. Skorobogata, and M. J. A. O. M. Skorobogatiy, "Silk foam terahertz waveguides," vol. 2, no. 12, pp. 1181-1192, 2014.

[282] A. Markov, H. Guerboukha, and M. J. J. B. Skorobogatiy, "Hybrid metal wire–dielectric terahertz waveguides: challenges and opportunities," vol. 31, no. 11, pp. 2587-2600, 2014.

[283] K. Nallappan, H. Guerboukha, Y. Cao, C. Nerguizian, and M. Skorobogatiy, "Experimental Demonstration of 5 Gbps Data Transmission Using Long Subwavelength Fiber at 140 GHz," in *2019 IEEE Radio and Wireless Symposium (RWS)*, 2019: IEEE, pp. 1-4.

[284] K. Nallappan, C. Nerguizian, H. Guerboukha, M. Skorobogatiy, and Y. Cao, "High Bitrate Data Transmission Using Polypropylene Fiber in Terahertz Frequency Range," in *2019 International Workshop on Antenna Technology (iWAT)*, 2019: IEEE, pp. 81-83.

[285] K. Nallappan, C. Nerguizian, H. Guerboukha, Y. Cao, and M. Skorobogatiy, "Signal Transmission Using Solid Core Terahertz Waveguide," in *The 8th International Conference on Optical Terahertz Science and Technology*, USA, 2019, pp. paper 102, Tu-P-23.

[286] F. Voineau *et al.*, "A 12 Gb/s 64QAM and OFDM compatible millimeter-wave communication link using a novel plastic waveguide design," in *2018 IEEE Radio and Wireless Symposium (RWS)*, 2018: IEEE, pp. 250-252.

[287] W. Volkaerts, N. Van Thienen, and P. Reynaert, "10.2 An FSK plastic waveguide communication link in 40nm CMOS," in *2015 IEEE International Solid-State Circuits Conference-(ISSCC) Digest of Technical Papers*, 2015: IEEE, pp. 1-3.

[288] K. Nallappan, Y. Cao, G. Xu, H. Guerboukha, C. Nerguizian, and M. Skorobogatiy, "Increasing Reliability of Terahertz Communication Links Using Onboard Fiber Connectivity," in *2020 10th Annual Computing and Communication Workshop and Conference (CCWC)*, 2020: IEEE, pp. 1065-1070.

[289] X. Yu *et al.*, "Terahertz fibre transmission link using resonant tunnelling diodes integrated with photonic-crystal waveguides," *Electronics Letters,* vol. 55, no. 7, pp. 398-400, 2019.

[290] B. Yu *et al.*, "Ortho-Mode Sub-THz Interconnect Channel for Planar Chip-to-Chip Communications," *IEEE Transactions on Microwave Theory and Techniques,* vol. 66, no. 4, pp. 1864-1873, 2018.

[291] W. Withayachumnankul, M. Fujita, and T. Nagatsuma, "Integrated Silicon Photonic Crystals Toward Terahertz Communications," *Advanced Optical Materials,* vol. 6, no. 16, p. 1800401, 2018.

[292] X. Yu, M. Sugeta, Y. Yamagami, M. Fujita, and T. Nagatsuma, "Simultaneous low-loss and low-dispersion in a photonic-crystal waveguide for terahertz communications," *Applied Physics Express,* vol. 12, no. 1, p. 012005, 2019.

[293] K. Tsuruda, M. Fujita, and T. Nagatsuma, "Extremely low-loss terahertz waveguide based on silicon photonic-crystal slab," *Optics express,* vol. 23, no. 25, pp. 31977-31990, 2015.

[294] A. Locatelli, G. E. Town, C. J. I. T. o. T. S. De Angelis, and Technology, "Graphene-based terahertz waveguide modulators," vol. 5, no. 3, pp. 351-357, 2015.

[295] K. I. Zaytsev *et al.*, "Overcoming the Abbe Diffraction Limit Using a Bundle of Metal-Coated High-Refractive-Index Sapphire Optical Fibers," p. 2000307.

[296] K. Nallappan, H. Guerboukha, C. Nerguizian, and M. Skorobogatiy, "Live streaming of uncompressed 4K video using terahertz wireless links," in *2018 IEEE International Conference on Communications (ICC)*, 2018: IEEE, pp. 1-7.

[297] R. Ortuño, C. García-Meca, and A. Martínez, "Terahertz metamaterials on flexible polypropylene substrate," *Plasmonics,* vol. 9, no. 5, pp. 1143-1147, 2014.

[298]   M. Afsar, "Dielectric measurements of common polymers at millimeter wavelength," in *1985 IEEE MTT-S International Microwave Symposium Digest*, 1985: IEEE, pp. 439-442.

[299]   M. Navarro-Cia, J. Wu, H. Liu, and O. J. S. r. Mitrofanov, "Generation of radially-polarized terahertz pulses for coupling into coaxial waveguides," vol. 6, p. 38926, 2016.

[300]   J. A. Deibel, K. Wang, M. D. Escarra, and D. M. J. O. e. Mittleman, "Enhanced coupling of terahertz radiation to cylindrical wire waveguides," vol. 14, no. 1, pp. 279-290, 2006.

[301]   J.-F. Roux, F. Aquistapace, F. Garet, L. Duvillaret, and J.-L. J. A. o. Coutaz, "Grating-assisted coupling of terahertz waves into a dielectric waveguide studied by terahertz time-domain spectroscopy," vol. 41, no. 30, pp. 6507-6513, 2002.

[302]   D. Marcuse, "Curvature loss formula for optical fibers," *JOSA,* vol. 66, no. 3, pp. 216-220, 1976.

[303]   R. T. Schermer and J. H. Cole, "Improved bend loss formula verified for optical fiber by simulation and experiment," *IEEE Journal of Quantum Electronics,* vol. 43, no. 10, pp. 899-909, 2007.

[304]   Y. Yang, A. Shutler, and D. Grischkowsky, "Measurement of the transmission of the atmosphere from 0.2 to 2 THz," *Optics Express,* vol. 19, no. 9, pp. 8830-8838, 2011/04/25 2011, doi: 10.1364/OE.19.008830.

[305]   J. Y. Suen, M. T. Fang, S. P. Denny, and P. M. Lubin, "Modeling of terabit geostationary terahertz satellite links from globally dry locations," *IEEE Transactions on Terahertz Science and Technology,* vol. 5, no. 2, pp. 299-313, 2015.

[306]   B. You, J.-Y. Lu, T.-A. Liu, J.-L. Peng, and C.-L. J. A. P. L. Pan, "Subwavelength plastic wire terahertz time-domain spectroscopy," vol. 96, no. 5, p. 051105, 2010.

[307]   F. Yan, C. Yu, H. Park, E. P. Parrott, and E. Pickwell-MacPherson, "Advances in polarizer technology for terahertz frequency applications," *Journal of infrared, millimeter, and terahertz waves,* vol. 34, no. 9, pp. 489-499, 2013.

[308]   I. Yamada, K. Takano, M. Hangyo, M. Saito, and W. Watanabe, "Terahertz wire-grid polarizers with micrometer-pitch Al gratings," *Optics letters,* vol. 34, no. 3, pp. 274-276, 2009.

[309]   A. Zubair *et al.*, "Carbon nanotube fiber terahertz polarizer," *Applied Physics Letters,* vol. 108, no. 14, p. 141107, 2016.

[310]   J. S. Cetnar, J. R. Middendorf, and E. R. Brown, "Extraordinary optical transmission and extinction in a Terahertz wire-grid polarizer," *Applied Physics Letters,* vol. 100, no. 23, p. 231912, 2012.

[311]   C.-F. Hsieh, Y.-C. Lai, R.-P. Pan, and C.-L. Pan, "Polarizing terahertz waves with nematic liquid crystals," *Optics letters,* vol. 33, no. 11, pp. 1174-1176, 2008.

[312]   A. Wojdyla and G. Gallot, "Brewster's angle silicon wafer terahertz linear polarizer," *Optics Express,* vol. 19, no. 15, pp. 14099-14107, 2011.

[313]   A. Hernandez-Serrano *et al.*, "Design and fabrication of 3-D printed conductive polymer structures for THz polarization control," *Optics express,* vol. 27, no. 8, pp. 11635-11641, 2019.

[314]   G. Gibson *et al.*, "Free-space information transfer using light beams carrying orbital angular momentum," *Optics Express,* vol. 12, no. 22, pp. 5448-5456, 2004.

[315]   J. Wang *et al.*, "Terabit free-space data transmission employing orbital angular momentum multiplexing," *Nature Photonics,* vol. 6, no. 7, pp. 488-496, 2012.

[316] Y. Yan *et al.*, "High-capacity millimetre-wave communications with orbital angular momentum multiplexing," *Nature communications,* vol. 5, 2014.

[317] A. M. Yao and M. J. Padgett, "Orbital angular momentum: origins, behavior and applications," *Advances in Optics and Photonics,* vol. 3, no. 2, pp. 161-204, 2011.

[318] G. Turnbull, D. Robertson, G. Smith, L. Allen, and M. Padgett, "The generation of free-space Laguerre-Gaussian modes at millimetre-wave frequencies by use of a spiral phaseplate," *Optics communications,* vol. 127, no. 4-6, pp. 183-188, 1996.

[319] X. Wei, L. Zhu, Z. Zhang, K. Wang, J. Liu, and J. Wang, "Orbit angular momentum multiplexing in 0.1-THz free-space communication via 3D printed spiral phase plates," in *Lasers and Electro-Optics (CLEO), 2014 Conference on*, 2014: IEEE, pp. 1-2.

[320] A. Tennant and B. Allen, "Generation of OAM radio waves using circular time-switched array antenna," *Electronics Letters,* vol. 48, no. 21, pp. 1365-1366, 2012.

[321] G. Xie *et al.*, "Tunable generation and angular steering of a millimeter-wave orbital-angular-momentum beam using differential time delays in a circular antenna array," in *Communications (ICC), 2016 IEEE International Conference on*, 2016: IEEE, pp. 1-6.

[322] S. Ge *et al.*, "Terahertz vortex beam generator based on a photopatterned large birefringence liquid crystal," *Optics Express,* vol. 25, no. 11, pp. 12349-12356, 2017.

[323] X.-w. Lin *et al.*, "Self-polarizing terahertz liquid crystal phase shifter," *Aip Advances,* vol. 1, no. 3, p. 032133, 2011.

[324] C. Liu, J. Liu, L. Niu, X. Wei, K. Wang, and Z. Yang, "Terahertz circular Airy vortex beams," *Scientific reports,* vol. 7, no. 1, p. 3891, 2017.

[325] H. Zhao, B. Quan, X. Wang, C. Gu, J. Li, and Y. Zhang, "Demonstration of orbital angular momentum multiplexing and demultiplexing based on a metasurface in the terahertz band," *ACS Photonics,* vol. 5, no. 5, pp. 1726-1732, 2017.

[326] X. Hui *et al.*, "Multiplexed millimeter wave communication with dual orbital angular momentum (OAM) mode antennas," *Scientific reports,* vol. 5, no. 1, pp. 1-9, 2015.

[327] Z. Zhao *et al.*, "Experimental demonstration of 16-Gbit/s millimeter-wave communications link using thin metamaterial plates to generate data-carrying orbital-angular-momentum beams," in *2015 IEEE International Conference on Communications (ICC)*, 2015: IEEE, pp. 1392-1397.

[328] Y. Yan *et al.*, "32-Gbit/s 60-GHz millimeter-wave wireless communication using orbital angular momentum and polarization multiplexing," in *2016 IEEE International Conference on Communications (ICC)*, 2016: IEEE, pp. 1-6.

[329] Z. Zhao *et al.*, "Fundamental system-degrading effects in THz communications using multiple OAM beams with turbulence," in *ICC 2020-2020 IEEE International Conference on Communications (ICC)*, 2020: IEEE, pp. 1-7.

[330] N. Ahmed *et al.*, "Mode-division-multiplexing of multiple Bessel-Gaussian beams carrying orbital-angular-momentum for obstruction-tolerant free-space optical and millimetre-wave communication links," *Scientific reports,* vol. 6, p. 22082, 2016.

[331] Y. Yan *et al.*, "Experimental measurements of multipath-induced intra-and inter-channel crosstalk effects in a millimeter-wave communications link using orbital-angular-momentum multiplexing," in *Communications (ICC), 2015 IEEE International Conference on*, 2015: IEEE, pp. 1370-1375.

[332] H. Li *et al.*, "Guiding terahertz orbital angular momentum beams in multimode Kagome hollow-core fibers," *Optics Letters,* vol. 42, no. 2, pp. 179-182, 2017.

[333] A. Stefani, S. C. Fleming, and B. T. Kuhlmey, "Terahertz orbital angular momentum modes with flexible twisted hollow core antiresonant fiber," *Apl Photonics,* vol. 3, no. 5, p. 051708, 2018.

[334] D. Wu *et al.*, "Terahertz plasmonic high pass filter," *Applied Physics Letters,* vol. 83, no. 1, pp. 201-203, 2003.

[335] K. Nielsen, H. K. Rasmussen, P. U. Jepsen, and O. Bang, "Broadband terahertz fiber directional coupler," *Optics letters,* vol. 35, no. 17, pp. 2879-2881, 2010.

[336] M.-D. He *et al.*, "Graphene-based terahertz tunable plasmonic directional coupler," *Applied Physics Letters,* vol. 105, no. 8, p. 081903, 2014.

[337] E. S. Lee, S.-G. Lee, C.-S. Kee, and T.-I. Jeon, "Terahertz notch and low-pass filters based on band gaps properties by using metal slits in tapered parallel-plate waveguides," *Optics express,* vol. 19, no. 16, pp. 14852-14859, 2011.

[338] X. Li, J. Yu, K. Wang, W. Zhou, and J. Zhang, "Photonics-aided 2× 2 MIMO wireless terahertz-wave signal transmission system with optical polarization multiplexing," *Optics Express,* vol. 25, no. 26, pp. 33236-33242, 2017.

[339] H. Sarieddeen, M.-S. Alouini, and T. Y. Al-Naffouri, "Terahertz-band ultra-massive spatial modulation MIMO," *IEEE Journal on Selected Areas in Communications,* vol. 37, no. 9, pp. 2040-2052, 2019.

[340] K. Nallappan *et al.*, "Multiplexing of terahertz wireless communication channels using vortex beams," in *2017 42nd International Conference on Infrared, Millimeter, and Terahertz Waves (IRMMW-THz)*: IEEE, pp. 1-1.

[341] Y. He *et al.*, "High-energy and ultra-wideband tunable terahertz source with DAST crystal via difference frequency generation," *Applied Physics B,* vol. 124, no. 1, p. 16, 2018.

[342] P. Liu *et al.*, "Widely tunable and monochromatic terahertz difference frequency generation with organic crystal DSTMS," *EPL (Europhysics Letters),* vol. 106, no. 6, p. 60001, 2014.

[343] A. Majkić *et al.*, "Terahertz source at 9.4 THz based on a dual-wavelength infrared laser and quasi-phase matching in organic crystals OH1," *Applied Physics Letters,* vol. 105, no. 14, p. 141115, 2014.

[344] C. Zhang, Y. Avetisyan, A. Glosser, I. Kawayama, H. Murakami, and M. Tonouchi, "Bandwidth tunable THz wave generation in large-area periodically poled lithium niobate," *Optics Express,* vol. 20, no. 8, pp. 8784-8790, 2012.

[345] R. W. Boyd, *Nonlinear optics*. Academic press, 2019.

[346] R. L. Sutherland, *Handbook of nonlinear optics*. CRC press, 2003.

[347] K. Suizu and K. Kawase, "Monochromatic-tunable terahertz-wave sources based on nonlinear frequency conversion using lithium niobate crystal," *IEEE Journal of Selected Topics in Quantum Electronics,* vol. 14, no. 2, pp. 295-306, 2008.

[348] Y. Cao, Y. E, P. Huang, and X.-C. Zhang, "Broadband terahertz wave emission from liquid metal," *Applied Physics Letters,* vol. 117, no. 4, p. 041107, 2020.

[349] N. T. Yardimci, H. Lu, and M. Jarrahi, "High power telecommunication-compatible photoconductive terahertz emitters based on plasmonic nano-antenna arrays," *Applied Physics Letters,* vol. 109, no. 19, p. 191103, 2016.

[350] N. T. Yardimci, S.-H. Yang, C. W. Berry, and M. Jarrahi, "High-power terahertz generation using large-area plasmonic photoconductive emitters," *IEEE Transactions on Terahertz Science and Technology,* vol. 5, no. 2, pp. 223-229, 2015.

[351] S. Preu, M. Mittendorff, H. Lu, H. B. Weber, S. Winnerl, and A. Gossard, "1550 nm ErAs: In (Al) GaAs large area photoconductive emitters," *Applied Physics Letters,* vol. 101, no. 10, p. 101105, 2012.

[352] M. Xu *et al.*, "Terahertz generation and detection with InGaAs-based large-area photoconductive devices excited at 1.55 µ m," *Applied Physics Letters,* vol. 103, no. 25, p. 251114, 2013.

[353] N. T. Yardimci and M. Jarrahi, "Plasmonic large-area photoconductive emitters operating at 1550 nm," in *2016 41st International Conference on Infrared, Millimeter, and Terahertz waves (IRMMW-THz)*, 2016: IEEE, pp. 1-2.

[354] R. J. Dietz, M. Gerhard, D. Stanze, M. Koch, B. Sartorius, and M. Schell, "THz generation at 1.55 µm excitation: six-fold increase in THz conversion efficiency by separated photoconductive and trapping regions," *Optics express,* vol. 19, no. 27, pp. 25911-25917, 2011.

[355] M. Mittendorff *et al.*, "Large area photoconductive terahertz emitter for 1.55 µm excitation based on an InGaAs heterostructure," *Nanotechnology,* vol. 24, no. 21, p. 214007, 2013.

[356] E. Brown, "THz generation by photomixing in ultrafast photoconductors," in *Terahertz Sensing Technology: Volume 1: Electronic Devices and Advanced Systems Technology*: World Scientific, 2003, pp. 147-195.

APPENDIX A   LIST OF PUBLICATIONS

Peer reviewed journal publications related to this thesis

1. **Kathirvel Nallappan**, Yang Cao, Guofu Xu, Hichem Guerboukha, Chahe Nerguizian, Maksim Skorobogatiy, **"Dispersion Limited versus Power Limited Terahertz Communication Links using Solid Core Subwavelength Dielectric Fibers"**, *OSA Photonics research,* vol.8, pp.1757-1775, (2020).

2. **Kathirvel Nallappan**, Hichem Guerboukha, Chahe Nerguizian, Maksim Skorobogatiy, **"Live Streaming of Uncompressed HD and 4K Videos Using Terahertz Wireless Links"** *IEEE Access*, vol.6, pp. 1-16, (2018).

Invited book chapter related to this thesis

1. **Kathirvel Nallappan**, Hichem Guerboukha, Yang Cao, Guofu Xu, Chahe Nerguizian, Daniel M.Mittleman, Maksim Skorobogatiy, **"Fiber-based THz Communication Links within THz Wireless Networks: Needs, Challenges and Perspectives"** in the Next Generation Wireless Terahertz Communication Networks, Editors: S. Ghafoor, M.H. Rehmani, and A. Davy (CRC Press, Taylor and Francis Group, USA, 2020)-Accepted.

Peer reviewed conference publications related to this thesis

1. *Plenary talk:* **Kathirvel Nallappan**, Yang Cao, Hichem Guerboukha, Maksim Skorobogatiy, **"Going Beyond 5G with Optics Based Terahertz Communications: Review of Wireless versus Fiber Links and Enabling Components"** Saratov Fall Meeting, Russia (2020).

2. **Kathirvel Nallappan**, Yang Cao, Guofu Xu, Hichem Guerboukha, Chahe Nerguizian, Maksim Skorobogatiy, **"High Bitrate Terahertz Fiber Communications"** SPIE Photonics North, OT-1-26-1, Canada (2020).

3. *Invited talk:* Maksim Skorobogatiy, Yang Cao, Guofu Xu, Hichem Guerboukha, **Kathirvel Nallappan**, **"Integrated Optical Circuits and Fiber-based Devices for Upcoming THz Communications"** SPIE Photonics North, HP-2-26-2, Canada (2020).

4. **Kathirvel Nallappan**, Yang Cao, Guofu Xu, Hichem Guerboukha, Chahe Nerguizian, Maksim Skorobogatiy, **"Increasing Reliability of Terahertz Communication Links**

Using Onboard Fiber Connectivity" IEEE-Annual Computing and Communication Workshop and Conference (CCWC), pp.1065-1070 (Jan, 2020)

5. <u>**Kathirvel Nallappan**</u>, Hichem Guerboukha, Yang Cao, Chahe Nerguizian, Maksim Skorobogatiy, **"High Bitrate Data Transmission Using Polypropylene Fiber in Terahertz Frequency Range"** The international workshop on Antenna Technology (iWAT), TI-3 USA (2019).

6. **Kathirvel Nallappan**, Hichem Guerboukha, Yang Cao, Chahe Nerguizian, <u>Maksim Skorobogatiy</u>, **"Experimental Demonstration of 5Gbps Data Transmission Using Long Subwavelength Fiber at 140 GHz"** Radio and Wireless Week (RWW), Poster I, 1570495143, USA (2019)

7. **Kathirvel Nallappan**, <u>Hichem Guerboukha</u>, Yang Cao, Chahe Nerguizian, Maksim Skorobogatiy, **"Signal Transmission Using Long Solid Core Terahertz Waveguide"** International conference on Optical Terahertz Science and Technology, P.23 USA (2019)

8. <u>**Kathirvel Nallappan**</u>, Hichem Guerboukha, Chahe Nerguizian, Maksim Skorobogatiy, **"Live Streaming of Uncompressed 4K Video Using Terahertz Wireless Links"** IEEE ICC 2018 Wireless Communications Symposium, I-WCS.01, USA (2018). *(IEEE Communication Society Special Mentioning, Featured Technology for communication - Tech Focus on Above 100 GHz and Terahertz).*

9. <u>**Kathirvel Nallappan**</u>, Hichem Guerboukha, Chahe Nerguizian, Maksim Skorobogatiy, **"Uncompressed HD and Ultra-HD Video Streaming Using Terahertz Wireless Communications"** 11th Global Symposium on Millimeter Waves (GSMM) - Sub-Millimeter-Wave and THz Technologies, USA (2018) (*Finalist in student paper competition*).

10. <u>**Kathirvel Nallappan**</u>, Roberto Morandatti, Maksim Skorobogatiy, **"Generation of High-Power Continuous Wave Terahertz Radiation Using Non-linear Crystals"** Photonics North, 255-se82-232, Canada (2018).

11. <u>**Kathirvel Nallappan**</u>, Hichem Guerboukha, Chahe Nerguizian, Maksim Skorobogatiy, **"Indoor Wireless Transmission of Uncompressed HD and 4K Videos Using Photonics Technologies"** Photonics North, 255-th63-232, Canada (2018).

12. **Kathirvel Nallappan**, Hichem Guerboukha, Chahe Nerguizian, and Maksim Skorobogatiy. **"Practical implementation of live uncompressed 4K video transmission at 140 GHz using photonics technologies"** IEEE, *Infrared, Millimeter, and Terahertz Waves (**IRMMW***), MA1.5, Mexico (2017).

13. **Kathirvel Nallappan**, Hichem Guerboukha, Mohamed Seghilani, Tian Ma, José Azaña, Chahé Nerguizian, and Maksim Skorobogatiy. **"Multiplexing of terahertz wireless communication channels using vortex beams"** IEEE, *Infrared, Millimeter, and Terahertz Waves (**IRMMW***), MB1.2, Mexico (2017).

14. **Kathirvel Nallappan**, Chahe Nerguizian, and Maksim Skorobogatiy. **"Error-Free Transmission of 5 Gbps Data at 140 GHz Using Difference Frequency Generation"** Canadian Association of Physicist congress (**CAP**), 2017.

15. **Kathirvel Nallappan**, Chahe Nerguizian, and Maksim Skorobogatiy. **"Real time transmission of ultra-high bit rate data using photonics based terahertz wireless communication system"** In *Photonics North (PN), 2017*, 8.60, 2017.

16. **Kathirvel Nallappan**, Chahe Nerguizian, and Maksim Skorobogatiy. **"Transmission of Uncompressed 4K Video using photonics based terahertz wireless communication system"** IEEE Research boost ("Give your research an industrial edge"), Montreal,2017

Peer reviewed Journal publications not related to this thesis (Co-author)

1. Yang Cao, **Kathirvel Nallappan**, Hichem Guerboukha, Guofu Xu, and Maksim Skorobogatiy, **"Additive manufacturing of highly reconfigurable plasmonic circuits for terahertz communications"** Optica vol. 7(9), pp. 1112-1125 (2020).

2. Hichem Guerboukha, Yang Cao, **Kathirvel Nallappan**, and Maksim Skorobogatiy **"Super-resolution Orthogonal Deterministic Imaging Technique for Terahertz Subwavelength Microscopy"** ACS Photonics, vol. 7 (7), pp. 1866–1875 (2020).

3. Hichem Guerboukha, **Kathirvel Nallappan**, Yang Cao, Mohamed Seghilani, Jose Azana, Maksim Skorobogatiy, **"Low-loss Porous Optical Components"** Optics Photonics News, December Special issue in Optics, p.49(2019).

4. Jingwen Li, **Kathirvel Nallappan**, **"Optimization of hollow-core photonic Bragg fibers towards practical sensing implementations"** Optical Materials Express, vol. 9(4), pp. 1640-1653 (2019).

5. Hichem Guerboukha, **Kathirvel Nallappan**, Yang Cao, Mohamed Seghilani, Jose Azana, Maksim Skorobogatiy, **"Planar Porous Components for Low-loss Terahertz Optics"** Advanced Optical Materials, P.1900236 (2019).

6. Yang Cao, **Kathirvel Nallappan**, Hichem Guerboukha, Thomas Gervais, Maksim Skorobogatiy, **"Additive Manufacturing of Resonant Fluidic Sensors based on Photonic Bandgap Waveguides for Terahertz Applications"** Optics Express, Vol.27, pp.27663-27681 (2019).

7. Hichem Guerboukha, **Kathirvel Nallappan**, and Maksim Skorobogatiy. **"Towards real-time THz imaging"** *Advances in Optics and Photonics*, vol. 10 (4), pp. 843-938 (2018).

8. Hichem Guerboukha, **Kathirvel Nallappan**, and Maksim Skorobogatiy. **"Exploiting k-space/frequency duality toward real-time terahertz imaging"** *Optica* 5, no. 2 (2018): 109-116.

9. Jingwen Li, **Kathirvel Nallappan**, Hichem Guerboukha, and Maksim Skorobogatiy. **"3D printed hollow core terahertz Bragg waveguides with defect layers for surface sensing applications"** *Optics express* 25, no. 4 (2017): 4126-4144.

10. Tian Ma, **Kathirvel Nallappan**, Hichem Guerboukha, and Maksim Skorobogatiy. **"Analog signal processing in the terahertz communication links using waveguide Bragg gratings: example of dispersion compensation"** *Optics Express* 25, no. 10 (2017): 11009-11026.

Peer reviewed Conference publications not related to this thesis

1. <u>**Kathirvel Nallappan**</u>, Hichem Guerboukha, Maksim Skorobogatiy, **"Reconfigurable Terahertz Array Antenna"** The international workshop on Antenna Technology (iWAT), Poster, WI-4 : Technical Interactive Session, 1570508171, USA (2019).

2. <u>**Kathirvel Nallappan**</u>, Jingwen Li, Hichem Guerboukha, Andrey Markov, Branko Petrov,Denis   Morris, Maksim Skorobogatiy, **"High Speed Terahertz Near-field**

Imaging Using Spatial Wavefront Modulator" Canadian Association of Physicist congress (CAP), **2017**.

3. **<u>Kathirvel Nallappan</u>**, Jingwen Li, Hichem Guerboukha, Andrey Markov, Branko Petrov,Denis   Morris, Maksim Skorobogatiy, **"A Dynamically Reconfigurable Terahertz Array Antenna for 2D-Imaging Applications"** 36.30, Photonic North, 36.30, Canada, 2017.